12-2000

Questing for the Grail: Core Collapse Supernova Simulations With Boltzmann Neutrino Transport

Otis Earl Messer
University of Tennessee - Knoxville

To the Graduate Council:

I am submitting herewith a dissertation written by Otis Earl Messer entitled "Questing for the Grail: Core Collapse Supernova Simulations With Boltzmann Neutrino Transport." I have examined the final electronic copy of this dissertation for form and content and recommend that it be accepted in partial fulfillment of the requirements for the degree of Doctor of Philosophy, with a major in Physics.

Anthony Mezzacappa, Major Professor

We have read this dissertation and recommend its acceptance:

Michael Strayer, Michael Guidry, Jack Dongarra

Accepted for the Council:
Carolyn R. Hodges

Vice Provost and Dean of the Graduate School

(Original signatures are on file with official student records.)

To the Graduate Council:

I am submitting herewith a dissertation written by Otis Earl Messer II entitled "Questing for the Grail: Core Collapse Supernova Simulations With Boltzmann Neutrino Transport." I have examined the final copy of this dissertation for form and content and recommend that it be accepted in partial fulfillment of the requirements for the degree of Doctor of Philosophy, with a major in Physics.

Anthony Mezzacappa

Anthony Mezzacappa, Major Professor

We have read this dissertation
and recommend its acceptance:

Michael Strayer

Michael Guidry

Jack Dongarra

Accepted for the Council:

Anne Mayhew

Interim Vice Provost
and Dean of the Graduate School

(Original signatures are on file in The Graduate Admissions and Records Office.)

Questing For the Grail: Spherically Symmetric Supernova Simulations With Boltzmann Neutrino Transport

A Dissertation

Presented for the

Doctor of Philosophy

Degree

The University of Tennessee, Knoxville

Otis Earl Messer II

December 2000

DEDICATION

This dissertation is dedicated

to the memory of my grandmother,

Dixie Messer.

Acknowledgments

First, I thank my major professor Tony Mezzacappa. He has indulged, prodded, supported, pushed, and, I think, bettered me. He has taught me, in many ways, how to be a professional scientist. I do not think it inappropriate to say I will always try to make him proud of me. *Viva il Duce!*

Mike Guidry deserves my thanks no less. He was particularly gracious, and apparently wise, in allowing me to work with Tony. He has been a remarkable advocate on my behalf with many people and has afforded me a level of respect I cannot help but think is rare for any student to receive.

I thank Mike Strayer for first roping me into doing computational astrophysics and being so kind and helpful for the several years I have spent in the Theoretical Physics Section at ORNL. I also appreciate Jack Dongarra doing something very difficult for him: finding time to serve on my committee.

This thesis would not have been possible without the contributions of Matthias Liebendörfer. He has been, with the exception of Tony, my closest collaborator on this project, and I have enjoyed every minute of it. He has become my close friend as well. I hope (and I belive) Matthias feels the same way about our collaboration as I do.

I heartily thank my "professional big brother," Raph Hix. Raph has been a wonderful sounding board, reality check, nuclear physics expert, and office mate. He also has been a superlative advocate on my behalf in many ways.

Thanks go to my original office mate at ORNL, Alan Calder. Our hours of learning supernova physics together are among the best memories I have of graduate school.

My parents deserve more thanks from me than I can convey, but this is a good place to try. Thank you for loving me. Thank you for teaching me life is tough, you just have to be tougher,

and that fact is no reason to despair. Thank you for never doubting my ability or purpose.

Finally, especially for the patience and steadfast certainty with which she has endured most of my graduate career, I thank my wife, Marissa. I'll never be able to accomplish it, but I promise to spend the rest of my life trying to repay you for your help and for loving me.

Abstract

The importance of exact neutrino transport in spherically symmetric core collapse supernova simulations is explored in this dissertation. The primary tool for these studies is the neutrino radiation hydrodynamics code AGILE-BOLTZTRAN (Mezzacappa & Bruenn 1993a,b,c; Mezzacappa & Messer 1998; Liebendörfer 2000). AGILE-BOLTZTRAN couples the solution of the Boltzmann equation for all three flavors of neutrinos and antineutrinos to a one-dimensional, implicit, adaptive grid hydrodynamics code. Emission, absorption, and scattering of neutrinos from nucleons and nuclei, neutrino-electron scattering, and pair production and annihilation are included as neutrino-matter couplings. Details of the code are described, including the equations solved and their finite difference representations. The radiation transport algorithm is also subjected to a suite of test problems.

Marked differences in neutrino observables computed with AGILE-BOLTZTRAN compared to a sophisticated approximate method (MGFLD) are seen in stationary state transport simulations in typical postbounce environments. Neutrino heating rates are seen to differ by as much as a factor of two between the transport methods. These differences are the result of small changes in neutrino RMS energies, coupled to larger differences in neutrino luminosity and isotropy.

Collapse simulations comparing two $15M_{\odot}$ progenitor models with small differences in initial Y_e (Woosley & Weaver 1995; Heger et al. 2000) exhibit no differences in Y_e at bounce, and, consequently, no difference in homologous core mass or postbounce evolution.

Simulations of core collapse, rebound, and shock propogation for $15M_{\odot}$ and $20M_{\odot}$ progenitor models of Nomoto & Hashimoto (1988) fail to produce explosions. In both cases, the shock stalls at $\approx$ 200 km, then recedes for several hundred milliseconds. The covergence of all the dynamic results highlights the need for further studies of a wide range of models and the need

for improved microphysics in AGILE-BOLTZTRAN. There exists a continued need for exact neutrino transport simulations in order to unequivocally establish the nature of the supernova explosion mechanism and to obtain accurate neutrino data for nucleosynthesis calculations and neutrino signature predictions.

Contents

1 Introduction **1**

1.1 The Life and Death of a Massive Star . . . 2

1.2 Shock Stagnation and Reheating . . . 5

1.3 A Short History of Neutrino Transport . . . 6

2 Radiation Hydrodynamics **12**

2.1 Equations . . . 13

2.1.1 Hydrodynamics with Radiation Coupling . . . 13

2.1.2 Neutrino Transport . . . 17

2.1.3 Lepton Conservation . . . 19

2.2 Neutrino Interactions . . . 20

2.2.1 Emission and Absorption . . . 21

2.2.2 Isoenergetic Scattering . . . 24

2.2.3 Neutrino–Electron Scattering . . . 29

2.2.4 Pair Emission and Absorption . . . 38

3 Finite Differencing and Numerical Implementation **42**

3.1 Grid . . . 42

3.1.1 Variables and Their Derivatives . . . 45
3.2 Differencing the Neutrino Boltzmann Equation . . . 48
3.3 Differencing the Neutrino Interaction Terms in the Energy Equation and the Y_e Equation . . . 61
3.4 Computing the Observer Corrections . . . 65
3.4.1 Frequency Shift . . . 65
3.4.2 Angular Aberration . . . 72
3.5 Differencing the Neutrino Stress . . . 76

4 Radiation Transport Test Problems **77**
4.1 Bruenn's Unisphere Problem . . . 77
4.2 Lund's Cooling Problem . . . 84
4.3 The Spherical Milne Problem . . . 92

5 Stationary State Simulations with BOLTZTRAN **101**
5.1 Introduction . . . 101
5.2 Initial Models, Codes, and Methodology . . . 102
5.3 Results . . . 106
5.4 Summary and Discussion . . . 120

6 Collapse Simulations of Two $15M_\odot$ Progenitor Models **125**
6.1 Introduction . . . 125
6.2 Pre-collapse Structure . . . 126
6.3 Results . . . 130
6.4 Trapping, Equilibration, and Core Convergence . . . 131

7 The Nomoto-Hashimoto 15 $M_\odot$ Simulation **144**

7.1 Introduction 144

7.2 Results 145

8 The Nomoto-Hashimoto 20 $M_\odot$ Simulation **170**

8.1 Introduction 170

8.2 Results 172

9 Conclusions and Outlook **196**

Bibliography **199**

Vita **205**

List of Tables

2.1 NES coefficients for various neutrino flavors 30

5.1 Maximum net heating/cooling rates 122

List of Figures

1.1 Postbounce core configuration. 7

3.1 Schematic example of recubing as the hydrodynamic trajectory evolves. The Ye dimension is suppressed for clarity. 49

4.1 Electron neutrino and antineutrino luminosities for the Unisphere problem. . . . 79

4.2 Electron neutrino and antineutrino RMS energies for the Unisphere problem. . . 81

4.3 Electron neutrino and antineutrino inverse flux factors for the Unisphere problem. 82

4.4 Closeup view near the edge of the core of electron neutrino and antineutrino inverse flux factors for the Unisphere problem. 83

4.5 Density profile for the Lund problem 85

4.6 Initial temperature profile for the Lund problem 87

4.7 Initial energy density profile for the Lund problem 88

4.8 Photon mean free path as a function of radius for the Lund problem 89

4.9 Average μ as a function of radius for the Lund problem 90

4.10 Eddington factor as a function of radius for the Lund problem 91

4.11 Internal energy, radiation energy, emitted energy, and total energy for the Lund problem 93

4.12 f_k versus radius for 6-point Gaussian quadrature and $R_0 = 0.01$, 0.1, 1, and 10 . 95

4.13 f_k and f_h versus radius for various Gaussian quadrature sets and $R_0 = 0.01, 1,$ and 10 97

4.14 f_k versus f_h for various Gaussian quadrature sets and $R_0 = 10$ and 0.33 99

5.1 Density, temperature, and Ye for model S15s7b at 106 ms after core bounce. . . . 103

5.2 Density, temperature, and Ye for model S15s7b at 233 ms after core bounce. . . . 104

5.3 Density, temperature, and Ye for model S25s7b at 156 ms after core bounce. . . . 105

5.4 RMS energies, luminosities, and mean inverse flux factors for model S15s7b at 233 ms after core bounce. 108

5.5 The density and MGBT electron neutrino and antineutrino luminosity sum are plotted versus radius for model S15s7b at $t_{\rm pb} = 233$ ms. 110

5.6 RMS energies, luminosities, and mean inverse flux factors for model S15s7b at 106 ms after core bounce. 112

5.7 The density and MGBT electron neutrino and antineutrino luminosity sum are plotted versus radius for model S15s7b at $t_{\rm pb} = 106$ ms. 113

5.8 RMS energies, luminosities, and mean inverse flux factors for model S25s7b at 156 ms after core bounce. 114

5.9 The density and MGBT electron neutrino and antineutrino luminosity sum are plotted versus radius for model S25s7b at $t_{\rm pb} = 156$ ms. 115

5.10 Net heating rates for model S15s7b at 233 ms after core bounce. 117

5.11 Net heating rates for model S15s7b at 106 ms after core bounce. 119

5.12 Net heating rates for model S25s7b at 156 ms after core bounce. 121

5.13 The sum of the electron neutrino and antineutrino luminosities from the MGFLD dynamic run for model S15s7b are plotted versus radius. The luminosities from five different postbounce times are shown. 123

6.1 Initial Y_e profiles for three different $15M_\odot$ models 127
6.2 Initial temperature profiles for the two Woosley $15M_\odot$ models 128
6.3 Initial density profiles for the two Woosley $15M_\odot$ models 129
6.4 Y_e profiles for central densities of 1×10^{11} and $1 \times 10^{12} g/cm^3$ 132
6.5 Y_e profiles for central densities of 1×10^{13} and $2.96 \times 10^{14} g/cm^3$ 133
6.6 Velocity profiles for central densities of 1×10^{11} and $1 \times 10^{12} g/cm^3$ 134
6.7 Velocity profiles for central densities of 1×10^{13} and $2.96 \times 10^{14} g/cm^3$ 135
6.8 Density profiles for central densities of 1×10^{11} – $2.96 \times 10^{14} g/cm^3$ 136
6.9 Temperature profiles for central densities of 1×10^{11} – $2.96 \times 10^{14} g/cm^3$ 137
6.10 Lepton fractions as a function of density for mass element at $0.05M_\odot$ with representative A and Z from the LS EOS 138
6.11 Lepton fractions as a function of density for mass element at $0.64M_\odot$ with representative A and Z from the LS EOS 141
6.12 Lepton fractions as a function of density for mass element at $1.0M_\odot$ with representative A and Z from the LS EOS 142

7.1 Initial conditions for the Nomoto-Hashimoto $15M_\odot$ model 146
7.2 Radial trajectories of equal mass shells for the Nomoto-Hashimoto $15M_\odot$ model 147
7.3 Density profiles at various central densities during collapse of the Nomoto-Hashimoto $15M_\odot$ model 149
7.4 Entropy profiles at various central densities during collapse of the Nomoto-Hashimoto $15M_\odot$ model 150
7.5 Y_e profiles at various central densities during collapse of the Nomoto-Hashimoto $15M_\odot$ model 151

7.6 Velocity profiles at various central densities during collapse of the Nomoto-Hashimoto $15M_\odot$ model . . . 152
7.7 Neutrino luminosities at 1000 km as a function of time since the onset of collapse for the Nomoto-Hashimoto $15M_\odot$ model . . . 153
7.8 Neutrino RMS energies at 1000 km as a function of time since the onset of collapse for the Nomoto-Hashimoto $15M_\odot$ model . . . 155
7.9 Core conditions at 0.5 ms after core bounce for the Nomoto-Hashimoto $15M_\odot$ model . . . 156
7.10 Core conditions at 7.2 ms after core bounce for the Nomoto-Hashimoto $15M_\odot$ model . . . 157
7.11 Core conditions at 37 ms after core bounce for the Nomoto-Hashimoto $15M_\odot$ model . . . 158
7.12 Core conditions at 58 ms after core bounce for the Nomoto-Hashimoto $15M_\odot$ model . . . 159
7.13 Core conditions at 114 ms after core bounce for the Nomoto-Hashimoto $15M_\odot$ model . . . 160
7.14 Core conditions at 214 ms after core bounce for the Nomoto-Hashimoto $15M_\odot$ model . . . 161
7.15 Core conditions at 283 ms after core bounce for the Nomoto-Hashimoto $15M_\odot$ model . . . 162
7.16 Core conditions at 335 ms after core bounce for the Nomoto-Hashimoto $15M_\odot$ model . . . 163
7.17 Core conditions at 379 ms after core bounce for the Nomoto-Hashimoto $15M_\odot$ model . . . 164

7.18 Animation depicting the velocity and Y_e profiles for the inner 500 km of the core (Quicktime format, Sorensen compression, 2.85 MB). 166
7.19 Inverse flux factors for electron neutrrinos at various post-bounce times for the Nomoto-Hashimoto $15M_\odot$ model 167
7.20 Net neutrino heating rates from emission and absorption of electron neutrinos and antineutrinos at various post-bounce times for the Nomoto-Hashimoto $15M_\odot$ model 169

8.1 Initial conditions for the Nomoto-Hashimoto $20M_\odot$ model 171
8.2 Radial trajectories of equal mass shells for the Nomoto-Hashimoto $20M_\odot$ model 173
8.3 Density profiles at various central densities during collapse for the Nomoto-Hashimoto $20M_\odot$ model 174
8.4 Entropy profiles at various central densities during collapse for the Nomoto-Hashimoto $20M_\odot$ model 175
8.5 Y_e profiles at various central densities during collapse for the Nomoto-Hashimoto $20M_\odot$ model 176
8.6 Velocity profiles at various central densities during collapse for the Nomoto-Hashimoto $20M_\odot$ model 177
8.7 Neutrino luminosities as a function of time since the onset of collapse at 1000 km for the Nomoto-Hashimoto $20M_\odot$ model 179
8.8 Neutrino RMS energies as a function of time since the onset of collapse at 1000 km for the Nomoto-Hashimoto $20M_\odot$ model 180
8.9 Core conditions at 0.5 ms after core bounce for the Nomoto-Hashimoto $20M_\odot$ model 181

8.10 Core conditions at 3.2 ms after core bounce for the Nomoto-Hashimoto $20M_{\odot}$ model . . . 182
8.11 Core conditions at 57 ms after core bounce for the Nomoto-Hashimoto $20M_{\odot}$ model . . . 183
8.12 Core conditions at 81 ms after core bounce for the Nomoto-Hashimoto $20M_{\odot}$ model . . . 184
8.13 Core conditions at 146 ms after core bounce for the Nomoto-Hashimoto $20M_{\odot}$ model . . . 185
8.14 Core conditions at 239 ms after core bounce for the Nomoto-Hashimoto $20M_{\odot}$ model . . . 186
8.15 Core conditions at 307 ms after core bounce for the Nomoto-Hashimoto $20M_{\odot}$ model . . . 187
8.16 Core conditions at 359 ms after core bounce for the Nomoto-Hashimoto $20M_{\odot}$ model . . . 188
8.17 Core conditions at 396 ms after core bounce for the Nomoto-Hashimoto $20M_{\odot}$ model . . . 189
8.18 Core conditions at 448 ms after core bounce for the Nomoto-Hashimoto $20M_{\odot}$ model . . . 190
8.19 Animation depicting the velocity and Y_e profiles for the inner 500 km of the core (Quicktime format, Sorensen compression, 3.41 MB). . . . 191
8.20 Inverse flux factors for electron neutrinos at various post-bounce times for the Nomoto-Hashimoto $20M_{\odot}$ model . . . 192

8.21 Net neutrino heating rates from emission and absorption of electron neutrinos and antineutrinos at various post-bounce times for the Nomoto-Hashimoto $20M_{\odot}$ model 194

List of Multimedia Objects

7.18 Animation depicting the velocity and Y_e profiles for the inner 500 km of the core (Quicktime format, Sorensen compression, 2.85 MB). 166

8.19 Animation depicting the velocity and Y_e profiles for the inner 500 km of the core (Quicktime format, Sorensen compression, 3.41 MB). 191

Chapter 1

Introduction

"... In the first year of the period Chih-ho, the fifth moon, the day chi-ch'ou, a guest star appeared approximately several inches south-east of Tien-Kuan [Zeta Tauri]. After more than a year, it gradually became invisible ..." (Mitton 1978)

On July 4, 1054, Chinese astrologers recorded the appearance of a "guest star" in what is known in the West as the constellation Taurus. The object was about four times brighter than Venus and was visible to the naked eye during the day for more than three weeks. This portent was, in fact, the visual display from a supernova[1] explosion some 3500 light years away. The remnant formed in that explosion is one of the most famous of all deep-space objects: M1, the Crab Nebula. Why and how do stars explode? Are there other, less ostentatious, consequences associated with such a mammoth energy release?

Core collapse supernovae are among the most energetic events in the Cosmos, releasing 10^{53} erg of energy on timescales of a few tens of seconds. They produce and disseminate many of

[1]The term 'supernova' in this dissertation is used to refer to a core collapse supernova. Core collapse supernovae (Type Ia, Ic, and II) result from the gravitational collapse of the iron core of an evolved star. In contrast, thermonuclear supernovae (Type Ib) occur when a white dwarf in a binary system has accreted enough matter from its companion to ignite a thermonuclear runaway.

the elements heavier than helium, making life as we know it possible. They mark the birth of neutron stars, and, perhaps, black holes. They are incredibly complex events, requiring input from all the major fields of modern physics – nuclear physics, particle physics, relativity, solid-state physics – and modern computational methods to describe them adequately. For all these reasons, the solution of the supernova problem has been called the Holy Grail of modern astrophysics.

For all their complexity, spectacular visual display, and other attendant phenomena, core collapse supernovae are neutrino events. Virtually all ($\sim$99%) of the 10^{53} ergs of gravitational binding energy released in the formation of the nascent neutron star is carried away in the form of neutrinos of all six flavors. Descriptions of supernova neutrino emission often sound like hyperbole, especially to those who possess some familiarity with neutrinos and their interactions with matter. Neutrinos are the apotheosis of "ghostly": witness their famous ability to pass through a light year of lead unimpeded. Nevertheless, the neutrino burst from a supernovae at the position of our Sun would kill a human observer standing on Pluto. More than being the subject of fantastic tales, neutrinos are an essential ingredient in producing supernovae explosions. They are the drivers of the explosion, whatever other effects might influence the final observables or aid explosion. How is such an implausible scenario realized? First, we need to examine supernovae progenitors.

1.1 The Life and Death of a Massive Star

Baade & Zwicky (1934) were the first to connect the death of a massive star in a supernova to the birth of a neutron star. Neutron stars themselves had been proposed only two years earlier by Landau (1932). Baade and Zwicky made simple energy arguments, noting the binding energy of a neutron star($\sim 10^{53}$ erg) seemed a natural source of the awesome energy of newly identified

supernovae. Burbidge et al. (1957) first developed the model of massive star evolution wherein successive thermonuclear burning stages of increasingly heavier elements lead to an "onion skin" configuration. An inner iron core is surrounded by shells of lighter elements, including, silicon, oxygen, helium, and hydrogen. In that paper and in Hoyle & Fowler (1960), supernovae are thought to be caused by an explosion of the oxygen shell as it is heated and compressed following the iron core inward during collapse. These papers, although proven incorrect in detail as observations improved and new microphysics were introduced, laid the foundation of the origins of supernova in the collapse of the iron core of a massive star and the subsequent formation of a neutron star.

Massive stars ($>\sim 10 M_\odot$), like those that produce supernovae, live exceedingly short lives compared to our Sun (tens of millions vs. ten billion years). The timescales associated with the formation of the stratified "onion skin" structure described above are remarkable. For example, an imaginary $25 M_\odot$ star born 11 million years ago exhausted the supply of hydrogen in its core about 700,000 B.C. The burning of the next available nuclear fuel, helium, continued from then until about 45,000 B.C., about the time *Homo sapiens* began to appear on Earth. The dawn of agriculture corresponds to core carbon ignition in our imaginary star ($\sim$ 10,000 B.C.). Neon burning started approximately two decades ago; oxygen ignition occurred only half a decade ago; silicon burns for only one week and a half as the star approaches its spectacular death. It is important to note that the outer layers of the star, beyond the silicon and oxygen layers, will not directly participate in the birth of the supernova. They are thousands of kilometers distant from events that will take only milliseconds. The important events from this point on all take place within the iron core of the star.

The iron core is inert to further nuclear burning because iron sits atop the curve of nuclear binding energy. The core does cool via neutrino emission and quasi-statically contracts as the

evolution continues. The neutrinos emitted at the central densities before collapse ($< 10^9 g/cm^3$) escape freely, carrying away energy and thermal pressure support from the core. Most of the pressure support, however, comes from the relativistic, degenerate sea of electrons in the core. This support is also being depleted by the neutrino emission: neutrinos are produced by electron captures on protons in the core, reducing the degeneracy of the electrons. More important, however, is the reduction in pressure caused by the photodissociation of iron as the temperature increases. This is an isentropic process, so a transfer of entropy occurs from the electrons to the newly liberated nucleons. Shortly after reaching a central density of $\sim 10^9 g/cm^3$, unable to support itself against its own gravity, the core collapses.

The velocity structure of the core quickly assumes a binary character. The inner part of the core collapses homologously and subsonically. The outer core collapses supersonically at about half the free-fall velocity. The division between inner and outer core is marked by the sonic point, i.e. the radius at which the local sound speed equals the infall velocity.

The collapse is accelerated by the increasing electron chemical potential, which increases the electron capture rate, removing even more of the pressure support provided by the electrons. The neutrinos produced by electron capture continue to stream from the core, until densities greater than $\sim 6x10^{11} g/cm^3$ are reached. At these densities, weak neutral-current interactions serve to reduce the neutrino mean free paths to less than the size of the collapsing core. The neutrinos become trapped in the infalling matter.

The trapped neutrinos are important to the subsequent evolution of the core. Trapping serves to keep the entropy low as the collapse continues. The core is therefore able to collapse to central densities exceeding that of nuclear matter. Before the realization of trapping (Mazurek 1975; Sato 1975), simulated cores bounced at much lower densities, $\sim 10^{13} g/cm^3$, as core neutronization continued unabated and neutron drip led to a stiff ($\gamma = 5/3$) gas of free neutrons

(Colgate & White 1966; Arnett 1967). With trapping, the pressure of the inner core continues to be dominated by the electrons, until the repulsive, nonrelativistic nuclear mater component serves to stiffen the equation of state. The inner core rebounds as a unit, sending pressure waves outward. These pressure waves steepen to form a shock at the sonic point, usually at a radius of some tens of kilometers. This shock begins to propagate outward, heating and dissociating material as it moves to larger radii.

1.2 Shock Stagnation and Reheating

For particular choices of progenitor mass and equation of state, the shock is seen to propagate out of the core producing an explosion in some simulations (e.g. Hillebrandt et al. (1984); Baron et al. (1985)). However, in most simulations, the shock stalls at at a radius of $\approx$ 200 km (cf. Bruenn (1985); Myra et al. (1987)), becoming a standing accretion shock. The shock is robbed of pressure support by two processes: (1) dissociation losses as nuclei pass through the shock and are converted to free nucleons and helium, and (2) electron capture on the resulting free protons, producing neutrinos that are able to escape the core. The inner core, which launched the shock, begins to settle into hydrostatic equilibrium over several milliseconds. This hot, distended object is the "protoneutron star" or PNS. The PNS radiates neutrinos of all types as it cools and contracts, becoming a canonical neutron star if the explosion is successful. Without the further propagation of the shock, the PNS is doomed to be swallowed by a forming black hole as it accretes infalling matter and grows in mass.

Wilson (Wilson 1985; Bethe & Wilson 1985) found that material behind the stalled shock can be heated by neutrinos radiated by the PNS, thereby reviving the shock and leading to an explosion. However, those early results have not been replicated by any other group, nor by Wilson, without the invocation of convection (Wilson & Mayle 1988, 1993). Nevertheless, the

notion of reenergizing the shock through neutrino heating has become the standard paradigm of modern supernovae theory. This "delayed explosion mechanism" is almost universally accepted as the way supernovae explode, at least for stars of mass $> 10M_{\odot}$. The typical delayed explosion configuration is shown in Figure 1.1. The neutrinosphere is analogous to the more familiar photosphere of stellar physics, and is the radius at which the neutrino optical depth equals 2/3. The neutrinosphere and the shock bound a region within which neutrino emission and absorption, primarily on shock dissociated nucleons, profoundly affect the local matter. There is a region of net neutrino cooling near the neutrinosphere below a region of net heating nearer the shock. The radius where cooling balances heating is called the gain radius. The efficiency with which matter is heated between the gain radius and the shock determines the success or failure of the delayed explosion mechanism. If a parcel of matter can be heated sufficiently to reverse its infall, the shock can be reenergized. Much recent activity in this regard has been centered on the role of convection as an aid in shock reheating (Mezzacappa et al. 1998a,b; Janka & Müller 1996a; Burrows et al. 1995). However, here we will concentrate on the role improved neutrino transport might have in this delayed shock mechanism.

1.3 A Short History of Neutrino Transport

Colgate & White (1966) were the first to perform accurate hydrodynamic modeling of core collapse and shock formation incorporating neutrino interactions. In those simulations, the collapsing core rebounded at nuclear matter densities as the completely neutronized inner core stiffened, forming an accretion shock. As matter was heated by this shock, thermal neutrino pairs were produced with a typical blackbody temperature of ~ 40 MeV. This sort of "reheating" scenario might be seen as a foreshadowing of the modern idea of shock reheating from core neutrinos. The "transport" of these neutrinos was crude at best: Colgate & White deposited

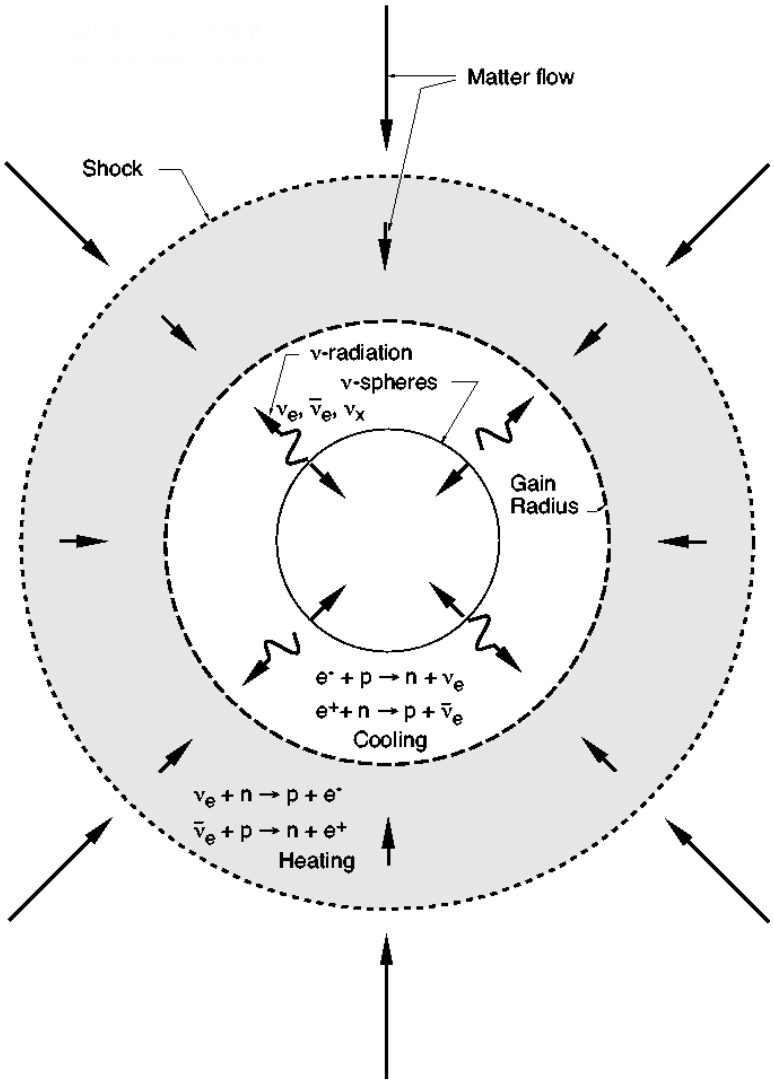

Figure 1.1: Postbounce core configuration.

one half of the energy of these thermal pairs in the infalling mantle, letting the remainder escape. This seemed a fair approximation to the energy transport for neutrinos with intermediate mean free paths. The deposited energy produced energetic explosions. Arnett (1966, 1967) refined the method of Colgate & White (1966), solving a diffusion equation for neutrino energy instead of relying on an *ad hoc* prescription to model energy transport. Foreshadowing a trend, this improved treatment of supernova physics led to failures rather than the hyper-energetic supernovae of Colgate & White (1966).

Neutrino leakage schemes were developed in the early 1980's (Van Riper & Lattimer 1981). These schemes approximate neutrino transport by allowing trapped neutrinos to leak out of a shell on some leakage timescale depending on the mean free path. This timescale is interpolated between a random walk timescale for diffusive zones to a light crossing time where the neutrinos are free streaming. This type of scheme reproduces gross energetics reasonably well, but the "leaked" neutrinos are not allowed to deposit energy or momentum once they leave a mass shell. It is therefore impossible to model neutrino reheating using this type of scheme.

Two-fluid schemes represent a logical improvement over leakage schemes (Cooperstein et al. 1986; Hillebrandt et al. 1984). The neutrinos and matter are treated as two interpenetrating fluids, each having a well-defined temperature. However, the two fluids are not thermally equilibrated with one another. The fluids exchange energy, momentum, and baryon and lepton number. The assumption of equilibrium for the neutrino component cannot be motivated physically and should be considered as a parameterization.

Before and contemporaneous with the development of these more approximate schemes was the development of multigroup flux-limited diffusion (MGFLD) schemes (Arnett 1977; Bowers & Wilson 1982; Bruenn 1985; Myra et al. 1987). MGFLD is the most sophisticated of all approximate approaches to neutrino transport. Its added realism comes at some computational

cost, so its uses to date have been mostly confined to spherically symmetric simulations.

MGFLD closes the hierarchy of neutrino radiation hydrodynamics equations at the level of the first moment (the neutrino flux) by imposing a relationship between the flux and the gradient of the neutrino energy density (the zeroth moment). For example,

$$\psi^1 = -\frac{c\Lambda}{3}\frac{\partial \psi^0}{\partial r} + ..., \tag{1.1}$$

$$\Lambda = \frac{1}{1/\lambda + |\partial \psi^0/\partial r|/3\psi^0}, \tag{1.2}$$

where λ is the neutrino mean free path (Bruenn 1985). (Other forms for the flux-limiter Λ can be found in Bowers & Wilson (1982); Levermore (1981); Myra et al. (1987).) The method is "multigroup" in that the transport is carried out for each neutrino energy separately. Because of the energy dependence of the neutrino interactions, and consequently, mean free paths, neutrinos of different energies may behave very differently. The term "flux limited" means that the flux is kept from exceeding the maximum flux, which would obtain if the neutrinos were streaming out radially at the speed of light. If diffusion theory were used to describe the transport in this instance, the neutrino flux would be superluminal. This happens because diffusion theory assumes that the neutrinos always propagate a distance given by their mean free path, even if this distance exceeds the distance that could be traversed by the neutrinos in a time Δt, moving at the speed of light (Mihalas & Mihalas 1984).

Whereas the limits $\lambda \rightarrow 0$ and $\lambda \rightarrow \infty$ produce the correct diffusion and free streaming fluxes, it is in the critical intermediate regime where the MGFLD approximation is of unknown accuracy. Unfortunately, the quantities central to the postshock neutrino heating, i.e., the neutrino luminosities, spectra, and distributions in angle, are determined in this regime, and

given the sensitivity of the neutrino heating to these quantities (e.g., see Burrows & Goshy (1993); Janka & Müller (1996b); Mezzacappa et al. (1998a); Messer et al. (1998)), it becomes necessary to consider more accurate transport schemes. Moreover, in detailed one-dimensional simulations that have implemented elaborate MGFLD neutrino transport (e.g., see Bruenn (1993); Wilson & Mayle (1993); Swesty & Lattimer (1994)), explosions were not obtained unless the neutrino heating was boosted by additional phenomena, such as convection.

Modern computing power has enabled consideration of full Boltzmann transport of neutrinos in supernovae simulations, at least in spherically symmetric models. This dissertation describes a series of studies performed with the computer code AGILE-BOLTZTRAN, a fully implicit neutrino radiation hydrodynamics code (Mezzacappa & Bruenn 1993a,b,c; Mezzacappa & Messer 1998; Liebendörfer 2000). It is the latest implemention of a neutrino transport algorithm coupled to hydrodynamics having its origins in Mezzacappa & Matzner (1989) and realized, in large part, in its current state in Mezzacappa & Bruenn (1993a,b,c). AGILE-BOLTZTRAN solves the neutrino Boltzmann equation for all three flavors of neutrinos and their corresponding antineutrinos. Emission, absorption, and scattering from nuclei and nucleons, neutrino-electron scattering, and pair production and annihilation are included in the interaction terms calculated. The Boltzmann solver is coupled to an implicit, adaptive mesh hydrodynamics code capable of evolving flows in both the Newtonian and general relativistic limits (Liebendörfer 2000). (In this dissertation, only Newtonian simulations are considered. The reader is directed to Liebendörfer (2000) for a full discussion of GR simulations).

In chapters 2 and 3 the equations solved by AGILE-BOLTZTRAN are presented in detail, and the finite differencing implemented is described. Chapter 4 contains results of three radiation transport test problems. The study of supernovae truly begins in Chapter 5, where neutrino quantities vital to shock reheating computed with Boltzmann transport and MGFLD

are compared in realistic post-bounce environments. In Chapter 6, core collapse simulations of two very similar progenitor stars with slightly different microphysics employed during evolution calculations is presented. Full radiation hydrodynamic simulations of core collapse, bounce, and shock propagation and stagnation are presented in Chapter 7 (for a $15M_{\odot}$ progenitor) and Chapter 8 (for a $20M_{\odot}$ progenitor). Conclusions and a list of future improvements and goals are given in Chapter 9.

Chapter 2

Radiation Hydrodynamics

In this chapter, the equations solved by AGILE-BOLTZTRAN and details of the microphysics employed in the code will be presented. Note that in the present version of AGILE-BOLTZTRAN, the equations presented here are the ones solved, but, in a few instances, details of the discretization and solution method are slightly different from those found in Mezzacappa & Bruenn (1993b) and Mezzacappa & Messer (1998). (The preponderance of this chapter is found in Mezzacappa & Bruenn (1993a) and Mezzacappa & Bruenn (1993c), with the exception of expressions involving neutrino pair creation and annihilation. Also, some expressions are presented here with antineutrino processes included explicitly.) The proper discretization of the hydrodynamics can be found in Liebendörfer (2000). The discretization of the Boltzmann equation, the electron fraction equation, and the radiation–matter coupling terms in the velocity and energy equations will be discussed in Chapter 3.

2.1 Equations

2.1.1 Hydrodynamics with Radiation Coupling

The Newtonian-gravity, $O(v/c)$, Lagrangian hydrodynamics equations are (in what follows, r is the Eulerian radial coordinate, and m is the Lagrangian mass coordinate) (Mihalas & Mihalas 1984):

$$\frac{\partial r}{\partial m} = \frac{1}{4\pi r^2 \rho} \ , \tag{2.1}$$

$$\begin{aligned}
\frac{\partial \epsilon}{\partial t} &= \frac{-P}{\rho}\frac{\partial ln\rho}{\partial t} - 4\pi r^2 Q \frac{\partial v}{\partial m} \\
&- \sum_{\nu_e,\bar{\nu}_e} \frac{2\pi c\, C_0}{h^3 c^3} \int dE E^3 d\mu (\frac{j}{\rho} - \tilde{\chi} F) \\
&+ \sum_{\nu_e,\bar{\nu}_e,\nu_{\mu,\tau},\bar{\nu}_{\mu,\tau}} \frac{2\pi C_0}{h^6 c^6} \int dE E^3 d\mu F \int dE' E'^2 d\mu' \tilde{R}^{\rm out}_{\rm NES}(\frac{1}{\rho} - F) \\
&- \sum_{\nu_e,\bar{\nu}_e,\nu_{\mu,\tau},\bar{\nu}_{\mu,\tau}} \frac{2\pi C_0}{h^6 c^6} \int dE E^3 d\mu (\frac{1}{\rho} - F) \int dE' E'^2 d\mu' \tilde{R}^{\rm in}_{\rm NES} F \\
&+ \sum_{\nu_e,\nu_{\mu,\tau}} \frac{2\pi C_0}{h^6 c^6} \int dE E^3 d\mu F \int dE' E'^2 d\mu' \tilde{R}^{\rm abs}_{\rm PAIR}(\bar{F}) \\
&- \sum_{\nu_e,\nu_{\mu,\tau}} \frac{2\pi C_0}{h^6 c^6} \int dE E^3 d\mu (\frac{1}{\rho} - F) \int dE' E'^2 d\mu' \tilde{R}^{\rm em}_{\rm PAIR}(\frac{1}{\rho} - \bar{F}),
\end{aligned} \tag{2.2}$$

$$\begin{aligned}
\frac{\partial v}{\partial t} &= -\frac{Gm}{r^2} - 4\pi r^2 \frac{\partial P}{\partial m} - 4\pi \frac{\partial (r^2 Q)}{\partial m} \\
&+ \sum_{\nu_e,\bar{\nu}_e} \frac{2\pi C_0}{h^3 c^3} \int dE E^3 d\mu\mu\, \tilde{\chi} F \\
&+ \sum_{\nu_e,\bar{\nu}_e,\nu_{\mu,\tau},\bar{\nu}_{\mu,\tau}} \frac{2\pi C_0}{h^6 c^7} \int dE E^5 d\mu\mu F \int d\mu' R_{\rm IS}
\end{aligned}$$

$$
\begin{aligned}
&- \sum_{\nu_e,\bar{\nu}_e,\nu_{\mu,\tau},\bar{\nu}_{\mu,\tau}} \frac{2\pi C_0}{h^6 c^7} \int dE E^5 d\mu\mu \int d\mu' R_{\rm IS} F \\
&+ \sum_{\nu_e,\bar{\nu}_e,\nu_{\mu,\tau},\bar{\nu}_{\mu,\tau}} \frac{2\pi C_0}{h^6 c^7} \int dE E^3 d\mu\mu F \int dE' E'^2 d\mu' \tilde{R}^{\rm out}_{\rm NES}(\frac{1}{\rho} - F) \\
&- \sum_{\nu_e,\bar{\nu}_e,\nu_{\mu,\tau},\bar{\nu}_{\mu,\tau}} \frac{2\pi C_0}{h^6 c^7} \int dE E^3 d\mu\mu (\frac{1}{\rho} - F) \int dE' E'^2 d\mu' \tilde{R}^{\rm in}_{\rm NES} F \\
&+ \sum_{\nu_e,\nu_{\mu,\tau}} \frac{2\pi C_0}{h^6 c^7} \int dE E^3 d\mu\mu F \int dE' E'^2 d\mu' \tilde{R}^{\rm abs}_{\rm PAIR} \bar{F} \\
&- \sum_{\nu_e,\nu_{\mu,\tau}} \frac{2\pi C_0}{h^6 c^7} \int dE E^3 d\mu\mu (\frac{1}{\rho} - F) \int dE' E'^2 d\mu' \tilde{R}^{\rm em}_{\rm PAIR} (\frac{1}{\rho} - \bar{F}). \qquad (2.3)
\end{aligned}
$$

In equation 2.2 and 2.3,

$$
\frac{\partial}{\partial t} = \left(\frac{\partial}{\partial t}\right)_m , \qquad (2.4)
$$

$$
\frac{\partial}{\partial m} = \left(\frac{\partial}{\partial m}\right)_t . \qquad (2.5)
$$

The quantities ρ, ϵ, v, and P are the fluid rest-mass density, specific internal energy (internal energy per gram; the internal energy is the energy of the fluid minus the kinetic energy associated with its bulk flow), velocity, and pressure, respectively. The flavor sums over terms containing the specific neutrino distribution function, $F \equiv f/\rho$, indicate that the equations contain one such term for each of the specified neutrino types. $\bar{F}$ is the specific distribution function for the corresponding antineutrino in the terms describing contributions from pair emission and absorption.

Equation 2.1 is the density equation. It is solved for the density, ρ, given a change in an infinitesimal fluid volume, $dV = 4\pi r^2 dr$, containing a constant mass, dm. Equation 2.2 is the specific internal energy equation. The first term in the energy equation is the PdV work done on the fluid as it is compressed. In the velocity equation 2.3, the first term is

the gravitational acceleration, and the second term is the fluid acceleration resulting from the fluid pressure gradient. The terms in equations 2.2 and 2.3 containing the quantity Q are the artificial viscosity terms. These terms are included to handle shocks (discontinuities) in the flow. In Nature, shocks are dissipated by microphysical viscosity on scales much smaller than the grid resolution in a numerical simulation. The artificial viscosity is added to mimic this microphysical viscous dissipation in the flow. Its result is to spread the shock over several numerical grid zones. The form of the artificial viscosity used in AGILE-BOLTZTRAN is given in Liebendörfer (2000).

To parameterize the neutrino momentum, we use spherical momentum coordinates: $p = E/c$, θ_0, and ϕ. p is the magnitude of the neutrino momentum, and E is the neutrino energy. In equations 2.2 and 2.3, $\mu \equiv \cos\theta$, which is the neutrino direction cosine relative to the outward-pointing radial vector. All of these quantities are measured by our inertial comoving observers. The advantage of this parameterization is that in spherical symmetry the neutrino distribution function, f, is a function of only E and μ, not ϕ. Moreover, because the comoving frame direction cosines and energies are used, the neutrino–matter interaction terms simplify greatly. In equations 2.2 and 2.3, $C_0 = 1.602 \times 10^{-6}\,\mathrm{erg\ MeV^{-1}}$. (Our neutrino energies are given in MeV, and the product hc is expressed in MeV cm.)

The third term in the energy equation is the energy exchange between the neutrinos and the fluid via emission and absorption of neutrinos by nucleons and nuclei. Specifically, we have electron capture on protons, producing electron neutrinos and neutrons, along with the inverse process, electron neutrino absorption on neutrons:

$$e^- + p \rightleftharpoons \nu_e + n. \tag{2.6}$$

We also have electron capture on nuclei and the inverse process, electron neutrino absorption on nuclei:

$$e^- + M(Z,N) \rightleftharpoons \nu_e + M(Z-1,N+1). \tag{2.7}$$

The integrand contains the neutrino emissivity, $j(E)$, the neutrino opacity, $\chi(E)$, and the specific neutrino distribution function, $F \equiv f/\rho$. The neutrino opacity, $\tilde{\chi}$, corrected for stimulated absorption, is defined by:

$$j - \tilde{\chi} f \equiv j - (j+\chi) f = (1-f) j - \chi f. \tag{2.8}$$

The next two terms in the energy equation give the energy exchange between the neutrinos and the fluid as a result of neutrino–electron scattering:

$$\nu_e + e^- \longrightarrow \nu_e + e^-. \tag{2.9}$$

The scattering kernels, $\tilde{R}^{\rm in/out}_{\rm NES}(\mu,\mu',E,E') \equiv \rho R^{\rm in/out}_{\rm NES}(\mu,\mu',E,E')$, are the in- and outscattering kernels, respectively, describing the scattering of an electron neutrino into or out of (μ, E). μ and E, are the incoming direction cosine and energy, and μ' and E' are the outgoing direction cosine and energy. The in/out scattering kernels are related to one another through the principle of detailed balance:

$$R^{\rm in}_{\rm NES}(\mu,\mu',E,E') = e^{-(E-E')/T} R^{\rm out}_{\rm NES}(\mu,\mu',E,E'). \tag{2.10}$$

$\tilde{R}^{\rm em/abs}_{\rm PAIR}(\mu,\mu',E,E') \equiv \rho R^{\rm em/abs}_{\rm PAIR}(\mu,\mu',E,E')$, are the pair emission and absorption kernels, respectively, describing the describing the production of a neutrino/antineutrino pair of energy E/E' and direction cosine μ/μ':

$$e^- + e^+ \rightleftharpoons \nu_e + \bar{\nu_e}. \tag{2.11}$$

The pair emission and absorption kernels are also related to one another through detailed balance as in equation 2.10.

The last seven terms in the velocity equation 2.3 are the neutrino stress terms. In this equation, $R_{\rm IS}(\mu, \mu', E)$ is the kernel for isoenergetic scattering of electron neutrinos on neutrons, protons, and nuclei:

$$\nu_{\rm e} + n \longrightarrow \nu_{\rm e} + n, \tag{2.12}$$

$$\nu_{\rm e} + p \longrightarrow \nu_{\rm e} + p, \tag{2.13}$$

$$\nu_{\rm e} + M(Z, N) \longrightarrow \nu_{\rm e} + M(Z, N). \tag{2.14}$$

Note that $R_{\rm IS}$ is a function only of μ, μ', and E, not E'. This is because the energy of the scattered neutrino is not changed in scattering on nucleons and nuclei; hence the term isoenergetic. The next two terms in the velocity equation give the neutrino stress exerted on the fluid as a result of non-isoenergetic neutrino–electron scattering. The last two terms describe the stress from pair emission and absorption.

2.1.2 Neutrino Transport

The neutrino distribution functions are evolved using the $O(v/c)$ Boltzmann equation (Castor 1972; Bruenn 1985; Mezzacappa & Bruenn 1993a). If we include emission, absorption, isoen-

ergetic scattering of neutrinos by nucleons and nuclei, neutrino–electron scattering, and pair emission and absorption, the Boltzmann equation is

$$
\begin{aligned}
\frac{1}{c}\frac{\partial F}{\partial t} &+ 4\pi\mu\frac{\partial(r^2\rho F)}{\partial m} \\
&+ \frac{1}{r}\frac{\partial[(1-\mu^2)F]}{\partial\mu} \\
&+ \frac{1}{c}(\frac{\partial ln\rho}{\partial t}+\frac{3v}{r})\frac{\partial[\mu(1-\mu^2)F]}{\partial\mu} \\
&+ \frac{1}{c}[\mu^2(\frac{\partial ln\rho}{\partial t}+\frac{3v}{r})-\frac{v}{r}]\frac{1}{E^2}\frac{\partial(E^3F)}{\partial E} \\
&= \frac{j}{\rho}-\tilde{\chi}F \\
&+ \frac{1}{c}\frac{1}{h^3c^3}E^2\int d\mu' R_{\rm IS}F \\
&- \frac{1}{c}\frac{1}{h^3c^3}E^2F\int d\mu' R_{\rm IS} \\
&+ \frac{1}{h^3c^4}(\frac{1}{\rho}-F)\int dE'E'^2d\mu'\tilde{R}^{\rm in}_{\rm NES}F \\
&- \frac{1}{h^3c^4}F\int dE'E'^2d\mu'\tilde{R}^{\rm out}_{\rm NES}(\frac{1}{\rho}-F) \\
&+ \frac{1}{h^3c^4}(\frac{1}{\rho}-F)\int dE'E'^2d\mu'\tilde{R}^{\rm em}_{\rm PAIR}(\frac{1}{\rho}-\bar{F}) \\
&- \frac{1}{h^3c^4}F\int dE'E'^2d\mu'\tilde{R}^{\rm abs}_{\rm PAIR}\bar{F}. \qquad (2.15)
\end{aligned}
$$

The Boltzmann equation is solved for each neutrino flavor independently: i.e. equation 2.15 is solved four times in each time step, once each for electron neutrinos, electron antineutrinos, μ/τ neutrinos, and μ/τ antineutrinos. The electron neutrinos and antineutrinos are solved for simultaneously, as are the μ/τ neutrinos and antineutrinos, since each neutrino flavor is coupled to its corresponding antineutrino through the pair emission and absorption terms. Note that μ and τ neutrinos are evolved as one flavor, as their couplings to matter are identical for the processes we consider. The μ and τ antineutrinos are treated similarly.

The mass derivative term on the left-hand side of the Boltzmann equation describes the propagation of neutrinos with respect to the Lagrangian mass coordinate, m. Outwardly propagating neutrinos have $\mu > 0$, whereas inwardly propagating neutrinos have $\mu < 0$. The first μ-derivative term describes the rate of change of the neutrino propagation direction with respect to the outward radial direction as the neutrino propagates inward or outward in mass. The second μ-derivative term describes the aberration in the neutrino propagation direction measured by an observer who is instantaneously comoving with the fluid. Because the fluid is accelerating, two consecutive comoving observers will measure different direction cosines. The energy-derivative term describes the shift in the neutrino energy measured by a comoving observer. Intuitively, this is a continual Doppler shift resulting from the change in the velocity of an accelerated fluid; two consecutive comoving observers will measure different frequencies (the frequency and neutrino energy are related by $E = h\nu_0$, where h is Planck's constant and ν_0 is the frequency measured by the comoving observer).

On the right-hand side of equation (2.15), the first two terms describe the change in the neutrino distribution function resulting from the absorption and emission of neutrinos by nucleons and nuclei. The next two terms describe the isoenergetic inscattering and outscattering, respectively, of neutrinos by nucleons and nuclei. The fourth and fifth terms describe non-isoenergetic neutrino–electron scattering, and the last two terms describe pair emission and absorption. As in equations 2.3 and 2.2, $\bar{F}$ is the corresponding antineutrino for each neutrino species evolved with equation 2.15.

2.1.3 Lepton Conservation

The hydrodynamics equations governing the evolution of the fluid's density and internal energy are expressions of conservation laws for the fluid mass and energy, and the neutrino transport

equation and its coupling to the hydrodynamics are an expression of the conservation of energy in the neutrino radiation field. In addition to these two globally conserved quantities, another important quantity is conserved: lepton number. (Flavor mixing can lead to lepton number nonconservation. None of the microphysics described in this work has been extended to include the possibility of mixing. For more details on flavor mixing, see Bahcall (1989) and Raffelt (1996).) Therefore, in addition to the hydrodynamics equations and the neutrino transport equations, we also have to solve, in a coupled fashion, the fluid electron fraction equation:

$$\frac{\partial Y_{\mathrm{e}}}{\partial t} = -\frac{2\pi m_{\mathrm{B}} c}{h^3 c^3}\left[\int dE E^2 d\mu\left(\frac{j_{\nu_e}}{\rho} - \tilde{\chi}_{\nu_e} F_{\nu_e}\right) - \int dE E^2 d\mu\left(\frac{j_{\bar{\nu}_e}}{\rho} - \tilde{\chi}_{\bar{\nu}_e} F_{\bar{\nu}_e}\right)\right]. \tag{2.16}$$

The Y_{e} evolved by equation 2.16 is actually the difference of the electron fraction minus the positron fraction: $Y_{\mathrm{e}} = Y_{\mathrm{e}^+} - Y_{\mathrm{e}^-}$. To see that this equation describes lepton number conservation, it is sufficient to point out that lepton number is exchanged between electrons and electron neutrinos via electron capture (mentioned earlier) and its inverse process and between positrons and electron antineutrinos via positron capture and its inverse. The right-hand side of equation 2.16 gives the change in the electron fraction resulting from these processes.

2.2 Neutrino Interactions

The expressions used in AGILE-BOLTZTRAN for the various neutrino–matter interactions are given in Mezzacappa & Bruenn (1993a) and Mezzacappa & Bruenn (1993c), with the exception of pair emission and absorption. They are reproduced here including pair emission and absorption for completeness and to point out some minor improvements in their implementation.

2.2.1 Emission and Absorption

We include emission and absorption of electron neutrinos from nucleons and nuclei and electron antineutrino emission and absorption from nucleons. The neutrino emissivity, j, is (Bruenn 1985)

$$j = j_{nucleon} + j_{nuclear}, \tag{2.17}$$

where

$$j_{nucleon} = \frac{(2\pi)^4 G_F^2}{\pi h^4 c^4} \left(g_V^2 + 3g_A^2\right) \eta_{pn} \left(E+Q\right)^2 \left[1 - \left(\frac{M_e}{E+Q}\right)^2\right]^{1/2} F_{e^-}(E+Q), \tag{2.18}$$

and

$$\begin{aligned} j_{nuclear} &= \frac{2}{7} \frac{(2\pi)^4 G_F^2}{\pi h^4 c^4} g_A^2 \frac{\rho X_H}{m_B A} N_p(Z) N_h(N) \\ &\times \left(E+Q'\right)^2 \left[1 - \left(\frac{M_e}{E+Q'}\right)^2\right]^{1/2} F_e(E+Q'). \end{aligned} \tag{2.19}$$

The neutrino emissivities, $j_{nucleon}$ and $j_{nuclear}$, are derived under the assumptions that no momentum is transferred between the neutrinos and the nucleons and that the nucleons are nonrelativistic.

In equation (2.18), $Q = 1.2935\, MeV$ is the difference between the neutron and proton rest energies. The factor η_{pn} takes into account the nucleon final-state blocking and is equal to n_p, the proton number density, when the nucleons are nondegenerate. It is defined by

$$\eta_{pn} = \frac{2}{h^3 c^3} \int d^3p \, F_p(E)[1 - F_n(E)] = \frac{1}{m_B} \rho \, (X_n - X_p) \, \frac{1}{e^{(\mu_n^0 - \mu_p^0)/T} - 1} \, , \tag{2.20}$$

where X_n and X_p are the neutron and proton fractions, respectively; μ_n^0 and μ_p^0 are the neutron and proton chemical potentials (the zero superscript denotes a chemical potential that does not include the rest-energy of the particle), respectively; and T is the fluid temperature. In equations (2.18) and (2.19), $F_N(E)$ is the Fermi–Dirac distribution function:

$$F_N(E) = \frac{1}{e^{(E - \mu_N)/T} + 1}, \tag{2.21}$$

where μ_N is the appropriate chemical potential.

The functions $N_p(Z)$ and $N_h(N)$ in equation (2.19) are defined by

$$N_p(Z) = \begin{cases} 0 & Z < 20 \\ Z - 20 & 20 < Z < 28 \\ 8 & Z > 28 \end{cases} \tag{2.22}$$

and,

$$N_h(N) = \begin{cases} 6 & N < 34 \\ 40 - N & 34 < N < 40 \\ 0 & N > 40. \end{cases} \tag{2.23}$$

Electron capture by nuclei is dominated by the Gamow–Teller transition from the single-particle $1f_{\frac{7}{2}}$ level to the single-particle $1f_{\frac{5}{2}}$ level unless the reaction is blocked by the absence of neutron holes, which occurs for $N \geq 40$ (Bethe et al. 1979). The function $N_p(Z)$ is an estimate of the number of protons in the level $1f_{\frac{7}{2}}$ based on a zero-order shell model. Similarly, $N_h(N)$ is an estimate of the number of neutron holes in the $1f_{\frac{5}{2}}$ level. The quantity $Q^{'}$ in equation (2.19) is

defined by $Q^{'} = \mu_n - \mu_p + \Delta$, where $\Delta = 3\,MeV$ is the energy of the $1f_{\frac{5}{2}}$ level above the ground state (Bethe et al. 1979).

Local thermodynamic equilibrium is assumed for the fluid. If we substitute f_{eq} for f in equation (2.8), where f_{eq} is a neutrino distribution equilibrated with the matter, we get $j - \tilde{\chi} f_{eq} = 0$; so j and $\tilde{\chi}$ are related by

$$\frac{j}{\tilde{\chi}} = f_{eq} = \frac{1}{e^{(E-\mu_\nu)/T} + 1} \; . \tag{2.24}$$

The right-hand side of equation (2.24) is the equilibrated neutrino distribution function. From equations (2.6) and (2.7) the neutrino chemical potential, μ_ν, for the equilibrated neutrino distribution is given by

$$\mu_\nu = \mu_e + \mu_p - \mu_n, \tag{2.25}$$

where μ_e, μ_p, and μ_n are the electron, proton, and neutron chemical potentials, respectively.

The expressions for antitneutrino emission are similar. We include only antineutrino emission from nucleons,

$$\bar{j}_{nucleon} = \frac{(2\pi)^4 G_F^2}{\pi h^4 c^4} \left(g_V^2 + 3g_A^2\right) \eta_{np} \left(E - Q\right)^2 \left[1 - \left(\frac{M_e}{E - Q}\right)^2\right]^{1/2} F_{e^+}(E - Q), \tag{2.26}$$

where

$$\eta_{np} = \frac{2}{h^3 c^3} \int d^3p \, F_n(E)[1 - F_p(E)] = \frac{1}{m_B} \, \rho \left(X_p - X_n\right) \frac{1}{e^{(\mu_p^0 - \mu_n^0)/T} - 1} \; , \tag{2.27}$$

is the correct blocking factor for antineutrinos and

$$F_{e^+}(E) = \frac{1}{e^{(E+\mu_{e^-})/T}+1}. \tag{2.28}$$

2.2.2 Isoenergetic Scattering

R_{IS} is the sum of the kernels for conservative scattering of electron neutrinos on protons and neutrons. R_{IS} is derived from the scattering kernel (Bruenn 1985):

$$R_{IS}(\cos\theta, E) = R_{IS}^{nucleons}(\cos\theta, E) + R_{IS}^{nuclei}(\cos\theta, E), \tag{2.29}$$

where

$$\cos\theta = \mu\mu^{'} + [(1-\mu^2)(1-\mu^{'2})]^{1/2}\,\cos\phi, \tag{2.30}$$

and

$$\begin{aligned} R_{IS}^{nucleons} = \frac{(2\pi)^2 G_F^2}{h}\{\ & \eta_{nn}[(h_V^n)^2 + 3(h_A^n)^2] + \eta_{pp}[(h_V^p)^2 + 3(h_A^p)^2] \\ & +\eta_{nn}[(h_V^n)^2 - (h_A^n)^2]\cos\theta \\ & +\eta_{pp}[(h_V^p)^2 - (h_A^p)^2]\cos\theta\}, \end{aligned} \tag{2.31}$$

and

$$\begin{aligned} R_{IS}^{nuclei} &= \frac{(2\pi)^2 G_F^2}{h}\,\frac{\rho X_H}{m_B}\,A\,(C_{V0} - \frac{1}{2}\frac{N-Z}{A}C_{V1})^2 \\ &\times \ (1+\cos\theta)\,e^{-4bE^2(1-\cos\theta)}. \end{aligned} \tag{2.32}$$

In equations (2.29) to (2.32), $\cos\theta$ is the cosine of the relative angle between the incoming neutrino (μ) and the outgoing neutrino ($\mu^{'}$) directions. Similarly, ϕ is the relative azimuthal angle between the two neutrino directions.

The kernel, equation (2.31), is derived under the assumptions that (1) there is zero momentum transfer between the neutrinos and the nucleons and (2) the nucleons are nonrelativistic. The factors η_{pp} and η_{nn} account for the nucleon final-state blocking. They are defined by

$$\eta_{pp} = T\,\frac{\partial n_p}{\partial \mu_p}, \tag{2.33}$$

and

$$\eta_{nn} = T\,\frac{\partial n_n}{\partial \mu_n}. \tag{2.34}$$

For nondegenerate, nonrelativistic nucleons, η_{pp} and η_{nn} are given by

$$\eta_{pp} = n_p \tag{2.35}$$

$$\eta_{nn} = n_n, \tag{2.36}$$

where n_p and n_n are the proton and neutron number densities, respectively. For degenerate, nonrelativistic nucleons we have instead

$$\eta_{pp} = \frac{3T}{2\epsilon_F^p}\,n_p \tag{2.37}$$

$$\eta_{nn} = \frac{3T}{2\epsilon_F^n}\,n_n, \tag{2.38}$$

where ϵ_F^p and ϵ_F^n are the proton and neutron Fermi energies, respectively. The latter are given by

$$\epsilon_F^p = \frac{h^2}{8\pi^2 m_B}(3\pi^2 n_p)^{2/3} \tag{2.39}$$

$$\epsilon_F^n = \frac{h^2}{8\pi^2 m_B}(3\pi^2 n_n)^{2/3}. \tag{2.40}$$

We find that the derivatives in equations (2.33) and (2.34) are subject to error when evaluated numerically. To ensure that the correct nondegenerate and degenerate limits are correctly attained, we use instead the following analytic interpolation formula:

$$\begin{aligned}\eta_{pp} &= \frac{(n_p)(3Tn_p/2\epsilon_F^p)}{[n_p^2 + (3Tn_p/2\epsilon_F^p)^2]^{1/2}} \\ &= n_p \frac{3T/2\epsilon_F^p}{[1 + (3T/2\epsilon_F^p)^2]^{1/2}},\end{aligned} \tag{2.41}$$

and

$$\eta_{nn} = n_n \frac{3T/2\epsilon_F^n}{[1 + (3T/2\epsilon_F^n)^2]^{1/2}}. \tag{2.42}$$

The constants in equation (2.31), h_V^p, h_V^n, h_A^p, and h_A^n, are the nucleon neutral current form factors arising from virtual strong-interaction processes: $h_V^p = \frac{1}{2} - 2\sin^2\theta_W$, $h_V^n = -\frac{1}{2}$, $h_A^p = \frac{1}{2}g_A$, and $h_A^n = -\frac{1}{2}g_A$, where θ_W is the Weinberg angle.

The kernel, equation (2.32), is derived under the following assumptions: (1) no momentum is transferred between the neutrino and the nucleus, (2) the nucleus is nonrelativistic, and (3)

the nucleus is nondegenerate. The quantity b is given by $b = 4.8 \times 10^{-6}\, A^{2/3}$. The Gaussian form factor includes the details of the nuclear wave function. The constants, C_{V0} and C_{V1}, are defined in terms of h_V^p and h_V^n: $C_{V0} = \frac{1}{2}(h_V^p + h_V^n)$ and $C_{V1} = h_V^p - h_V^n$.

In terms of $R_{IS}(cos\theta, E)$, the scattering kernel in the Boltzmann equation is given by (Mezzacappa & Bruenn 1993a)

$$\begin{aligned} R_{IS}(\mu, \mu^{'}, E) &= \int_0^{2\pi} d\phi R_{IS}(cos\theta, E) \\ &= \int_0^{2\pi} d\phi R_{IS}^{nucleons}(cos\theta, E) + \int_0^{2\pi} d\phi R_{IS}^{nuclei}(cos\theta, E) \\ &\equiv R_{IS}^{nucleons}(\mu, \mu^{'}, E) + R_{IS}^{nuclei}(\mu, \mu^{'}, E). \end{aligned} \tag{2.43}$$

The integrals over ϕ can be done analytically using (Gradshteyn & Ryzhik 1980)

$$\int_0^{\pi} dx\, e^{\pm\beta cos(x)} \sin^{2\nu}(x) = \pi^{1/2} \left(\frac{2}{\beta}\right)^{\nu} \Gamma(\nu + \frac{1}{2})\, I_{\nu}(\beta), \tag{2.44}$$

which is true for $Re(\nu) > -1/2$;

$$\int_0^{\pi} dx\, e^{i\beta \cos(x)} \cos(nx) = i^n \pi J_n(\beta), \tag{2.45}$$

with

$$I_{\nu}(z) = e^{3\pi\nu\, i/2}\, J_{\nu}(e^{-3\pi i/2} z), \tag{2.46}$$

which is true for $\pi/2 < arg(z) \leq \pi$; and

$$I_1(z) = -I_1(-z). \tag{2.47}$$

The function $J_\nu(z)$ is the Bessel function of the first kind, of order ν, and $I_\nu(z)$ is the modified Bessel function of the first kind, of order ν. The results of the ϕ integration are

$$\begin{aligned} R_{IS}^{nucleons} = \frac{8\pi^3 G_F^2}{h}\{ \; & \eta_{nn}[(h_V^n)^2 + 3(h_A^n)^2] + \eta_{pp}[(h_V^p)^2 + 3(h_A^p)^2] \\ & + \eta_{nn}[(h_V^n)^2 - (h_A^n)^2]\mu\mu^{'} \\ & + \eta_{pp}[(h_V^p)^2 - (h_A^p)^2]\mu\mu^{'}\}, \end{aligned} \tag{2.48}$$

and

$$\begin{aligned} R_{IS}^{nuclei}(\mu, \mu^{'}, E) &= \frac{8\pi^3 G_F^2}{h}\,\frac{\rho X_H}{m_B}\,A\,(C_{V0} - \frac{1}{2}\frac{N-Z}{A}C_{V1})^2\,e^{-4bE^2(1-\mu\mu^{'})} \\ &\times \{(1+\mu\mu^{'})\,I_0(4bE^2[(1-\mu^2)(1-\mu^{'2})]^{1/2}) \\ &+ [(1-\mu^2)(1-\mu^{'2})]^{1/2}\,I_1(4bE^2[(1-\mu^2)(1-\mu^{'2})]^{1/2})\,\}. \end{aligned} \tag{2.49}$$

For large enough A (and, therefore, large b) in equation 2.49, R_{IS}^{nuclei} can be smaller than the corresponding value for scattering off an equal number of free nucleons. If this occurs in the code, R_{IS}^{nuclei} is set to zero and η_{pp} and η_{nn} are recalculated including an additional $Z\rho X_H/m_B$ free protons and $(1-Z)\rho X_H/m_B$ free neutrons, where Z is the atomic number of the representative nucleus returned from the EOS. $R_{IS}^{nucleons}$ is then recalculated and becomes the total R_{IS}.

2.2.3 Neutrino–Electron Scattering

For $E \neq E'$, the $\nu_e + e^-$ scattering kernels are written as (Schinder & Shapiro 1982)

$$\begin{aligned} R^{\rm out}_{\rm NES}(E,E',\omega) &= R^{\rm out}_{\rm NES}(E,E',\mu,\mu',\phi) \\ &= \frac{1}{2}\frac{1}{(2\pi)^3}\frac{\pi\sigma_0 c}{(m_{\rm e}c^2)^2}\frac{1}{EE'} \\ &\times \quad [\beta_1 I_1(E,E',\omega)+\beta_2 I_2(E,E',\omega)+\beta_3 I_3(E,E',\omega)], \end{aligned} \tag{2.50}$$

where $\beta_1 = (C_{\rm V}+C_{\rm A})^2, \beta_2 = (C_{\rm V}-C_{\rm A})^2, \beta_3 = C_{\rm A}^2 - C_{\rm V}^2, C_{\rm V} = \frac{1}{2} + 2\theta_W = 0.96, C_{\rm A} = \frac{1}{2}, \sigma_0 = 1.764 \times 10^{-44}{\rm cm}^2$, and

$$\omega = \mu\mu' + [(1-\mu^2)(1-\mu'^2)]^{1/2}\cos\phi, \tag{2.51}$$

and where the functions $I_{1,2,3}(E,E',\omega)$ are defined by

$$\begin{aligned} I_1(E,E',\omega) &= \frac{2\pi T E^2 E'^2 (1-\omega)^2}{\Delta^5} f_\gamma(E'-E) \\ &\times \quad \{AT^2[G_2(y_0)+2y_0G_1(y_0)+y_0^2G_0(y_0)] + BT[G_1(y_0)+y_0G_0(y_0)] + CG_0(y_0)\}, \end{aligned} \tag{2.52}$$

and

$$I_2(E,E',\omega) = I_1(E \to -E', E' \to -E, \omega), \tag{2.53}$$

Table 2.1: NES coefficients for various neutrino flavors

neutrino type	β_1	β_2	β_3
ν_e	$(C_{\rm V}+C_{\rm A})^2$	$(C_{\rm V}-C_{\rm A})^2$	$C_{\rm V}^2-C_{\rm A}^2$
$\bar{\nu}_e$	$(C_{\rm V}-C_{\rm A})^2$	$(C_{\rm V}+C_{\rm A})^2$	$C_{\rm V}^2-C_{\rm A}^2$
$\nu_{\mu,\tau}$	$(C_{\rm V}+C_{\rm A}-2)^2$	$(C_{\rm V}-C_{\rm A})^2$	$(C_{\rm V}-1)^2-(C_{\rm A}-1)^2$
$\bar{\nu}_{\mu,\tau}$	$(C_{\rm V}-C_{\rm A})^2$	$(C_{\rm V}+C_{\rm A}-2)^2$	$(C_{\rm V}-1)^2-(C_{\rm A}-1)^2$

and

$$I_3(E,E',\omega)=\frac{2\pi TEE'(1-\omega)(m_{\rm e}c^2)^2}{\Delta}f_\gamma(E'-E)G_0(y_0). \tag{2.54}$$

The kernel for NES of $\bar{\nu_e}$ is obtained through a crossing symmetry of the ν_e kernel. The difference in momenta labels is equivalent to replacing $C_{\rm V}$ by $-C_{\rm V}$. The NES for ν_μ and ν_τ proceeds only through the exchange of a neutral vector boson. This difference is equivalent to replacing $C_{\rm V}$ and $C_{\rm A}$ with $C_{\rm V}-1$ and $C_{\rm A}-1$, respectively (Bruenn 1985). The values of β_1, β_2, and β_3 in terms of $C_{\rm V}$ and $C_{\rm A}$ are given in Table 2.1.

In equations (2.52) through (2.54),

$$\Delta = (E^2+E'^2-2EE'\omega)^{1/2}, \tag{2.55}$$

$$y_0 = \frac{1}{T}\{-\frac{E-E'}{2}+\frac{\Delta}{2}[1+\frac{2(m_{\rm e}c^2)^2}{EE'(1-\omega)}]^{1/2}\}, \tag{2.56}$$

$$A = E^2+E'^2+EE'(3+\omega), \tag{2.57}$$

$$B = E[2E^2+EE'(3-\omega)-E'^2(1+3\omega)], \tag{2.58}$$

$$C = E^2[(E-E'\omega)^2-\frac{E'^2(1-\omega^2)}{2}-\frac{(1+\omega)(m_{\rm e}c^2)^2\Delta^2}{2(1-\omega)E^2}], \tag{2.59}$$

$$f_\gamma(x) = \frac{1}{e^{x/T}-1}, \tag{2.60}$$

and the functions $G_n(y)$ are defined in terms of Fermi integrals:

$$G_n(y) = F_n(\eta' - y) - F_n(\eta - y), \tag{2.61}$$

where

$$\eta = \frac{\mu_e}{T}, \tag{2.62}$$

$$\eta' = \eta - \frac{E - E'}{T}, \tag{2.63}$$

$$F_n(\eta) = \int_0^\infty \frac{x^n dx}{e^{x-\eta}+1}. \tag{2.64}$$

The Fermi integrals can be related to the polylogarithms, $S_n(x)$, as follows (Kolbig et al. 1970):

$$S_n(x) = \frac{(-1)^{n-1}}{(n-2)!}\int_0^1 \frac{\log^{n-2}(t)\log(1-xt)dt}{t} = \frac{x}{(n-1)!}\int_0^\infty \frac{t^{n-1}dt}{e^t - x}. \tag{2.65}$$

Thus,

$$F_n(x) = -n! S_{n+1}(-e^x). \tag{2.66}$$

In turn, the polylogarithms can be accurately computed numerically using Chebychev expansions (Kolbig et al. 1970). Note that the Chebychev expansions given in Kolbig et al. (1970) are valid for $-1 \le -e^{-x} \le 1/2$. As a result, in the range $-\infty \le -e^{-x} \le -1$, we use the inversion

formulas (Mezzacappa & Bruenn 1993c)

$$S_2(x) = -S_2(\frac{1}{x}) - \frac{1}{2}\log^2(-x) - \frac{\pi^2}{6}, \tag{2.67}$$

$$S_3(x) = S_3(\frac{1}{x}) - \frac{1}{6}\log^3(-x) - \frac{\pi^2}{6}\log(-x), \tag{2.68}$$

which are also given in Kolbig et al. (1970).

For $E = E'$, the functions $I_{1,2,3}(E, E', \omega)$ in equation (2.50) are replaced by (Schinder 1990)

$$I_1(E,\omega) = \frac{2\pi T E^4 (1-\omega)^2}{\Delta^5}\{\ AT^2[2F_1(\eta - y_0) + 2y_0F_0(\eta - y_0) + y_0^2F_{-1}(\eta - y_0)] \tag{2.69}$$

$$+BT[F_0(\eta - y_0) + y_0F_{-1}(\eta - y_0)] + CF_{-1}(\eta - y_0)\},$$

and

$$I_2(E,\omega) = I_1(E,\omega), \tag{2.70}$$

and

$$I_3(E,\omega) = \frac{2\pi T E^2 (1-\omega)(m_e c^2)^2}{\Delta} F_{-1}(\eta - y_0), \tag{2.71}$$

with the appropriate simplification of Δ, y_0, A, B, and C in equations (2.55) through (2.59) and with

$$F_{-1}(\eta) = \frac{1}{e^{-\eta} + 1}. \tag{2.72}$$

The neutrino-electron scattering kernels that appear in the Boltzmann equation, equation (2.15), are functions of μ, μ', E, and E'. However, the scattering kernels, equation (2.50), are functions of μ, μ', E, E', and ϕ. There are two procedures for performing the dimensional reduction from $R^{\rm out}_{\rm NES}(E, E', \mu, \mu', \phi)$ to $R^{\rm out}_{\rm NES}(E, E', \mu, \mu')$. One method is simply to integrate $R^{\rm out}_{\rm NES}(E, E', \omega)$ over ϕ numerically, i.e.,

$$R^{\rm out}_{\rm NES}(E, E', \mu, \mu') = \int_0^{2\pi} d\phi R^{\rm out}_{\rm NES}(E, E', \omega). \tag{2.73}$$

The other method (Schinder & Shapiro 1982) is to expand the scattering kernel in a Legendre series:

$$R^{\rm out}_{\rm NES}(E, E', \omega) = \sum_{l=0}^{\infty} \frac{2l+1}{2} \Phi^{\rm out}_{NES,l}(E, E') P_l(\omega), \tag{2.74}$$

where the Legendre coefficients are given by

$$\Phi^{\rm out}_{NES,l}(E, E') = \int_{-1}^{1} d\omega P_l(\omega) R^{\rm out}_{\rm NES}(E, E', \omega). \tag{2.75}$$

Using the addition theorem (Gradshteyn & Ryzhik 1980), we can express $P_l(\omega)$ as follows:

$$P_l(\omega) = P_l(\mu) P_l(\mu') + 2 \sum_{m=1}^{l} \frac{(l-m)!}{(l+m)!} P_l^m(\mu) P_l^m(\mu') \cos m\phi. \tag{2.76}$$

If we substitute equation (2.76) for $P_l(\omega)$ in equation (2.74) and integrate over ϕ, using equation (2.73), we obtain an expansion for $R^{\rm out}_{\rm NES}(E, E', \mu, \mu')$ in terms of $P_l(\mu)$ and $P_l(\mu')$:

$$R^{\rm out}_{\rm NES}(E, E', \mu, \mu') = 2\pi \sum_{l=0}^{\infty} \frac{2l+1}{2} \Phi^{\rm out}_{NES,l}(E, E') P_l(\mu) P_l(\mu'). \tag{2.77}$$

Although equation (2.77) gives the scattering kernel as an infinite sum of moments, in practice the sum is truncated at some finite value, l_{max}, which is dictated by the number of quadrature points used for μ.

A problem for any method used to compute $R^{\rm out}_{\rm NES}(E, E', \mu, \mu')$ is that it is infinite for forward scattering ($\omega \rightarrow 1$: $\mu = \mu', E = E', \phi = 0$). The singular behavior of $R^{\rm out}_{\rm NES}(E, E', \mu, \mu')$ can be clearly exhibited by considering the behavior of the functions $I_{1,2,3}(E, \omega)$, given by equations (2.69) through (2.71), as $\omega \rightarrow 1$ (Mezzacappa & Bruenn 1993c):

$$I_{1,2}(E, \omega) \sim \frac{1}{(1-\omega)^{1/2}}, \tag{2.78}$$

$$I_3(E, \omega) \sim (1-\omega)^{1/2}. \tag{2.79}$$

Furthermore, if we define $x \equiv \cos\phi$, for forward scattering we obtain $1 - \omega = (1 - \mu^2)(1 - x)$. If we perform this transformation of variables in the integral, equation (2.73), we get the following limiting behavior for $x \rightarrow 1$ ($\omega \rightarrow 1$):

$$\int_0^{2\pi} d\phi R^{\rm out}_{\rm NES}(E, E, \omega) \sim \int_{-1}^{+1} \frac{dx}{(1-x^2)^{1/2}(1-\omega)^{1/2}} \sim \int_{-1}^{+1} \frac{dx}{(1-x)(1+x)^{1/2}}, \tag{2.80}$$

which is divergent. Thus, $R^{\rm out}_{\rm NES}(E, E', \mu, \mu')$ is infinite for $\mu = \mu', E = E'$.

Schinder & Shapiro (1982) avoided this problem by staggering their energy grids slightly, with $E' = E + 0.01$. However, in so doing they do not actually compute forward scattering. We have chosen a different approach (Mezzacappa & Bruenn 1993c). Although $R^{\rm out}_{\rm NES}(E, E', \mu, \mu')$ is infinite for $\mu = \mu'$ and $E = E'$, we use the fact that it is integrably finite, i.e., the integral of

$R^{\rm out}_{\rm NES}(E,E,\mu,\mu')$ over any finite range in μ' is finite. The kernels $R^{\rm out}_{\rm NES}(E,E',\mu,\mu')$ appearing in the Boltzmann equation should be considered as averages over the finite zone widths of the μ-grid and should therefore be finite. To obtain a well-defined and physically reasonable value for $R^{\rm out}_{\rm NES}(E,E,\mu,\mu)$, Mezzacappa & Bruenn (1993c) integrate the expansion, equation (2.77), over μ' to obtain

$$\begin{aligned}\int_{-1}^{+1} d\mu' R^{\rm out}_{\rm NES}(E,E',\mu,\mu') &= 2\pi\sum_{l=0}^{\infty}\Phi^{\rm out}_{NES,l}(E,E')P_l(\mu)\frac{2l+1}{2}\int_{-1}^{+1}d\mu' P_l(\mu') \\ &= 2\pi\Phi^{\rm out}_{NES,0}(E,E'). \qquad (2.81)\end{aligned}$$

On a discrete μ-grid we can separate out the forward scattering contribution to $\Phi^{\rm out}_{NES,0}(E,E')$:

$$\begin{aligned}2\pi\Phi^{\rm out}_{NES,0}(E_{k+1/2},E_{k+1/2}) &= \sum_{l=1}^{jmax} w_l R^{\rm out}_{\rm NES}(E_{k+1/2},E_{k+1/2},\mu_{j+1/2},\mu_{l+1/2}) \\ &= w_{j+1/2}R^{\rm out}_{\rm NES}(E_{k+1/2},E_{k+1/2},\mu_{j+1/2},\mu_{j+1/2}) \\ &+ \sum_{l\neq j} w_l R^{\rm out}_{\rm NES}(E_{k+1/2},E_{k+1/2},\mu_{j+1/2},\mu_{l+1/2}). \qquad (2.82)\end{aligned}$$

In equation (2.82), $\mu_{j+1/2}$ are the discrete direction cosines, which in our case are given by Gaussian quadratures and are numbered 1 to jmax; the w_j are the corresponding weights. The energies, $E_{k+1/2}$, are the discrete neutrino energies, numbered 1 to kmax. Solving equation (2.82) for $R^{\rm out}_{\rm NES}(E_{k+1/2},E_{k+1/2},\mu_{j+1/2},\mu_{j+1/2})$ gives

$$R^{\rm out}_{\rm NES}(E_{k+1/2},E_{k+1/2},\mu_{j+1/2},\mu_{j+1/2}) = \frac{1}{w_{j+1/2}}\{2\pi\Phi^{\rm out}_{NES,0}(E_{k+1/2},E_{k+1/2}) \qquad (2.83)$$

$$- \sum_{l \neq j} w_l R^{\rm out}_{\rm NES}(E_{k+1/2}, E_{k+1/2}, \mu_{j+1/2}, \mu_{l+1/2})\}.$$

Thus, for forward scattering, the neutrino-electron scattering kernel can be obtained numerically from equation (2.83) once a well-defined value for $\Phi^{\rm out}_{NES,0}(E_{k+1/2}, E_{k+1/2})$ is computed; for all other cases we obtain values for the neutrino-electron scattering kernel by numerically performing the ϕ-quadrature in equation (2.73) (Mezzacappa & Bruenn 1993c). For the latter we use 32-point Gaussian quadrature for ϕ.

To obtain accurate values for $\Phi^{\rm out}_{NES,0}(E, E)$, we avoid the (integrably) singular behavior of $R^{\rm out}_{\rm NES}(E, E', \omega)$ in equation (2.75) and exploit the fact that integrating over ω before integrating over the electron energy leads to a singularity free numerical integration for $\Phi^{\rm out}_{NES,0}(E, E)$. We write (Bruenn 1985)

$$\Phi^{\rm out}_{NES,0}(E, E') = \frac{(2\pi)^4 G_{\rm F}^2 c}{\pi (hc)^4} \frac{1}{E^2 E'^2} \int dE_{\rm e} \;\; F_{\rm e}(E_{\rm e})[1 - F_{\rm e}(E_{\rm e} + E - E')] \times [\beta_1 H_0^{\rm I}(E, E', E_{\rm e}) + \beta_2 H_0^{\rm II}(E, E', E_{\rm e})], \tag{2.84}$$

where $E_{\rm e}$ is the electron energy, $F_{\rm e}(E_{\rm e})$ is the electron Fermi-Dirac distribution, and the functions $H_0^{\rm I,II}(E, E', E_{\rm e})$ are given by (Yueh & Buchler 1977)

$$H_0^{\rm I}(E, E', E_{\rm e}) = \begin{cases} \frac{4}{15}E_{\rm e}^5 + \frac{4}{3}E_{\rm e}^4 E + \frac{8}{3}E_{\rm e}^3 E^2 + \Theta(E' - E)\Gamma_0^{\rm I}(E, E') & E' > E_{\rm e} \\ a_0^{\rm I}(E, E') + b_0^{\rm I}(E, E')E_{\rm e} + c_0^{\rm I}(E, E')E_{\rm e}^2 & E' < E_{\rm e} \end{cases}, \tag{2.85}$$

$$H_0^{\rm II}(E, E', E_{\rm e}) = \begin{cases} \frac{4}{15}E_{\rm e}^5 - \frac{4}{3}E_{\rm e}^4 E' + \frac{8}{3}E_{\rm e}^3 E'^2 + \Theta(E' - E)\Gamma_0^{\rm II}(E, E') & E' > E_{\rm e} \\ a_0^{\rm II}(E, E') + b_0^{\rm II}(E, E')E_{\rm e} + c_0^{\rm II}(E, E')E_{\rm e}^2 & E' < E_{\rm e} \end{cases} \tag{2.86}$$

where

$$a_0^{\mathrm{I}}(E,E') = (\frac{8}{3}E^2E'^3 - 4EE'^4 + \frac{8}{5}E'^5)\Theta(E-E') + \frac{4}{15}E^5\Theta(E'-E), \quad (2.87)$$

$$b_0^{\mathrm{I}}(E,E') = (\frac{16}{3}EE'^3 - 4E'^4)\Theta(E-E') + \frac{4}{3}E^4\Theta(E'-E), \quad (2.88)$$

$$c_0^{\mathrm{I}}(E,E') = \frac{8}{3}E'^3\Theta(E-E') + \frac{8}{3}E^3\Theta(E'-E), \quad (2.89)$$

$$\Gamma_0^{\mathrm{I}}(E,E') = \tfrac{8}{3}E_{\mathrm{e}}^2(E^3-E'^3) + 4E_{\mathrm{e}}(E-E')^2(\tfrac{E^2}{3} + \tfrac{2EE'}{3} + E'^2) \quad (2.90)$$

$$+4(E-E')^3(\tfrac{E^2}{15} + \tfrac{EE'}{5} + \tfrac{2E'^2}{5}),$$

and

$$a_0^{\mathrm{II}}(E,E') = a_0^{\mathrm{I}}(E',E), \quad (2.91)$$

$$b_0^{\mathrm{II}}(E,E') = -b_0^{\mathrm{I}}(E',E), \quad (2.92)$$

$$c_0^{\mathrm{II}}(E,E') = c_0^{\mathrm{I}}(E',E), \quad (2.93)$$

$$\Gamma_0^{\mathrm{II}}(E,E') = \Gamma_0^{\mathrm{I}}(-E',-E). \quad (2.94)$$

The integral in equation (2.84) is performed numerically using 24-point Gaussian and Laguerre quadratures for the electron energy.

Once the outscattering kernels are computed using this method, the inscattering kernels are computed from equation 2.10 (Mezzacappa & Bruenn 1993c).

2.2.4 Pair Emission and Absorption

Pair emission and absorption is a cross channel of NES. Consequently, the expressions for the scattering kernels are quite similar, with only a few substitutions.

The pair emission kernel can be written as (Schinder & Shapiro 1982)

$$\begin{aligned} R^{\rm em}_{\rm PAIR}(E,E',\omega) &= R^{\rm em}_{\rm PAIR}(E,E',\mu,\mu',\phi) \\ &= \frac{1}{2}\frac{1}{(2\pi)^3}\frac{\pi\sigma_0 c}{(m_e c^2)^2}\frac{1}{EE'} \\ &\times \ [\beta_1 I_1(E,E',\omega)+\beta_2 I_2(E,E',\omega)+\beta_3 I_3(E,E',\omega)]. \end{aligned} \tag{2.95}$$

The functions $I_{1,2,3}(E,E',\omega)$ for pair emission and absorption are

$$\begin{aligned} I_1(E,E',\omega) &= -\frac{2\pi T E^2 E'^2(1-\omega)^2}{\Delta^5} f_\gamma(E'-E) \\ &\times \ \{AT^2[G_2(y_{0,max})-G_2(y_{0,min}) \\ &+ \ 2y_{0,max}G_1(y_{0,max})-2y_{0,min}G_1(y_{0,min}) \\ &+ \ y^2_{0,max}G_0(y_{0,max})-y^2_{0,min}G_0(y_{0,min})] \\ &+ \ BT[G_1(y_{0,max})-G_1(y_{0,min}) \\ &+ \ y_{0,max}G_0(y_{0,max})-y_{0,min}G_0(y_{0,min})] \\ &+ \ C[G_0(y_{0,max})G_0(y_{0,min})]\}, \end{aligned} \tag{2.96}$$

$$I_2(E,E',\omega) = I_1(E\rightarrow E', E'\rightarrow E,\omega), \tag{2.97}$$

and

$$I_3(E,E',\omega) = -\frac{2\pi TEE'(1-\omega)(m_e c^2)^2}{\Delta} f_\gamma(E'+E)(G_0(y_{0,max}) - G_0(y_{0,min})). \tag{2.98}$$

The definitions of f_γ, $G_n(y)$, and η are the same as in section 2.2.3. The rest of the expressions appearing in the scattering kernel formulae are given by

$$\begin{aligned}
\Delta &= (E^2 + E'^2 + 2EE'\omega)^{1/2}, && (2.99)\\
y_{0,max} &= \frac{1}{T}\{\frac{E+E'}{2} + \frac{\Delta}{2}[1 - \frac{2(m_e c^2)^2}{EE'(1-\omega)}]^{1/2}\}, && (2.100)\\
y_{0,min} &= \frac{1}{T}\{\frac{E+E'}{2} - \frac{\Delta}{2}[1 - \frac{2(m_e c^2)^2}{EE'(1-\omega)}]^{1/2}\}, && (2.101)\\
A &= E^2 + E'^2 - EE'(3+\omega), && (2.102)\\
B &= E[-2E^2 + EE'(3-\omega) + E'^2(1+3\omega)], && (2.103)\\
C &= E^2[(E+E'\omega)^2 - \frac{E'^2(1-\omega^2)}{2} - \frac{(1+\omega)(m_e c^2)^2\Delta^2}{2(1-\omega)E^2}], && (2.104)\\
\eta' &= \eta + \frac{E+E'}{T}. && (2.105)\\
& && (2.106)
\end{aligned}$$

The same procedure of dimensional reduction performed on the NES kernels is used to obtain $R^{\rm em}_{\rm PAIR}(E,E',\omega)$ (Mezzacappa & Bruenn 1993c). The pair kernels also suffer from singular behavior akin to the NES kernels. In the pair case, the kernel for "back to back" production or "head on" destruction of a pair is singular. We perform the same procedure as in the NES case (Mezzacappa & Bruenn 1993c) to obtain singularity free values for the kernels by integrating the Legendre expansion of $R^{\rm em}_{\rm PAIR}$ and separate out the contributions from production or destruction

when $j = jmax + 1 - j'$, i.e. when the direction cosines for the pair are diametrically opposed to one another. The expression for the kernel in that case becomes:

$$R^{\rm em}_{\rm PAIR}(E_{k+1/2}, E_{k+1/2}, \mu_{j+1/2}, \mu_{(jmax+1-j)+1/2}) = \tag{2.107}$$

$$\frac{1}{w_{j+1/2}}\{2\pi\Phi^{\rm em}_{PAIR,0}(E_{k+1/2}, E_{k+1/2}) \tag{2.108}$$

$$- \sum_{l\neq jmax+1-j} w_l R^{\rm em}_{\rm PAIR}(E_{k+1/2}, E_{k+1/2}, \mu_{j+1/2}, \mu_{l+1/2})\}.$$

The moments, $\Phi^{\rm em}_{PAIR,0}$, in equation 2.108 are given by (Bruenn 1985)

$$\Phi^{\rm em}_{PAIR,0}(E, E') = \frac{(2\pi)^4 G_{\rm F}^2 c}{\pi(hc)^4}\frac{1}{E^2 E'^2}\int dE_{\rm e}\ \ F_{\rm e}(E_{\rm e})(F_{\rm e^+}(E + E' - E_{\rm e})] \tag{2.109}$$

$$\times[\beta_1 J^{\rm I}_0(E, E', E_{\rm e}) + \beta_2 J^{\rm II}_0(E, E', E_{\rm e})],$$

where $F_{\rm e^+}(E + E' - E_{\rm e})$ is the positron Fermi-Dirac distribution and

$$J^{\rm II}_0(E, E', E_{\rm e}) = J^I_0(E', E, E_{\rm e}), \tag{2.110}$$

and

$$J^{\rm I}_0(E, E', E_{\rm e}) = \Theta(E + E' - E_{\rm e})\,\{[\Theta(E - E_{\rm e})\Theta(E' - E) \tag{2.111}$$

$$+ \ \Theta(E' - E_{\rm e})\Theta(E - E')]$$

$$\times \ a_0(E, E', E_{\rm e}) \tag{2.112}$$

$$+ \ [\Theta(E_{\rm e} - E)\Theta(E - E') + \Theta(E_e - E')\Theta(E' - E)] \tag{2.113}$$

$$\times \ b_0(E, E', E_{\rm e}) + \Theta(E_e - E)\Theta(E' - E_{\rm e})c_0(E, E', E_{\rm e})$$

$$+ \ \Theta(E_e - E')\Theta(E - E_e)d_0(E, E', E_{\rm e})\}\,,$$

with

$$a_0(E,E',E_{\rm e}) = \frac{1}{EE'}[\frac{4}{15}E^5E'^3 - \frac{4}{3}E_{\rm e}^4E' + \frac{8}{3}E_{\rm e}^3E'^2], \tag{2.114}$$

$$\begin{aligned} b_0(E,E',E_{\rm e}) &= \frac{1}{EE'}[-a_0 + \frac{8}{3}E_{\rm e}(E^3+E'^3) - \frac{4}{3}E_{\rm e}(E+E')^2(E'^2-2EE'+3E^2) \\ &+ \frac{4}{15}(E+E')^3(E'^2-3EE'+6E^2), \end{aligned} \tag{2.115}$$

$$c_0(E,E',E_{\rm e}) = \frac{E^2}{E'}[\frac{8}{3}E'^2 + 4EE' + \frac{8}{5}E^2] - E_{\rm e}[\frac{16}{3}E^2 + 4\frac{E^3}{E'}] + \frac{8}{3}E_{\rm e}\frac{E^2}{E'}, \tag{2.116}$$

$$d_0(E,E',E_{\rm e}) = \frac{4}{15}\frac{E'^4}{E^4} - \frac{4}{3}\frac{E'^3}{E}E_{\rm e} + \frac{8}{3}\frac{E'^2}{E}E_{\rm e}^2. \tag{2.117}$$

Chapter 3

Finite Differencing and Numerical Implementation

In this chapter the computational grid used in AGILE-BOLTZTRAN is described along with the computational method used to calculate several numerical derivatives and derived quantities. Also, the finite differencing of the neutrino Boltzmann equation, the electron fraction equation, and the radiation terms in the velocity and energy equations presented in Chapter 2 are given.

3.1 Grid

We define a grid in (m, μ_0, E_0)-space as follows (Mezzacappa & Bruenn 1993b). The stellar core is divided into $imax-1$ mass shells, whose outer edges are located at the discrete mass points, $m_{i+1} : i = 1, 2, ..., imax-1$. The mass point $m_1 \equiv 0$ corresponds to the origin, $r = 0$. Each mass shell contains a mass, $\Delta m_{i+1/2}$, defined by

$$\Delta m_{i+1/2} \equiv m_{i+1} - m_i \tag{3.1}$$

for $i = 1, 2, ..., imax - 1$. The half integer index, $i + 1/2$, denotes the shell (zone) center. The zone centers are defined to enclose half the mass in a zone:

$$m_{i+1/2} \equiv m_i + \frac{1}{2}\Delta m_{i+1/2} = \frac{1}{2}(m_i + m_{i+1}) \tag{3.2}$$

for $i = 1, 2, imax$–1. The zone centers also define a sequence of concentric shells, each containing a mass, Δm_i, given by

$$\Delta m_i = m_{i+1/2} - m_{i-1/2} \tag{3.3}$$

for $i = 2, 3, ..., imax$. If we substitute equation (3.2) in equation (3.3), we obtain

$$\Delta m_i = \frac{1}{2}(\Delta m_{i-1/2} + \Delta m_{i+1/2}) \tag{3.4}$$

for $i = 2, 3, ..., imax$. We define $\Delta m_{imax+1/2} \equiv \Delta m_{imax-1/2}$. Note that the m grid is modified dynamically by the adaptivity of AGILE-BOLTZTRAN. For details of the grid equation, which governs the movement of grid points between mass coordinates, see Liebendörfer (2000).

The μ_0-grid is made up of N discrete direction cosines, $\mu_{j+1/2} : j = 1, 2, ..., N$, corresponding to an N-point Gaussian quadrature set with weights, $w_{j+1/2} : j = 1, 2, ..., N$. The Gaussian quadrature points are symmetric about $\mu_0 = 0$:

$$\sum_{j=1}^{N} \mu_{j+1/2} w_{j+1/2} = 0 \tag{3.5}$$

The weights, $w_{j+1/2}$, are normalized to

$$\sum_{j=1}^{N} w_{j+1/2} = 2 \tag{3.6}$$

Gaussian quadrature is chosen because quadratures in an N-point scheme are exact for polynomials in μ_0 up to order $2N-1$. Thus, the neutrino distribution function would be accurate to order $2N-1$ in μ_0. The exact (continuum) distribution is, of course, accurate to all orders in μ_0.

The E_0-grid is made up of $kmax$ discrete energies, $E_k : k = 1, 2, ..., kmax$. In order to span the complete range of electron-neutrino energies relevant for the collapse problem, the discrete energies, E_k, are geometrically spaced:

$$E_{k+1} = \sqrt{s} E_k \tag{3.7}$$

where s is some scale factor chosen to span a reasonable energy range with $kmax$ zones. It is typically set to 2. The energies E_k and E_{k+1} define $kmax-1$ energy zones, whose centers correspond to the energies $E_{k+1/2}$, given by

$$E_{k+1/2} = \frac{1}{2}(E_k + E_{k+1}) \tag{3.8}$$

for $k = 1, 2, ..., kmax-1$. We also have the energy zone widths:

$$\Delta E_{k+1/2} = E_{k+1} - E_k \tag{3.9}$$

for $k = 1, 2, ..., kmax-1$.

3.1.1 Variables and Their Derivatives

Because of the short time scales associated with neutrino–matter coupling and the short Courant time given by the radial zone widths and the speed of light propagation of the neutrinos, and because the neutrinos and matter are in thermal and chemical (beta) equilibrium deep in the stellar core where the neutrino emission and absorption rates are large and canceling, the Boltzmann equation and the coupling of this equation to the matter internal energy and electron fraction equations are finite differenced with respect to time in a fully implicit manner (a.k.a. backward Euler differencing). This ensures two things: (1) Unconditional stability for time steps that are large relative to neutrino transport and interaction time scales. (2) Beta equilibrium in regions where it occurs.

The implicit solution of (a) the Boltzmann equation, (b) the neutrino–matter coupling in the specific internal energy equation, and (c) the electron fraction equation, requires the values of derivatives of a number of variables with respect to temperature and electron fraction (e.g., the internal energy and the neutrino absorption, emission, and scattering rates). Moreover, under the extreme conditions present in stellar cores, matter is in nuclear statistical equilibrium (NSE) and its thermodynamic state (e.g., its pressure, entropy, etc.) is completely determined by its density, temperature, and electron fraction.

Let $\upsilon \equiv \upsilon(\rho_0, T, Y_e, E_0, \mu_0)$ be a variable whose derivative with respect to temperature or electron fraction is required. [In what follows, to avoid too many subscripts, we will ignore the indices tying υ to a particular point on the (m, μ_0, E_0)-grid.] We construct a local cube about the point (ρ_0, T, Y_e) with corners at the points $(\rho_l, T_m, Y_n) : l, m, n = 1, 2$, where

$$\log_{10}[\frac{\rho_2}{\rho_1}] \quad = \quad \frac{1}{N_\rho} \tag{3.10}$$

$$\log_{10}[\frac{T_2}{T_1}] = \frac{1}{N_T} \tag{3.11}$$

$$Y_2 - Y_1 = \frac{1}{N_Y} \tag{3.12}$$

(Mezzacappa & Bruenn 1993b). The numbers N_ρ, N_T, and N_Y define the resolution of our cube: N_ρ and N_T are the number of points per decade in density and temperature, and N_Y is the number of points per 1/2 in Y_e. In our applications, we use $N_\rho = 10$, $N_T = 40$, and $N_Y = 50$. These values were determined by comparing directly computed and interpolated values of various thermodynamic quantities, such as the pressure, and ensuring that the two methods yielded results that were in good agreement. Having defined our cube, we obtain a value for the variable υ at each of the eight cube corners. At the given point (ρ, T, Y_e) in the cube, we compute the value of $\bar{\upsilon}$ by linearly interpolating in $\bar{\rho_0}$, $\bar{T}$, and Y_e, where $\bar{O} \equiv \log_{10}(O)$. Thus,

$$\begin{aligned}
\bar{\upsilon} = C_3 \; [\; & (1-C_1)(1-C_2)\,\bar{\upsilon}(\rho_1, T_1, Y_2) \\
& + C_1(1-C_2)\,\bar{\upsilon}(\rho_2, T_1, Y_2) \\
& + C_2(1-C_1)\,\bar{\upsilon}(\rho_1, T_2, Y_2) \\
& + C_1 C_2\,\bar{\upsilon}(\rho_2, T_2, Y_2) \;] \\
+ \; (1-C_3) \; [\; & (1-C_1)(1-C_2)\,\bar{\upsilon}(\rho_1, T_1, Y_1) \\
& + C_1(1-C_2)\,\bar{\upsilon}(\rho_2, T_1, Y_1) \\
& + C_2(1-C_1)\,\bar{\upsilon}(\rho_1, T_2, Y_1) \\
& + C_1 C_2\,\bar{\upsilon}(\rho_2, T_2, Y_1) \;]
\end{aligned} \tag{3.13}$$

where

$$C_1 = \log_{10}(\frac{\rho_0}{\rho_1})/\log_{10}(\frac{\rho_2}{\rho_1}), \tag{3.14}$$

$$C_2 = \log_{10}(\frac{T}{T_1})/\log_{10}(\frac{T_2}{T_1}), \tag{3.15}$$

$$C_3 = (Y_e - Y_1)/(Y_2 - Y_1). \tag{3.16}$$

The derivative of υ with respect to ρ_0, T, or Y_e can be obtained simply by differentiating equation (3.13) with respect to each variable. For example,

$$\begin{aligned}
(\frac{\partial \upsilon}{\partial T})_{\rho_0,Y_e} &= \frac{\upsilon}{T}(\frac{\partial \bar{\upsilon}}{\partial \bar{T}})_{\rho_0,Y_e} \\
&= \frac{\upsilon}{T}\frac{dC_2}{d\bar{T}}(\frac{\partial \bar{\upsilon}}{\partial C_2})_{C_1,C_3} \\
&= -\upsilon/(T\log_{10}[T_2/T_1]) \\
&\quad \times\{C_3\ [\ (1-C_1)\,\bar{\upsilon}(\rho_1,T_1,Y_2) \\
&\qquad +C_1\,\bar{\upsilon}(\rho_2,T_1,Y_2) \\
&\qquad -(1-C_1)\,\bar{\upsilon}(\rho_1,T_2,Y_2) \\
&\qquad -C_1\,\bar{\upsilon}(\rho_2,T_2,Y_2)\ ] \\
&\quad +(1-C_3)\ [\ (1-C_1)\,\bar{\upsilon}(\rho_1,T_1,Y_1) \\
&\qquad +C_1\,\bar{\upsilon}(\rho_2,T_1,Y_1) \\
&\qquad -(1-C_1)\,\bar{\upsilon}(\rho_1,T_2,Y_1) \\
&\qquad -C_1\,\bar{\upsilon}(\rho_2,T_2,Y_1)\ ]\}.
\end{aligned} \tag{3.17}$$

This scheme has several advantages. First, the relation between values of the variable and its derivatives inside the cube is exact, both being derived from the same interpolation formula.

This helps convergence in what we will see is the multidimensional Newton–Raphson iteration we must solve. Second, the subroutine generating the variable υ need not be used at each time step, but only if the point (ρ, T, Y_e) moves outside the cube, in which case a new cube is generated, centered about the point (ρ_0, T, Y_e). (This is checked at the *end* of each time step after all evolved variables are completely updated.) Consequently, we are not restricted to simple numerical recipes for generating υ. Third, we avoid discontinuous changes in υ, or any of its derivatives, which can be traumatic for a multidimensional (or one-dimensional) Newton–Raphson iteration. If the thermodynamic trajectory in $(\rho_0, T, Y_\mathrm{e})$ space moves out of a local $(\rho_0, T, Y_\mathrm{e})$ cube, *extrapolation* rather than interpolation is used, which preserves the continuity of the derivatives across cube boundaries. If we were to use an adjacent cube to compute *interpolated* quantities and their derivatives, the derivatives would be discontinuous in a scheme, such as ours, that uses linear interpolation. Before the next time step a new local cube is constructed centered on the current value of (ρ_0, T, Y_e) (see Figure 3.1).

3.2 Differencing the Neutrino Boltzmann Equation

Here we discuss the finite differencing for the Boltzmann equation and its coupling to lepton conservation and the hydrodynamics. From equations (2.2), (2.15), and (2.16), the system of equations we need to solve is

$$\begin{aligned}\frac{1}{c}\frac{\partial F}{\partial t} &= -4\pi\mu_0\frac{\partial(r^2\rho_0 F)}{\partial m} \\ &\quad -\frac{1}{r}\frac{\partial[(1-\mu_0^2)F]}{\partial\mu_0} \\ &\quad +\frac{j}{\rho_0} - \tilde{\chi}\,F\end{aligned}$$

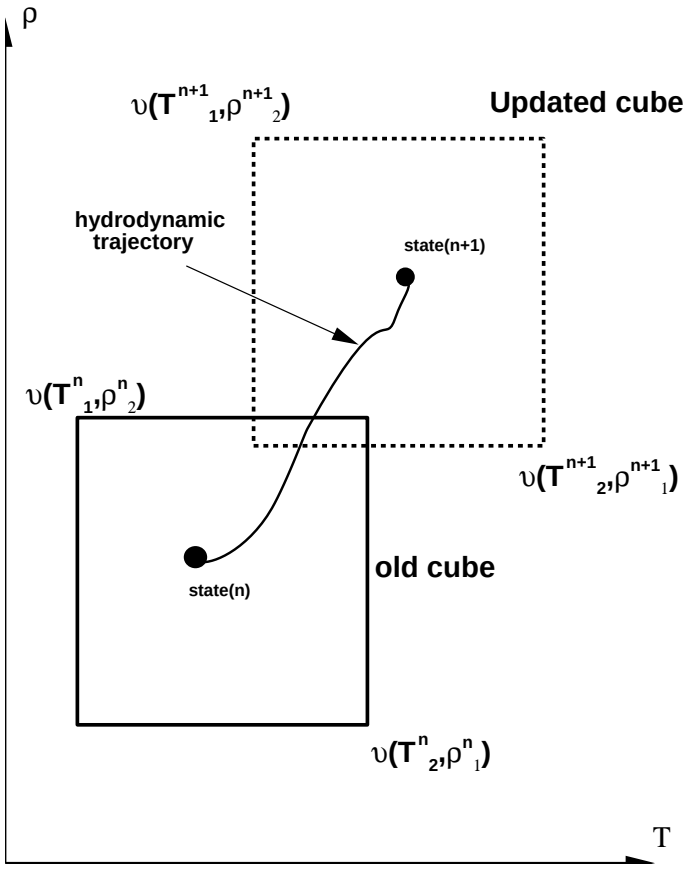

Figure 3.1: Schematic example of recubing as the hydrodynamic trajectory evolves. The Ye dimension is suppressed for clarity.

$$
\begin{aligned}
&+\frac{1}{c}\frac{1}{h^3c^3}\,E_0^2\int d\mu_0' R_{\rm IS} F \\
&-\frac{1}{c}\frac{1}{h^3c^3}\,E_0^2\,F\int d\mu_0' R_{\rm IS} \\
&+\frac{1}{h^3c^4}(\frac{1}{\rho_0}-F)\int dE_0' E_0'^2 d\mu_0' \tilde{R}^{\rm in}_{\rm NES} F \\
&-\frac{1}{h^3c^4}F(\mu_0,E_0)\int dE_0' E_0'^2 d\mu_0' \tilde{R}^{\rm out}_{\rm NES}(\frac{1}{\rho_0}-F) \\
&+\frac{1}{h^3c^4}(\frac{1}{\rho_0}-F)\int dE_0' E_0'^2 d\mu_0' \tilde{R}^{\rm em}_{\rm PAIR}(\frac{1}{\rho_0}-\bar{F}) \\
&-\frac{1}{h^3c^4}F(\mu_0,E_0)\int dE_0' E_0'^2 d\mu_0' \tilde{R}^{\rm abs}_{\rm PAIR}\bar{F} \qquad (3.18)
\end{aligned}
$$

$$
\begin{aligned}
\frac{1}{c}\frac{\partial\epsilon}{\partial t} &= -\frac{2\pi C_0}{h^3c^3}\int dE_0 E_0^3 d\mu_0(\frac{j}{\rho_0}-\tilde{\chi}F) \\
&+\sum_{\nu,\bar{\nu}}\frac{2\pi C_0}{h^6c^6}\int dE_0 E_0^3 d\mu_0 F\int dE_0' E_0'^2 d\mu_0' \tilde{R}^{\rm out}_{\rm NES}(\frac{1}{\rho_0}-F) \\
&-\sum_{\nu,\bar{\nu}}\frac{2\pi C_0}{h^6c^6}\int dE_0 E_0^3 d\mu_0(\frac{1}{\rho_0}-F)\int dE_0' E_0'^2 d\mu_0' \tilde{R}^{\rm in}_{\rm NES} F \\
&+\frac{2\pi C_0}{h^6c^6}\int dE E^3 d\mu F\int dE' E'^2 d\mu' \tilde{R}^{\rm abs}_{\rm PAIR}(\bar{F}) \\
&-\frac{2\pi C_0}{h^6c^6}\int dE E^3 d\mu(\frac{1}{\rho}-F)\int dE' E'^2 d\mu' \tilde{R}^{\rm em}_{\rm PAIR}(\frac{1}{\rho}-\bar{F}) \qquad (3.19)
\end{aligned}
$$

$$
\begin{aligned}
\frac{1}{c}\frac{\partial Y_e}{\partial t} &= -\frac{2\pi m_B}{h^3c^3}\int dE_0 E_0^2 d\mu_0(\frac{j}{\rho_0}-\tilde{\chi}F) \\
&+ \frac{2\pi m_B}{h^3c^3}\int dE_0 E_0^2 d\mu_0(\frac{j}{\rho_0}-\tilde{\chi}\bar{F}). \qquad (3.20)
\end{aligned}
$$

The aberration and frequency shift terms in the Boltzmann equation have been split off and will be solved separately. We will discuss the finite differencing for these terms later. As noted in Chapter 2, each neutrino flavor is solved for along with its corresponding antiparticle. The flavor sums in equation 3.19 now run over only a neutrino–antineutrino pair. $\bar{F}$ is the corresponding antineutrino for a given flavor. Equation 3.20 is evolved with the electron type equations only, as μ and τ neutrino interactions are unable to change the matter Y_e. Finally, we must solve two linear systems: one for electron flavor neutrinos and antineutrinos including all three equations 3.18, 3.19, and 3.20, and another for μ/τ neutrinos and antineutrinos consisting only of equations

3.18 and 3.19.

The Boltzmann equation (3.18) is finite differenced as (Mezzacappa & Bruenn 1993b; Liebendörfer 2000)

$$
\begin{aligned}
& (F^{*}_{i+1/2,j+1/2,k+1/2} - (\frac{\Delta m^{n}_{i+1/2}}{\Delta m^{n+1}_{i+1/2}}) F^{n}_{i+1/2,j+1/2,k+1/2})/c\Delta t \\
+ \quad & \frac{1}{\Delta m^{n+1}_{i+1/2}} \left[u^{grid}_{i+1} \, \hat{F}^{*}_{i+1,j+1/2,k+1/2} - u^{grid}_{i} \, \hat{F}^{*}_{i,j+1/2,k+1/2} \right] \\
+ \quad & \frac{4\pi |\mu_{j+1/2}| \lambda}{\Delta m^{n+1}_{i+1/2}} \left[(r^{n+1}_{i+1})^2 \, \rho^{n+1}_{i+1} \, F^{*}_{i+1,j+1/2,k+1/2} - (r^{n+1}_{i})^2 \, \rho^{n+1}_{i} \, F^{*}_{i,j+1/2,k+1/2} \right] \\
+ \quad & \frac{3[(r^{n+1}_{i+1})^2 - (r^{n+1}_{i})^2]}{(r^{n+1}_{i+1})^3 - (r^{n+1}_{i})^3} \, \frac{1}{w_{j+1/2}} \left(\alpha_{j+1} \, F^{*}_{i+1/2,j+1,k+1/2} - \alpha_{j} \, F^{*}_{i+1/2,j,k+1/2} \right) \\
- \quad & \frac{j^{n+1}_{i+1/2,k+1/2}}{\rho^{n+1}_{i+1/2}} + \tilde{\chi}^{n+1}_{i+1/2,k+1/2} \, F^{*}_{i+1/2,j+1/2,k+1/2} \\
- \quad & \frac{1}{ch^3c^3} \, E^{2}_{k+1/2} \sum_{l=1}^{jmax} w_{l+1/2} \, (R_{\rm IS})^{n+1}_{i+1/2,j+1/2,l+1/2,k+1/2} \, F^{*}_{i+1/2,l+1/2,k+1/2} \\
+ \quad & \frac{1}{ch^3c^3} \, E^{2}_{k+1/2} \, F^{*}_{i+1/2,j+1/2,k+1/2} \sum_{l=1}^{jmax} w_{l+1/2} \, (R_{\rm IS})^{n+1}_{i+1/2,j+1/2,l+1/2,k+1/2} \\
- \quad & \frac{1}{ch^3c^3} \, (1/\rho^{n+1}_{i+1/2} - F^{*}_{i+1/2,j+1/2,k+1/2}) \sum_{m=1}^{kmax} \Delta E_{m+1/2} E^{2}_{m+1/2} \sum_{l=1}^{jmax} w_{l+1/2} \\
\times \quad & (\tilde{R}^{\rm in}_{\rm NES})^{n+1}_{i+1/2,j+1/2,l+1/2,k+1/2,m+1/2} \, F^{*}_{i+1/2,l+1/2,m+1/2} \\
+ \quad & \frac{1}{ch^3c^3} \, F^{*}_{i+1/2,j+1/2,k+1/2} \sum_{m=1}^{kmax} \Delta E_{m+1/2} E^{2}_{m+1/2} \sum_{l=1}^{jmax} w_{l+1/2} \\
\times \quad & (\tilde{R}^{\rm out}_{\rm NES})^{n+1}_{i+1/2,j+1/2,l+1/2,k+1/2,m+1/2} \, (1/\rho^{n+1}_{i+1/2} - F^{*}_{i+1/2,l+1/2,m+1/2}) \\
- \quad & \frac{1}{ch^3c^3} \, (1/\rho^{n+1}_{i+1/2} - F^{*}_{i+1/2,j+1/2,k+1/2}) \sum_{m=1}^{kmax} \Delta E_{m+1/2} E^{2}_{m+1/2} \sum_{l=1}^{jmax} w_{l+1/2} \\
\times \quad & (\tilde{R}^{\rm em}_{\rm PAIR})^{n+1}_{i+1/2,j+1/2,l+1/2,k+1/2,m+1/2} \, (1/\rho^{n+1}_{i+1/2} - \bar{F}^{*}_{i+1/2,l+1/2,m+1/2}) \\
+ \quad & \frac{1}{ch^3c^3} \, F^{*}_{i+1/2,j+1/2,k+1/2} \sum_{m=1}^{kmax} \Delta E_{m+1/2} E^{2}_{m+1/2} \sum_{l=1}^{jmax} w_{l+1/2} \\
\times \quad & (\tilde{R}^{\rm abs}_{\rm PAIR})^{n+1}_{i+1/2,j+1/2,l+1/2,k+1/2,m+1/2} \, (1/\rho^{n+1}_{i+1/2} - \bar{F}^{*}_{i+1/2,l+1/2,m+1/2}) \\
= \quad & 0
\end{aligned}
\tag{3.21}
$$

where $\lambda = +1$ for $\mu_{j+1/2} > 0$, and $\lambda = -1$ for $\mu_{j+1/2} < 0$. The distribution function, $F^*_{i+1/2,j+1/2,k+1/2}$, is partially updated. A fully updated value is obtained after the change in the distribution function from angular aberration and frequency shift is computed. The neutrino emissivity, opacity, and scattering kernels appear in equation (3.21) with an $n+1$ superscript because they are functions of ρ_0, ϵ, and Y_e, the first of which has been fully updated and the latter two of which will be fully updated when the system of equations (3.18) to (3.20) is solved. There are two terms in this finite difference equation not apparent from simply differencing equation 2.15. Note the presence of the ratio $\Delta m^n_{i+1/2}/\Delta m^{n+1}_{i+1/2}$ in the first term and the addition of the second term involving the grid velocity, u^{grid}. These changes to the differencing given in Mezzacappa & Bruenn (1993b), Mezzacappa & Messer (1998) result from the adaptive grid in the current version of AGILE-BOLTZTRAN. The mass enclosed by a given zone changes with time, resulting in the addition to the first term. There is also an effective advection caused by the motion of the grid points that is described by the addition of the second term. $\hat{F}^*$ in the second term is defined as:

$$\hat{F}^*_{i,j+1/2,k+1/2} = \begin{cases} \hat{F}^*_{i-1/2,j+1/2,k+1/2} & \text{if } u^{grid}_i \geq 0 \\ \hat{F}^*_{i+1/2,j+1/2,k+1/2} & \text{otherwise} \end{cases} \tag{3.22}$$

(Liebendörfer 2000).

This finite difference representation of the Boltzmann equation is fully implicit, and hence has first-order truncation error in Δt. It is centered in m, μ_0, and E_0, and hence has second-order truncation error in each of these phase-space coordinates. This representation also conserves neutrino number and energy. For the mass derivative term, "upwind differencing" (e.g., see Roache (1998)) is used. Upwind differencing is constructed so that the radial and angular advection on a discrete grid is faithful to the continuum advection with regard to the direction of

neutrino propagation. For the μ-derivative term, the standard differencing for discrete ordinates codes with Gaussian quadratures is used (Lewis & Miller 1984). The discrete representation of the coefficient, $1/r$, in the μ-derivative term is chosen so that, in an infinite homogeneous medium with $\rho_0 F$ in equilibrium with the medium, $\rho_0 F$ = constant is a solution of the finite difference equation. (This is true in our application, where, deep within the stellar core, $\rho_0 F = 1$ everywhere, for all neutrino direction cosines and energies. In this region, the neutrinos are degenerate.) Setting $\rho_{i+1/2} F_{i+1/2,j+1/2,k+1/2} = j^{n+1}_{i+1/2,k+1/2} / \tilde{\chi}^{n+1}_{i+1/2,k+1/2}$ = constant in equation (3.21) with

$$\alpha_{j+1} - \alpha_j = -\mu_{j+1/2} w_{j+1/2}, \tag{3.23}$$

we obtain

$$\begin{aligned} & \frac{4\pi|\mu_{j+1/2}|\lambda}{\Delta m_{i+1/2}} \left[(r^{n+1}_{i+1})^2 - (r^{n+1}_i)^2 \right] \\ + \quad & \frac{3[(r^{n+1}_{i+1})^2 - (r^{n+1}_i)^2]}{(r^{n+1}_{i+1})^3 - (r^{n+1}_i)^3} \frac{1}{\rho^{n+1}_{i+1/2}} \frac{1}{w_{j+1/2}} (\alpha_{j+1} - \alpha_j) = 0. \end{aligned} \tag{3.24}$$

Equation (3.23) is the standard definition for the angular difference coefficients, α_j. The finite difference equation for the Boltzmann equation is solved with the boundary condition:

$$F^n_{imax+1/2,j+1/2,k+1/2} \equiv 0 \tag{3.25}$$

for $\mu_{j+1/2} < 0$ and $k = 1, 2, ..., kmax$. (There are no incoming neutrinos at the outer boundary of our collapsing core.)

Because the opacity, $\tilde{\chi}$, and the scattering kernels, $R_{\rm IS}$, $\tilde{R}^{\rm in,out}_{\rm NES}$, and $\tilde{R}^{\rm em,abs}_{\rm PAIR}$ depend on ρ_0,

T, and Y_e, the $\tilde{\chi}F$, $R_{\rm IS}F$, $\tilde{R}^{\rm in,out}_{\rm NES}F$, and $\tilde{R}^{\rm em,abs}_{\rm PAIR}$ terms in the Boltzmann equation are implicitly nonlinear. Because of the blocking factors, $(1/\rho - F)$, the equation is explicitly nonlinear in F. Therefore we linearize in F, T, and Y_e:

$$F^{*}_{i+1/2,j+1/2,k+1/2} = F^{0}_{i+1/2,j+1/2,k+1/2} + \delta F_{i+1/2,j+1/2,k+1/2}, \tag{3.26}$$

and

$$\begin{aligned} j^{n+1}_{i+1/2,k+1/2} = j^{0}_{i+1/2,k+1/2} &+ [(\frac{\partial j}{\partial T})_{\rho_0,Y_e}]^{0}_{i+1/2,k+1/2}\,\delta T_{i+1/2} \\ &+ [(\frac{\partial j}{\partial Y_e})_{\rho_0,T}]^{0}_{i+1/2,k+1/2}\,\delta (Y_e)_{i+1/2}, \end{aligned} \tag{3.27}$$

$$\begin{aligned} \chi^{n+1}_{i+1/2,k+1/2} = \chi^{0}_{i+1/2,k+1/2} &+ [(\frac{\partial \chi}{\partial T})_{\rho_0,Y_e}]^{0}_{i+1/2,k+1/2}\,\delta T_{i+1/2} \\ &+ [(\frac{\partial \chi}{\partial Y_e})_{\rho_0,T}]^{0}_{i+1/2,k+1/2}\,\delta (Y_e)_{i+1/2}, \end{aligned} \tag{3.28}$$

$$\begin{aligned} (R_{\rm IS})^{n+1}_{i+1/2,j+1/2,l+1/2,k+1/2} = (R_{\rm IS})^{0}_{i+1/2,j+1/2,l+1/2,k+1/2} &+ [(\frac{\partial R_{\rm IS}}{\partial T})_{\rho_0,Y_e}]^{0}_{i+1/2,j+1/2,l+1/2,k+1/2}\,\delta T_{i+1/2} \\ &+ [(\frac{\partial R_{\rm IS}}{\partial Y_e})_{\rho_0,T}]^{0}_{i+1/2,j+1/2,l+1/2,k+1/2}\,\delta (Y_e)_{i+1/2}, \end{aligned} \tag{3.29}$$

$$(\tilde{R}^{\rm in/out}_{\rm NES})^{n+1}_{i+1/2,j+1/2,l+1/2,k+1/2,m+1/2} = (\tilde{R}^{\rm in/out}_{\rm NES})^{0}_{i+1/2,j+1/2,l+1/2,k+1/2,m+1/2}$$

$$
\begin{aligned}
&+[(\frac{\partial R^{\mathrm{in/out}}_{\mathrm{NES}}}{\partial T})_{\rho_0,Y_e}]^0_{i+1/2,j+1/2,l+1/2,k+1/2,m+1/2}\,\delta T_{i+1/2} \\
&+[(\frac{\partial R^{\mathrm{in/out}}_{\mathrm{NES}}}{\partial Y_e})_{\rho_0,T}]^0_{i+1/2,j+1/2,l+1/2,k+1/2,m+1/2}\,\delta(Y_e)_{i+1/2},
\end{aligned}
\tag{3.30}
$$

$$
\begin{aligned}
(\tilde{R}^{\mathrm{em/abs}}_{\mathrm{PAIR}})^{n+1}_{i+1/2,j+1/2,l+1/2,k+1/2,m+1/2} &= (\tilde{R}^{\mathrm{em/abs}}_{\mathrm{PAIR}})^0_{i+1/2,j+1/2,l+1/2,k+1/2,m+1/2} \\
&+[(\frac{\partial R^{\mathrm{em/abs}}_{\mathrm{PAIR}}}{\partial T})_{\rho_0,Y_e}]^0_{i+1/2,j+1/2,l+1/2,k+1/2,m+1/2}\,\delta T_{i+1/2} \\
&+[(\frac{\partial R^{\mathrm{em/abs}}_{\mathrm{PAIR}}}{\partial Y_e})_{\rho_0,T}]^0_{i+1/2,j+1/2,l+1/2,k+1/2,m+1/2}\,\delta(Y_e)_{i+1/2}.
\end{aligned}
\tag{3.31}
$$

The "0" superscript in equation (3.26) indicates a current guess for F about which the solution to the nonlinear equation (3.18) is being linearized. Initially $F^0_{i+1/2,j+1/2,k+1/2} = F^n_{i+1/2,j+1/2,k+1/2}$. In equations (3.27) to (3.30), the zero superscripts indicate values of the emissivity, opacity, and scattering kernels and their derivatives at the point $(\rho^{n+1}_{i+1/2}, T^0_{i+1/2}, (Y_e)^0_{i+1/2})$, where $T^0_{i+1/2}$ and $(Y_e)^0_{i+1/2}$ are current guesses for T and Y_e, about which the solutions to the nonlinear equations (3.19) and (3.20) are being linearized. The derivatives in equations (3.27) to (3.30) are computed numerically according to equation (3.17).

The finite differenced Boltzmann equation (3.21) is supplemented by equations relating the distribution function at the zone edges in m and μ_0 to its values at the zone centers in those variables:

$$
\begin{aligned}
\rho^n_i F^n_{i,j+1/2,k+1/2} &= \beta^{>}_{i,j+1/2,k+1/2}\,\rho^n_{i-1/2}\,F^n_{i-1/2,j+1/2,k+1/2} \\
&+ (1-\beta^{>}_{i,j+1/2,k+1/2})\,\rho^n_{i+1/2}\,F^n_{i+1/2,j+1/2,k+1/2}
\end{aligned}
\tag{3.32}
$$

for $\mu_{j+1/2} > 0$,

$$\begin{aligned} \rho_i^n \, F_{i,j+1/2,k+1/2}^n &= \beta_{i,j+1/2,k+1/2}^{<} \, \rho_{i+1/2}^n \, F_{i+1/2,j+1/2,k+1/2}^n \\ &+ (1 - \beta_{i,j+1/2,k+1/2}^{<}) \, \rho_{i-1/2}^n \, F_{i-1/2,j+1/2,k+1/2}^n \end{aligned} \tag{3.33}$$

for $\mu_{j+1/2} < 0$, and

$$\begin{aligned} F_{i+1/2,j,k+1/2}^n &= \gamma_{i+1/2,j,k+1/2} \, F_{i+1/2,j-1/2,k+1/2}^n \\ &+ (1 - \gamma_{i+1/2,j,k+1/2}) \, F_{i+1/2,j+1/2,k+1/2}^n \end{aligned} \tag{3.34}$$

for all $\mu_{j+1/2}$. In equations (3.32), (3.33), and (3.34), $\beta_{i,j+1/2,k+1/2}^{>}$, $\beta_{i,j+1/2,k+1/2}^{<}$, and $\gamma_{i+1/2,j,k+1/2}$ are parameters. They carry a mass shell index and an energy index and are set locally. For $\beta_{i,j+1/2,k+1/2}^{>} = \beta_{i,j+1/2,k+1/2}^{<} = 1$ and $\gamma_{i+1/2,j,k+1/2} = 1$, we obtain the "step" relations (e.g., see Duderstadt & Martin (1979); Lewis & Miller (1984)):

$$\rho_i^n \, F_{i,j+1/2,k+1/2}^n = \rho_{i-1/2}^n \, F_{i-1/2,j+1/2,k+1/2}^n \tag{3.35}$$

for $\mu_{j+1/2} > 0$,

$$\rho_i^n \, F_{i,j+1/2,k+1/2}^n = \rho_{i+1/2}^n \, F_{i+1/2,j+1/2,k+1/2}^n \tag{3.36}$$

for $\mu_{j+1/2} < 0$, and

$$F_{i+1/2,j,k+1/2}^n = F_{i+1/2,j-1/2,k+1/2}^n \tag{3.37}$$

for all $\mu_{j+1/2}$. For $\beta^{<}_{i,j+1/2,k+1/2} = \beta^{>}_{i,j+1/2,k+1/2} = 1/2$ and $\gamma_{i+1/2,j,k+1/2} = 1/2$, we obtain the relations

$$\rho^n_i \, F^n_{i,j+1/2,k+1/2} = \frac{1}{2}(\rho^n_{i-1/2} \, F^n_{i-1/2,j+1/2,k+1/2} + \rho^n_{i+1/2} \, F^n_{i+1/2,j+1/2,k+1/2}) \quad (3.38)$$

$$F^n_{i+1/2,j,k+1/2} = \frac{1}{2}(F^n_{i+1/2,j-1/2,k+1/2} + F^n_{i+1/2,j+1/2,k+1/2}). \quad (3.39)$$

Note that the relations (3.38) and (3.39) differ from the standard "diamond" relations (e.g., see Duderstadt & Martin (1979); Lewis & Miller (1984)):

$$f^n_{i+1/2,j+1/2,k+1/2} = \frac{1}{2}(f^n_{i,j+1/2,k+1/2} + f^n_{i+1,j+1/2,k+1/2}), \quad (3.40)$$

$$f^n_{i+1/2,j+1/2,k+1/2} = \frac{1}{2}(f^n_{i+1/2,j,k+1/2} + f^n_{i+1/2,j+1,k+1/2}), \quad (3.41)$$

in that the diamond relations express the zone *center* distribution function in terms of the distribution function at the zone edges.

In equation (3.32) and (3.33), $\beta^{>}_{i,j+1/2,k+1/2}$ and $\beta^{<}_{i,j+1/2,k+1/2}$ are defined as follows:

$$\beta^{><}_{i,j+1/2,k+1/2} \equiv 1 - \frac{1}{2}\frac{R^n_{\nu_e,k+1/2}/\lambda^n_{i,j+1/2,k+1/2}}{1 + R^n_{\nu_e,k+1/2}/\lambda^n_{i,j+1/2,k+1/2}} \quad (3.42)$$

where $R^n_{\nu_e,k+1/2}$ is the electron neutrinosphere at time slice n for neutrinos of energy $E_{k+1/2}$. The neutrinosphere is a characteristic *physical* length scale in the problem that can be used to determine whether the neutrinos are diffusing or free streaming. It is a measure of the neutrino transport that is independent of the grid spacing, and in this regard represents an improvement over what was used in Mezzacappa & Bruenn (1993a,b,c). It is defined using the neutrino optical

depth:

$$\tau_{\nu_e} \equiv \int_{\infty}^{r} dr^{'}/\lambda \tag{3.43}$$

where λ is the neutrino-energy–dependent mean free path [see the definition (3.45) below]. The neutrinosphere for a given neutrino energy is located where $\tau_{\nu_e} = 2/3$.

In equation (3.42), the zone-edge neutrino mean free path is defined by

$$\lambda^n_{i,j+1/2,k+1/2} = \frac{1}{2}(\lambda^n_{i-1/2,j+1/2,k+1/2} + \lambda^n_{i+1/2,j+1/2,k+1/2}) \tag{3.44}$$

where

$$\lambda^n_{i+1/2,j+1/2,k+1/2} \equiv 1/(\chi^t)^n_{i+1/2,j+1/2,k+1/2}. \tag{3.45}$$

In equation (3.45), χ^t is the *transport* opacity, defined by

$$\begin{aligned} \chi^t &= \tilde{\chi} + \frac{E_0^2}{2c(hc)^3}\int d\mu_0 d\mu_0'(1-3\mu_0\mu_0')R_{\rm IS} \\ &+ \frac{2\pi}{c(hc)^3}\int d\mu_0\mu_0^2 \int dE_0' E_0'^2 d\mu_0'[R^{\rm in}_{\rm NES} f + R^{\rm out}_{\rm NES}(1-f)]. \end{aligned} \tag{3.46}$$

For $\lambda_{i,j+1/2,k+1/2} >> R^n_{\nu_e,k+1/2}$, that is, for neutrino thin regions, $\beta^{>}_{i,j+1/2,k+1/2} = 1$ and $\beta^{<}_{i,j+1/2,k+1/2} = 1$, and we recover the step relations (3.35) and (3.36). For $\lambda_{i,j+1/2,k+1/2} << R^n_{\nu_e,k+1/2}$, that is, for neutrino thick regions, $\beta^{>}_{i,j+1/2,k+1/2} = 1/2$ and $\beta^{<}_{i,j+1/2,k+1/2} = 1/2$, and we recover the relations (3.38).

The parameters $\beta^{<}$, $\beta^{>}$, and γ play an important role in obtaining the correct solution to the finite difference Boltzmann equation. For example, one of the fundamental difficulties asso-

ciated with solving the Boltzmann equation on a discrete grid is obtaining the correct solution in the diffusion limit while using discrete zones that are "optically thick," that is, that have zone widths much greater than the particle mean free paths. Because in most applications it is prohibitive to have numerous optically thin zones, this is a paramount issue. It has been rigorously demonstrated for time-independent transport with isotropic scattering in one-dimensional slab geometry that the diamond relations give the correct diffusion limit, whereas the step relations do not (Larsen et al. 1987). Similarly we have found that we obtain the correct diffusion limit when we use the relations (3.38) and not when we use the step relations. However, the relations (3.38) do not guarantee that the distribution function is everywhere positive. This is also characteristic of the diamond relations (3.40) (Duderstadt & Martin 1979; Lewis & Miller 1984). In our case, the tendency for the distribution function to become negative occurs in regions where the emission, absorption, and scattering terms in the Boltzmann equation are small relative to the terms describing radial and angular advection. Negative distributions ultimately result from oscillations in monotonically decreasing distributions (with r). In stationary state (steady state), in a region in which the neutrinos are radially free streaming, all terms in the Boltzmann equation (3.21) other than the radial transport term are negligible, leaving

$$(r_{i+1}^{n+1})^2 f^*_{i+1,j+1/2,k+1/2} - (r_i^{n+1})^2 f^*_{i,j+1/2,k+1/2} = 0. \tag{3.47}$$

If we use the relations (3.38), equation (3.47) can be rewritten as

$$\begin{aligned}
&(r_{i+1}^{n+1})^2 (f^*_{i+1/2,j+1/2,k+1/2} + f^*_{i+3/2,j+1/2,k+1/2}) \\
&-(r_i^{n+1})^2 (f^*_{i-1/2,j+1/2,k+1/2} + f^*_{i+1/2,j+1/2,k+1/2}) \\
&\approx (r_i^{n+1})^2 (f^*_{i+3/2,j+1/2,k+1/2} - f^*_{i+1/2,j+1/2,k+1/2})
\end{aligned}$$

$$= 0 \tag{3.48}$$

where we have used the fact that $\Delta r_{i+1/2} \equiv r_{i+1} - r_i << r_i$ for large r_i. Equation (3.48) illustrates that, in the limit we are considering, the distribution function in every other zone is nearly identical, leading to an oscillatory behavior in f superimposed on its monotonic radial fall off. In neutrino transparent regions well out beyond the neutrinosphere, the neutrino luminosity is constant with radius. This is just a statement of conservation of energy: The energy per unit time (luminosity) that comes into a region must leave the region unless there are local sources or sinks of energy. Because the neutrino luminosity at radius r is equal to the neutrino flux multiplied by the area of the sphere at that radius ($4\pi r^2$), the flux must fall off as $1/r^2$, and consequently, so must the neutrino distribution from which the flux is computed.

Thus, as a result of these oscillations in the neutrino distributions, we find it necessary to interpolate between the relations (3.35)–(3.36) and the relations (3.38), which amounts to an interpolation between a first- and second-order finite difference representation of the neutrino radial advection. [Strictly speaking, the relations (3.38) are second order on a uniform m-mesh, whereas the diamond relations (3.40) are second order regardless of whether or not the m-mesh is uniform.]

In equation (3.34), we set $\gamma_{i+1/2,j,k+1/2} \equiv 1$, to obtain the step relations (3.37). In neutrino-thick regions, the radiation field is isotropic, and the step relations (3.37) and the relations (3.39) define the same zone-edge value of the distribution function. In neutrino-thin regions, the relations (3.39) do not guarantee that the distribution function will be positive. As a result, the relations (3.37) are used everywhere.

3.3 Differencing the Neutrino Interaction Terms in the Energy Equation and the Y_e Equation

We will write the operator-split equation (3.19) as an equation in $\bar{\epsilon}$. This introduces a natural scaling in the system of equations (3.18) to (3.20). With $\partial\bar{\epsilon}/\partial t = (\log_{10} e)\,\partial \log(\epsilon)/\partial t$, equation (3.19) for a given neutrino flavor can be rewritten as

$$\begin{aligned}
\frac{\epsilon}{c\,\log_{10} e}\frac{\partial\bar{\epsilon}}{\partial t} &= -\frac{2\pi C_0}{h^3c^3\rho_0}\int dE_0 E_0^3 d\mu_0 (j-\tilde{\chi}f) \\
&\quad +\frac{2\pi C_0}{h^6c^6}\int dE_0 E_0^3 d\mu_0 F \int dE_0' E_0'^2 d\mu_0' \tilde{R}^{\rm out}_{\rm NES}(\frac{1}{\rho_0}-F) \\
&\quad -\frac{2\pi C_0}{h^6c^6}\int dE_0 E_0^3 d\mu_0 (\frac{1}{\rho_0}-F) \int dE_0' E_0'^2 d\mu_0' \tilde{R}^{\rm in}_{\rm NES} F. \\
&\quad +\frac{2\pi C_0}{h^6c^6}\int dE E^3 d\mu F \int dE' E'^2 d\mu' \tilde{R}^{\rm abs}_{\rm PAIR}(\bar{F}) \\
&\quad -\frac{2\pi C_0}{h^6c^6}\int dE E^3 d\mu (\frac{1}{\rho}-F) \int dE' E'^2 d\mu' \tilde{R}^{\rm em}_{\rm PAIR}(\frac{1}{\rho}-\bar{F}).
\end{aligned} \tag{3.49}$$

In finite difference form (Mezzacappa & Bruenn 1993b),

$$\begin{aligned}
&< \epsilon_{i+1/2} > (\bar{\epsilon}^{n+1}_{i+1/2} - \bar{\epsilon}^{*}_{i+1/2})/c\,\Delta t\,\log_{10} e = \\
-\quad &\frac{2\pi C_0}{h^3c^3}\sum_{k=1}^{kmax}\sum_{j=1}^{jmax} \Delta E_{k+1/2}\, E^3_{k+1/2}\, w_{j+1/2} \\
\times\quad &(\frac{j^{n+1}_{i+1/2,k+1/2}}{\rho^{n+1}_{i+1/2}} - \tilde{\chi}^{n+1}_{i+1/2,k+1/2}\, F^{*}_{i+1/2,j+1/2,k+1/2}) \\
+\quad &\frac{2\pi C_0}{h^6c^7}\sum_{k=1}^{kmax}\sum_{m=1}^{kmax} \Delta E_{k+1/2}\, E^3_{k+1/2} \Delta E_{m+1/2}\, E^2_{m+1/2} \sum_{j=1}^{jmax}\sum_{l=1}^{jmax} w_{j+1/2}\, w_{l+1/2} \\
&\times (\tilde{R}^{\rm in}_{\rm NES})^{n+1}_{i+1/2,j+1/2,l+1/2,k+1/2,m+1/2} \\
&\times F^{*}_{i+1/2,j+1/2,k+1/2}(1/\rho^{n+1}_{i+1/2} - F^{*}_{i+1/2,l+1/2,m+1/2})
\end{aligned}$$

$$
\begin{aligned}
- \quad & \frac{2\pi C_0}{h^6 c^7} \sum_{k=1}^{kmax} \sum_{m=1}^{kmax} \Delta E_{k+1/2}\, E^3_{k+1/2} \Delta E_{m+1/2}\, E^2_{m+1/2} \sum_{j=1}^{jmax} \sum_{l=1}^{jmax} w_{j+1/2}\, w_{l+1/2} \\
& \times (\tilde{R}^{\rm out}_{\rm NES})^{n+1}_{i+1/2,j+1/2,l+1/2,k+1/2,m+1/2} \\
& \times (1/\rho^{n+1}_{i+1/2} - F^*_{i+1/2,j+1/2,k+1/2}) F^*_{i+1/2,l+1/2,m+1/2} \\
+ \quad & \frac{2\pi C_0}{h^6 c^7} \sum_{k=1}^{kmax} \sum_{m=1}^{kmax} \Delta E_{k+1/2}\, E^3_{k+1/2} \Delta E_{m+1/2}\, E^2_{m+1/2} \sum_{j=1}^{jmax} \sum_{l=1}^{jmax} w_{j+1/2}\, w_{l+1/2} \\
& \times (\tilde{R}^{\rm abs}_{\rm PAIR})^{n+1}_{i+1/2,j+1/2,l+1/2,k+1/2,m+1/2} \\
& \times \bar{F}^*_{i+1/2,j+1/2,k+1/2} F^*_{i+1/2,l+1/2,m+1/2} \\
- \quad & \frac{2\pi C_0}{h^6 c^7} \sum_{k=1}^{kmax} \sum_{m=1}^{kmax} \Delta E_{k+1/2}\, E^3_{k+1/2} \Delta E_{m+1/2}\, E^2_{m+1/2} \sum_{j=1}^{jmax} \sum_{l=1}^{jmax} w_{j+1/2}\, w_{l+1/2} \\
& \times (\tilde{R}^{\rm em}_{\rm PAIR})^{n+1}_{i+1/2,j+1/2,l+1/2,k+1/2,m+1/2} \\
& \times (1/\rho^{n+1}_{i+1/2} - F^*_{i+1/2,j+1/2,k+1/2})(1/\rho^{n+1}_{i+1/2} - \bar{F}^*_{i+1/2,l+1/2,m+1/2}) \qquad (3.50)
\end{aligned}
$$

where $\bar{\epsilon}^*_{i+1/2}$ is the logarithm of the partially updated specific internal energy and

$$
< \epsilon_{i+1/2} >= \frac{1}{2}(\epsilon^0_{i+1/2} + \epsilon^*_{i+1/2}). \qquad (3.51)
$$

To solve equation (3.50), we linearize in F, $\bar{\epsilon}$, and Y_e, using equations (3.26) to (3.30) and

$$
\bar{\epsilon}^{n+1}_{i+1/2} = \bar{\epsilon}^0_{i+1/2} + \delta\bar{\epsilon}_{i+1/2}. \qquad (3.52)
$$

After linearization, we convert the variations in $\bar{\epsilon}$ to variations in T by dividing through by the heat capacity, $\partial\epsilon/\partial T$. This conversion makes it possible to use our linearized expressions, equations 3.27 – 3.30, without complication.

The Y_e equation (3.20) is differenced in a straightforward manner:

$$
\begin{aligned}
& [(Y_e)^{n+1}_{i+1/2} - (Y_e)^{n}_{i+1/2}]/c\Delta t = \\
- \quad & \frac{2\pi m_B}{h^3 c^3} \sum_{k=1}^{kmax} \sum_{j=1}^{jmax} \Delta E_{k+1/2}\, E^2_{k+1/2}\, w_{j+1/2} \\
\times \quad & (\frac{j^{n+1}_{i+1/2,k+1/2}}{\rho^{n+1}_{i+1/2}} - \tilde{\chi}^{n+1}_{i+1/2,k+1/2}\, F^{*}_{i+1/2,j+1/2,k+1/2}),
\end{aligned}
\tag{3.53}
$$

with

$$
(Y_e)^{n+1}_{i+1/2} = (Y_e)^{0}_{i+1/2} + (\delta Y_e)_{i+1/2}. \tag{3.54}
$$

Initially $(Y_e)^{0}_{i+1/2} = (Y_e)^{n}_{i+1/2}$.

If we substitute the supplementary relations (3.32) to (3.34) in the finite difference Boltzmann equation and then linearize the system of finite difference equations [equations (3.21), (3.50), and (3.53)] using (a) equations (3.26) to (3.30), (b) equation (3.52), and (c) equation (3.54), the linearized system of finite difference equations takes on the form

$$
-\mathbf{C}_i \vec{V}_{i-1} + \mathbf{A}_i \vec{V}_i - \mathbf{B}_i \vec{V}_{i+1} = \vec{U}_i, \tag{3.55}
$$

where $\vec{V}_i$ is the solution vector for a given mass shell, $\Delta m_{i+1/2}$,

$$\vec{V}_i = \begin{pmatrix} \delta f_{i+1/2,1+1/2,1+1/2} \\ \delta f_{i+1/2,2+1/2,1+1/2} \\ . \\ . \\ . \\ \delta f_{i+1/2,1+1/2,2+1/2} \\ \delta f_{i+1/2,2+1/2,2+1/2} \\ . \\ . \\ . \\ \delta\bar{\epsilon}_{i+1/2} \\ (\delta Y_e)_{i+1/2} \end{pmatrix} . \tag{3.56}$$

In the solution vector, the quantity that appears is the distribution function, f, not the specific distribution, F.

The matrices $\mathbf{B}_i$ and $\mathbf{C}_i$ are diagonal. The matrix $\mathbf{A}_i$ has the following structure:

$$\mathbf{A}_i = \begin{pmatrix} \mathbf{A}_1 & \mathbf{A}_2 \\ \mathbf{A}_3 & \mathbf{A}_4 \end{pmatrix} . \tag{3.57}$$

It is doubly bordered; i.e., $\mathbf{A}_i$ is an $M \times M$ matrix, where $M = jmax \times kmax + 2$; the submatrices $\mathbf{A}_2$ and $\mathbf{A}_3$ are $2 \times (M-2)$ and $(M-2) \times 2$ matrices, respectively; and the submatrix $\mathbf{A}_4$ is a 2×2 matrix. The submatrix $\mathbf{A}_1$ is dense — for a given mass shell, $\Delta m_{i+1/2}$, isoenergetic neutrino–nucleon and neutrino–nucleus scattering and nonisoenergetic neutrino–electron scattering couple all neutrino direction cosines and energy. Pair emission and absorption couple a given neutrino

flavor to its corresponding antineutrino, doubling the size of linear system that must be solved. We have implemented several different solution algorithms for this linear system. The Feautrier elimination scheme (see Mezzacappa & Bruenn (1993b)), also called the Thomas algorithm, provides good performance on vector machines. The solution method used for all the simulations described in this dissertation is a band direct solver due to Press et al. (1996). This solver can give performance comparable to the Thomas algorithm, if care is taken in coding the algorithm. As presented in Press et al. (1996), the coding causes bank conflicts on Cray-type architectures, as loops are performed across rows of the matrix. This is natural for C-style storage, but the column major ordering in FORTRAN results in a factor of 3 decrease in speed. A number of Krylov methods have been tested with a parallel version of the code and we have seen good scaling up to 32 processors on the Intel Paragon.

3.4 Computing the Observer Corrections

The angular aberration and frequency shift terms in the Boltzmann equation are operator split from the rest of the solution. These terms must be differenced in a specific manner so total energy is conserved over tens of thousands of time steps. The particular discretization described below is due to Liebendörfer (2000) and builds on the discretization from Mezzacappa & Bruenn (1993a). It is designed to meet the stringent requirements of number and energy conservation.

3.4.1 Frequency Shift

The frequency shift term

$$\frac{1}{c}\frac{\partial F}{\partial t} = -\frac{1}{c}\left[\mu_0^2\left(\frac{\partial \ln \rho_0}{\partial t} + \frac{3v}{r}\right) - \frac{v}{r}\right]\frac{1}{E_0^2}\frac{\partial [E_0^3 F]}{\partial E_0} \tag{3.58}$$

is treated by generalizing and extending the scheme developed by Bruenn (1985), which was developed for multigroup flux-limited diffusion. The scheme described below is conservative for *both* neutrino number and neutrino energy and respects Fermi statistics.

We begin by defining

$$H \equiv E^3 \, F. \tag{3.59}$$

With the definition for the fluid velocity and equation 3.59, equation 3.58 can be rewritten as

$$\frac{\partial H}{\partial t} + \frac{\partial \ln(\rho^{\mu^2} r^{3\mu^2-1})}{\partial t} E \frac{\partial H}{\partial E} = 0. \tag{3.60}$$

If we define

$$R \equiv (\rho^{\mu^2} \, r^{3\mu^2-1}), \tag{3.61}$$

we can rewrite equation 3.60:

$$\frac{\partial H}{\partial t} + \frac{\partial \ln R}{\partial t} E \frac{\partial H}{\partial E} = 0. \tag{3.62}$$

The specific radiation energy in the angular range $[\mu, \mu + d\mu]$ and energy range $[E, E + dE]$ is

$$d\epsilon_R(m, t; \mu, E) = \frac{2\pi C_0}{h^3 c^3} \, d\mu \, dE \, E^3 \, F(m, t; \mu, E). \tag{3.63}$$

So, using equations 3.62 and 3.59, the specific radiation energy transforms as

$$d\epsilon_R(m, t_f; \mu, E/R) = \frac{\partial \ln R}{\partial t} \; d\epsilon_R(m, t_i; \mu, E) \, \Delta t. \tag{3.64}$$

To understand the necessity of careful differencing, we construct the quantity $\epsilon_R + (v/c)F_R$, where v is the matter velocity and F is the specific flux of neutrinos. This quantity is conserved to first in (v/c) for comoving observers in the absence of matter-neutrino interactions:

$$\frac{d\epsilon_R}{dt} + \frac{v}{c}\frac{dF_R}{dt} = 0. \tag{3.65}$$

We obtain the first term by integrating the left hand side of the Boltzmann equation for energy, i.e. using the operator $\frac{2\pi C_0}{h^3c^3}\int E^3 de d\mu$:

$$\begin{aligned}\frac{1}{c}\frac{d\epsilon_R}{dt} &= -\frac{4\pi}{c}\frac{\partial}{\partial m}(r^2\rho F_R) + \frac{P_R}{c}\left(\frac{\partial ln\rho}{\partial t} + \frac{2v}{r}\right) \\ &\quad -\frac{v}{cr}\left(\epsilon_R - P_R\right),\end{aligned} \tag{3.66}$$

where P_R is the specific neutrino radiation pressure. The second term is obtained by integrating the the left hand side of the Boltzmann equation for momentum, with the operator $\frac{2\pi C_0}{h^3c^3}\int E^3 de\mu d\mu$:

$$\begin{aligned}\frac{1}{c^2}\frac{dF_R}{dt} &= -4\pi\frac{\partial}{\partial m}\left(r^2\rho P_R\right) + \frac{F_R}{c^2}\left(\frac{\partial ln\rho}{\partial t} + \frac{2v}{r}\right) \\ &\quad +\frac{1}{r}\left(\epsilon_R - P_R\right).\end{aligned} \tag{3.67}$$

It is clear the last terms in equations 3.66 and 3.67 cancel each other when 3.65 is solved. They must be constructed to cancel each other in the finite difference representation as well. A complication occurs since the last term in 3.66 is obtained from the frequency shift term in the Boltzmann equation, whereas the final term in equation 3.67 comes from integrating the angular advection term in the Boltzmann equation. This term has already been solved for in

the implicit update of the distribution function. The discretization used for the frequency shift is therefore determined: it must be identical to that used in differencing the angular advection term.

Note that

$$\frac{\partial \ln R}{\partial t} = \mu^2 \left(\frac{\partial \ln \rho}{\partial t} + \frac{3v}{r} \right) \frac{v}{r}. \tag{3.68}$$

We can decompose $\frac{\partial \ln R}{\partial t}$ into two terms, A and B, given by

$$A = - \left(\frac{\partial \ln \rho}{\partial t} + \frac{3v}{r} \right), \tag{3.69}$$

$$B = (1 - \mu^2) \frac{v}{r}, \tag{3.70}$$

so that

$$\frac{\partial \ln R}{\partial t} = -(\mu^2 A + B). \tag{3.71}$$

(Liebendörfer 2000) We have already chosen differencing for terms like A and B: the third and fourth term in equation 3.21. Consequently, we difference A and B as

$$\begin{aligned} A_{i+1/2,j+1/2,k+1/2} &= \frac{4\pi \rho^{n+1}_{i+1/2}}{\Delta m^{n+1}_{i+1/2}} \\ &\times \left[(r^{n+1}_{i+1})^2 \, (v^{n+1}_{i+2} - v^{n+1}_{i+1})(1 - \beta^{<}_{i+1,j+1/2,k+1/2}) \right. \\ &+ \left. (r^{n+1}_{i})^2 \, (v^{n+1}_{i+1} - v^{n+1}_{i})\beta^{<}_{i,j+1/2,k+1/2} \right], \end{aligned} \tag{3.72}$$

for $\mu - j + 1/2 < 0$,

$$\begin{aligned} A_{i+1/2,j+1/2,k+1/2} &= \frac{4\pi\rho^{n+1}_{i+1/2}}{\Delta m^{n+1}_{i+1/2}} \\ &\times [(r^{n+1}_{i+1})^2\,(v^{n+1}_{i+2} - v^{n+1}_{i+1})\beta^{>}_{i+1,j+1/2,k+1/2} \\ &+ (r^{n+1}_{i})^2\,(v^{n+1}_{i+1} - v^{n+1}_{i})(1 - \beta^{>}_{i,j+1/2,k+1/2})], \end{aligned} \tag{3.73}$$

for $\mu - j + 1/2 > 0$, and

$$\begin{aligned} B_{i+1/2,j+1/2,k+1/2} &= 3\frac{(r^{n+1}_{i+1})^2 - (r^{n+1}_{i})^2}{(r^{n+1}_{i+1})^3 - (r^{n+1}_{i})^3}\,v^{n+1}_{i+1}\,\frac{1}{w_{j+1/2}} \\ &\times [\alpha_{j+1}\,\gamma_{i+1/2,k+1/2}(\mu_{j+3/2} - \mu_{j+1/2}) \\ &- \alpha_j\,(1 - \gamma_{i+1/2,k+1/2})\,(\mu_{j+1/2} - \mu_{j-1/2})]. \end{aligned} \tag{3.74}$$

In each of the expressions above, the auxiliary relations, equations 3.32, 3.33, and 3.34 have been used. Once we have a finite difference representation for $\frac{\partial \ln R}{\partial t}$, we can then write down expressions for number and energy conservation as in Mezzacappa & Bruenn (1993b). First, for number conservation,

$$\begin{aligned} \frac{2\pi}{h^3c^3}\,\Delta m_{i+1/2}\,[(F^n_{i+1/2,j+1/2,k+1/2} - \delta^{(-)}_{i+1/2,j+1/2,k+1/2})\,w_{j+1/2}\,E^2_{k+1/2}\,\Delta E_{k+1/2} \\ +\delta^{(+)}_{i+1/2,j+1/2,k+3/2}\,w_{j+1/2}\,E^2_{k+3/2}\,\Delta E_{k+3/2}] \\ = \tfrac{2\pi}{h^3c^3}\Delta m_{i+1/2}\,F^n_{i+1/2,j+1/2,k+1/2}\,w_{j+1/2}\,E^2_{k+1/2}\,\Delta E_{k+1/2} \end{aligned} \tag{3.75}$$

if $\frac{\partial \ln R}{\partial t} > 0$, and

$$\frac{2\pi}{h^3c^3}\,\Delta m_{i+1/2}\,[(F^n_{i+1/2,j+1/2,k+1/2} - \delta^{(-)}_{i+1/2,j+1/2,k+1/2})\,w_{j+1/2}\,E^2_{k+1/2}\,\Delta E_{k+1/2}$$

$$+\delta^{(+)}_{i+1/2,j+1/2,k-1/2}\, w_{j+1/2}\, E^2_{k-1/2}\, \Delta E_{k-1/2}] \tag{3.76}$$
$$= \tfrac{2\pi}{h^3c^3} \Delta m_{i+1/2}\, F^n_{i+1/2,j+1/2,k+1/2}\, w_{j+1/2}\, E^2_{k+1/2}\, \Delta E_{k+1/2}$$

for $\frac{\partial \ln R}{\partial t} < 0$. The expressions for energy conservation are

$$\begin{aligned}
& \frac{2\pi C_0}{h^3c^3}\, \Delta m_{i+1/2}\, [(F^n_{i+1/2,j+1/2,k+1/2} \\
- \quad & \delta^{(-)}_{i+1/2,j+1/2,k+1/2}) w_{j+1/2}\, E^3_{k+1/2} \Delta E_{k+1/2} \\
+ \quad & \delta^{(+)}_{i+1/2,j+1/2,k+3/2} w_{j+1/2}\, E^3_{k+3/2}\, \Delta E_{k+3/2}] \\
= \quad & -(\mu^2_{j+1/2} A_{i+1/2,j+1/2,k+1/2} + B_{i+1/2,j+1/2,k+1/2} + \Delta^{(+)}) \Delta t \\
\times \quad & \frac{2\pi C_0}{h^3c^3}\, \Delta m_{i+1/2}\, F^n_{i+1/2,j+1/2,k+1/2}\, w_{j+1/2}\, E^3_{k+1/2}\, \Delta E_{k+1/2} \\
+ \quad & \frac{2\pi C_0}{h^3c^3}\, \Delta m_{i+1/2}\, F_{i+1/2,j+1/2,k+1/2} w_{j+1/2} \\
\times \quad & E^3_{k+1/2}\, \Delta E_{k+1/2}
\end{aligned} \tag{3.77}$$

for $\frac{\partial \ln R}{\partial t} > 0$, and

$$\begin{aligned}
& \frac{2\pi C_0}{h^3c^3}\, \Delta m_{i+1/2}\, [(F^n_{i+1/2,j+1/2,k+1/2} \\
- \quad & \delta^{(-)}_{i+1/2,j+1/2,k+1/2}) w_{j+1/2}\, E^3_{k+1/2} \Delta E_{k+1/2} \\
+ \quad & \delta^{(+)}_{i+1/2,j+1/2,k-1/2} w_{j+1/2}\, E^3_{k+3/2}\, \Delta E_{k+3/2}] \\
= \quad & [-(\mu^2_{j+1/2} A_{i+1/2,j+1/2,k+1/2} + B_{i+1/2,j+1/2,k+1/2}) + \Delta^{(+)}] \Delta t \\
\times \quad & \frac{2\pi C_0}{h^3c^3}\, \Delta m_{i+1/2}\, F^n_{i+1/2,j+1/2,k+1/2}\, w_{j+1/2}\, E^3_{k+1/2}\, \Delta E_{k+1/2} \\
+ \quad & \frac{2\pi C_0}{h^3c^3}\, \Delta m_{i+1/2}\, F_{i+1/2,j+1/2,k+1/2} w_{j+1/2} \\
\times \quad & E^3_{k+1/2}\, \Delta E_{k+1/2}
\end{aligned} \tag{3.78}$$

for $\frac{\partial \ln R}{\partial t} < 0$. In equations 3.77 and 3.78, $\delta^{(-)}$ is the decrease and $\delta^{(+)}$ is the increase in the distribution function in a given energy zone from frequency shift. $\Delta^{(+)}$ is a quantity used to account for Fermi statistics, i.e. if the distribution function in a given energy zone would exceed 1 by the addition of $\delta^{(+)}$, the energy error made by constraining $F \leq 1$ is attributed to $\Delta^{(+)}$ in the manner described below. Solving these equations for $\delta^{(-)}$ and $\delta^{(+)}$, we obtain

$$\delta^{(-)}_{i+1/2,j+1/2,k+1/2} = \frac{E_{k+1/2}}{E_{k+3/2} - E_{k+1/2}} F^n_{i+1/2,j+1/2,k+1/2} \times \quad [-(\mu^2_{j+1/2} A_{i+1/2,j+1/2,k+1/2} + B_{i+1/2,j+1/2,k+1/2}) + \Delta^{(+)}], \tag{3.79}$$

$$\delta^{(+)}_{i+1/2,j+1/2,k+3/2} = \frac{E^2_{k+1/2}\,\Delta E_{k+1/2}}{E^2_{k+3/2}\,\Delta E_{k+3/2}}\,\delta^{(-)}_{i+1/2,j+1/2,k+1/2}, \tag{3.80}$$

for $\frac{\partial \ln R}{\partial t} > 0$, and

$$\delta^{(-)}_{i+1/2,j+1/2,k+1/2} = \frac{E_{k+1/2}}{E_{k-1/2} - E_{k+1/2}} F^n_{i+1/2,j+1/2,k+1/2} \times \quad [-(\mu^2_{j+1/2} A_{i+1/2,j+1/2,k+1/2} + B_{i+1/2,j+1/2,k+1/2}) + \Delta^{(+)}], \tag{3.81}$$

$$\delta^{(+)}_{i+1/2,j+1/2,k+3/2} = \frac{E^2_{k+1/2}\,\Delta E_{k+1/2}}{E^2_{k-1/2}\,\Delta E_{k-1/2}}\,\delta^{(-)}_{i+1/2,j+1/2,k+1/2}, \tag{3.82}$$

for $\frac{\partial \ln R}{\partial t} < 0$. $\Delta^{(+)}$ is defined as

$$\Delta_{i+1/2,j+1/2,k+3/2} = \frac{C_{i+1/2,j+1/2}\Xi_{i+1/2,j+1/2,k+3/2}}{\sum_{k=k_1+1,k_{max}} \Xi_{i+1/2,j+1/2,k+1/2}\,F^*_{i+1/2,j+1/2,k+1/2}E^3_{k+1/2}dE_{k+1/2}}, \tag{3.83}$$

where

$$\Xi_{i+1/2,j+1/2,k+1/2} = \begin{cases} -1 & \text{if} \quad F^*_{i+1/2,j+1/2,k+1/2} < 0 \quad \text{and} \\ & \sum_j F^*_{i+1/2,j+1/2,k+1/2} w_{j+1/2} > 0 \\ 1 & \text{otherwise,} \end{cases} \tag{3.84}$$

and

$$C_{i+1/2,j+1/2} = \sum_{k+3/2}^{kmax+1/2} \max\{0, F^*_{i+1/2,j+1/2,k+1/2} - 1/\rho^{n+1}_{i+1/2}\} E^3_{k+1/2}\, dE_{k+1/2}. \tag{3.85}$$

We update the distribution function for each radial and angular zone by sweeping up the energy grid, calculating $\delta^{(-)}$ and $\delta^{(+)}$ and setting

$$F_{i+1/2,j+1/2,k+1/2} = F^{**}_{i+1/2,j+1/2,k+1/2} - \delta^{(-)}_{i+1/2,j+1/2,k+1/2} + \delta^{(+)}_{i+1/2,j+1/2,k+1/2}. \tag{3.86}$$

3.4.2 Angular Aberration

The angular aberration term from the Boltzmann equation,

$$\frac{1}{c}\frac{\partial F}{\partial t} = -\frac{1}{c}\left(\frac{\partial \ln \rho}{\partial t} + \frac{3v}{r}\right)\frac{\partial[\mu(1-\mu^2)F]}{\partial \mu}, \tag{3.87}$$

is calculated in a similar manner to the frequency shift (Liebendörfer 2000). This is a departure from Mezzacappa & Bruenn (1993a), where an upwind differencing in angle space was used. In this instance, we note that by defining

$$R = r^3\rho, \tag{3.88}$$

we can immediately write

$$\frac{\partial \ln R}{\partial t} = \left(\frac{\partial \ln \rho}{\partial t} + \frac{3v}{r}\right). \tag{3.89}$$

In this instance, the quantity we are interested in is the specific luminosity in an angular bin:

$$dL_\mu = \frac{8\pi^2 C_0}{h^3 c^3 r^2}\left(1-3\mu^2\right)\mu F d\mu E^3 dE. \tag{3.90}$$

By defining a quantity $(1-3\mu^2)\mu F$, analogous to H defined in equation 3.59, and plugging into equation 3.87 we obtain

$$dL_{\mu,f} = (1-\mu^2)\frac{\partial \ln R}{\partial t} dL_{\mu,i}\Delta t. \tag{3.91}$$

where the subscripts i and f refer to inital and final values, respectively. We note, using equations 3.69 and 3.70, $(1-\mu^2)\frac{\partial \ln R}{\partial t} = B - (1-\mu^2)A$. Therefore, we already have in hand a finite difference representation for this quantity.

Analogously with the frequency shift, using expressions for number conservation:

$$\begin{aligned}\frac{2\pi}{h^3c^3}\,\Delta m_{i+1/2}\,[(F^n_{i+1/2,j+1/2,k+1/2} - \delta^{(-)}_{i+1/2,j+1/2,k+1/2})\,w_{j+1/2}\,E^2_{k+1/2}\,\Delta E_{k+1/2} \\ +\delta^{(+)}_{i+1/2,j+3/2,k+3/2}\,w_{j+3/2}\,E^2_{k+1/2}\,\Delta E_{k+1/2}] \\ = \tfrac{2\pi}{h^3c^3}\Delta m_{i+1/2}\,F^n_{i+1/2,j+1/2,k+1/2}\,w_{j+1/2}\,E^2_{k+1/2}\,\Delta E_{k+1/2},\end{aligned} \tag{3.92}$$

when $\mu_{j+1/2} < 0$ and

$$\frac{2\pi}{h^3c^3}\,\Delta m_{i+1/2}\,[(F^n_{i+1/2,j+1/2,k+1/2}-\delta^{(-)}_{i+1/2,j+1/2,k+1/2})\,w_{j+1/2}\,E^2_{k+1/2}\,\Delta E_{k+1/2}$$
$$+\delta^{(+)}_{i+1/2,j-1/2,k+3/2}\,w_{j-1/2}\,E^2_{k+1/2}\,\Delta E_{k+1/2}] \tag{3.93}$$
$$=\tfrac{2\pi}{h^3c^3}\Delta m_{i+1/2}\,F^n_{i+1/2,j+1/2,k+1/2}\,w_{j+1/2}\,E^2_{k+1/2}\,\Delta E_{k+1/2}\quad,$$

when $\mu_{j+1/2}>0$, and expressions for energy(luminosity) conservation:

$$\begin{aligned}
&\frac{2\pi C_0}{h^3c^3}\,\Delta m_{i+1/2}\,[(F^n_{i+1/2,j+1/2,k+1/2}\\
-\quad&\delta^{(-)}_{i+1/2,j+1/2,k+1/2})w_{j+1/2}\,\mu_{j+1/2}\,E^3_{k+1/2}\Delta E_{k+1/2}\\
+\quad&\delta^{(+)}_{i+1/2,j+3/2,k+1/2}w_{j+3/2}\,\mu_{j+3/2}\,E^3_{k+1/2}\,\Delta E_{k+1/2}]\\
=\quad&[-(1-\mu^2_{j+1/2})\,A_{i+1/2,j+1/2,k+1/2}+B_{i+1/2,j+1/2,k+1/2}]\Delta t\\
\times\quad&\frac{2\pi C_0}{h^3c^3}\,\Delta m_{i+1/2}\,F^n_{i+1/2,j+1/2,k+1/2}\,w_{j+1/2}\,\mu_{j+1/2}\,E^3_{k+1/2}\,\Delta E_{k+1/2}\\
+\quad&\frac{2\pi C_0}{h^3c^3}\,\Delta m_{i+1/2}\,F_{i+1/2,j+1/2,k+1/2}w_{j+1/2}\mu_{j+1/2}\\
\times\quad&E^3_{k+1/2}\,\Delta E_{k+1/2},
\end{aligned}\tag{3.94}$$

for $\mu_{j+1/2}<0$, and

$$\begin{aligned}
&\frac{2\pi C_0}{h^3c^3}\,\Delta m_{i+1/2}\,[(F^n_{i+1/2,j+1/2,k+1/2}\\
-\quad&\delta^{(-)}_{i+1/2,j+1/2,k+1/2})w_{j+1/2}\,\mu_{j+1/2}\,E^3_{k+1/2}\Delta E_{k+1/2}\\
+\quad&\delta^{(+)}_{i+1/2,j-1/2,k+1/2}w_{j-1/2}\,\mu_{j-1/2}\,E^3_{k+1/2}\,\Delta E_{k+1/2}]\\
=\quad&[-(1-\mu^2_{j+1/2})\,A_{i+1/2,j+1/2,k+1/2}+B_{i+1/2,j+1/2,k+1/2}]\Delta t
\end{aligned}$$

$$\times \quad \frac{2\pi C_0}{h^3 c^3}\,\Delta m_{i+1/2}\,F^n_{i+1/2,j+1/2,k+1/2}\,w_{j+1/2}\,\mu_{j+1/2}\,E^3_{k+1/2}\,\Delta E_{k+1/2}$$
$$+ \quad \frac{2\pi C_0}{h^3 c^3}\,\Delta m_{i+1/2}\,F_{i+1/2,j+1/2,k+1/2} w_{j+1/2}\mu_{j+1/2}$$
$$\times \quad E^3_{k+1/2}\,\Delta E_{k+1/2}, \tag{3.95}$$

for $\mu_{j+1/2} > 0$, we obtain

$$\delta^{(-)}_{i+1/2,j+1/2,k+1/2} = \frac{\mu_{j+1/2}}{\mu_{j+3/2} - \mu_{j+1/2}}\,F^n_{i+1/2,j+1/2,k+1/2}$$
$$\times \quad [-(1-\mu^2_{j+1/2})A_{i+1/2,j+1/2,k+1/2} + B_{i+1/2,j+1/2,k+1/2})], \tag{3.96}$$

$$\delta^{(+)}_{i+1/2,j+3/2,k+1/2} = \delta^{(-)}_{i+1/2,j+1/2,k+1/2}\frac{w_{j+1/2}}{w_{j+3/2}}, \tag{3.97}$$

for $\mu_{j+1/2} < 0$, and

$$\delta^{(-)}_{i+1/2,j+1/2,k+1/2} = \frac{\mu_{j+1/2}}{\mu_{j-1/2} - \mu_{j+1/2}}\,F^n_{i+1/2,j+1/2,k+1/2}$$
$$\times \quad [-(1-\mu^2_{j+1/2})A_{i+1/2,j+1/2,k+1/2} + B_{i+1/2,j+1/2,k+1/2})], \tag{3.98}$$

$$\delta^{(+)}_{i+1/2,j-1/2,k+1/2} = \delta^{(-)}_{i+1/2,j+1/2,k+1/2}\frac{w_{j+1/2}}{w_{j-1/2}}, \tag{3.99}$$

for $\mu_{j+1/2} > 0$. We apply

$$F_{i+1/2,j+1/2,k+1/2} = F^{**}_{i+1/2,j+1/2,k+1/2} - \delta^{(-)}_{i+1/2,j+1/2,k+1/2} + \delta^{(+)}_{i+1/2,j+1/2,k+1/2}, \tag{3.100}$$

to each angular bin, using the proper set of δ's from above based on the sign of the direction cosine.

3.5 Differencing the Neutrino Stress

The differencing for the neutrino stress terms in the velocity equation is straightforward and is given by

$$
\begin{aligned}
&[(\frac{\partial v}{\partial t})_\nu]^n_{i+1/2} = \\
&\frac{2\pi C_0}{h^3c^3}\sum_{k=1}^{kmax}\Delta E_{k+1/2}\,E^3_{k+1/2}\sum_{j=1}^{jmax} w_{j+1/2} \\
&\times\mu_{j+1/2}\,(\chi^T)^n_{i+1/2,j+1/2,k+1/2}\,F^n_{i+1/2,j+1/2,k+1/2} \\
-\quad&\frac{2\pi C_0}{h^6c^7}\sum_{k=1}^{kmax}\Delta E_{k+1/2}\,E^5_{k+1/2}\sum_{j=1}^{jmax}\sum_{l=1}^{jmax} w_{j+1/2}\,w_{l+1/2} \\
&\times\mu_{j+1/2}\,(R_{\rm IS})^n_{i+1/2,j+1/2,l+1/2,k+1/2}\,F^n_{i+1/2,l+1/2,k+1/2} \\
+\quad&\frac{2\pi C_0}{h^6c^7}\sum_{k=1}^{kmax}\sum_{m=1}^{kmax}\Delta E_{k+1/2}\,E^3_{k+1/2}\Delta E_{m+1/2}\,E^2_{m+1/2}\sum_{j=1}^{jmax}\sum_{l=1}^{jmax} w_{j+1/2}\,w_{l+1/2} \\
&\times\mu_{j+1/2}\,(\tilde{R}^{\rm in}_{\rm NES})^n_{i+1/2,j+1/2,l+1/2,k+1/2,m+1/2} \\
&\times F^n_{i+1/2,j+1/2,k+1/2}(1/\rho^n_{i+1/2} - F^n_{i+1/2,l+1/2,m+1/2}) \\
-\quad&\frac{2\pi C_0}{h^6c^7}\sum_{k=1}^{kmax}\sum_{m=1}^{kmax}\Delta E_{k+1/2}\,E^3_{k+1/2}\Delta E_{m+1/2}\,E^2_{m+1/2}\sum_{j=1}^{jmax}\sum_{l=1}^{jmax} w_{j+1/2}\,w_{l+1/2} \\
&\times\mu_{j+1/2}\,(\tilde{R}^{\rm out}_{\rm NES})^n_{i+1/2,j+1/2,l+1/2,k+1/2,m+1/2} \\
&\times(1/\rho^n_{i+1/2} - F^n_{i+1/2,j+1/2,k+1/2})F^n_{i+1/2,l+1/2,m+1/2} \\
+\quad&\frac{2\pi C_0}{h^6c^7}\sum_{k=1}^{kmax}\sum_{m=1}^{kmax}\Delta E_{k+1/2}\,E^3_{k+1/2}\Delta E_{m+1/2}\,E^2_{m+1/2}\sum_{j=1}^{jmax}\sum_{l=1}^{jmax} w_{j+1/2}\,w_{l+1/2} \\
&\times\mu_{j+1/2}\,(\tilde{R}^{\rm abs}_{\rm PAIR})^n_{i+1/2,j+1/2,l+1/2,k+1/2,m+1/2} \\
&\times F^n_{i+1/2,j+1/2,k+1/2}\bar{F}^n_{i+1/2,l+1/2,m+1/2}) \\
-\quad&\frac{2\pi C_0}{h^6c^7}\sum_{k=1}^{kmax}\sum_{m=1}^{kmax}\Delta E_{k+1/2}\,E^3_{k+1/2}\Delta E_{m+1/2}\,E^2_{m+1/2}\sum_{j=1}^{jmax}\sum_{l=1}^{jmax} w_{j+1/2}\,w_{l+1/2} \\
&\times\mu_{j+1/2}\,(\tilde{R}^{\rm em}_{PAIR})^n_{i+1/2,j+1/2,l+1/2,k+1/2,m+1/2} \\
&\times(1/\rho^n_{i+1/2} - F^n_{i+1/2,j+1/2,k+1/2})(1/\rho^n_{i+1/2} - \bar{F}^n_{i+1/2,l+1/2,m+1/2}). \qquad (3.101)
\end{aligned}
$$

Chapter 4

Radiation Transport Test Problems

This chapter describes a suite of three test problems designed to analyze the capabilities of the neutrino transport algorithm used in AGILE-BOLTZTRAN. Two somewhat realistic models, Bruenn's Unisphere (Bruenn 1998, private communication) and the Lund Problem (Lund 1985; Mezzacappa & Matzner 1989) are discussed first. The chapter concludes with an analysis of the spherical Milne, or Kosirev, problem (Kosirev 1934; Hummer & Rybicki 1971) and a discussion of the differences between the S_n transport method used in AGILE-BOLTZTRAN and tangent-ray methods.

4.1 Bruenn's Unisphere Problem

A version of this test problem is discussed in Bruenn (1985). A static stellar core of radius 100 km surrounded by a tenuous atmosphere was constructed with density, temperature, and Ye

profiles

$$\rho = \begin{cases} 3 \times 10^{11} g/cm^3 & : \quad r < 100km \\ 1 \times 10^{8} g/cm^3 & : \quad r \geq 100km \end{cases}, \tag{4.1}$$

$$T = \begin{cases} 4MeV & : \quad r < 100km \\ 0.2MeV & : \quad r \geq 100km \end{cases}, \tag{4.2}$$

$$Y_e = \begin{cases} 0.2 & : \quad r < 100km \\ 0.4643 & : \quad r \geq 100km \end{cases}. \tag{4.3}$$

The computational domain out to 9120 km is spanned by 100 radial zones, 77 of these lying within the dense core out to 100 km. An "analytic" solution for this configuration can be found. The solution is analytic in the sense that it can be reduced to one straightforward numerical integration over angle.

The edge of the core is sharp numerically, i.e. the transition from the interior values to the exterior values occurs over a single radial zone of width $\approx$ 1 km. The material inside the core is assumed to be in nuclear statistical equilibrium corresponding to the values of ρ, T, and Y_e. The only neutrino processes calculated are absorption and emission of electron neutrinos and antineutrinos. The neutrino distribution functions are initially set to zero and are evolved until a stationary radiation field is obtained (i.e. until the change in any distribution function on the grid over a time step is zero). Twelve geometrically spaced energy groups spanning the range from 5 MeV to 225 MeV were used to discretize the neutrino energies. Eight-point Gaussian quadrature was used to discretize the neutrino direction cosines.

Figure 4.1 compares the neutrino and antineutrino luminosities computed with AGILE-BOLTZTRAN to the analytical values. The AGILE-BOLTZTRAN luminosities for both neu-

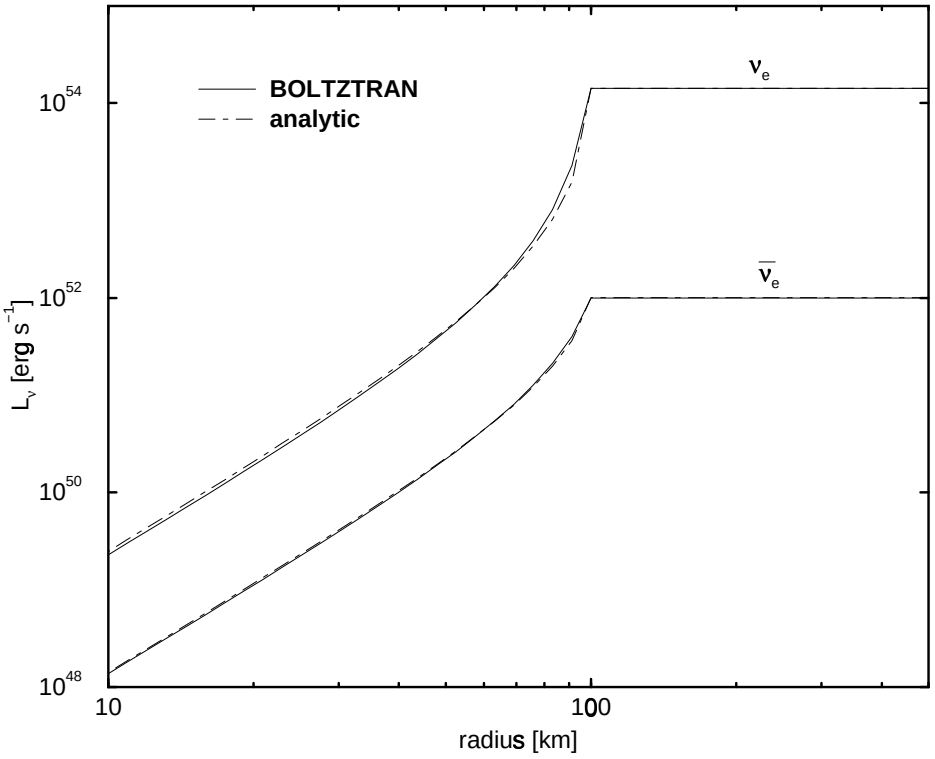

Figure 4.1: Electron neutrino and antineutrino luminosities for the Unisphere problem.

trinos and antineutrinos differ from the analytical results by less that 3% throughout most of the core, until the outermost two zones are reached. The neutrino luminosities differ by 18% and 35% in the second most outer and outermost zones, respectively. The antineutrino luminosities differ by 7% and 10% in these same spatial zones. Outside the core, a constant difference of 0.2% (0.9% for antineutrinos) is maintained to the edge of the computational domain.

Figure 4.2 shows the RMS energies of the emitted neutrinos. The agreement with the analytical values is exquisite, being 0.3% (0.2% for the antineutrinos) at the edge of the core for both neutrinos and antineutrinos, a difference that is maintained to the edge of the computational domain. The computed RMS energies for neutrinos are greater than the analytical values just interior to the edge of the core, while those for antineutrinos are less than the analytical values at the same radii. Both sets of computed RMS energies fall below the analytical values exterior to the core.

In addition to the RMS energies and luminosities, the "shape" of the radiation field is important. The mean inverse flux factor provides a measure of this. The inverse flux factor is the ratio of the local energy density to the flux, i.e.

$$\frac{1}{\mathsf{F}} = \frac{\int dE_{\nu_e} d\mu_{\nu_e} E^3_{\nu_e} f}{\int dE_{\nu_e} d\mu_{\nu_e} E^3_{\nu_e} \mu_{\nu_e} f} = \frac{cU_{\nu_e}}{F_{\nu_e}}. \tag{4.4}$$

It is infinite for a completely isotropic radiation field and tends towards unity as the neutrinos become free streaming at infinite radius. The importance of this quantity in the neutrino heating rate will be demonstrated in Chapter 5.

Figure 4.3 displays the analytical and AGILE-BOLTZTRAN computed inverse flux factors for both neutrinos and antineutrinos for the test case. Figure 4.4 is a closeup view of the curves in 4.3 near the edge of the core. Good agreement with the analytical results is seen throughout the

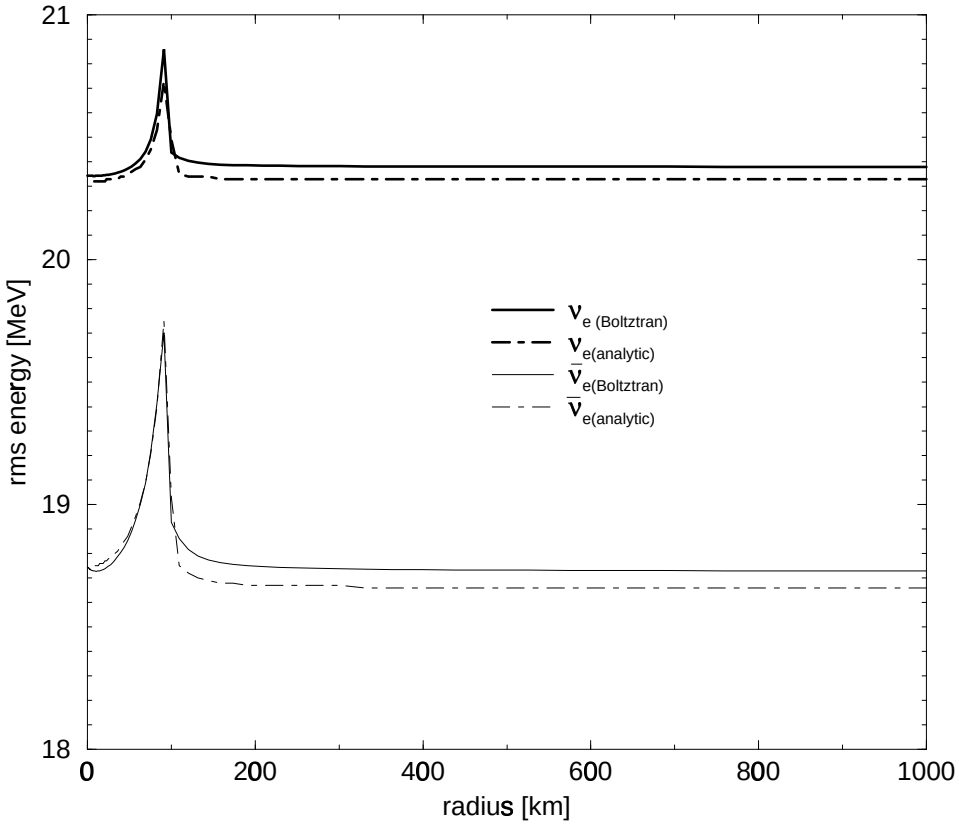

Figure 4.2: Electron neutrino and antineutrino RMS energies for the Unisphere problem.

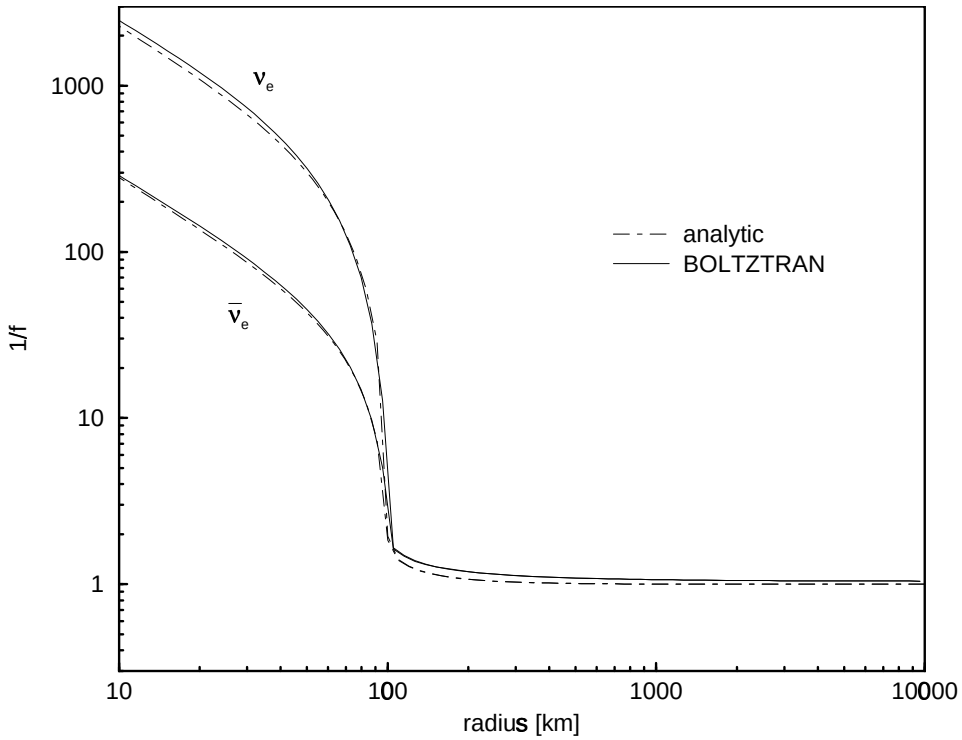

Figure 4.3: Electron neutrino and antineutrino inverse flux factors for the Unisphere problem.

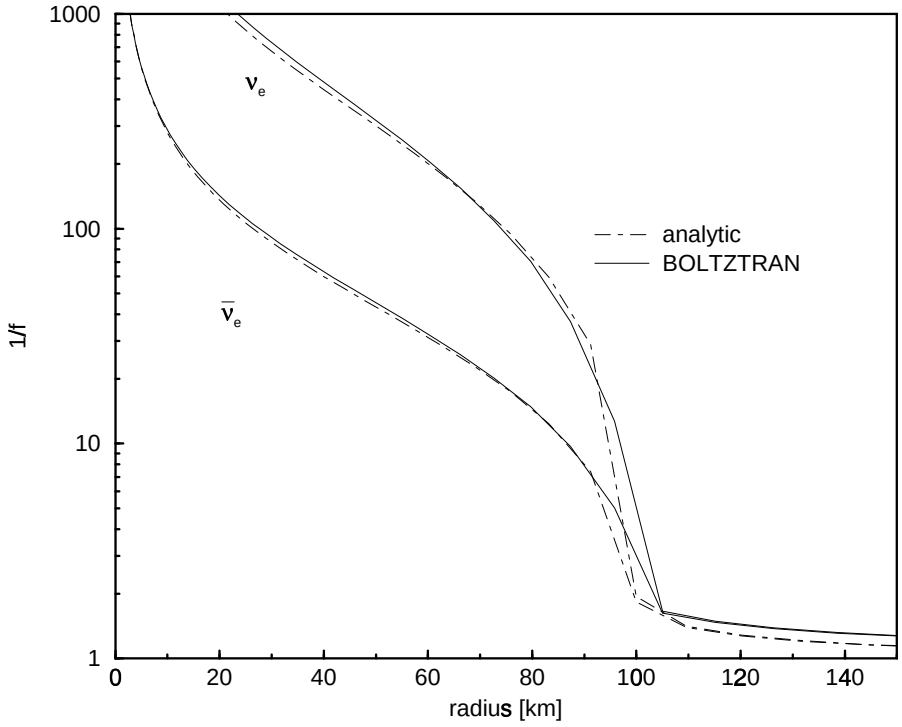

Figure 4.4: Closeup view near the edge of the core of electron neutrino and antineutrino inverse flux factors for the Unisphere problem.

core for both neutrinos and antineutrinos. At a given radius the neutrinos are more isotropic (i.e. their inverse flux factor is greater) than the antineutrinos since low proton fraction in the core (0.2) produces a much higher absorptive opacity for the neutrinos compared to the antineutrinos. At the extreme edge of the core the AGILE-BOLTZTRAN results are slightly higher than their analytic counterparts. Immediately outside the core the analytic values are slightly higher. The analytic inverse flux factors quickly asymptote to 1 before the edge of the computational domain. The computed inverse flux factors for both neutrinos and antineutrinos are 1.044 at the edge of the grid, somewhat above the geometrical value. This is, in fact, close to the minimum inverse flux factor achievable with AGILE-BOLTZTRAN for 8–point Gaussian quadrature, 1.041, the inverse of the maximum value of μ found in the quadrature set (Mezzacappa & Bruenn (1993a) and see the discussion of the Milne problem in this chapter).

4.2 Lund's Cooling Problem

Here we present the results for the schematic neutron star cooling problem of Lund (1985). We consider a static star with density profile

$$\rho = \rho_0 e^{-r/r_0}, \tag{4.5}$$

where $\rho_0 = 10^{15} g/cm^3$ and $r_0 = 10^6\ cm$. The star has constant heat capacity per unit volume of $10^{15}\ erg\ g^{-1}\ MeV^{-1}$. The initial temperature profile is that of a polytrope

$$T = T_0 \left(\frac{\rho}{\rho_0} \right)^{\gamma - 1}, \tag{4.6}$$

with $\gamma = \frac{4}{3}$ and $T_0 = 24.4\ MeV$. In Figure 4.5 we plot the density profile of the star. Figure

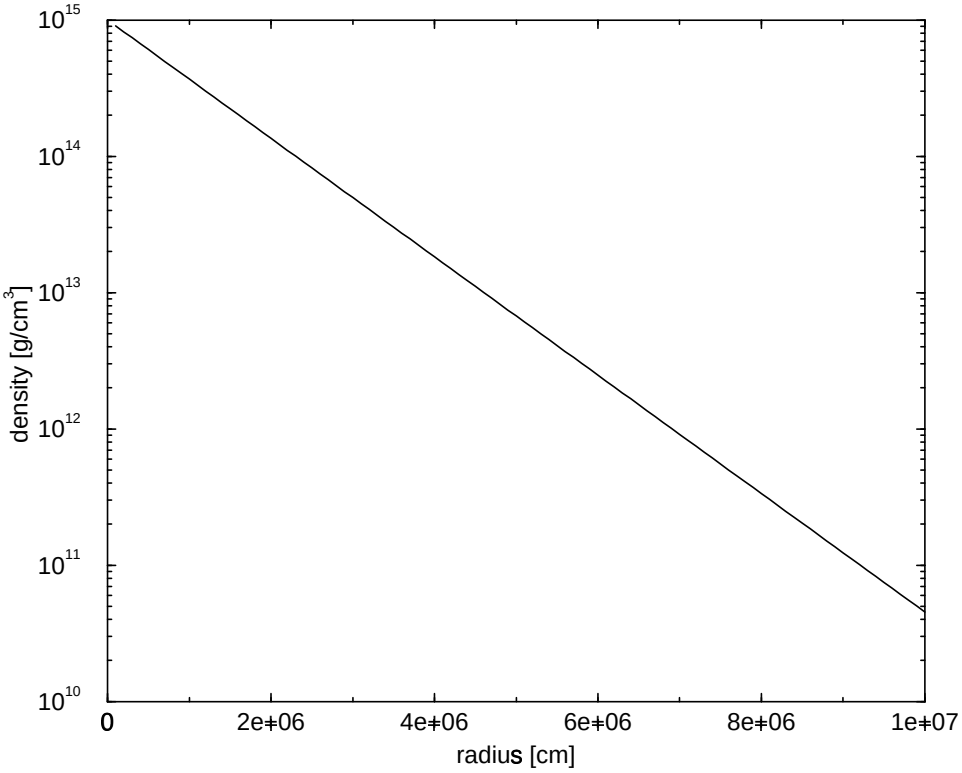

Figure 4.5: Density profile for the Lund problem

4.6 contains the initial temperature profile. We also plot the initial energy density of the star as a function of radius in Figure 4.7. The initial radiation field (which is composed of photons for this problem) is isotropic and given by a Planck distribution. The opacity is given by

$$\chi = \kappa\rho, \tag{4.7}$$

$$\kappa = \kappa_0 E^2, \tag{4.8}$$

where $\kappa_0 = 1.24 \times 10^{-20} cm^2 g^{-1} MeV^{-1}$. The emissivity is then

$$j = \chi B(T), \tag{4.9}$$

where

$$B(T) = \frac{1}{e^{E/T} - 1}, \tag{4.10}$$

where E is the photon energy.

The simulation uses 100 equally spaced radial zones from 0 to 100 km. 8-point Gaussian quadrature was used to resolve the photon direction cosines. 20 geometrically spaced energy groups spanning the range from 5 MeV to 326 MeV were used to discretize the photon energies. The run was stopped at a an elapsed time of 100 ms, as in Lund (1985) and Mezzacappa & Matzner (1989).

In Figure 4.8 we plot the mean free path of the photons in the star as a function of radius at the final time.

Figure 4.9 contains the average value of μ, the direction cosine of the radiation with the outgoing radial direction.

Figure 4.10 is a plot of the Eddington factor versus radius at the final time. The Eddington

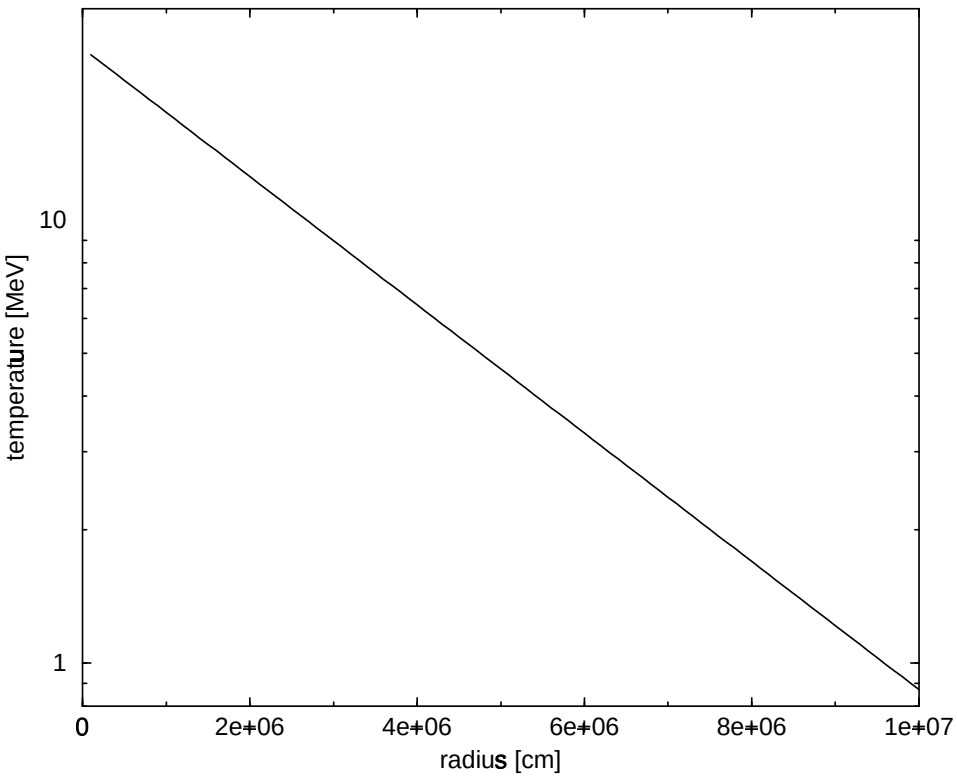

Figure 4.6: Initial temperature profile for the Lund problem

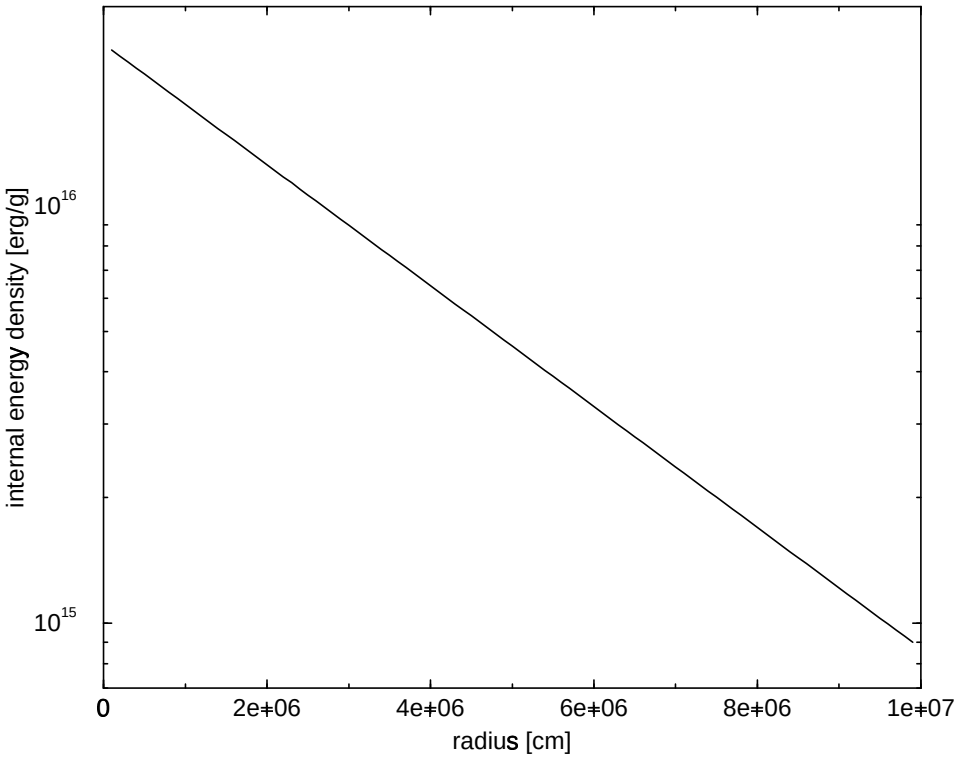

Figure 4.7: Initial energy density profile for the Lund problem

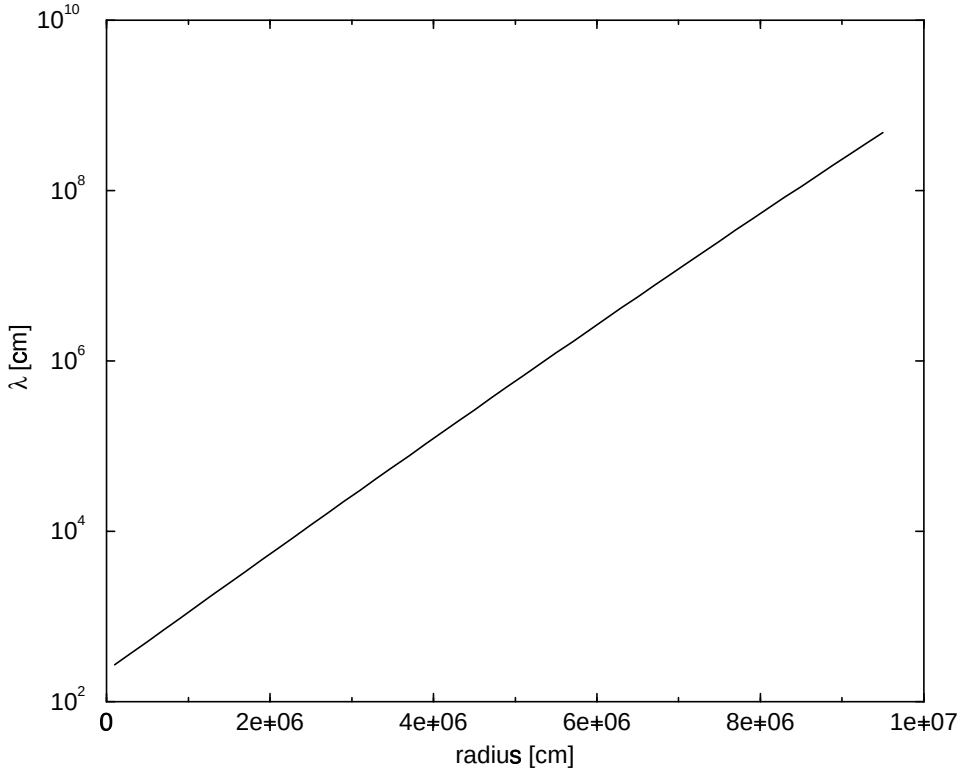

Figure 4.8: Photon mean free path as a function of radius for the Lund problem

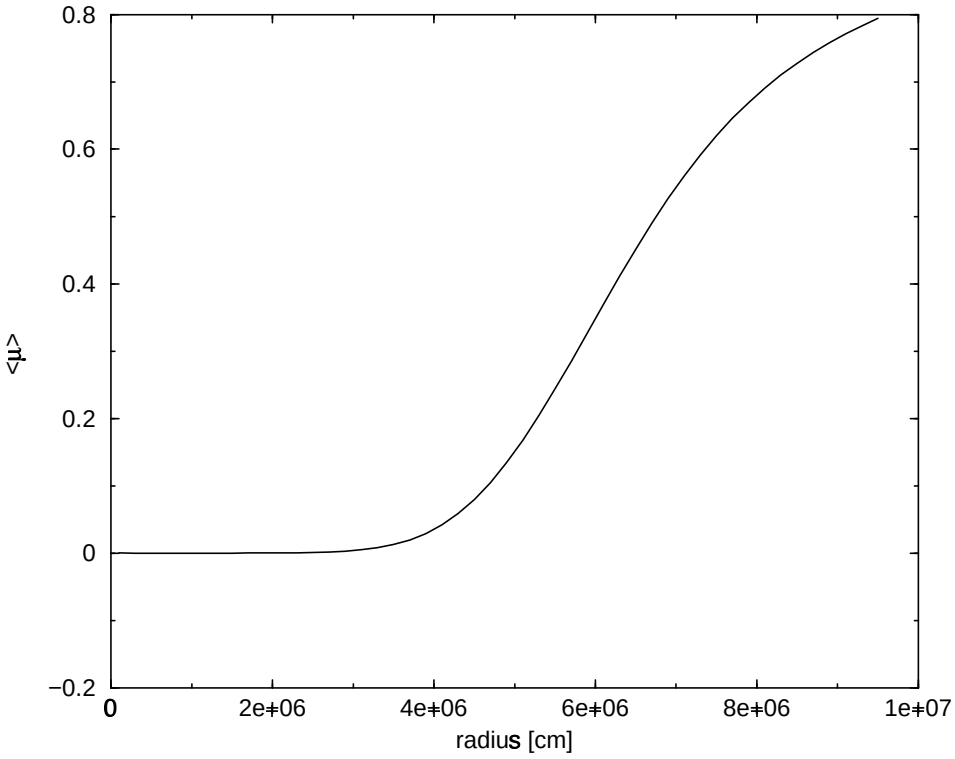

Figure 4.9: Average μ as a function of radius for the Lund problem

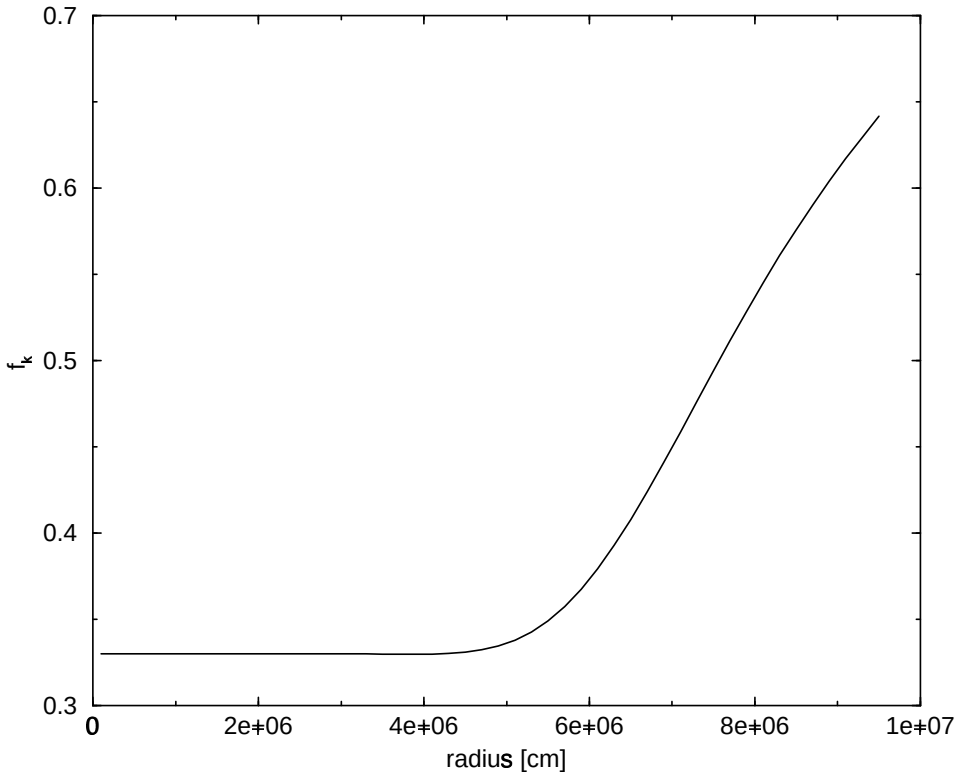

Figure 4.10: Eddington factor as a function of radius for the Lund problem

factor is defined as the ratio of the second moment of the radiation field to the first moment (see Section 4.3).

Finally, we plot the internal matter energy, the radiation energy, the energy emitted from the edge of the grid, and the sum of these as function of time in Figure 4.11. Note the total energy is well conserved. All these results are in excellent agreement with Lund (1985) and Mezzacappa & Matzner (1989).

4.3 The Spherical Milne Problem

The Milne problem consists of a semi-infinite, pure scattering planar atmosphere in radiative equilibrium with an opacity depending on the depth of the atmosphere as an inverse power law (Milne 1928). Kosirev (1934) was the first to consider the spherical analogue of this problem, where the opacity depends on the radius of a spherical atmosphere as

$$\chi = \chi_0 r^{-n} \ , \quad n > 1. \tag{4.11}$$

Scattering atmospheres of this type have also been studied by Hummer & Rybicki (1971) and Schinder & Bludman (1989). Both of these later works involved solving the transfer equation via a tangent-ray method (Mihalas & Mihalas 1984), where the equation of transfer is solved along a set of rays tangent to spherical shells. The intersection of these rays with outer shells define an angular mesh that increases in resolution with increasing radius. This method is quite standard in photon transport and has recently been advertised as a good choice for neutrino transport in supernovae simulations (Burrows et al. 2000; Rampp & Janka 2000).

For the study at hand we take $\chi = (R_0/r)^2$. The source is optically infinitely thick with a geometric thickness of $R_s = 1$. Therefore, the emissivity and opacity are infinite at the origin,

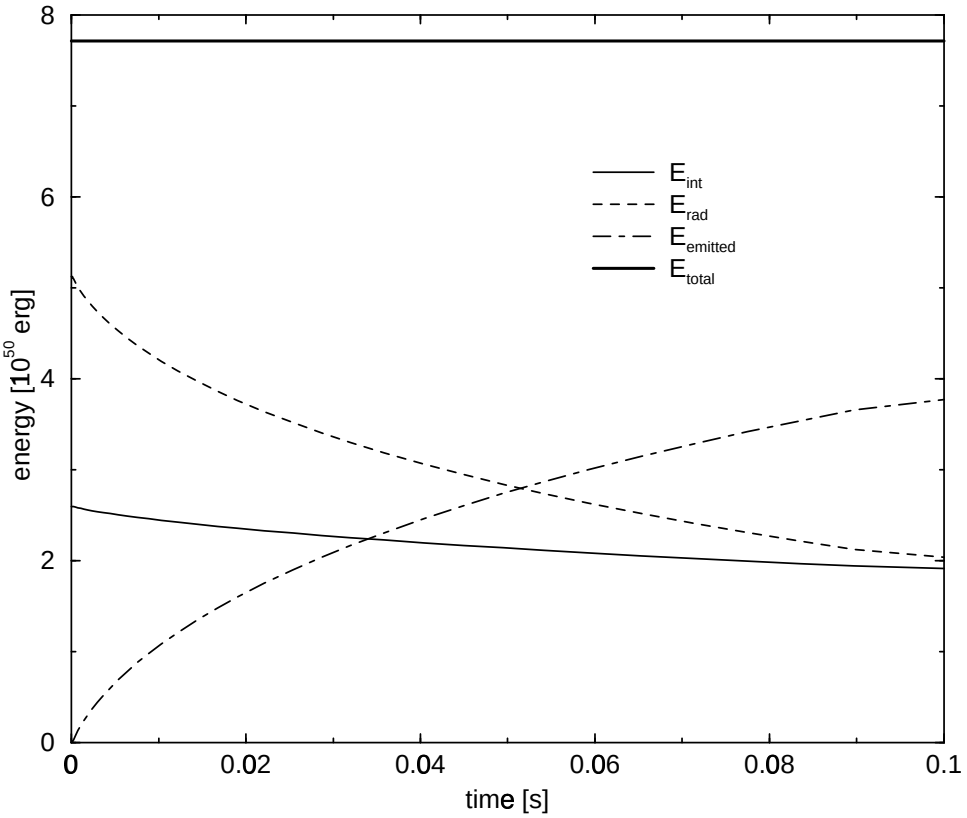

Figure 4.11: Internal energy, radiation energy, emitted energy, and total energy for the Lund problem

and all the cases reviewed here are characterized by a constant luminosity, L_0. The equation we solve becomes the Boltzmann equation for a conservative scattering in a gray atmosphere

$$\begin{aligned} \frac{1}{c}\frac{\partial F}{\partial t} &+ 4\pi\mu\frac{\partial(r^2\rho F)}{\partial m} \\ &+ \frac{1}{r}\frac{\partial[(1-\mu^2)F]}{\partial\mu} \\ &= 2\chi(\psi^0(E) - F), \end{aligned} \tag{4.12}$$

where ψ^0 is the zeroth angular moment of $F(E,\mu)$:

$$\psi^0(E) = \frac{1}{2}\int d\mu F. \tag{4.13}$$

Note that the radiation described by this equation is no longer fermionic. No blocking factors are present on the right hand side. The radiation is photon-like.

The source is discretized as 100 equally spaced radial zones spanning radii from 0 to 1. No attempt to capture rapid changes in optical depth by using variably spaced zoning was attempted. Equal zoning represents a "worst case" for small values of R_0, where the source becomes optically thin very quickly. Calculations were started with the distribution function for the radiation equal to zero everywhere but the origin, where $f = 0.7$ for all angles. The calculations were stopped when steady-state distributions were realized, as in the Unisphere problem.

Figure 4.12 is a plot of the Eddington factor, f_k versus scaled radius for $R_0 = 0.01, 0.1, 1,$ and 10 using 6-point Gaussian quadrature to resolve the direction cosines of the radiation. The Eddington factor is defined as

$$f_k = \frac{\int d\mu\mu^2 f(\mu)}{\int d\mu f(\mu)}. \tag{4.14}$$

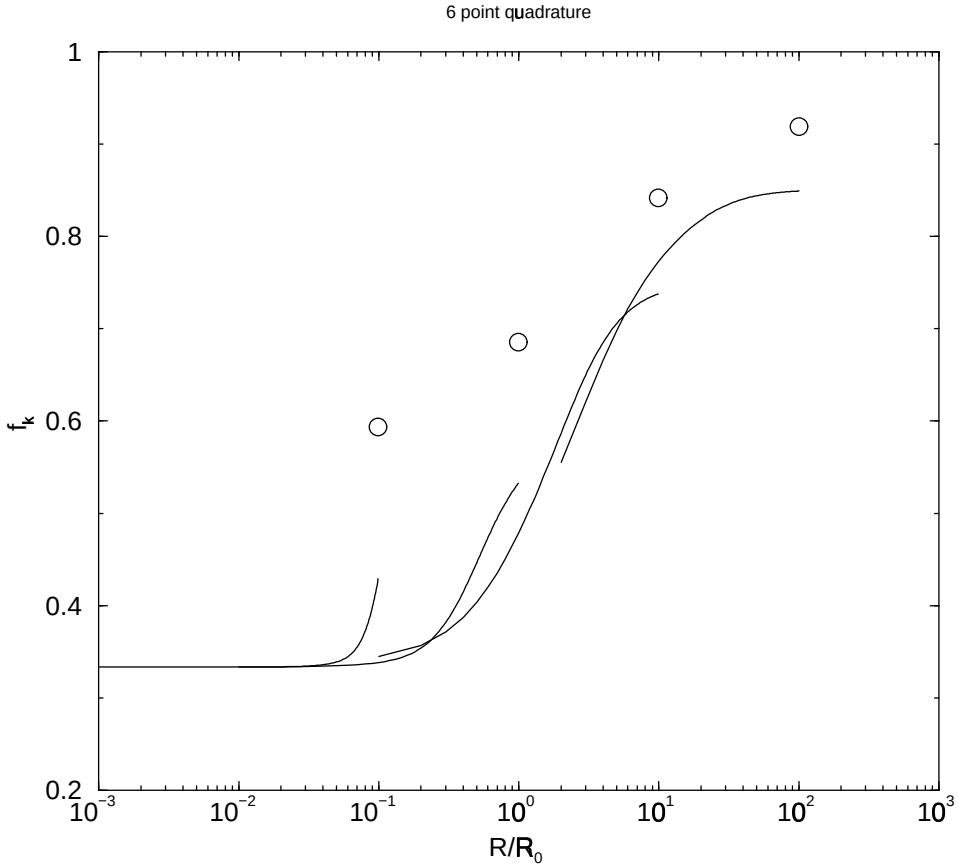

Figure 4.12: f_k versus radius for 6-point Gaussian quadrature and $R_0 = 0.01$, 0.1, 1, and 10

Also on the plot, marked with circles, are the values of the Eddington boundary factors, f_h, at the edge of the source. The Eddington boundary factor is

$$f_h = \frac{\int d\mu \mu f(\mu)}{\int d\mu f(\mu)}. \tag{4.15}$$

These results are quite close to those obtained by Schinder & Bludman (1989) for the larger values of R_0. The results for $R_0 = 10$ are almost identical to Schinder & Bludman (1989), and for $R_0 = 1$ f_h and the outermost value of f_k are less than 25% different than their counterparts in Schinder & Bludman (1989). In these cases, the source is optically thick until large radii are reached. Although Schinder & Bludman (1989) used over 50 rays, and almost all of those were available for resolution in the outermost zones, the quality of their solution is not markedly better when compared to the discrete ordinates solution with rather modest resolution.

For small values of R_0 the results are qualitatively different from Schinder & Bludman (1989) at small optical depth. The curves for f_k begin to turn over and asymptote to a constant value as the edge of the source is approached. This behavior is beginning to become evident for $R_0 = 1$ and is obvious for $R_0 = 0.01$. The radiation is becoming strongly forward peaked as the edge of the source is approached in these cases. The shape of the discrete ordinates curves is a manifestation of a well known symptom of the method when Gaussian quadrature is used: the inability to reproduce "true" free streaming, marked by f_k approaching 1. Instead, the maximum f_k is limited to the square of the maximum direction cosine in the chosen quadrature set, μ^2_{jmax} (Mezzacappa & Bruenn 1993a). The same effect is seen in the value of f_h: $f_h \leq \mu_{jmax}$ (cf. equations 4.14 and 4.15).

This effect is further highlighted in Figure 4.13, where f_k and f_h are plotted versus scaled radius for a variety of quadrature sets and for $R_0 = 0.01, 1,$ and 10. The values of f_h at R_S for

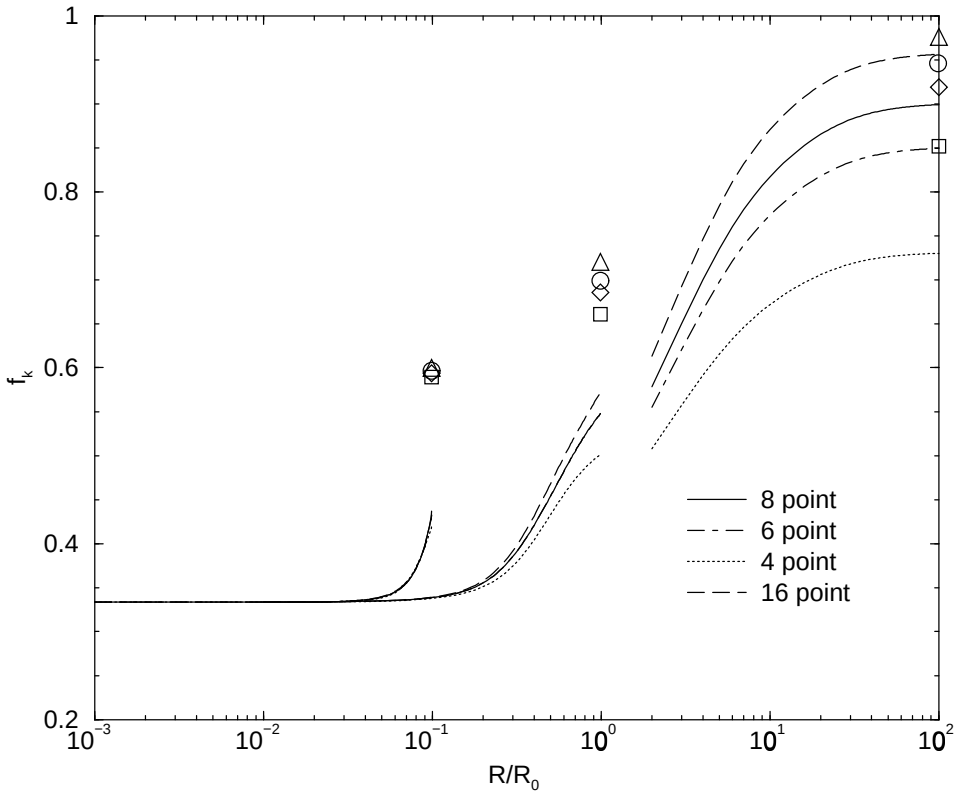

Figure 4.13: f_k and f_h versus radius for various Gaussian quadrature sets and $R_0 = 0.01, 1, \text{and } 10$

the various quadrature sets are denoted by the squares, diamonds, circles, and triangles as the number of quadratures increases. For $R_0 = 0.01$, the maximum values of f_k and f_h are each less than 2% different from μ_{jmax}^2 and μ_{jmax} for each quadrature set. Nevertheless, the 16-point results are less than 10% different in the last zone from the results of Schinder & Bludman (1989).

Also evident in Figure 4.13 is the convergence of the results for $R_0 = 10$. The results for $R_0 = 1$ are almost converged. This demonstrates the precision attainable with discrete ordinates with modest resolution for values of $R_0 > 1$.

Mihalas & Mihalas (1984) discuss the advantages and disadvantages of discrete ordinates and tangent-ray methods. They point out that tangent-ray methods provide outstanding angular resolution in regions where the radiation field becomes strongly forward peaked. Conversely, S_n methods are more computationally efficent for problems consisting of a large diffusive region surrounded by a thin transport layer, where geometric effects are important, but the field is close to isotropic. The latter situation describes the shock reheating phase in supernovae quite closely. Typical of the shock reheating epoch are neutrinosphere radii of $\approx 60km$ and shock stand-off radii of $\approx 200km$. Idealizing this configuration to our pure scattering atmosphere provides $R_s/R_0 \approx 3.33$. Figure 4.14 plots f_k versus f_h for a variety of quadrature sets and for $R_0 = 10$ and 0.33. For $R_0 = 0.33$ the relation between f_k and f_h is essentially identical for all the quadrature sets, especially for 6-point and above. This is equivalent to having identical closure relations in, for example, a MGFLD scheme. The relation for $R_0 = 10$ is quite different for the various quadrature sets, but the aspect ratio is like that of an small central source with a large, extended atmosphere. The heating region in delayed supernovae is nothing like this situation. The neutrino heating takes place across a rather thin transport layer immediately above the PNS. Therefore, for the problem discussed in this dissertation, namely neutrino transport in

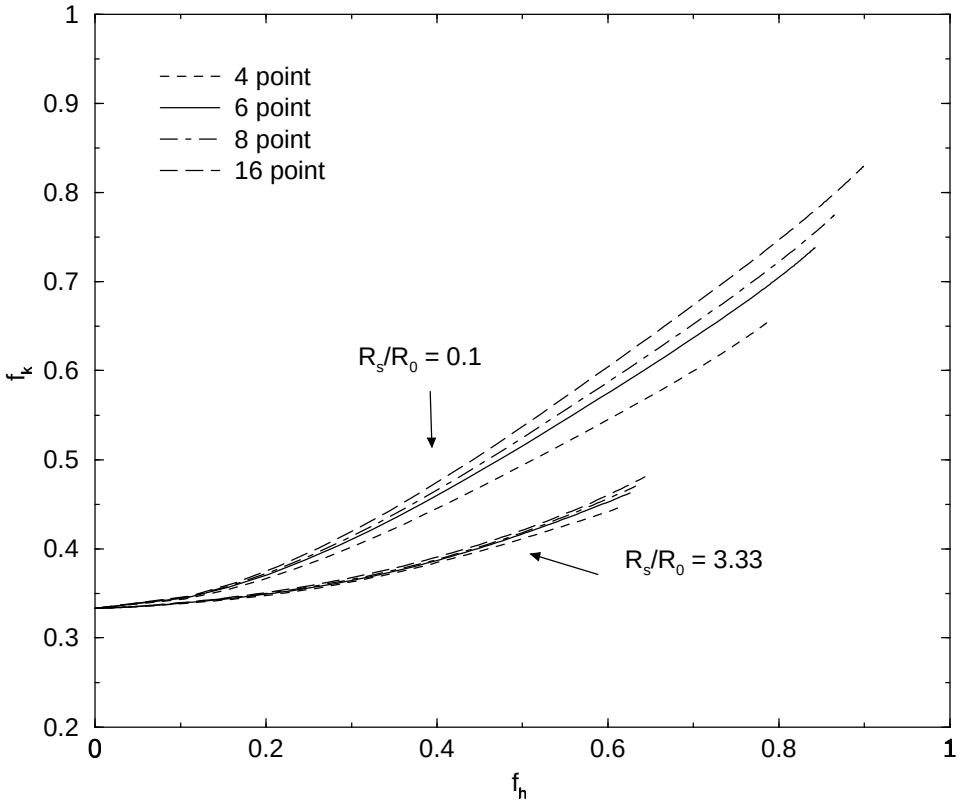

Figure 4.14: f_k versus f_h for various Gaussian quadrature sets and $R_0 = 10$ and 0.33

a rather thin gain region above a highly diffusive interior, S_n methods can be considered the method of choice due to their computational efficiency and good accuracy.

Chapter 5

Stationary State Simulations with BOLTZTRAN

5.1 Introduction

This chapter describes a series of studies designed to isolate and quantify the differences expected from using Boltzmann neutrino transport in a supernova simulation (Messer et al. 1998). We compare three-flavor multigroup Boltzmann neutrino transport (MGBT) and (Bruenn's) MGFLD in spherically symmetric, hydrostatic, thermally frozen, postbounce profiles, with an eye toward quantities central to the postbounce neutrino heating mechanism for reviving the stalled shock. In particular, for both transport methods, we compute and compare the neutrino luminosities, RMS energies, mean inverse flux factors, and net heating rates as functions of radius, time, and precollapse model. We then discuss the ramifications our results have for the supernova mechanism. This work is a continuation and extension of core collapse simulations (Mezzacappa & Matzner 1989; Mezzacappa & Bruenn 1993a,b,c), in which exact Boltzmann

neutrino transport and multigroup flux-limited diffusion were compared.

5.2 Initial Models, Codes, and Methodology

We begin with 15 $M_\odot$ and 25 $M_\odot$ precollapse models S15s7b and S25s7b provided by Woosley (1995). The initial models were evolved through core collapse and bounce using one-dimensional Lagrangian hydrodynamics and MGFLD neutrino transport coupled to the Lattimer–Swesty equation of state (Lattimer & Swesty 1991). The data at 106 ms and 233 ms after bounce for S15s7b and 156 ms after bounce for S25s7b were thermally and hydrodynamically frozen. The run of density, temperature and Ye for each of these time slices are plotted in Figures 5.1, 5.2, and 5.3. Stationary-state neutrino distributions were computed for these profiles using both MGBT and MGFLD.

The MGBT simulations were performed using a hydrostatic version of BOLTZTRAN: no hydrodynamics are included, nor is the radiation field coupled to the matter background. The MGFLD simulations were performed using MGFLD-TRANS: a Newtonian gravity, $O(v/c)$, three-flavor, MGFLD neutrino transport code, which has been used for both core collapse and postbounce evolution (Bruenn 1985, 1993).

The MGBT simulations used 110 nonuniform spatial zones spanning radii from the origin to 4744 km and 4673 km for model S15s7b at $t_{\rm pb} = 106$ ms and 233 ms respectively, and to 2096 km for model S25s7b at $t_{\rm pb} = 156$ ms. Twelve energy zones spanning a range between 5 and 225 MeV were used to resolve the neutrino spectra. The MGFLD used the same spatial and energy grids.

For the MGBT simulations there is an added dimension: neutrino direction cosine. Because MGBT computes the neutrino distributions as a function of direction cosine and energy for each spatial zone, the isotropy of the neutrino radiation field as a function of radius and neutrino

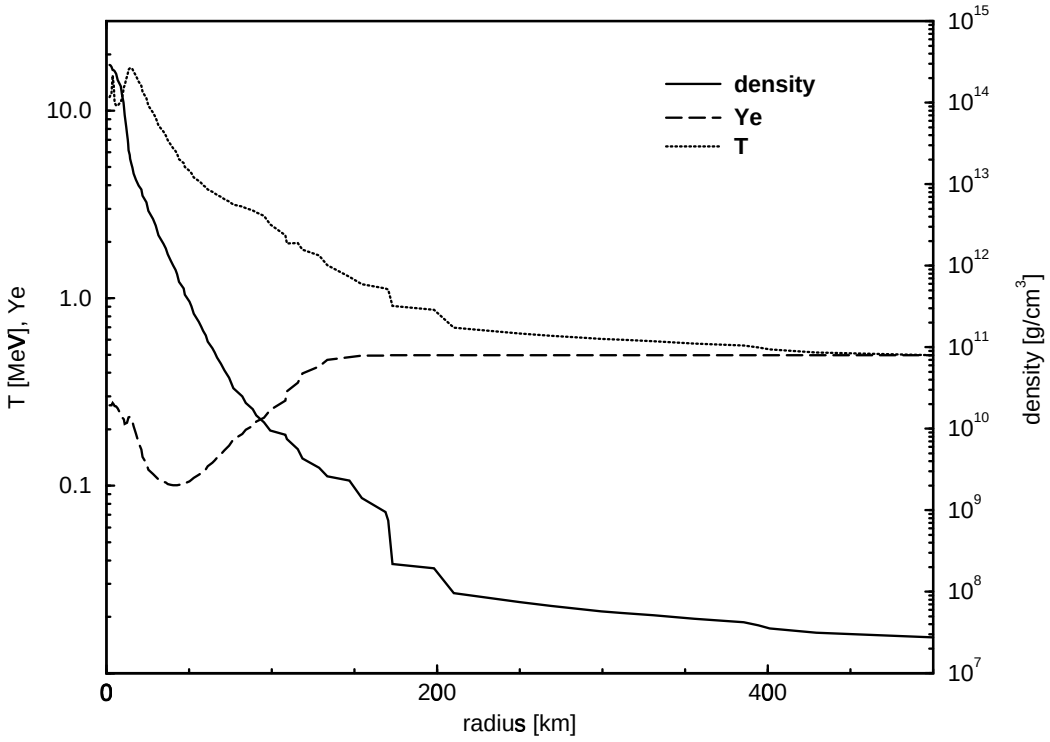

Figure 5.1: Density, temperature, and Ye for model S15s7b at 106 ms after core bounce.

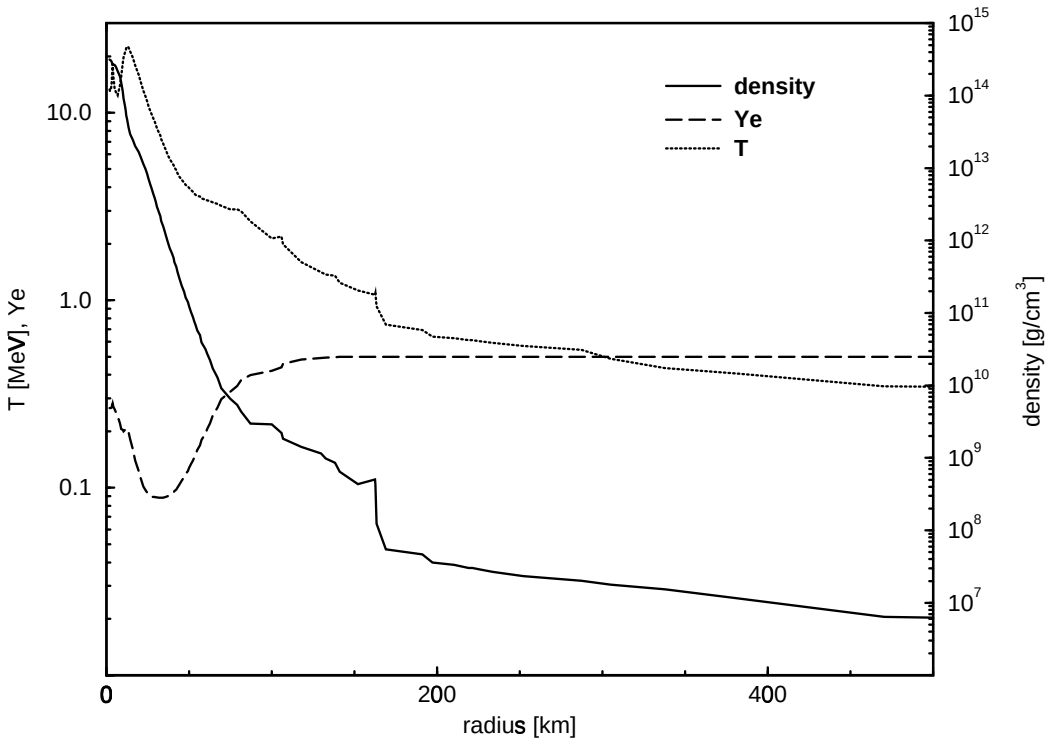

Figure 5.2: Density, temperature, and Ye for model S15s7b at 233 ms after core bounce.

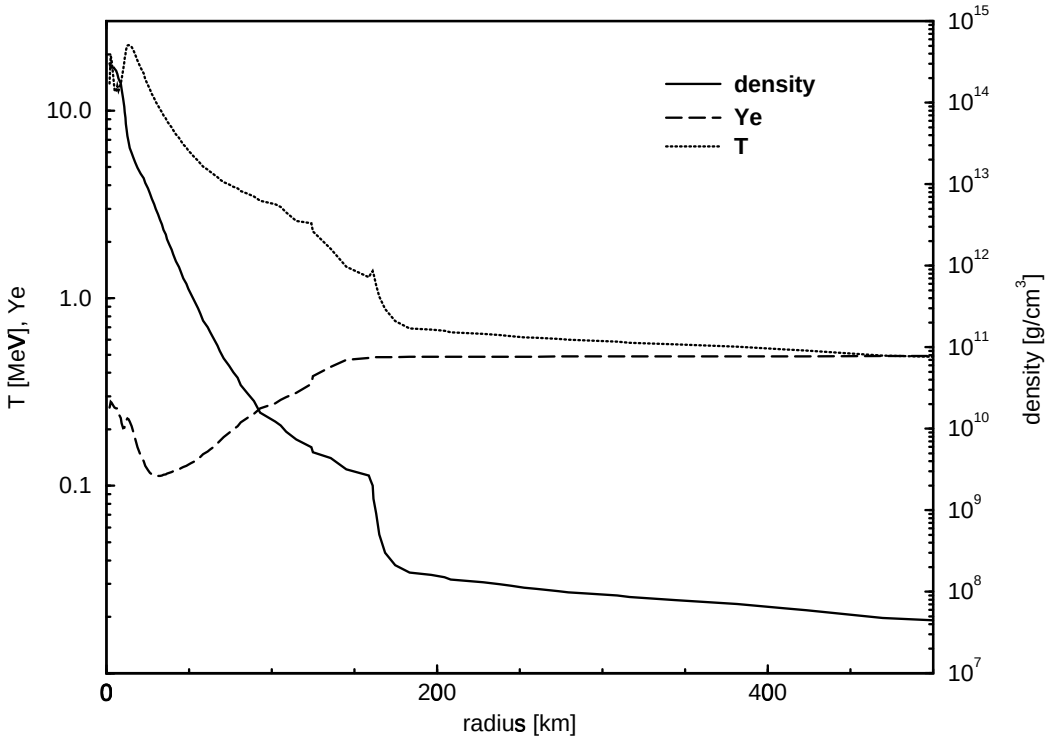

Figure 5.3: Density, temperature, and Ye for model S25s7b at 156 ms after core bounce.

energy is computed from first principles. This is one of the key features distinguishing MGBT and MGFLD. Because the isotropy of the neutrino radiation field is critical to the shock reheating/revival, four Gaussian quadrature sets (2–, 4–, 6–, and 8–point) were implemented in the MGBT simulations to ensure numerical convergence of the results.

5.3 Results

For electron neutrino and antineutrino absorption on neutrons and protons, the neutrino heating rate (in MeV/nucleon) in the region between the neutrinospheres and the shock can be written as

$$\dot{\epsilon} = \frac{X_n}{\lambda_0^a}\frac{L_{\nu_e}}{4\pi r^2} < E_{\nu_e}^2 >< \frac{1}{\mathsf{F}} > + \frac{X_p}{\bar{\lambda}_0^a}\frac{L_{\bar{\nu}_e}}{4\pi r^2} < E_{\bar{\nu}_e}^2 >< \frac{1}{\bar{\mathsf{F}}} >, \tag{5.1}$$

where: $X_{n,p}$ are the neutron and proton fractions; $\lambda_0^a = \bar{\lambda}_0^a = G_F^2\rho(g_V^2 + 3g_A^2)/\pi(hc)^4 m_B$; $G_F/(\hbar c)^3 = 1.166 \times 10^{-5}$ GeV^{-2} is the Fermi coupling constant; ρ is the matter density; $g_V = 1.0$, $g_A = 1.23$; m_B is the baryon mass; and $L_{\nu_e,\bar{\nu}_e}$, $< E_{\nu_e,\bar{\nu}_e}^2 >$, and $\mathsf{F}, \bar{\mathsf{F}}$ are the electron neutrino and antineutrino luminosities, RMS energies, and mean inverse flux factors, defined by

$$L_{\nu_e} = 4\pi r^2 \frac{2\pi c}{(hc)^3}\int dE_{\nu_e} d\mu_{\nu_e} E_{\nu_e}^3 \mu_{\nu_e} f, \tag{5.2}$$

$$\langle E_{\nu_e}^2 \rangle = \frac{\int dE_{\nu_e} d\mu_{\nu_e} E_{\nu_e}^5 f}{\int dE_{\nu_e} d\mu_{\nu_e} E_{\nu_e}^3 f}, \tag{5.3}$$

$$\langle \frac{1}{\mathsf{F}} \rangle = \frac{\int dE_{\nu_e} d\mu_{\nu_e} E_{\nu_e}^3 f}{\int dE_{\nu_e} d\mu_{\nu_e} E_{\nu_e}^3 \mu_{\nu_e} f} = \frac{cU_{\nu_e}}{F_{\nu_e}}. \tag{5.4}$$

In equations (5.2)–(5.4), f is the electron neutrino distribution function, which is a function of the electron neutrino direction cosine, μ_{ν_e}, and energy, E_{ν_e}. In equation (5.4), U_{ν_e} and F_{ν_e} are the electron neutrino energy density and flux. Corresponding quantities can be defined for the electron antineutrinos. Success or failure to generate explosions via neutrino reheating must ultimately rest on the three quantities defined in equations (5.2)–(5.4). Both the MGBT and the MGFLD stationary state distributions were computed in the same thermally and hydrodynamically frozen matter configuration.

In Figure 5.4, at 233 ms after bounce for model S15s7b, we plot the electron neutrino and antineutrino RMS energies, luminosities, and mean inverse flux factors as functions of radius for our (8–point Gaussian quadrature) MGBT and MGFLD runs. Energy-averaged electron neutrino- and antineutrino-spheres were located by calculating an energy-integrated neutrino depth defined by

$$\overline{\tau} = \frac{\int_{\infty}^{r} dr' \int_{0}^{\infty} dE_\nu d\mu_\nu E_\nu^3 f/\lambda}{\int_{0}^{\infty} dE_\nu d\mu_\nu E_\nu^3 f}, \tag{5.5}$$

and determining the radius at which $\overline{\tau} = 2/3$. The neutrinospheres (at 57 km and 48 km, for electron neutrinos and antineutrinos, respectively), and the location of the shock (at 191 km), are indicated by arrows. The gain radius (neutrino-energy integrated), located at 98 km, is also marked by an arrow. For the electron neutrinos, the differences in RMS energies between MGBT and MGFLD are at most 2% throughout most of the region plotted, although MGBT consistently gives higher energies. The differences between MGBT and MGFLD antineutrino RMS energies are smaller, and neither transport scheme yields consistently higher values. It

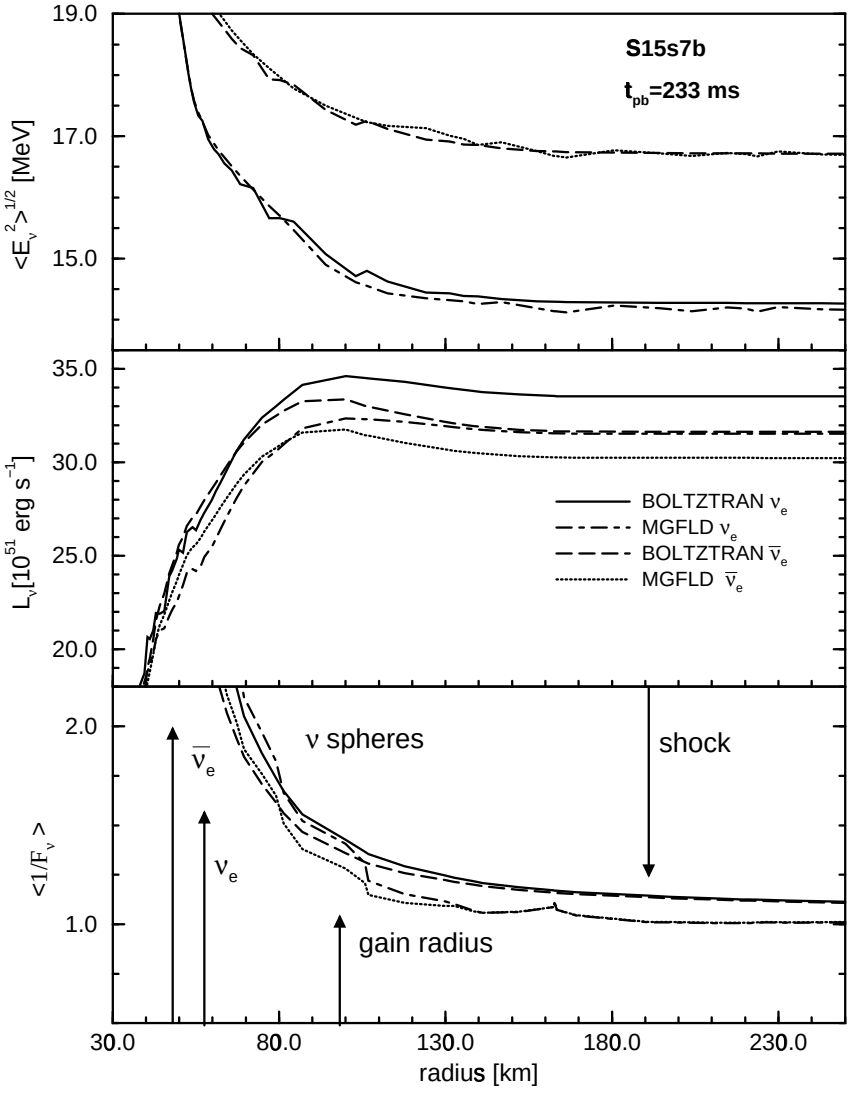

Figure 5.4: RMS energies, luminosities, and mean inverse flux factors for model S15s7b at 233 ms after core bounce.

should be noted that we would expect larger differences in a fully hydrodynamic simulation, with MGBT giving harder spectra (Mezzacappa & Bruenn 1993a,c; Burrows 1998). In a static matter configuration, differences that result from different treatments of the neutrino energy shift measured by comoving observers do not occur.

Significant differences between MGBT and MGFLD are evident when comparing the neutrino and antineutrino luminosities and mean inverse flux factors. The luminosity curves for both electron neutrinos and antineutrinos coincide for both transport methods until the neutrinospheres are approached from below. Just below the neutrinospheres, the MGBT luminosities diverge upward from the MGFLD luminosities, differing by 7% (4% for antineutrinos) at the neutrinospheres. The root cause of this difference is that the MGFLD interpolation underestimates the flux in this region. After a decline from this maximum difference, the fractional difference grows from approximately 3% at the base of the gain region to a constant difference of 6% beyond about 170 km. Similar behavior is exhibited by the antineutrino luminosities, with the same fractional differences, 3% and 6%, seen at the base of the gain region and near the shock, respectively.

For the electron neutrinos, the fractional difference between $< 1/\mathsf{F} >_{\mathrm{MGFLD}}$ and $< 1/\mathsf{F} >_{\mathrm{MGBT}}$ is 2%, 8%, and 12% at the neutrinosphere, gain radius, and shock, respectively. Just above the shock, the difference converges to 10%, and is maintained to the edge of the core. Focusing on the semitransparent region, $< 1/\mathsf{F} >_{\mathrm{MGFLD}}$ is greater until the gain radius is approached from below; i.e., the MGFLD neutrino radiation field is more isotropic than the MGBT radiation field below these radii. At 80 km, as the gain radius is approached, MGFLD computes a sharp decrease in $< 1/\mathsf{F} >$. Looking at Figure 5.5, where we plot the density and the sum of the MGBT electron neutrino and antineutrino luminosities for this time slice as functions of radius, it is evident as the gain radius is approached from below that the luminosity sum begins to turn

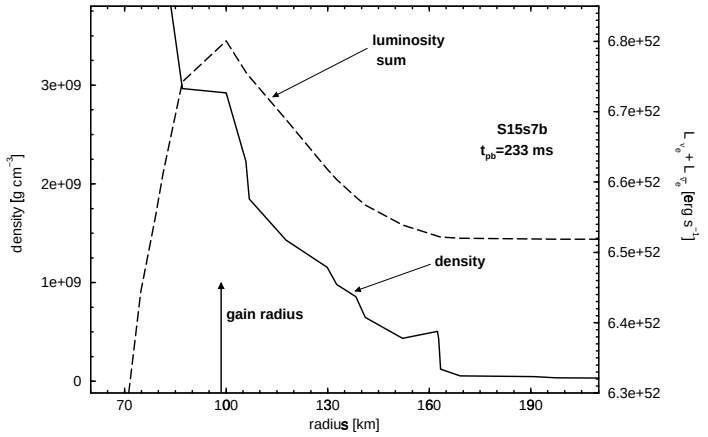

Figure 5.5: The density and MGBT electron neutrino and antineutrino luminosity sum are plotted versus radius for model S15s7b at $t_{\rm pb} = 233$ ms.

over, marking the enclosure of the neutrino and antineutrino source. Therefore, for MGFLD, the accelerated transition to free streaming occurs not at the neutrinospheres, as might have been anticipated, but at a radius within which most of the neutrino and antineutrino source is enclosed. For example, for this time slice the electron neutrino luminosity at the neutrinosphere is only 76% of its peak value.

In Figure 5.4, there is a second dip and a small spike in $< 1/\mathsf{F} >_{\rm MGFLD}$ at 106 km and 163 km, respectively; $< 1/\mathsf{F} >_{\rm MGBT}$ is smooth through these radii. Again, examining Figure 5.5, the density shows discontinuities at 106 km and 163 km, which produce these features. The density profile flattens at 106 km and then drops precipitously. There is a corresponding flattening and sharp drop in $< 1/\mathsf{F} >_{\rm MGFLD}$ in this region. The density actually increases at 160 km, then immediately falls off. This results in an increase in $< 1/\mathsf{F} >_{\rm MGFLD}$ at that radius, followed by a sharp decrease. In both cases, the isotropy of the MGFLD neutrino radiation field is altered by local conditions.

For the electron antineutrinos, the same features are seen in $< 1/\mathsf{F} >_{\rm MGFLD}$. The fractional

difference is 0%, 11%, and 11% at the neutrinosphere, gain radius, and shock, respectively. The initial sharp decrease in $< 1/\mathsf{F} >_{\mathrm{MGFLD}}$ occurs at a smaller radius. The antineutrino luminosity maximum, i.e., the point at which the antineutrino source is enclosed, is at a smaller radius.

In Figure 5.6, we plot the same three quantities for the earlier time slice in our 15 $M_\odot$ model ($t_{\mathrm{pb}} = 106$ ms). The differences between MGBT and MGFLD are similar to those seen at the later postbounce time ($t_{\mathrm{pb}} = 233$ ms). The electron neutrino RMS energies are slightly higher for MGBT, again by about 2%. The differences in antineutrino RMS energies are again variable in both sign and magnitude, but are never more than 2%. The difference in luminosity is 11% (8% for antineutrinos) at the neutrinosphere, 11% (7% for antineutrinos) at the gain radius, and settles to a constant difference of 9% (6% for antineutrinos) above 170 km. As in the later time slice, MGFLD underestimates the flux beginning below the neutrinospheres, extending everywhere above the neutrinospheres, which in turn results in a lower luminosity.

For electron neutrinos, the fractional difference between $< 1/\mathsf{F} >_{\mathrm{MGFLD}}$ and $< 1/\mathsf{F} >_{\mathrm{MGBT}}$ is 4%, 2%, and 17% at the neutrinosphere, gain radius, and shock, respectively. Most important, the same abrupt decrease in $< 1/\mathsf{F} >_{\mathrm{MGFLD}}$ beginning just above the gain radius is evident. In Figure 5.7, we plot the density and the sum of the MGBT electron neutrino and antineutrino luminosities for $t_{\mathrm{pb}} = 106$ ms. The decrease in $< 1/\mathsf{F} >_{\mathrm{MGFLD}}$ again occurs near the radius where the luminosity sum turns over: 128 km. There is also a small dip in $< 1/\mathsf{F} >_{\mathrm{MGFLD}}$ at 172 km. Looking at Figure 5.7, the only significant dip in density occurs at 172 km, causing a local decrease in the isotropy of the MGFLD radiation field.

For the electron antineutrinos, the difference between $< 1/\mathsf{F} >_{\mathrm{MGFLD}}$ and $< 1/\mathsf{F} >_{\mathrm{MGBT}}$ is 3%, 2%, and 16% at the neutrinosphere, gain radius, and shock, respectively. The point at which $< 1/\mathsf{F} >_{\mathrm{MGFLD}}$ drops below $< 1/\mathsf{F} >_{\mathrm{MGBT}}$ is translated inwards, as expected, towards the antineutrino luminosity maximum. For both electron neutrinos and antineutrinos, a difference

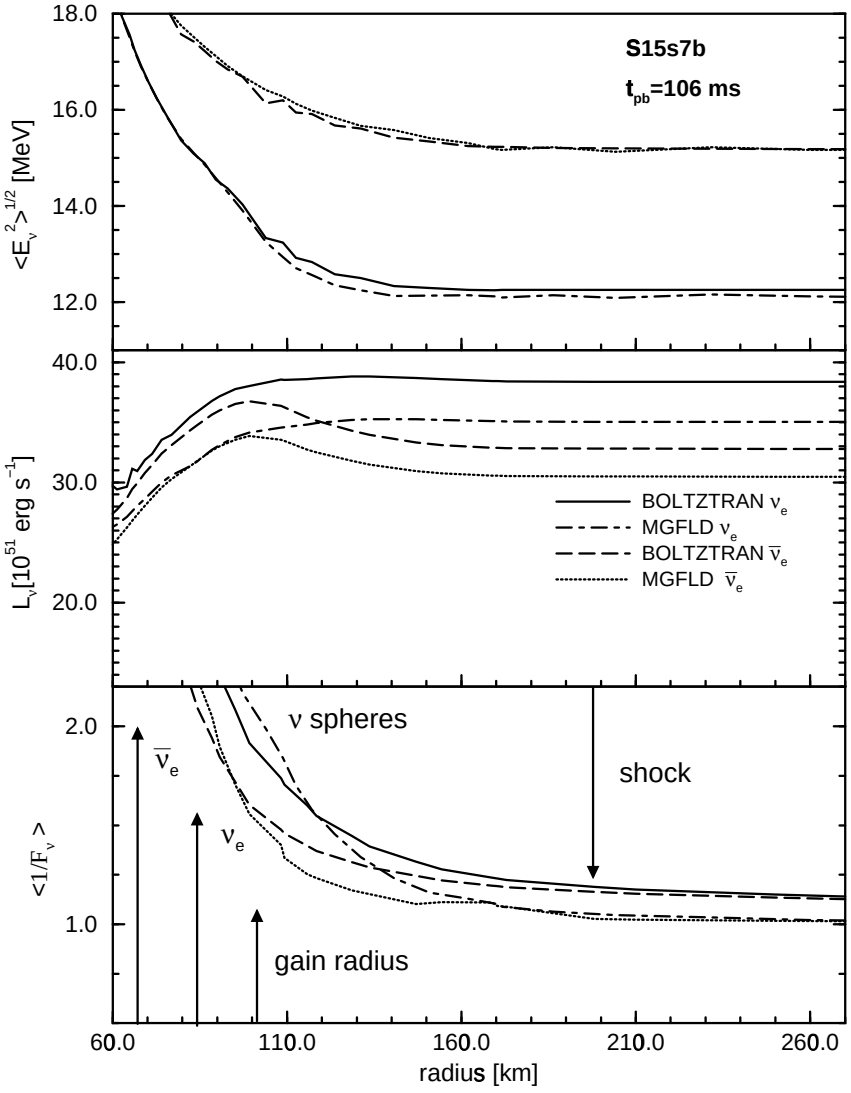

Figure 5.6: RMS energies, luminosities, and mean inverse flux factors for model S15s7b at 106 ms after core bounce.

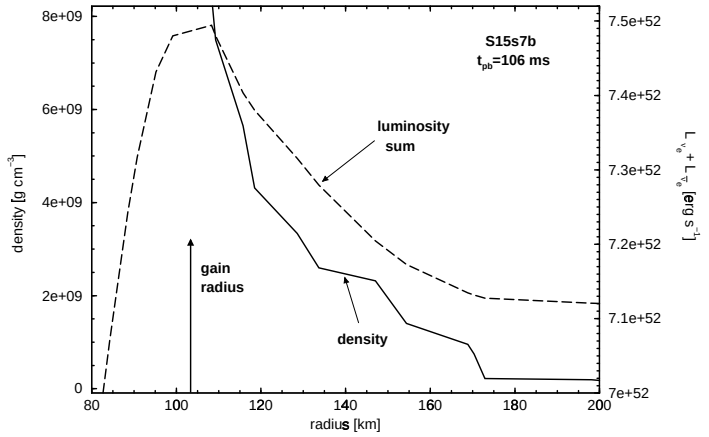

Figure 5.7: The density and MGBT electron neutrino and antineutrino luminosity sum are plotted versus radius for model S15s7b at $t_{\rm pb} = 106$ ms.

of about 13% is maintained with increasing radius above the shock.

Figure 5.8 contains the same information as Figures 5.4 and 5.6, but for our 25 $M_\odot$ model at 156 ms after bounce. The similarities between the 25 $M_\odot$ and the 15 $M_\odot$ results are striking, considering the marked difference in core structure. The identical trend in RMS energies is again seen: there are small differences for the electron neutrinos, but consistently higher values are obtained with MGBT (again, $\sim 2\%$ higher); there are smaller, sometimes oscillating, differences between MGBT and MGFLD for the electron antineutrinos. The absolute value of the neutrino luminosities at the gain radius is almost a factor of 2 greater than in either of the 15 $M_\odot$ slices, yet the relative differences between the luminosities computed by the two transport methods are similar. The electron neutrino luminosities differ by 9% (5% for antineutrinos) at the neutrinosphere, 11% (9% for antineutrinos) at the gain radius, and 9% (7% for antineutrinos) at the shock. The difference at the shock is maintained to the edge of the core. Again, this difference in luminosity is caused by an underestimation of the flux by MGFLD.

Among the three slices considered, the 25 $M_\odot$ core gives rise to the most dramatic differences

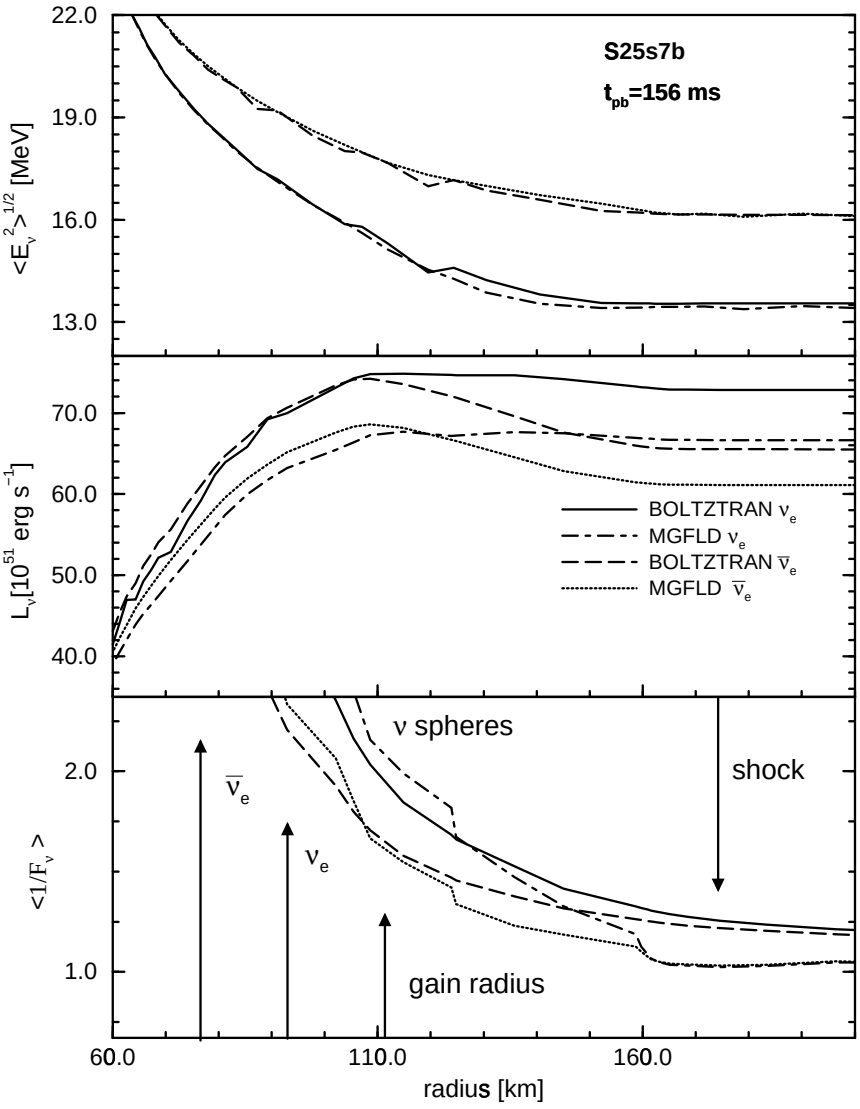

Figure 5.8: RMS energies, luminosities, and mean inverse flux factors for model S25s7b at 156 ms after core bounce.

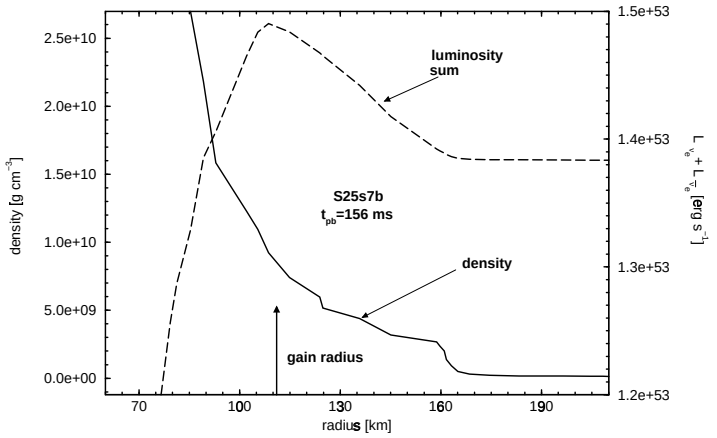

Figure 5.9: The density and MGBT electron neutrino and antineutrino luminosity sum are plotted versus radius for model S25s7b at $t_{\rm pb} = 156$ ms.

in $< 1/\mathsf{F} >$. For electron neutrinos, we find fractional differences of 1%, 2%, and 24% in $< 1/\mathsf{F} >$ at the neutrinosphere, gain radius, and shock, respectively. There is a sharp decrease in $< 1/\mathsf{F} >_{\rm MGFLD}$ at 109 km. As in the 15 $M_\odot$ case, this change in $< 1/\mathsf{F} >_{\rm MGFLD}$ is correlated with the enclosure of the neutrino source. This correlation is evident in Figure 5.9, where we plot the density and sum of the MGBT electron neutrino and antineutrino luminosities for this time slice. Note that the MGBT luminosity sum begins to turn over near 109 km, coincident with the sharp decrease in $< 1/\mathsf{F} >_{\rm MGFLD}$.

There are other precipitous drops in $< 1/\mathsf{F} >_{\rm MGFLD}$ at 125 km and 162 km. Also apparent in Figure 5.9 are precipitous drops in density at these radii. These drops in density produce changes in the local neutrino radiation field computed by MGFLD.

For electron antineutrinos, $< 1/\mathsf{F} >_{\rm MGFLD}$ exhibits similar structure, with fractional differences of 0%, 1%, and 19% at the neutrinosphere, gain radius, and shock, respectively. $< 1/\mathsf{F} >_{\rm MGFLD}$ for antineutrinos also contains three dips: $< 1/\mathsf{F} >_{\rm MGFLD}$ drops below $< 1/\mathsf{F} >_{\rm MGBT}$ at 105 km, where most of the antineutrino source is enclosed, and additional dips

at 125 km and 162 km are also evident, again resulting from the density dips visible in Figure 5.9. For both electron neutrinos and antineutrinos, constant differences $\sim 12\%$ are seen above the shock.

Because each of the quantities plotted in Figures 5.4, 5.6, and 5.8 is consistently greater for MGBT (while this is not strictly true for the antineutrino RMS energies in our stationary state comparisons, in a fully dynamical simulation these energies will be consistently higher for MGBT [Mezzacappa and Bruenn, 1993a,c; see also Burrows 1998]), and because the neutrino heating rate is proportional to each of them, MGBT yields a significantly higher heating rate. As an example, just above the gain radius for model S15s7b at $t_{\rm pb} = 233$ ms, at the point of peak heating, MGBT yields a heating rate from neutrino absorption that is $(102\%)^2 \times 110\% \times 112\%$ of the MGFLD rate. Note in equation (5.1) that the heating rate depends linearly on *both* the neutrino luminosity and the mean inverse flux factor. A reliable determination of the heating rate in and around the gain region therefore depends on a realistic solution of the transport equation in which both of these quantities are determined self consistently.

In Figure 5.10, for MGBT and MGFLD, we plot the *net* neutrino heating rates as functions of radius for model S15s7b at $t_{\rm pb} = 233$ ms.

As described in Section 5.2, the results from four Gaussian quadrature sets are plotted to demonstrate numerical convergence. As the number of quadrature points is increased, the net heating rate is decreased until the difference between the 6– and 8–point quadrature results is less than 3% at the peak of the heating curve and is indistinguishable in the cooling region immediately below the gain radius. This differences between 6– and 8–point Gaussian quadrature is inconsequential in dynamic simulations, as the error in total energy conservation in full radiation hydrodynamic simulations exceeds these differences.

These rates include the contributions from both the electron neutrinos and antineutrinos,

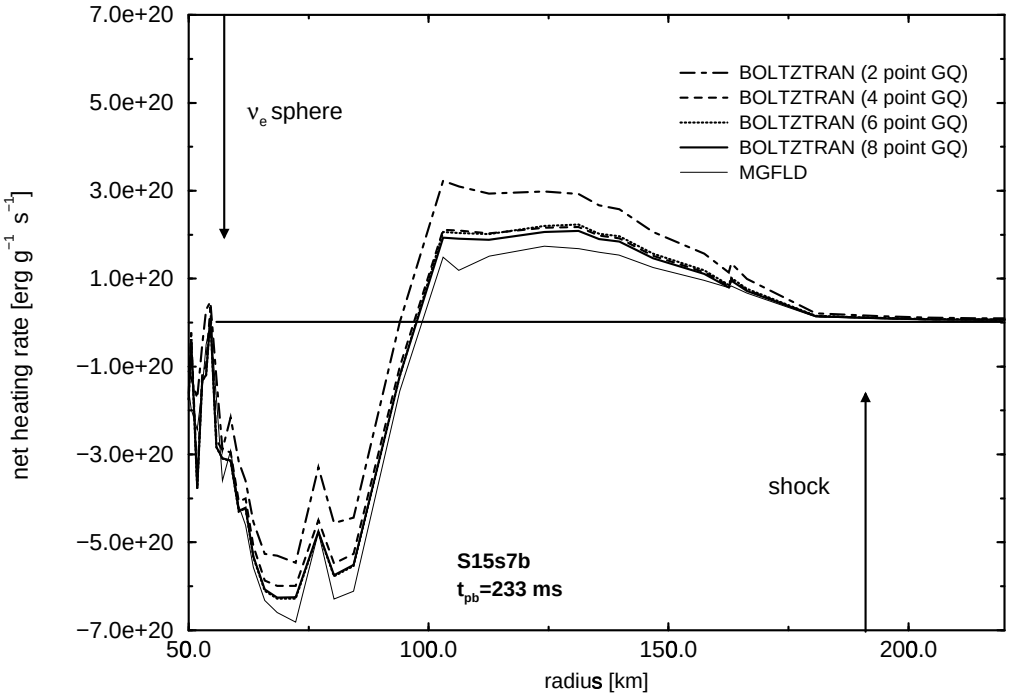

Figure 5.10: Net heating rates for model S15s7b at 233 ms after core bounce.

and were computed using the following formulae:

$$(d\epsilon/dt)_i = c \int E_\nu^3 dE_\nu [\psi_i^0/\lambda_i^{(a)} - j_i(1-\psi_i^0)]/\rho(hc)^3 \tag{5.6}$$

where ϵ is the internal energy per gram; E_ν, ψ_i^0, $\lambda_i^{(a)}$, and j_i are the electron neutrino or antineutrino energy, zeroth angular moment, absorption mean free path, and emissivity, respectively; $i = 1$ corresponds to electron neutrinos, and $i = 2$ corresponds to electron antineutrinos. Only the contributions from neutrino emission and absorption were included: in our models, contributions from neutrino–electron scattering and other processes contribute only a few percent to the neutrino heating rate at and before 233 ms after bounce; they become more important ($\sim$15%) at later times. The (8-point Gaussian quadrature) MGBT simulation yields a net heating rate just above the gain radius that is $\sim$1.3 times the MGFLD rate, and a net cooling rate below the gain radius that is consistently $\sim$0.8 times the MGFLD rate. Comparing the net heating rate to the luminosity sum in Figure 5.5, the extent of the gain region (from 98 km to 180 km) is well correlated with the region between the luminosity maximum and the radius where the luminosity levels off to a constant value (from 101 km to 170 km). Note also that the gain radius is located at a smaller radius for MGBT, and consequently, the size of the net heating region below the shock is somewhat larger.

For (8–point Gaussian quadrature) MGBT and MGFLD, Figure 5.11 shows the net heating curves for S15s7b at an earlier postbounce time, $t_{\rm pb} = 106$ ms.

The region between the neutrinospheres and the shock is a bit smaller: The shock is approximately at the same radius, but the energy-averaged electron neutrinosphere is closer to the shock (at 84 km, versus 58 km for $t_{\rm pb} = 233$ ms). Similar net heating profiles are seen, but the differences between MGBT and MGFLD are even greater. MGBT yields a net heating rate that is $\sim$2 times the MGFLD rate just above the base of the gain region. Again, the cooling rate is

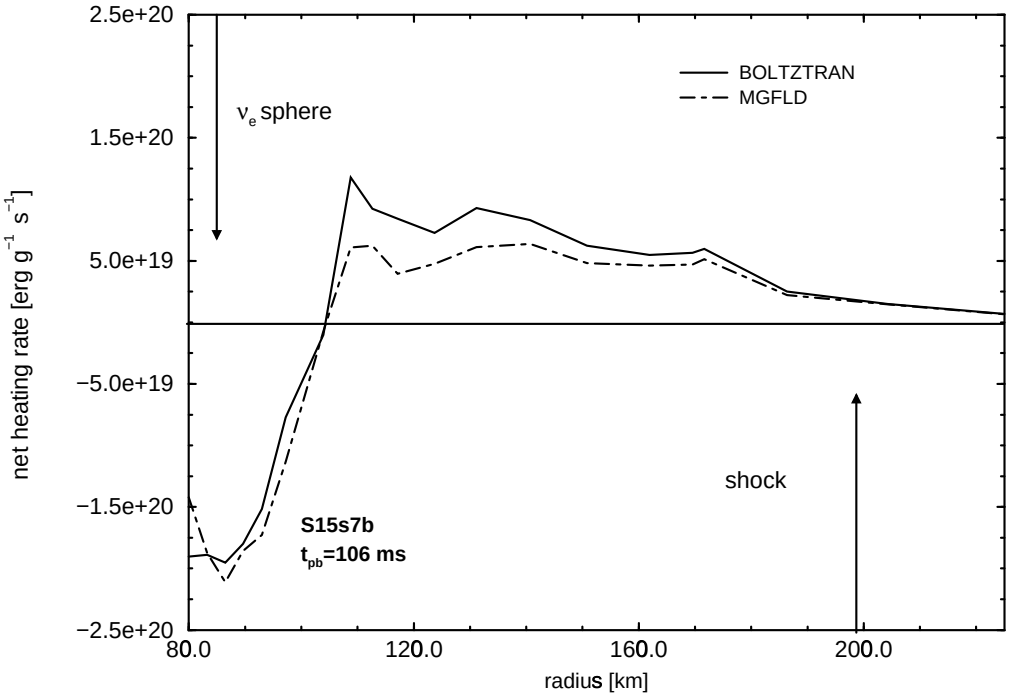

Figure 5.11: Net heating rates for model S15s7b at 106 ms after core bounce.

consistently ∼0.8 times the MGFLD rate below the gain radius. The correlation between the gain region and the region between the luminosity-sum maximum and the point at which the luminosity sum is constant is also quite strong for this time slice. The gain radius (103 km) is just below the luminosity maximum (107 km); also, the luminosity levels off at a radius (173 km) near the upper edge of the gain region (182 km).

Figure 5.12 contains the net heating curves for our 25 $M_\odot$ model at $t_{pb} = 156$ ms. Again, in this case the (8–point Gaussian quadrature) MGBT net heating rate is ∼2 times the MGFLD rate just above the base of the gain region, and the net cooling rate below the gain radius is consistently ∼0.8 times the MGFLD rate. The gain radius (111 km) and the luminosity-sum maximum (108 km) are strongly correlated, as are the radius marking the upper extent of the gain region (180 km) and the radius at which the luminosity sum levels off (170 km). Although the differences in the net heating rate are comparable to those seen in the $t_{pb} = 106$ ms slice for model S15s7b, they occur at a significantly later postbounce time. At a given postbounce time, MGBT provides the greatest enhancement in net heating for larger progenitor masses.

5.4 Summary and Discussion

Comparing three-flavor MGBT and three-flavor MGFLD in postbounce supernova environments, we find that MGBT leads to a significant increase/decrease in the *net* heating/cooling rate, particularly above/below the gain radius. The MGBT net heating rate can be as much as ∼2 times the MGFLD net heating rate above the gain radius, with net cooling rates that are typically ∼0.8 times the MGFLD rate below the gain radius. These differences stem primarily from differences in the neutrino luminosities and mean inverse flux factors; the heating rate is linearly proportional to both these quantities, and differences in both add to produce a significant difference in the net heating rate.

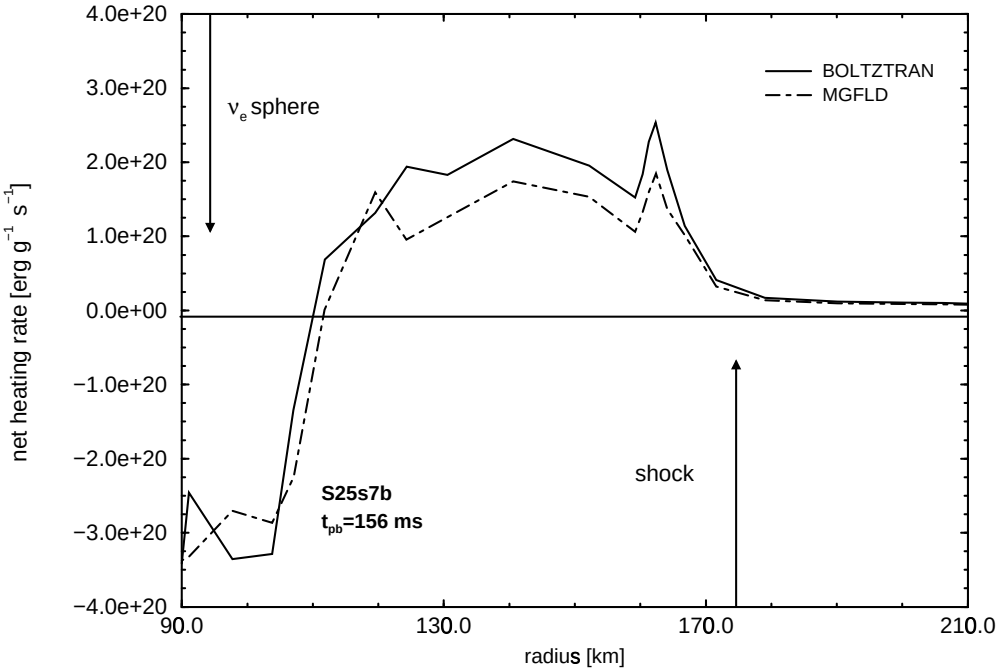

Figure 5.12: Net heating rates for model S25s7b at 156 ms after core bounce.

Table 5.1: Maximum net heating/cooling rates

Progenitor Mass [$M_\odot$]	t_{pb} [ms]	Maximum Net Heating Ratio	Maximum Net Cooling Ratio
15	106	2.0	0.8
	233	1.3	0.8
25	156	2.0	0.8

In Figure 5.13, we plot the sum of the electron neutrino and antineutrino luminosities computed in the MGFLD S15s7b dynamic simulation for several different postbounce times. It is important to note that the total luminosity changes by ∼5–15% between 100 km and 200 km on time scales ∼30 ms. Moreover, the light crossing time between 100 km and 200 km is ∼1/3 ms. Therefore, the neutrino source in our simulations changes on time scales that are two orders of magnitude greater than the time scales on which stationary state is established in this region. This suggests our stationary state results closely reflect what will occur in dynamic simulations.

We also observe that the differences in the net heating rate are greatest at earlier postbounce times for a given progenitor mass, and greater at any given postbounce time for greater progenitor mass. This is illustrated in Table 5.1. The increase in net heating with increased progenitor mass is advantageous because of the slower fall-off in the preshock accretion ram pressure.

These results have at least two important ramifications for the supernova mechanism:

(1) With the dramatic increase in net heating above the gain radius, which is seen in all of our postbounce slices, it may be possible to obtain explosions in one dimension without multidimensional effects such as convection; this will be aided by the decrease in net cooling below the gain radius. It should be noted that our postbounce slices come from full radiation hydrodynamics simulations implementing MGFLD that marginally failed to produce explosions (Bruenn 1993). The marginality of Bruenn's simulations is an important motivating factor in comparing our MGBT results solely with his MGFLD results. All else being equal, increases in

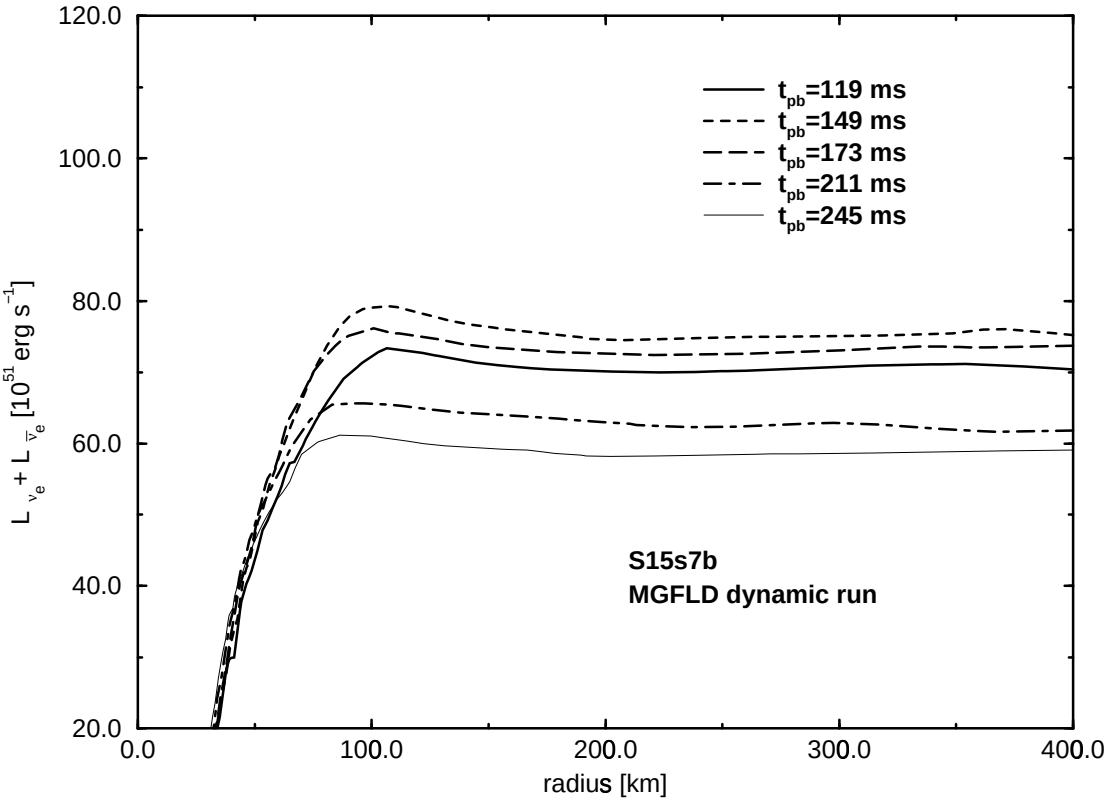

Figure 5.13: The sum of the electron neutrino and antineutrino luminosities from the MGFLD dynamic run for model S15s7b are plotted versus radius. The luminosities from five different postbounce times are shown.

net heating of the magnitude documented here might lead to explosions. However, simulations coupling MGBT and the core hydrodynamics must be carried out in order to compute any feedbacks. Simulations of this type are the subject of the remainder of this work.

(2) With the dramatic increase in net heating occurring near the base of the gain region, we anticipate that MGBT coupled to two-dimensional hydrodynamics will yield more vigorous neutrino-driven convection than was seen in Mezzacappa et al. (1998b), where two-dimensional hydrodynamics was coupled to one-dimensional MGFLD. The combination of increased net heating and more vigorous neutrino-driven convection would be more favorable for shock revival.

Chapter 6

Collapse Simulations of Two $15M_{\odot}$ Progenitor Models

Here we compare core collapse of two very similar $15M_{\odot}$ progenitor models. The inclusion of new electron capture rates in one of the models leads to significant differences in Y_e, but few other differences in pre-collapse structure. The simulations show these initial differences in Y_e are retained until close to core bounce, when they converge. The differences in Y_e are shown to have no dynamic effects, as a shock is formed at the same mass ($\approx 0.64M_{\odot}$) in both models.

6.1 Introduction

The $15M_{\odot}$ model of Woosley & Weaver (1995)(WW95) is a standard progenitor for supernova modeling (Bruenn 1993; Rampp & Janka 2000). Recently, Heger et al. (2000)(HLMW00) have updated this model in a meaningful way. The calculation for the evolution of the WW95 $15M_{\odot}$ model was repeated, except for replacing the weak interaction rates for beta decays and electron

captures. The WW95 model used the electron capture rates of Fuller et al. (1980)(FFN) and older sets of beta decay rates (Mazurek 1973; Hansen 1966). HLMW00 have updated these with a new set of shell model weak interaction rates for electron capture, positron emission, and beta decay. This has increased the electron fraction over much of the core before collapse. Since the size of the homologous core, and, therefore, the shock formation radius, is proportional to the trapped lepton fraction squared ($Y_l{}^2$) at core bounce (Yahil 1983), the initial differences in Y_e might have a discernable effect on the shock energetics. Increasing the Y_e at core bounce would cause the shock to form at a greater radius, allowing it to propogate farther before stalling.

6.2 Pre-collapse Structure

Figure 6.1 plots the original Y_e profiles for both s15s7b2 models, along with the same information for the Nomoto-Hashimoto $15M_\odot$ core (Nomoto & Hashimoto 1988) which will be discussed in Chapter 7. Note that throughout the iron core the difference between the WW95 and HLMW00 Y_e is about 0.1, decreasing slightly to about 0.08 near the edge of the silicon layer. This difference is, in fact, larger throughout most of the profile than the differences between WW95 and the Nomoto-Hashimoto core N15. From 1.1 to 1.2 $M_\odot$, the N15 Y_e is equal to to the WW95 Y_e. This appears to be coincidence, rather than any sort of similarity between the models just at that point. The temperature and density structures of the cores are quite similar, as can be seen in Figures 6.2 and 6.3. The small differences in density and temperature can be partially attributed to the fact that each evolution calculation was not stopped at precisely the same point.

We have performed full radiation hydrodynamic collapse simulations with both progenitors using AGILE-BOLTZTRAN. Both runs used 12 energy groups spanning 5 to 330 MeV to resolve the neutrino spectra and 6-point Gaussian quadrature to resolve the neutrino angles. The

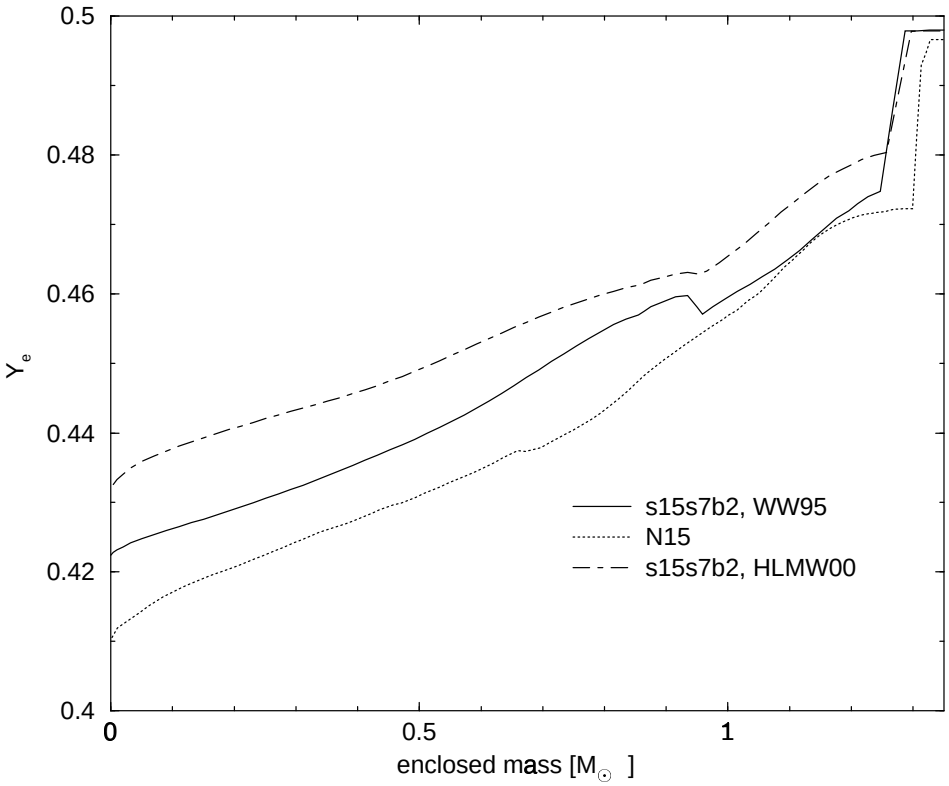

Figure 6.1: Initial Y_e profiles for three different $15M_\odot$ models

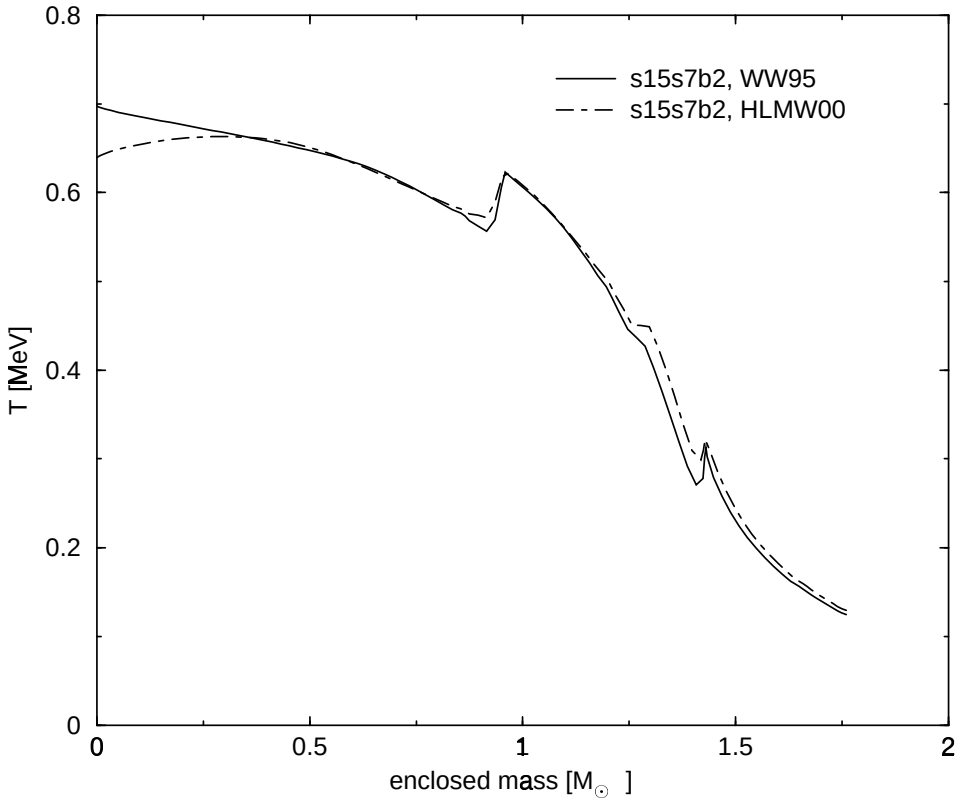

Figure 6.2: Initial temperature profiles for the two Woosley $15M_{\odot}$ models

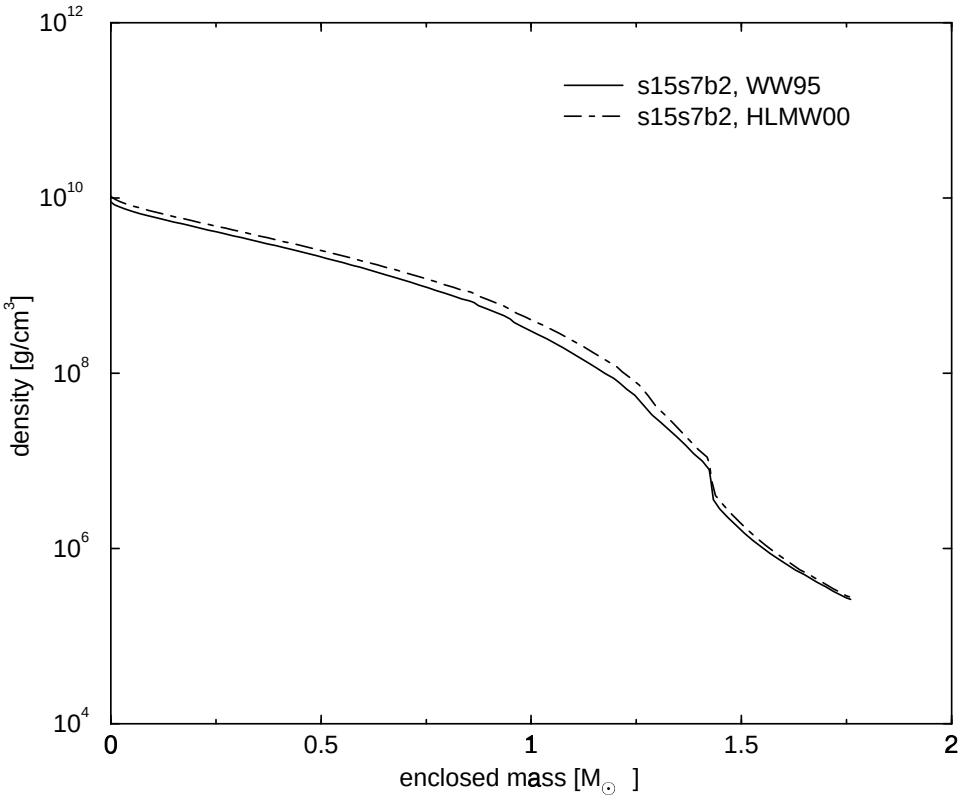

Figure 6.3: Initial density profiles for the two Woosley $15M_{\odot}$ models

equation of state of Lattimer & Swesty (1991) (LS EOS) is used to calculate the thermodynamic state of matter in nuclear statistical equilibrium (NSE). During most of the collapse, the smoothing timescale for movement of the adaptive mesh was set to 0.01 s. This is the representative timescale on which the mesh will adapt to changes in density and velocity. At a central density of 1×10^{14} this timescale was reduced to 1×10^{-4}. The reason for these changes is our prescription for handling nuclear burning as the silicon shell is compressed and heated on infall. For matter initially in the silicon layer, the temperatures are insufficient to achieve NSE. In this region, the radiation and electron components of the LS EOS are used, while an ideal gas of Si is assumed for the nuclear component. For typical hydrodynamic timesteps ($\sim$ .1 millisecond), silicon burning occurs within a single timestep for T $\sim 5GK$ (Hix & Thielemann 1999). Therefore, when a fluid element exceeds a temperature of 5 GK in our simulation, the silicon is instantaneously burned, achieving NSE and releasing thermal energy equal to the difference in nuclear binding energy between Si and the composition determined by the LS EOS. This "flashing" can introduce numerical problems for the adaptive grid for certain pre-collapse temperature structures. As grid points beyond the flashing radius move in during core collapse, zones are "deflashed" to conserve energy. This energy is restored when the entire zone is inside the flashing radius. If the temperature has been reduced too much by deflashing, the EOS is unable to converge when the flashing energy is introduced. We ensure that grid points initially well in the silicon layer at the onset of collapse are not flashed to NSE until after bounce by increasing the grid timescale as described above.

6.3 Results

Considering the magnitude of the differences in Y_e, the subsequent evolution of the cores is surprising. Looking at Figure 6.4, where we plot Y_e profiles at central densities of 1×10^{11}

and $1 \times 10^{12} g/cm^3$, we note the two cores are already beginning to converge to the same Y_e profile inside $1 M_\odot$ by the time a central density of $1 \times 10^{11} g/cm^3$ is reached. The convergence is complete inside $1 M_\odot$ by the time a central density of $10^{13} g/cm^3$ is reached. Examining Figure 6.5, the Y_e profiles at central densities of 1×10^{13} and $2.96 \times 10^{14} g/cm^3$(the central density at core bounce) are indistinguishable.

This convergence in core structure is even more striking when the velocity profiles are examined. Figure 6.6 shows the velocity profiles for central densities of 1×10^{11} and $1 \times 10^{12} g/cm^3$. The velocity structure of the homologous core is identical for both models by the time a central density of $1 \times 10^{11} g/cm^3$ is reached. Note the outer parts of both cores retain much of their original velocity structure.

In Figure 6.7 we plot the velocity profiles for central densities of 1×10^{13} and $2.96 \times 10^{14} g/cm^3$. The bounce shock is launched at precisely the same point in mass in both models. The subsequent evolution of both models will be identical if the density and temperature profiles have also remained identical throughout collapse. We see that this is the case in Figures 6.8 and 6.9, where the density and temperature profiles are plotted for each each central density described in Figures 6.6 and 6.7.

The initial differences in Y_e structure have been erased, and any impact naively expected on core evolution is not seen.

6.4 Trapping, Equilibration, and Core Convergence

To understand why and how the initial Y_e differences make no difference in core evolution, we examine the Y_e evolution of several mass elements during collapse. Figure 6.10 shows the evolution of Y_e, the electron neutrino fraction (Y_ν), and the total lepton fraction (Y_l) for the mass element at 0.05 $M_\odot$ as a function of density reached by the element. Several distinct periods of

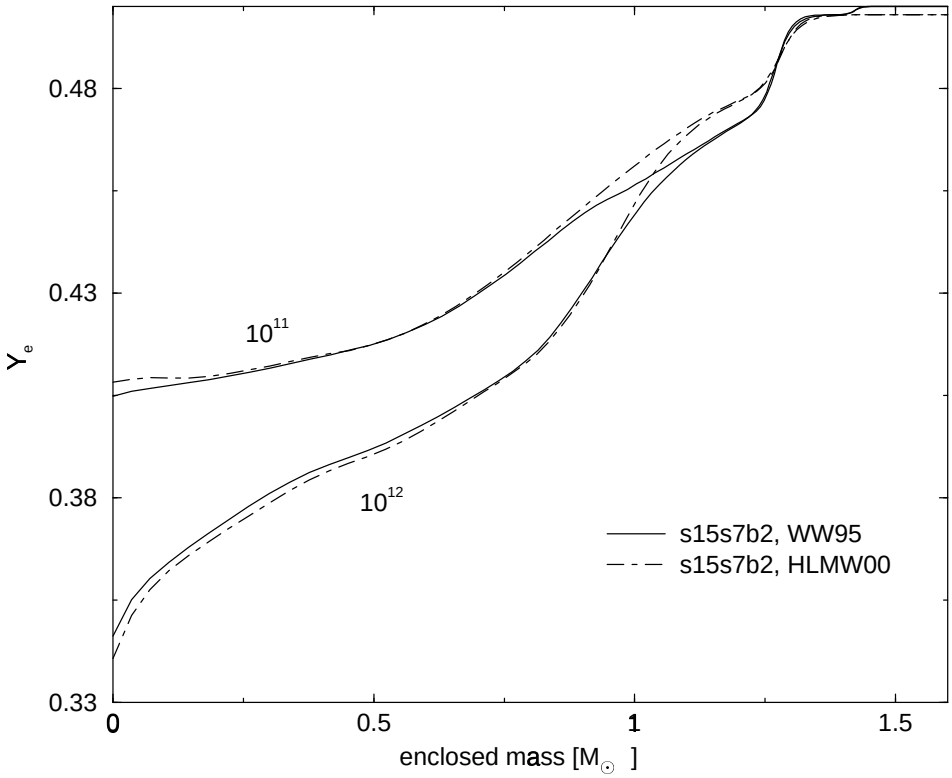

Figure 6.4: Y_e profiles for central densities of 1×10^{11} and $1 \times 10^{12} g/cm^3$

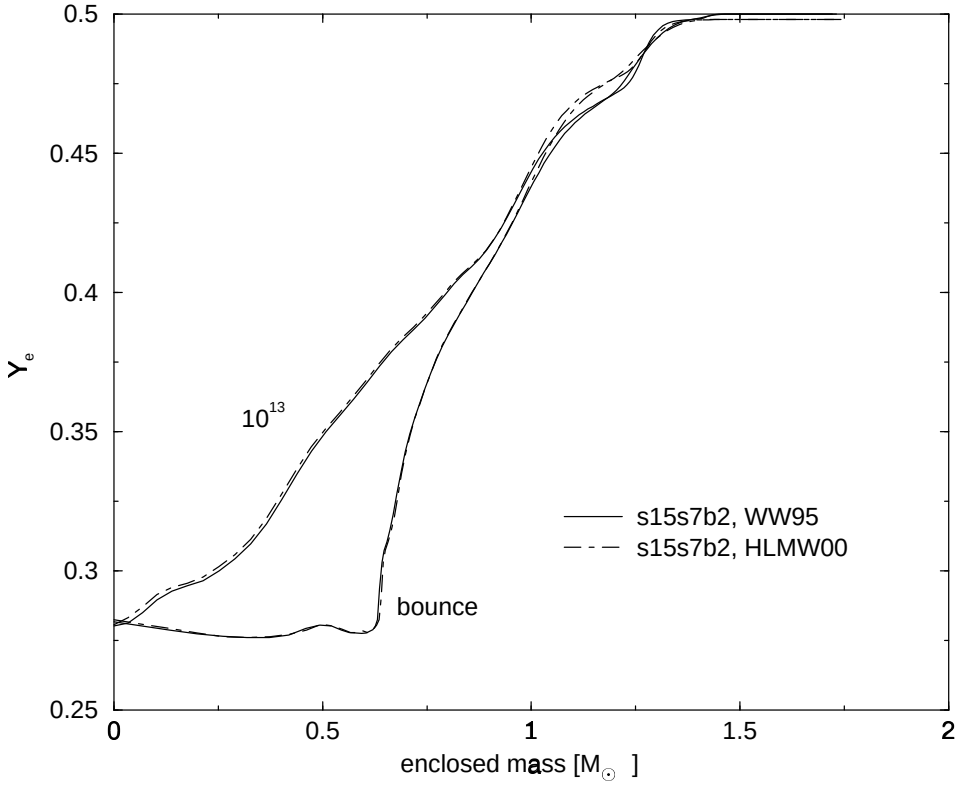

Figure 6.5: Y_e profiles for central densities of 1×10^{13} and $2.96 \times 10^{14} g/cm^3$

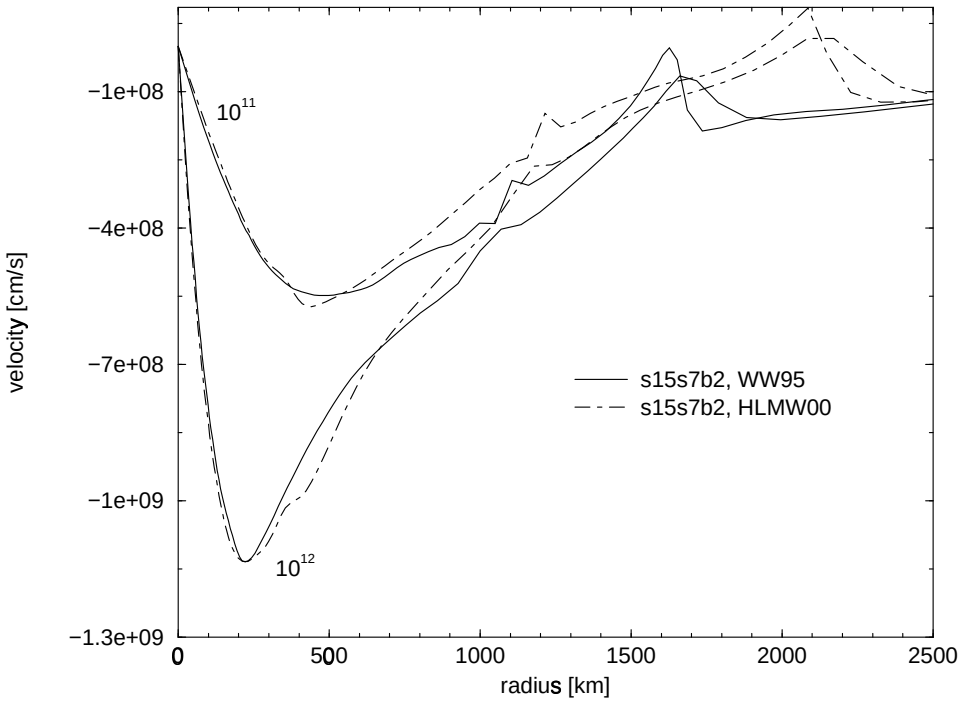

Figure 6.6: Velocity profiles for central densities of 1×10^{11} and $1 \times 10^{12} g/cm^3$

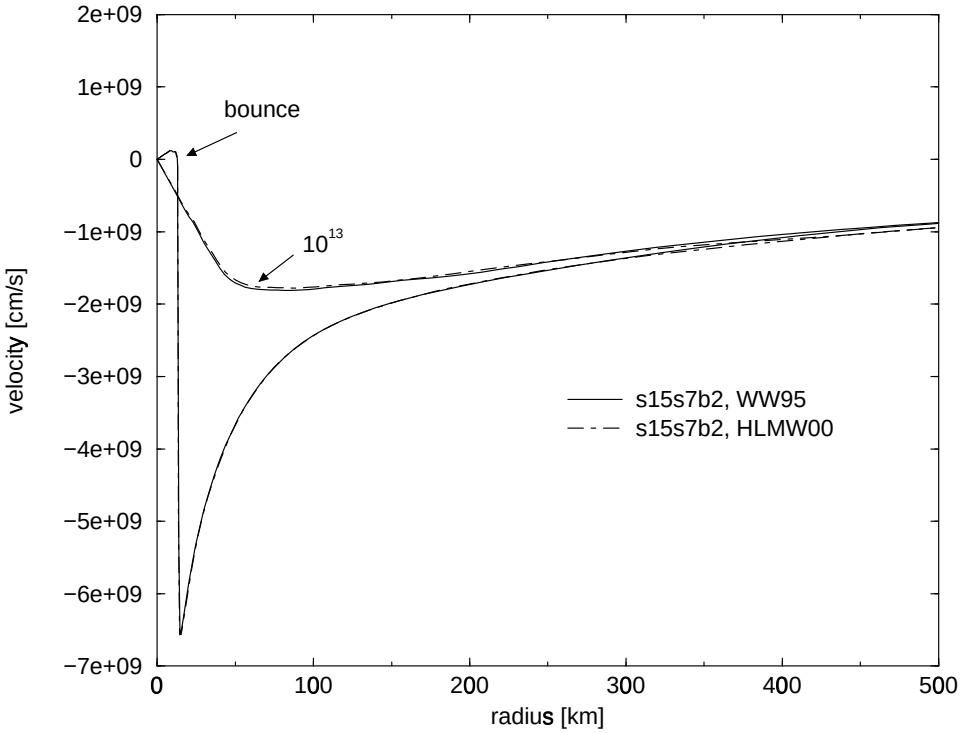

Figure 6.7: Velocity profiles for central densities of 1×10^{13} and $2.96 \times 10^{14} g/cm^3$

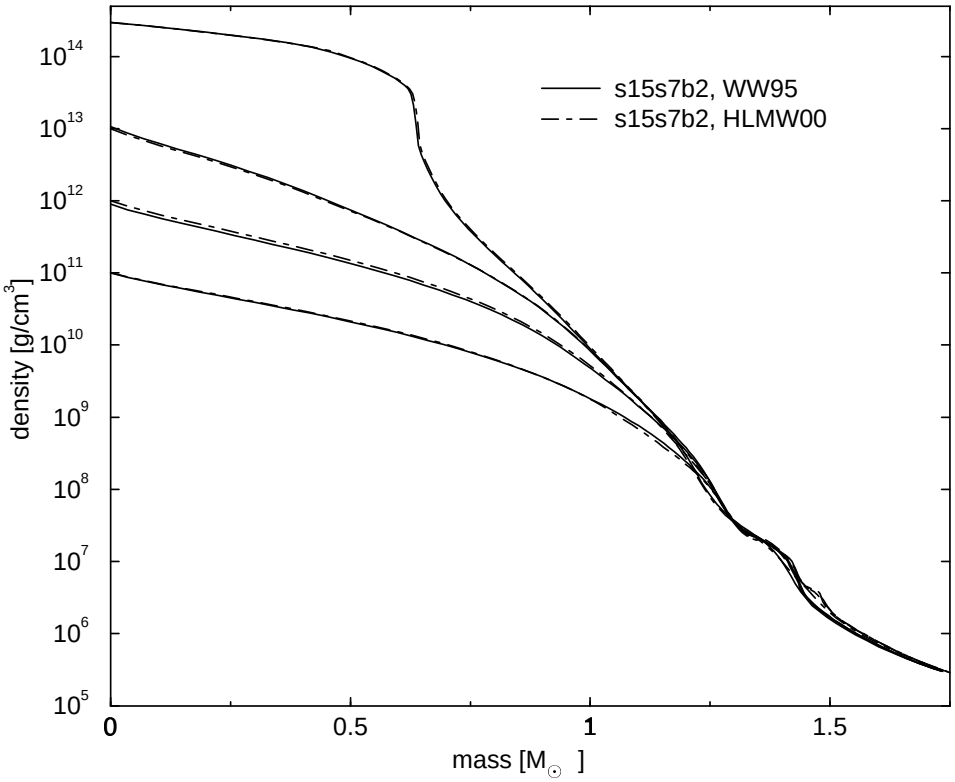

Figure 6.8: Density profiles for central densities of 1×10^{11} – $2.96 \times 10^{14} g/cm^3$

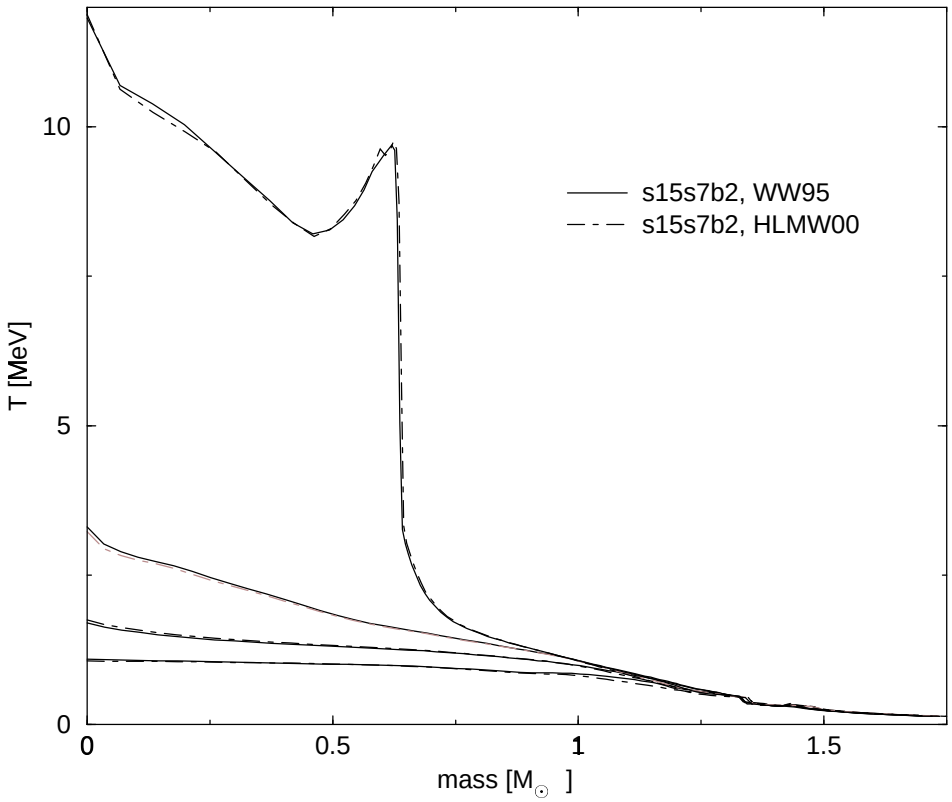

Figure 6.9: Temperature profiles for central densities of 1×10^{11} – $2.96 \times 10^{14} g/cm^3$

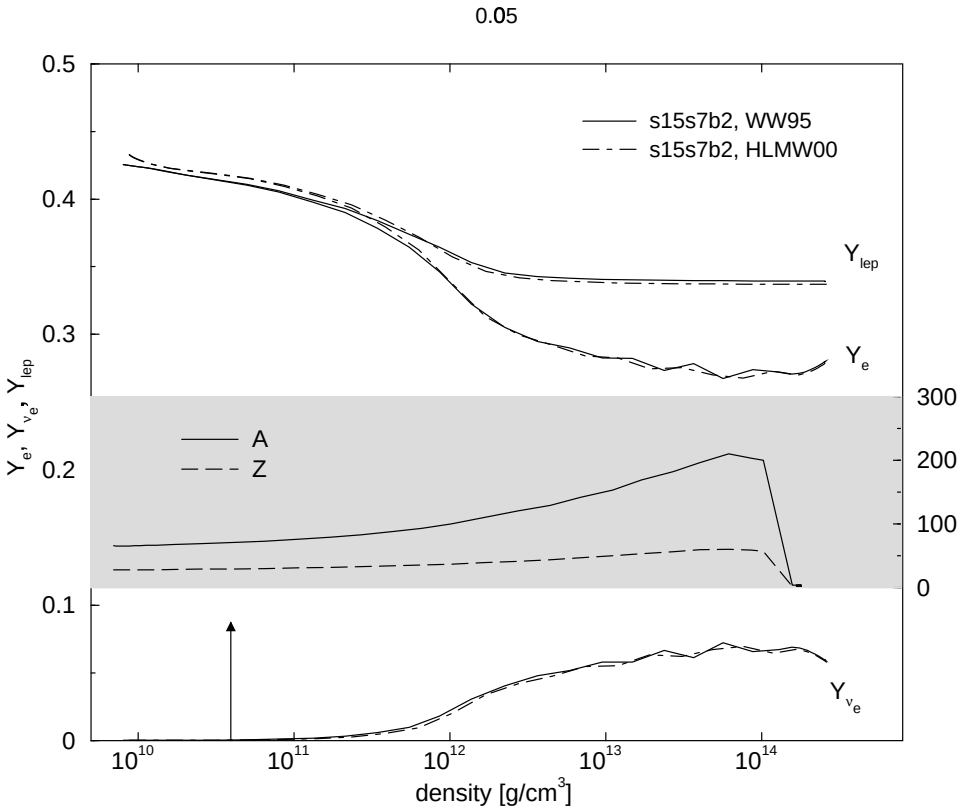

Figure 6.10: Lepton fractions as a function of density for mass element at $0.05 M_{\odot}$ with representative A and Z from the LS EOS

evolution are evident in this figure. Until the mass element reaches a density of $3 \times 10^{10} g/cm^3$ the electron capture rate is dominated by capture on nuclei. However, this capture rate turns off at $3 \times 10^{10} g/cm^3$. This density is marked with an arrow in the figure. At this density and above, the representative nucleus returned by the EOS has $N > 40$, eliminating the absorption rate on nuclei (see equation 2.23). Inset is the evolution of the representative A and Z returned by the EOS.

The total rate of electron capture begins to increase from $3 \times 10^{10} g/cm^3$ as the Y_e for both models starts to drop. The ΔY_e between the models remains roughly constant until neutrino trapping begins at roughly $5 \times 10^{11} g/cm^3$. At $1 \times 10^{12} g/cm^3$, neutrino trapping is complete: Y_l becomes constant, as the total number of leptons in the mass element remains the same from that point on. The individual Y_e have converged at this density ($\Delta Y_e \longrightarrow 0$). Y_l has become the independent variable determing the state of the mass element. From this point until bounce occurs, the neutrino and electrons establish an equilibrium. Much of the noise in Y_e and Y_ν after trapping is numerical, as the massive electron capture and neutrino absorption rates attempt to cancel each other. The accurate cancellation of these rates is very difficult to reproduce numerically. In an average sense, allowing for the numerical noise, Y_e becomes constant after about $5 \times 10^{13} g/cm^3$. At equilibrium, the electron capture and neutrino absorption rates are related to one another through detailed balance, and the final Y_e becomes a function of the local temperature and density through the electron chemical potential. Since the temperature and density profiles differ very little between both models, it is not surprising that each settles to the same equilibrium Y_e. This phenomenon is an extension of core convergence in pre-collapse models (e.g. see Burrows (1990)). Degenerate pre-collapse cores become unstable at roughly the same Chandrasehkar mass, regardless of the mass of the progenitor star, modulo large Y_e or entropy differences. Here we see that Y_e differences too small to have a meaningful effect on the

density and temperature evolution of the core result in homologous core masses that are roughly equal. We will see in Chapters 7 and 8 that, given our choice of microphysics and transport algorithm, core collapse is alarmingly similar for a range of progenitors. The homologous core mass and final Y_e for both these Woosley models are very similar to the values found for the Nomoto-Hashimoto $15M_\odot$ *and* $20M_\odot$ models.

Figure 6.11 shows the lepton fraction evolution for a mass shell at $0.64M_\odot$ as a function of density. As in Figure 6.10, the representative A and Z from the EOS are inset, also plotted as a function of density. This mass element displays the same behavior as the element at $0.05M_\odot$, but an equilibrium between Y_e and Y_ν is never reached. The final density at core bounce is somewhat less than $6 \times 10^{13} g/cm^3$, barely exceeding the observed equilibrium density for the deeper mass element. The rapid rise of electron capture at $\approx 3 \times 10^{10} g/cm^3$ is evident as in the $0.05M_\odot$ plot. Complete trapping at $\approx 5 \times 10^{12} g/cm^3$, marked by the constancy of Y_l, is also noted.

A different scenario is evident in Figure 6.12, where we plot the lepton fractions for a mass element at $1.0M_\odot$ as a function of density. Y_ν is not shown on this plot because of the scale. Y_ν is much smaller for this trajectory than in the $0.05M_\odot$ and $0.64M_\odot$ cases. This element does not experience the wide range in density found in the elements at $0.05M_\odot$ and $0.64M_\odot$. Neutrino absorption on nuclei is never turned off, as the maximum density reached in the element is $\approx 1.5 \times 10^{10} g/cm^3$. This is evident by looking at the inset plot of A and Z as well. A never exceeds 65. The initial ΔY_e is maintained until about $5 \times 10^9 g/cm^3$ in this plot. After this Y_e for the two models converge somewhat, as neutrino trapping begins to occur, but only from an initial difference of 1.3% to one of 0.5% at bounce. Y_l increases steadily, as neutrinos are locally produced and transported from below. Note the turns at the end of each trajectory. This mass element gets turned around by core bounce and rebound, reversing its trend in density as it is

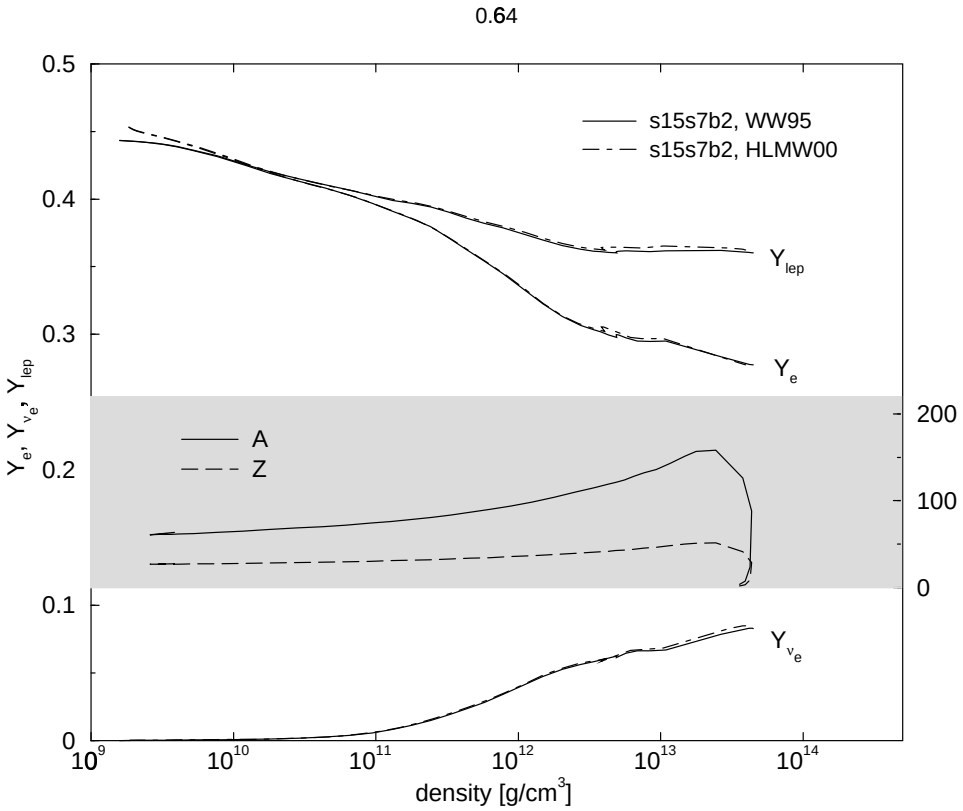

Figure 6.11: Lepton fractions as a function of density for mass element at $0.64 M_{\odot}$ with representative A and Z from the LS EOS

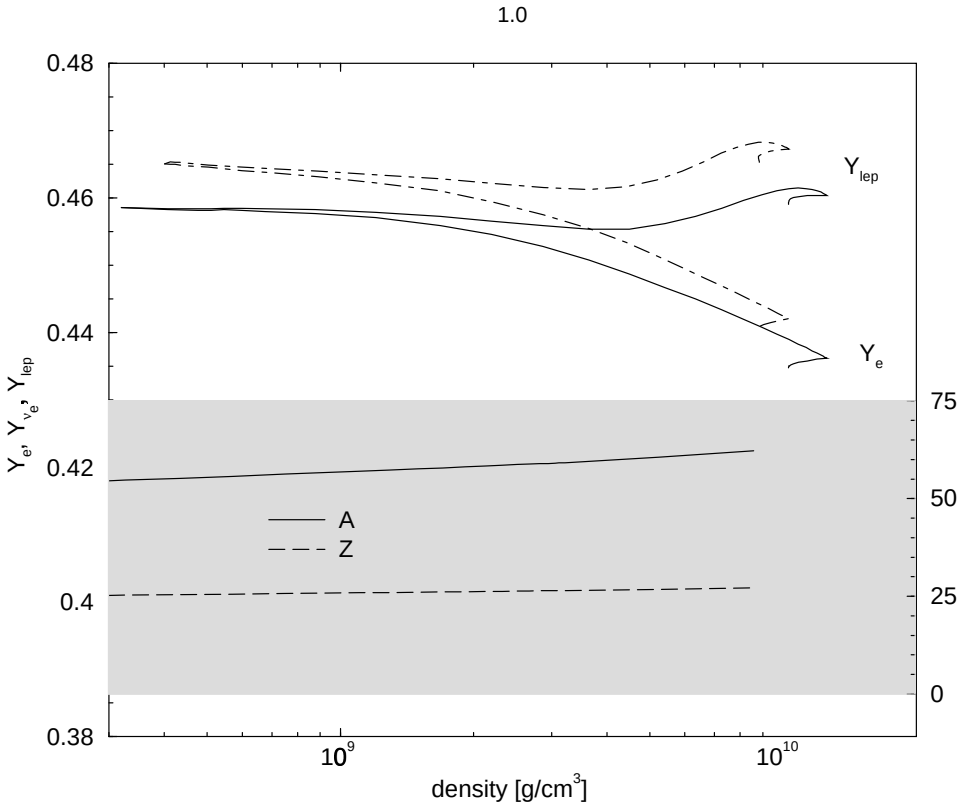

Figure 6.12: Lepton fractions as a function of density for mass element at $1.0M_{\odot}$ with representative A and Z from the LS EOS

pushed out. The results for this element are typical for all the mass elements outside of $1.0 M_{\odot}$, where the eventual mass cut for an explosion might occur. Consequently, the nucleosynthetic signature of the two models might be quite different, as the ejected material in each case will have a different Y_e. Small ($\approx 1\%$) differences in Y_e can have profound effects on the nucleosythesis properties of the ejecta.

Chapter 7

The Nomoto-Hashimoto 15 $M_\odot$ Simulation

This chapter describes the simulation of core collapse, bounce, shock propogation and stagnation of the core of a $15M_\odot$ progenitor star (Nomoto & Hashimoto 1988).

7.1 Introduction

We begin with the core of the 15 $M_\odot$ model of Nomoto & Hashimoto (1988) out to 1.343 $M_\odot$ and a radius of 1409 km. The core is divided into 99 zones in radius which are adaptive and move in mass coordinates based on changes in density and velocity (see Liebendörfer (2000)). Twelve geometrically spaced energy groups spanning the range from 5 to 330 MeV are used to resolve neutrino energies and 6–point Gaussian quadrature is used to resolve the neutrino directions relative to the outgoing radial direction. The simulation includes coupled evolution of the hydrodynamics and transport of all three flavors of neutrinos and their associated antineutrinos.

Emission, absorption, and scattering on nuclei and free nucleons, neutrino-electron scattering, and pair creation and annihilation processes are included. As in the simulations described in Chapter 6, the adaptive grid timescale was initially set to 0.01 s. After a central density of 1×10^{14} was reached, this timescale was reduced to 1×10^{-4} s. The initial conditions are displayed in Figure 7.1.

7.2 Results

Trajectories of equal mass shells are shown in Figure 7.2 for the duration of the run. The upper line accross the plot marks the boundary between NSE and silicon throughout the simulation. The lower, heavy line marks the shock position. The shock is launched at 0.587 $M_{\odot}$ ($\approx$ 12 km) and propagates out to a radius of 195 km. It subsequently recedes throughout the remainder of the simulation and sits at 118 km at the end of the run. No explosion occurs.

The boundary between NSE and silicon (see Chapter 6) is determined at the beginning of the simulation and is updated throughout the run. If the temperature of a mass element exceeds the flashing temperature (0.44 MeV), the NSE-silicon bounadry is moved to the outer edge of that zone. Therefore, the position of the NSE front changes discountinously in mass. This behavior is evident in Figure 7.2 from $\approx$50 ms through $\approx$70 ms, where the NSE front moves outward in two discrete steps. Its position in mass remains constant after these adjustments. AGILE-BOLTZTRAN employs an advection boundary condition to keep the radial domain approximately constant throughout the simulation. This prescription advects mass onto the grid, one shell at a time, at a constant density when the outermost radial zone falls inside 2000 km. Our method for handling the transition to NSE allows us to include only the iron core and silicon layer on our initial computational grid. Only the first few zones of the silicon layer in the initial model were retained at the start of the run, resulting in a computational domain that

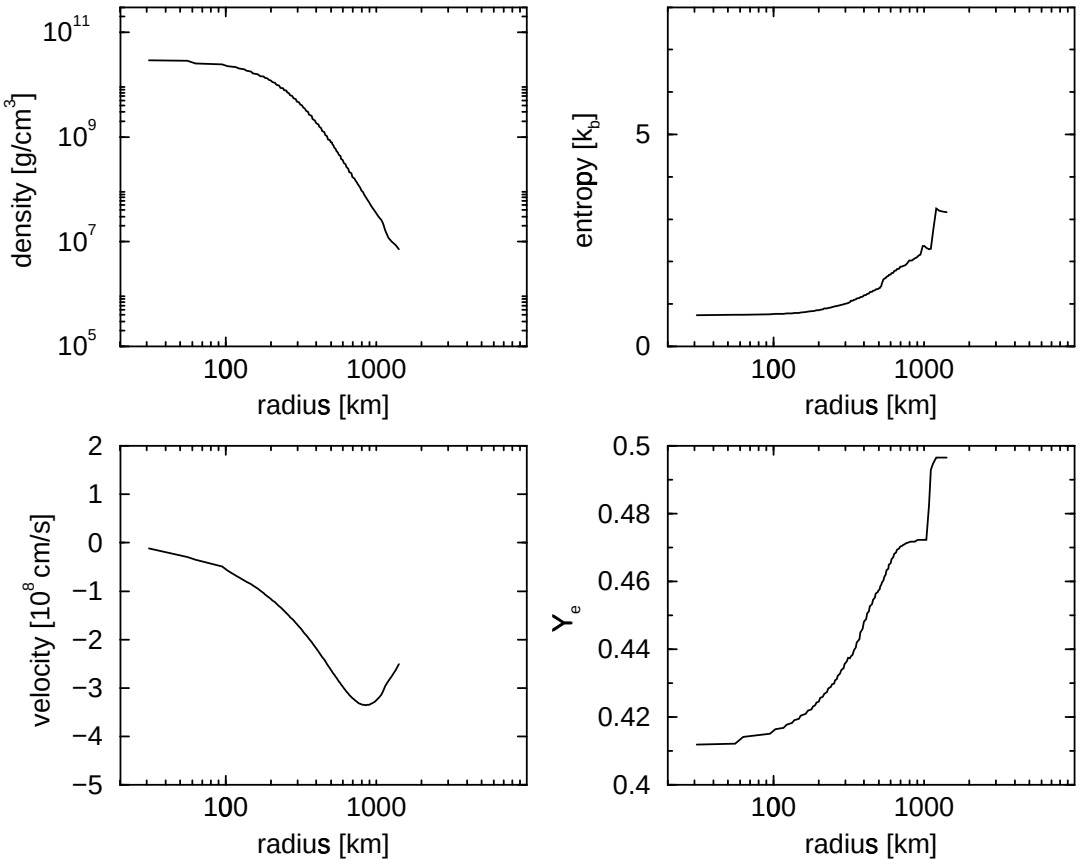

Figure 7.1: Initial conditions for the Nomoto-Hashimoto $15M_\odot$ model

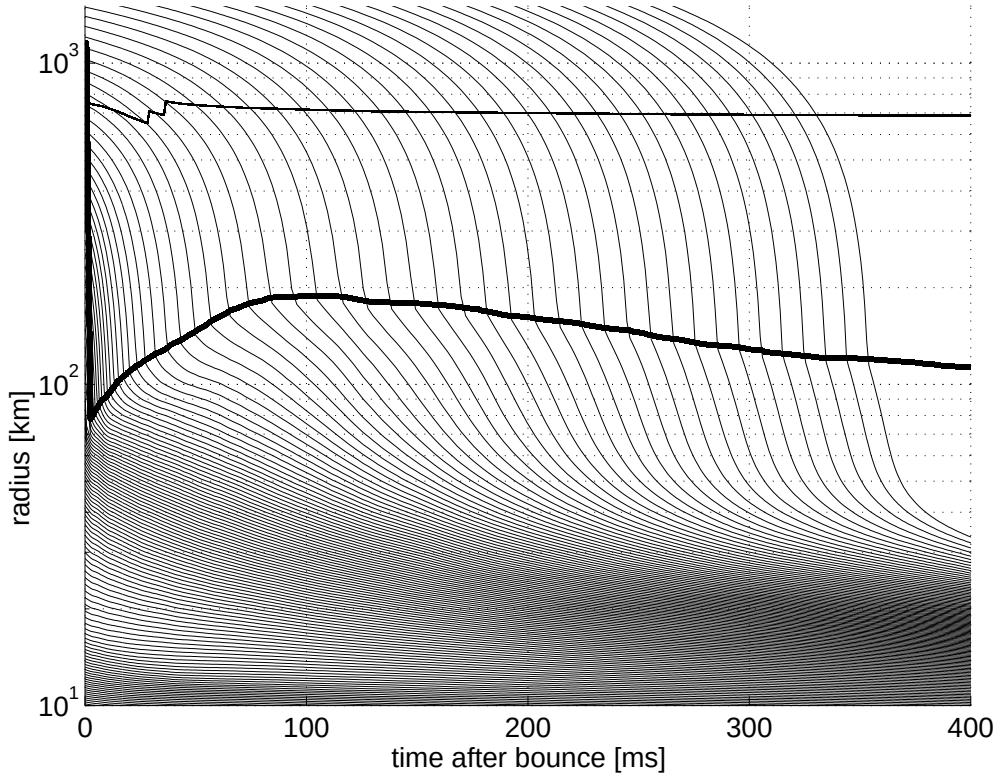

Figure 7.2: Radial trajectories of equal mass shells for the Nomoto-Hashimoto $15M_\odot$ model

extended just beyond 2000 km, causing the almost immmediate introduction of the advection boundary condition. The first of the artificially introduced mass elements has impacted the shock at $\approx$ 150 ms. The simulation was continued for another 350 ms, although the constant density inflow is pessimistic for shock revival. Future development of the code will include more realistic prescriptions for handling nuclear burning, enabling us to retain zones in the initial model out to the oxygen shell and, perhaps, beyond.

Figures 7.3 through 7.6 display the evolution of density, entropy, electron fraction, and velocity at various central densities during collapse. The movement of the inner radial edge of the grid is evident in all the plots, as the innermost radius plotted decreases with increasing central density. The edge of the iron shell is evident in Figure 7.4 as the sharp increase in entropy at about 1000 km. The core deleptonizes to a central Y_e of 0.276 at bounce. Core bounce occurs at 67.4 ms after the onset of collapse at a central density of $3.08 \times 10^{14} g/cm^3$. The density at the shock formation radius is $6.20 \times 10^{13} g/cm^3$. The location of shock formation is evident in the entropy, velocity, and electron fraction plots, where each of these quantites has a sharp discontinuity at 12 km.

The shock begins to propagate outward, encountering the electron antineutrino and mu/tau neutrinospheres $\approx$ 1 ms after bounce, and the electron neutrinosphere $\approx$ 2.6 ms after bounce. In Figure 7.7 the neutrino luminosities at 1000 km are plotted versus time. As the shock passes the neutrinospheres, matter below neutrino trapping densities is heated and the neutrino luminosities increase markedly as the copiously produced neutrinos are allowed to escape. The rise in electron antineutrino and mu/tau neutrino luminosities is apparent, as is the electron neutrino luminosity burst as the shock "breaks out." The rise in electron antineutrino luminosity is noticeably slower than the abrupt increase in electron luminosity. This is primarily due to the degeneracy of the electrons. The large electron chemical potential implies a large negative

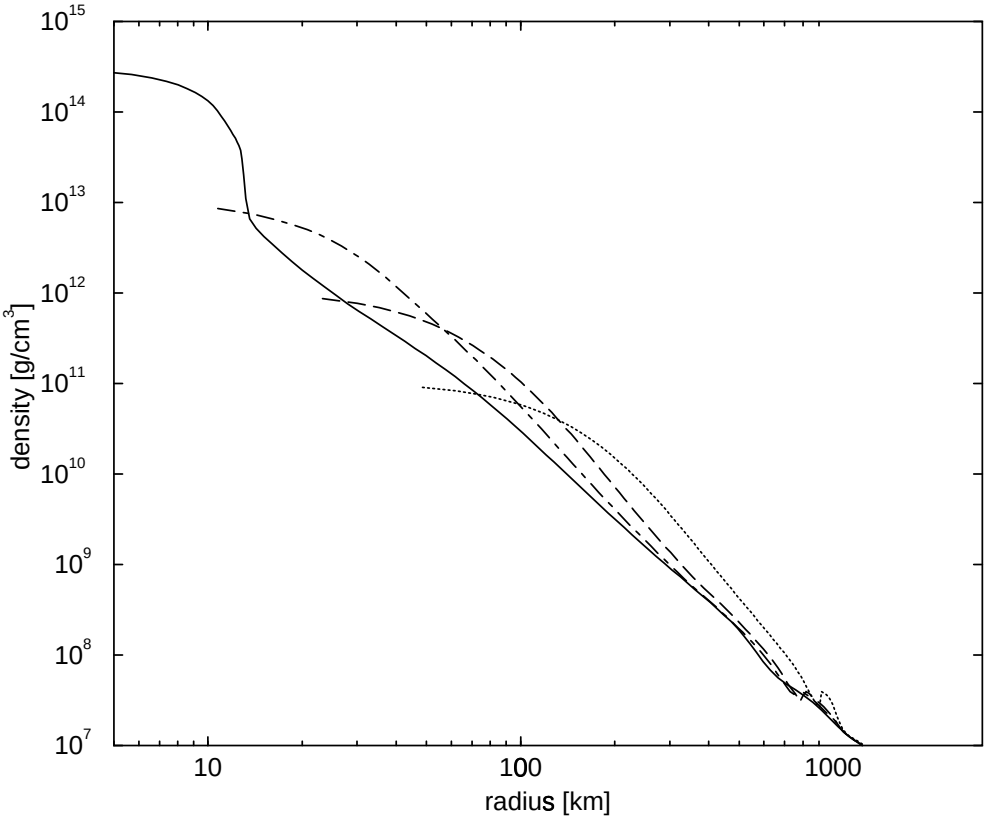

Figure 7.3: Density profiles at various central densities during collapse of the Nomoto-Hashimoto $15M_\odot$ model

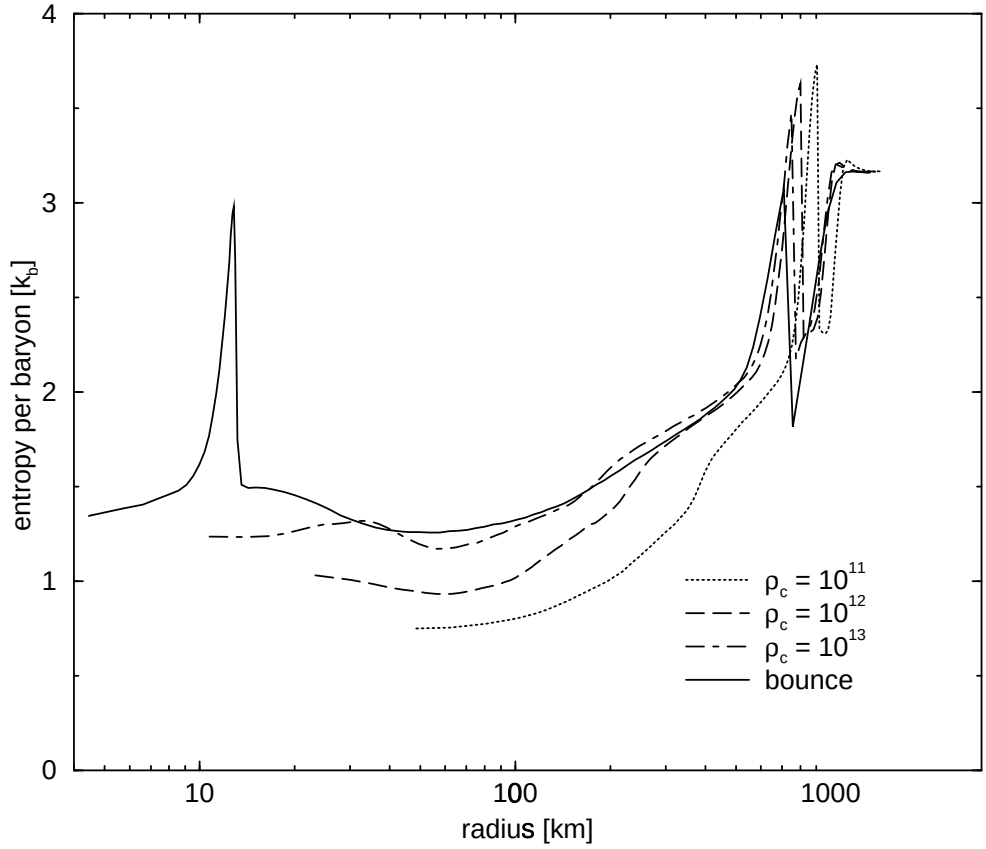

Figure 7.4: Entropy profiles at various central densities during collapse of the Nomoto-Hashimoto $15M_{\odot}$ model

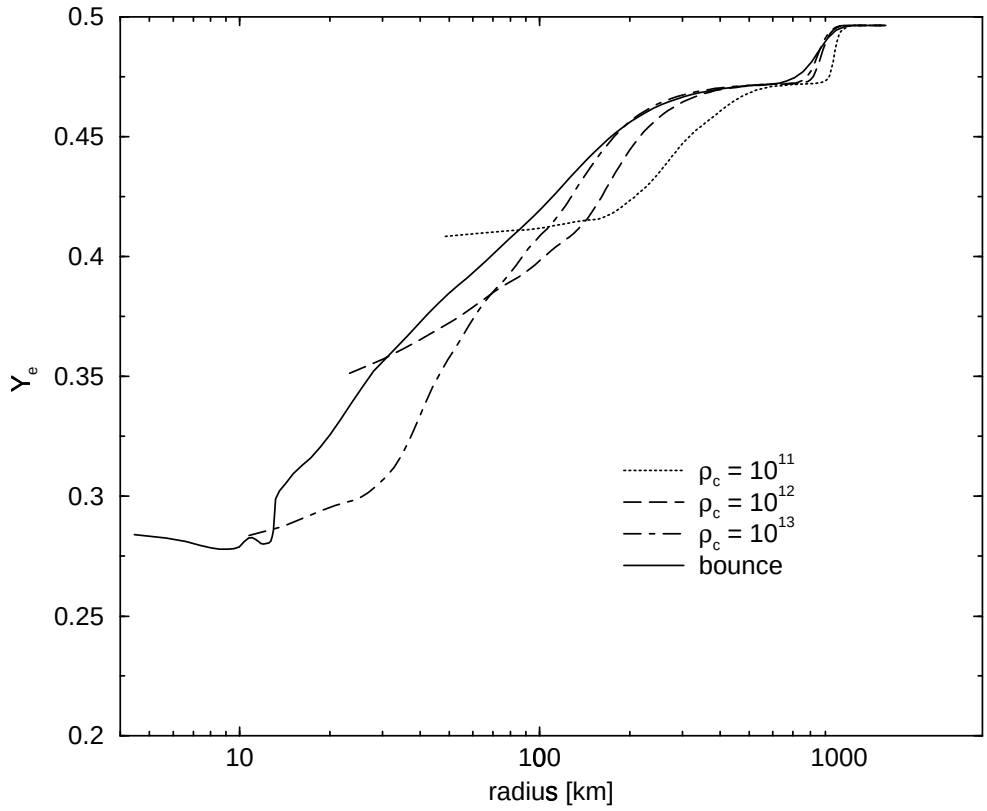

Figure 7.5: Y_e profiles at various central densities during collapse of the Nomoto-Hashimoto $15M_\odot$ model

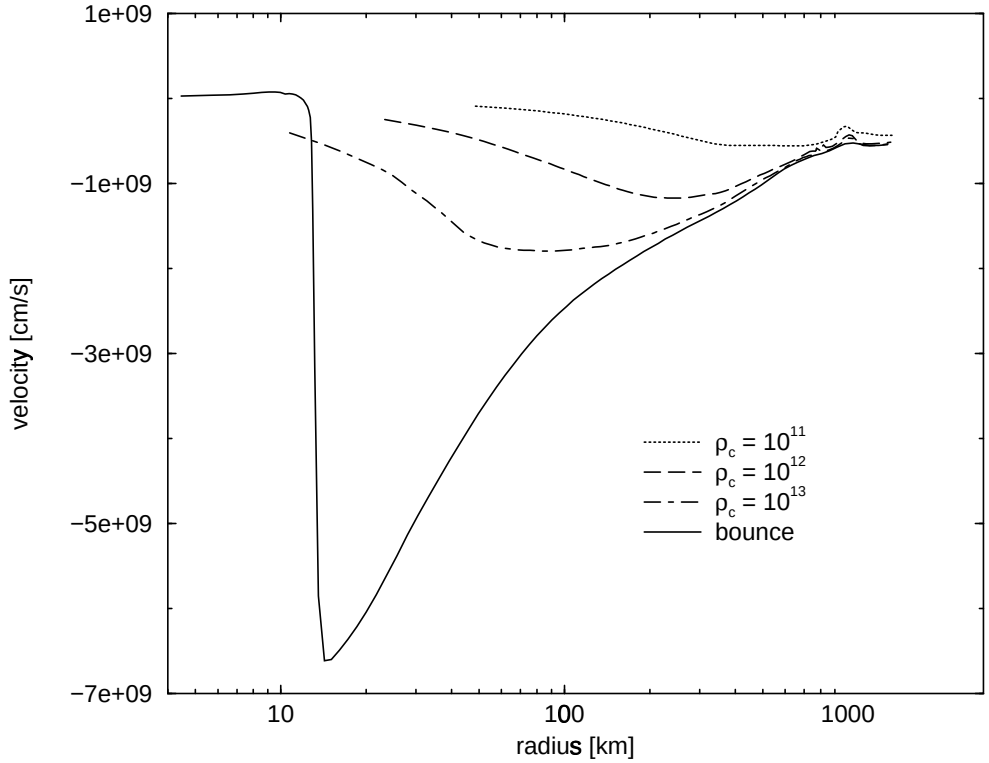

Figure 7.6: Velocity profiles at various central densities during collapse of the Nomoto-Hashimoto $15M_{\odot}$ model

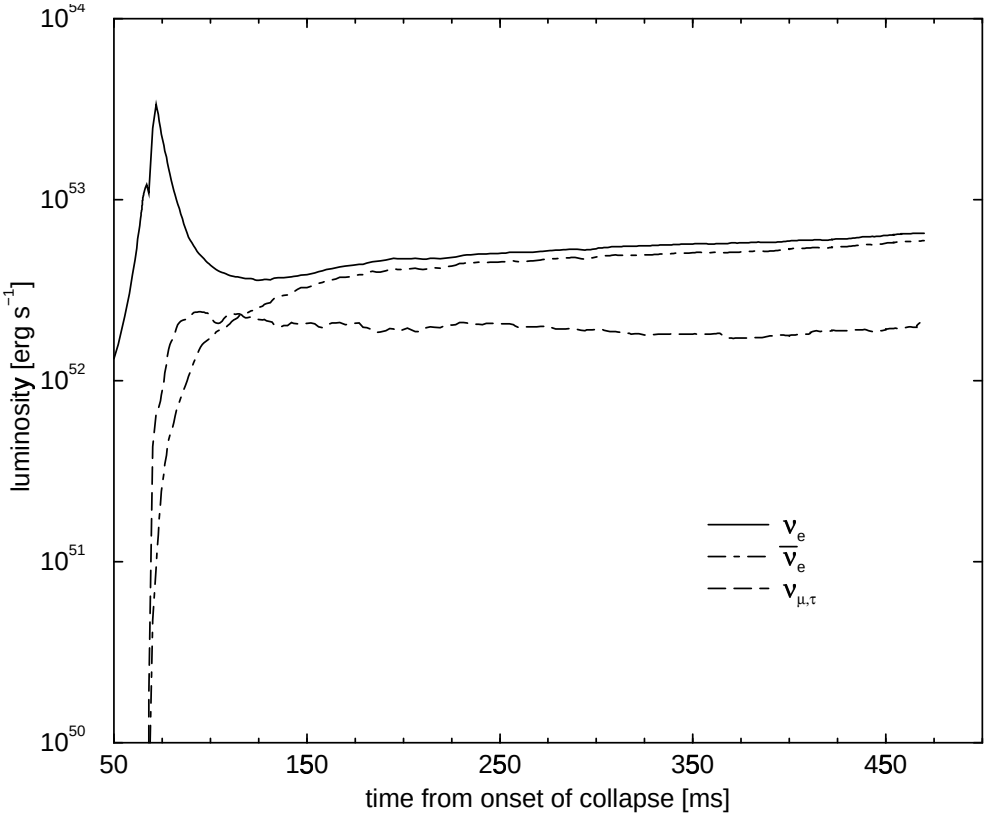

Figure 7.7: Neutrino luminosities at 1000 km as a function of time since the onset of collapse for the Nomoto-Hashimoto $15M_\odot$ model

positron chemical potential, which serves to suppress the production of electron antineutrinos through positron absorption. Of less importance is the effect of electron neutrino degeneracy at shock breakout. The large chemical potential of the electron neutrinos suppresses the production of electron antineutrinos via pair processes (Myra & Burrows 1990; Herant et al. 1994). The mu/tau neutrino luminosity is not affected by degeneracy and exhibits a sharper increase than the electron antineutrino luminosity. The RMS energies of the neutrinos are plotted versus time in Figure 7.8. The canonical hierarchy of energies for each flavor is apparent after bounce. The mu/tau neutrinos have the highest RMS energies. Their mean free paths in the matter are longer than the electron flavor neutrinos because the mu/tau neutrinos participate only in neutral current interactions. The core becomes transparent sooner for the mu/tau neutrinos at a depth with higher temperature. The neutron richness of the core reduces the absorption opacity for the electron antineutrinos. Therefore, they also decouple from the matter at a slightly higher temperature than the electron neutrinos, but lower than the decoupling temperature for mu/tau neutrinos. Examining Figure 7.7, we observe the neutrino luminosities increase slightly with time. The constant density inflow does not allow the mass accretion rate to decline. Rather, the increasing velocities at constant density increase the mass accretion rate. Accretion on the PNS is powering the late-time neutrino emission, so the flux actually increases with time. Increasing RMS energies are also seen in 7.8, as the neutrinospheres recede along with the shock. The increasing temperatures, as the neutrinospheres drop to lower radii, hardens the neutrino spectra. This increase in mean neutrino energy coupled with the increasing neutrino flux resulting from the imposed accretion rate produces the overall increase in luminosity seen in Figure 7.7.

Figures 7.9 through 7.17 display density, entropy, velocity, and electron fraction profiles for several postbouce times. Comparing 7.9 and 7.10, we clearly see the effects of shock breakout.

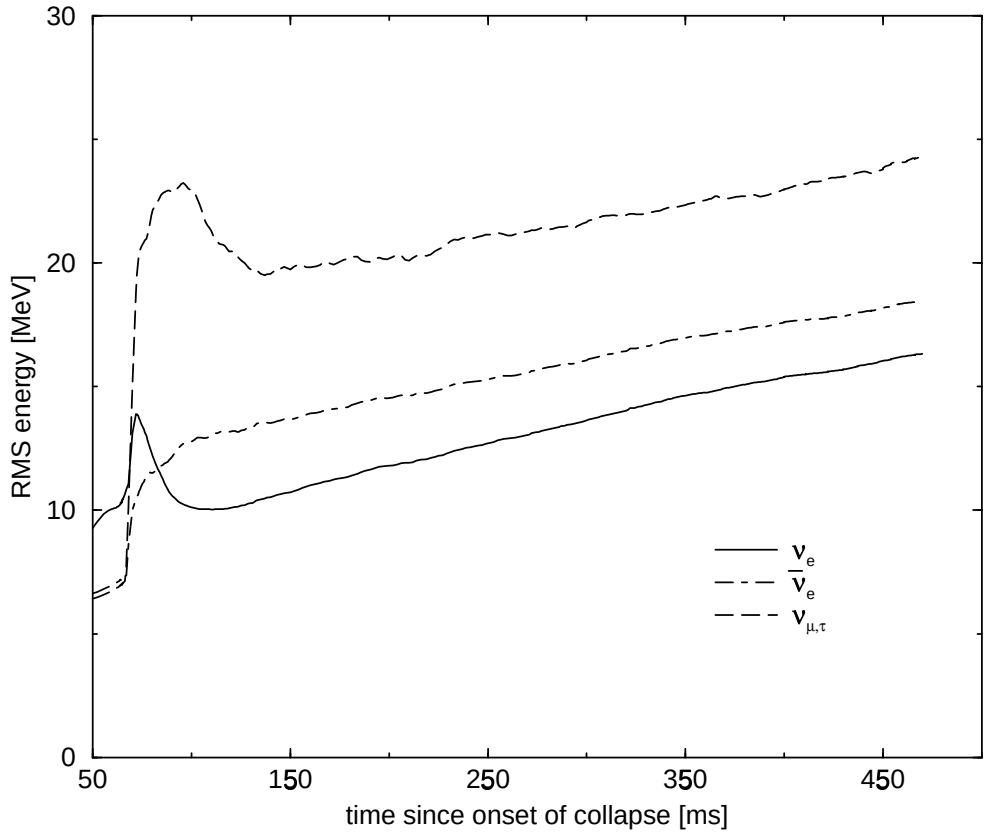

Figure 7.8: Neutrino RMS energies at 1000 km as a function of time since the onset of collapse for the Nomoto-Hashimoto $15M_\odot$ model

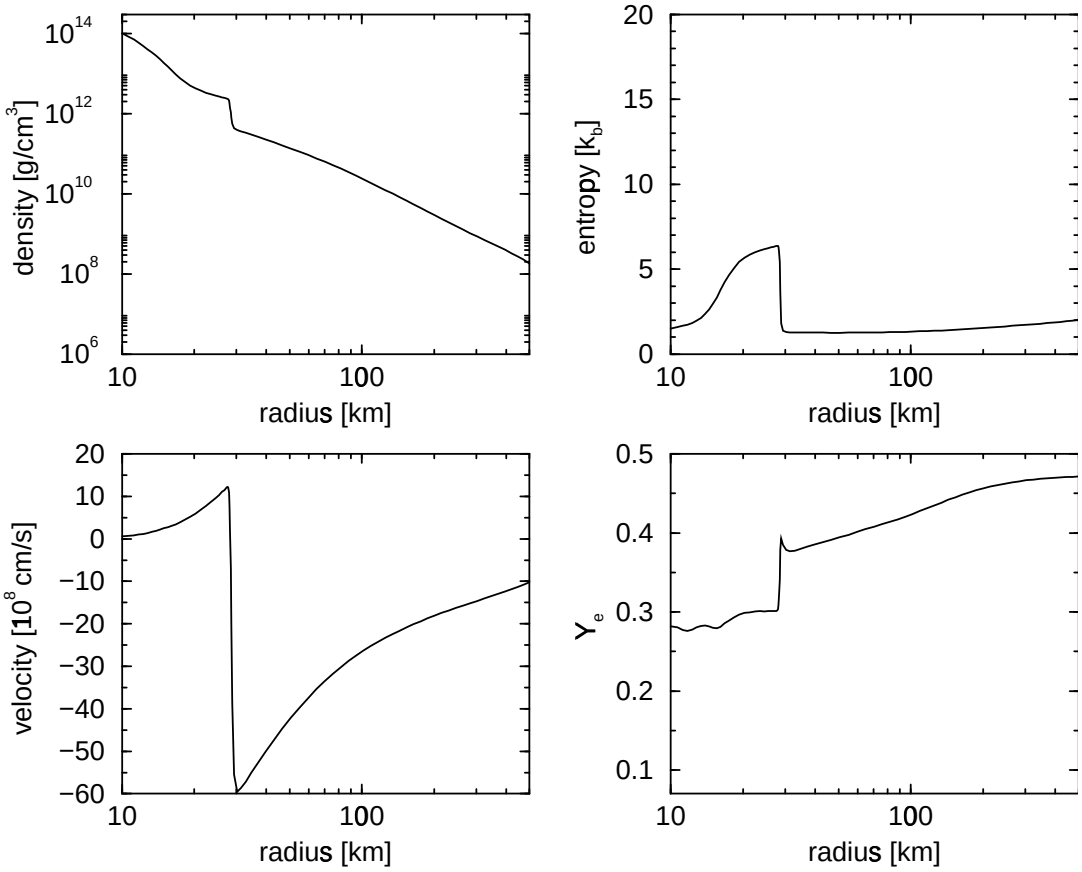

Figure 7.9: Core conditions at 0.5 ms after core bounce for the Nomoto-Hashimoto $15M_\odot$ model

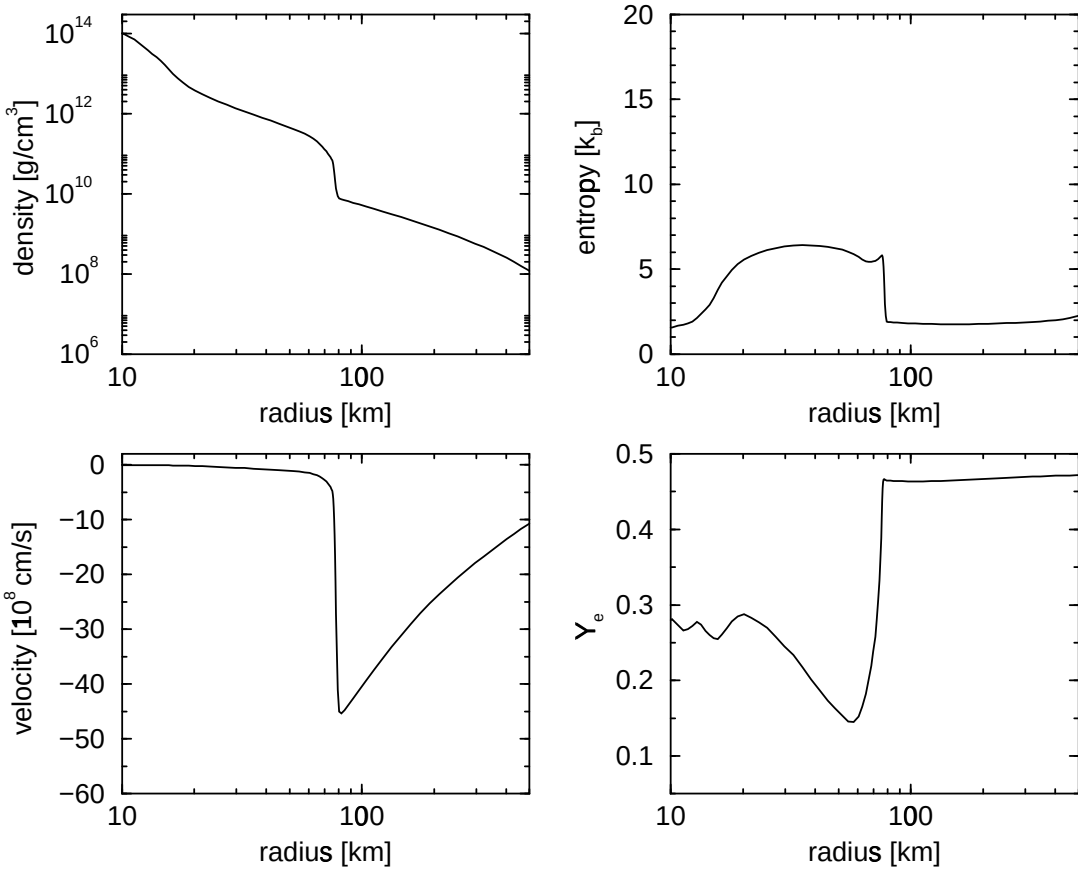

Figure 7.10: Core conditions at 7.2 ms after core bounce for the Nomoto-Hashimoto $15M_\odot$ model

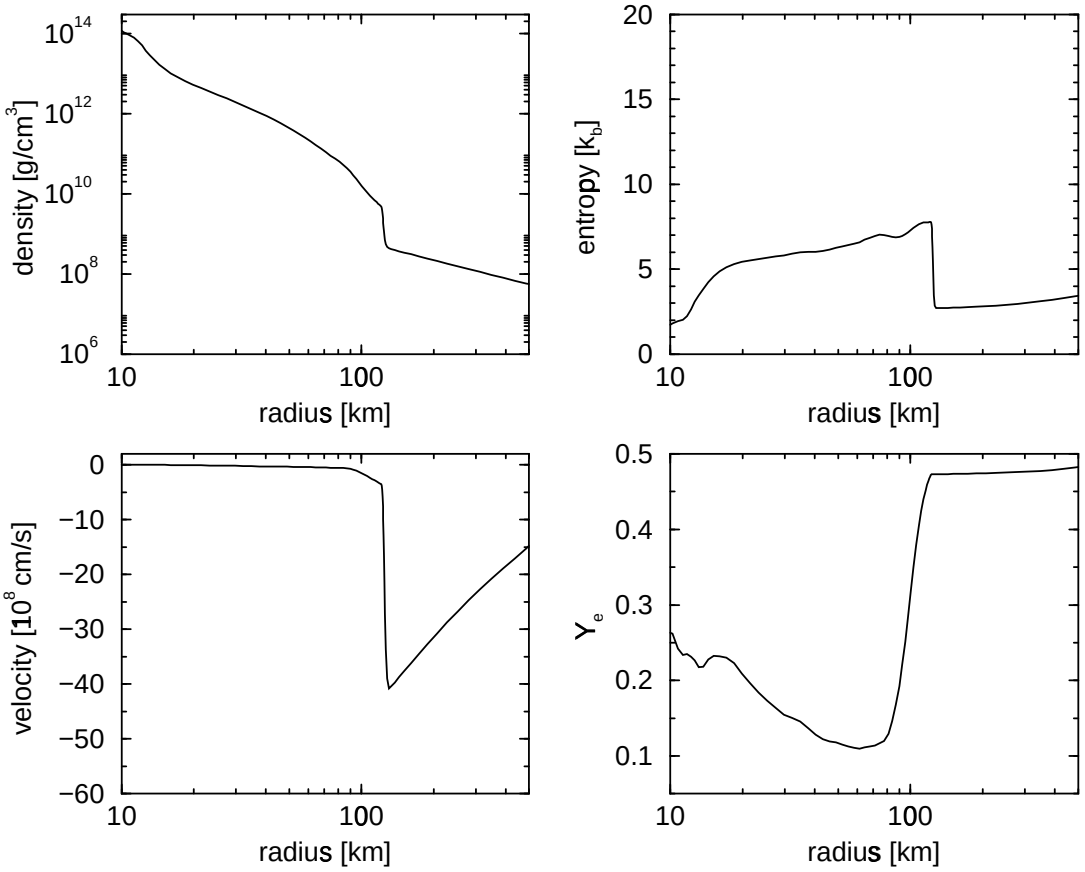

Figure 7.11: Core conditions at 37 ms after core bounce for the Nomoto-Hashimoto $15M_\odot$ model

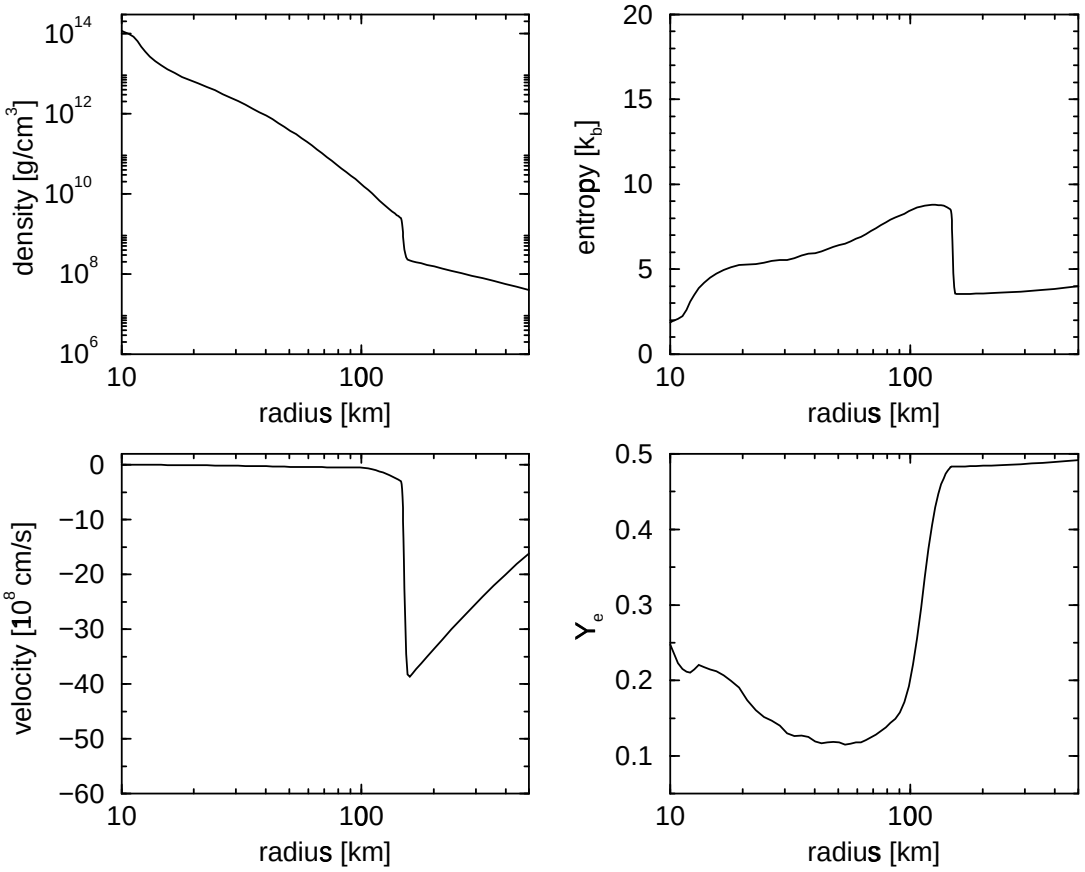

Figure 7.12: Core conditions at 58 ms after core bounce for the Nomoto-Hashimoto $15M_\odot$ model

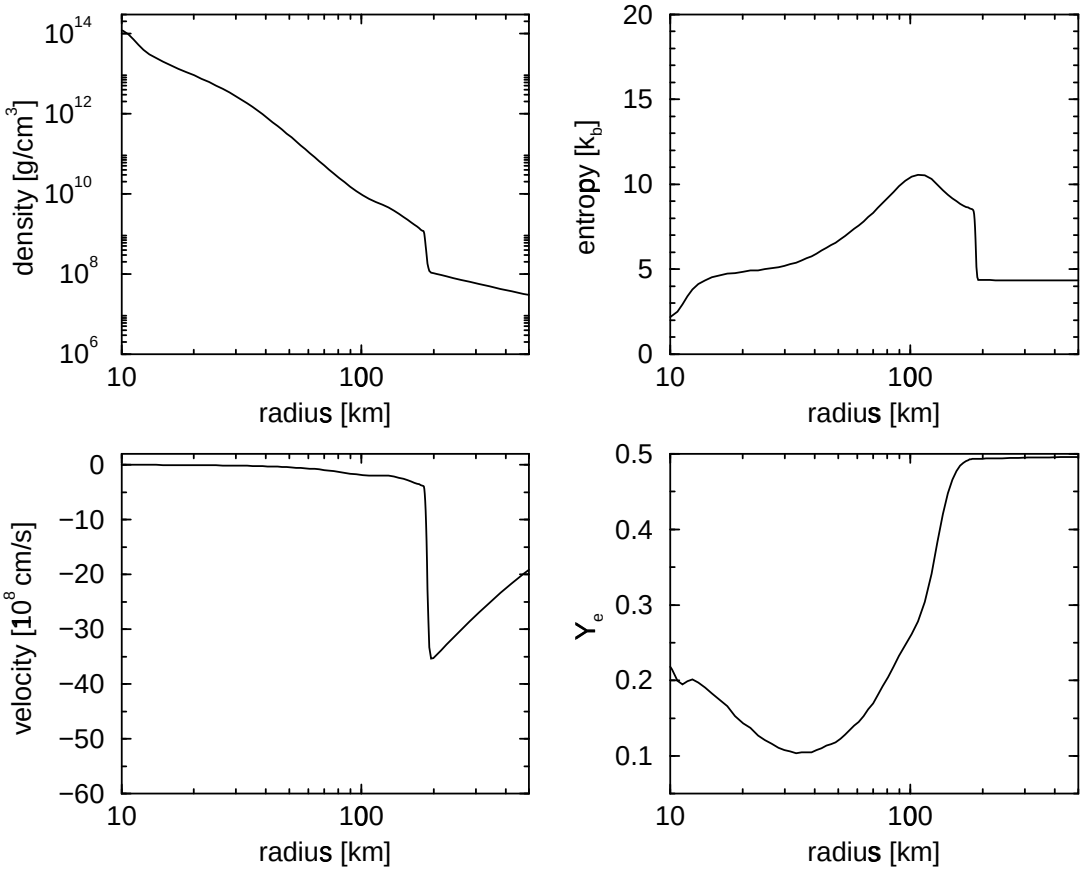

Figure 7.13: Core conditions at 114 ms after core bounce for the Nomoto-Hashimoto $15M_\odot$ model

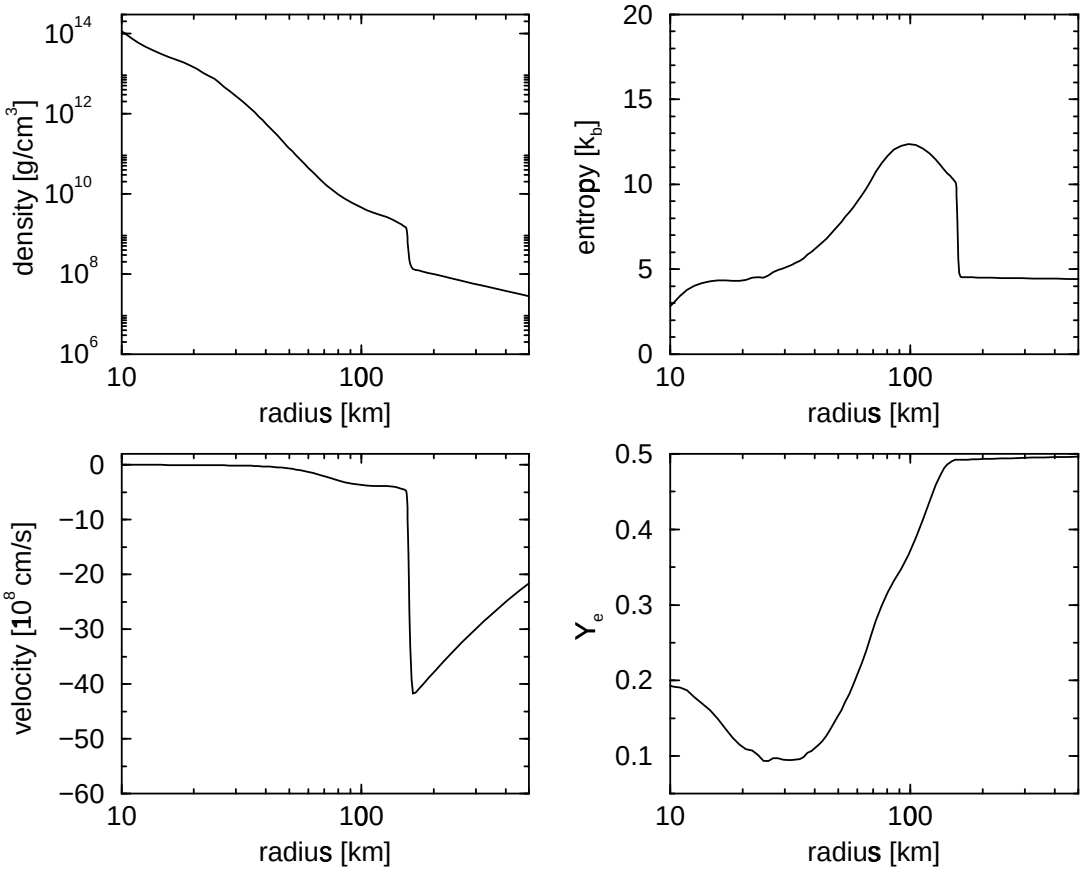

Figure 7.14: Core conditions at 214 ms after core bounce for the Nomoto-Hashimoto $15M_\odot$ model

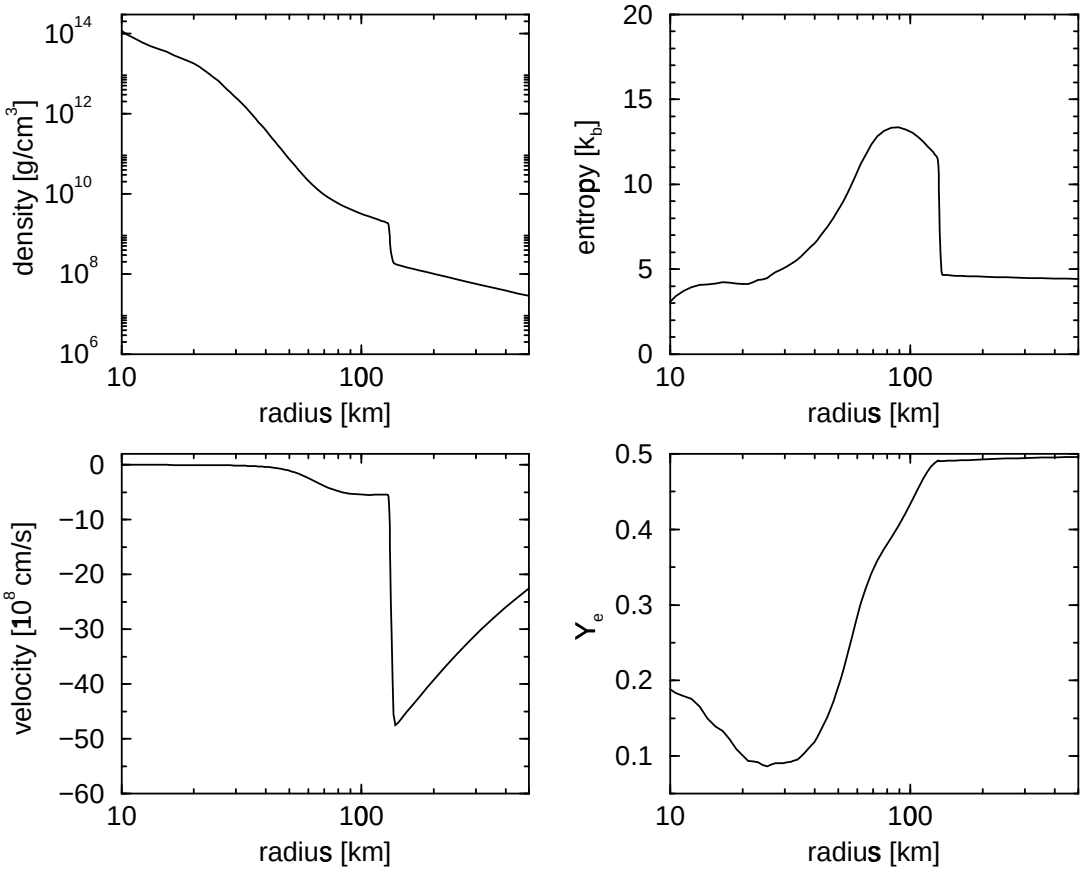

Figure 7.15: Core conditions at 283 ms after core bounce for the Nomoto-Hashimoto $15M_\odot$ model

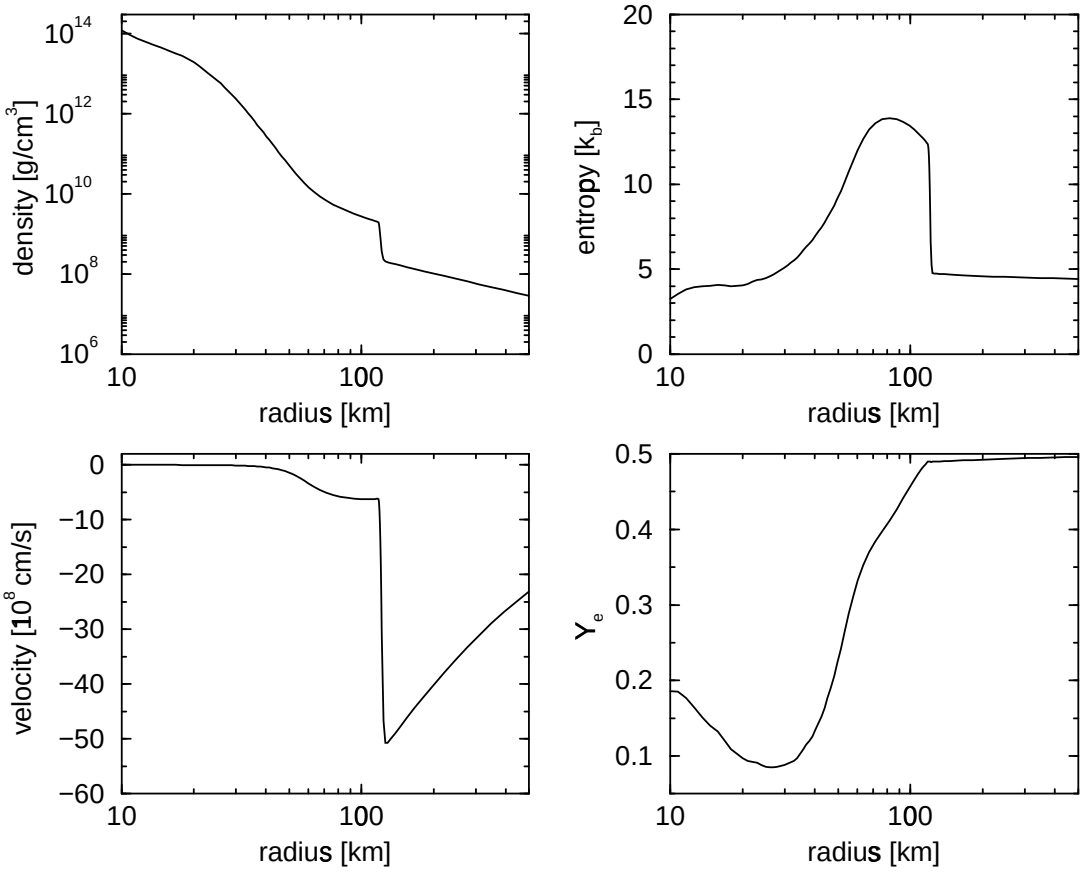

Figure 7.16: Core conditions at 335 ms after core bounce for the Nomoto-Hashimoto $15M_{\odot}$ model

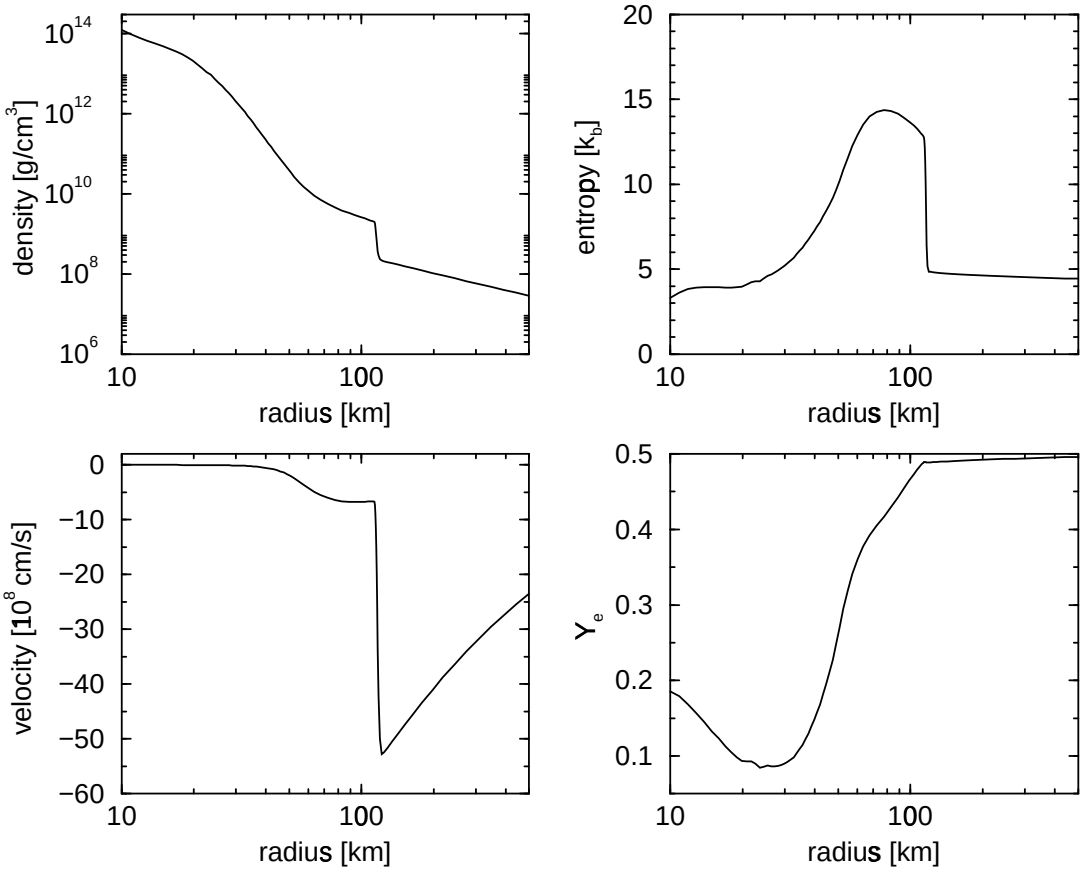

Figure 7.17: Core conditions at 379 ms after core bounce for the Nomoto-Hashimoto $15M_{\odot}$ model

After breakout, in the second time slice (7.2 ms), the shock has been transformed to an accretion shock, as much of its energy has been robbed by the prodigious burst of neutrinos. This neutrino burst has also formed a deep trough in Y_e directly behind the shock. This trough grows deeper as the simulation continues, reaching a minumium Y_e of 0.082 by the last time slice at 396 ms after bounce. The oscillations in Y_e seen in Figure 7.10 and 7.11 are due to discretization effects in resolving the Fermi surface of the degenerate neutrinos (Mezzacappa & Bruenn 1993b). The neutrino Fermi surface decreases as radius increases. As the Fermi surface crosses energy zone centers in certain spatial zones, the neutrino number density changes discontinuously. These sudden decreases in neutrino number density, coupled with the continuously decreasing baryon density, conspire to introduce oscillations in Y_{ν_e}. These oscillations are transferred to Y_e since Y_{lep} is constant deep in the core. In Figure 7.13 the shock has reached its maximum radius of $\approx$ 194 km. From this point on, the shock steadily recedes. The postshock velocities steadily become more and more negative after the shock initially stalls. The postshock entropies continue to increase behind the shock as it recedes, but the region of $s > 5$ is compressed in radius during the recession.

An animation containing velocity and Y_e profiles of the inner 500 km of the core is available in Figure 7.18. The time index at the top of the animation is measured from the onset of collapse.

Figure 7.19 plots the inverse flux factor (see Chapters 4 and 5) for electron neutrinos versus radius for the later postbounce time slices. The position of the shock at each time slice is indicated by an arrow. Although both the shock and the neutrinospheres are receeding, the shock is doing so faster, and is approaching the neutrinospheres. The inverse flux factor curves become more shallow as the neutrino radiation field becomes less isotropic with time. The sharp features seen in each curve just inside the shock positions are due to observer corrections.

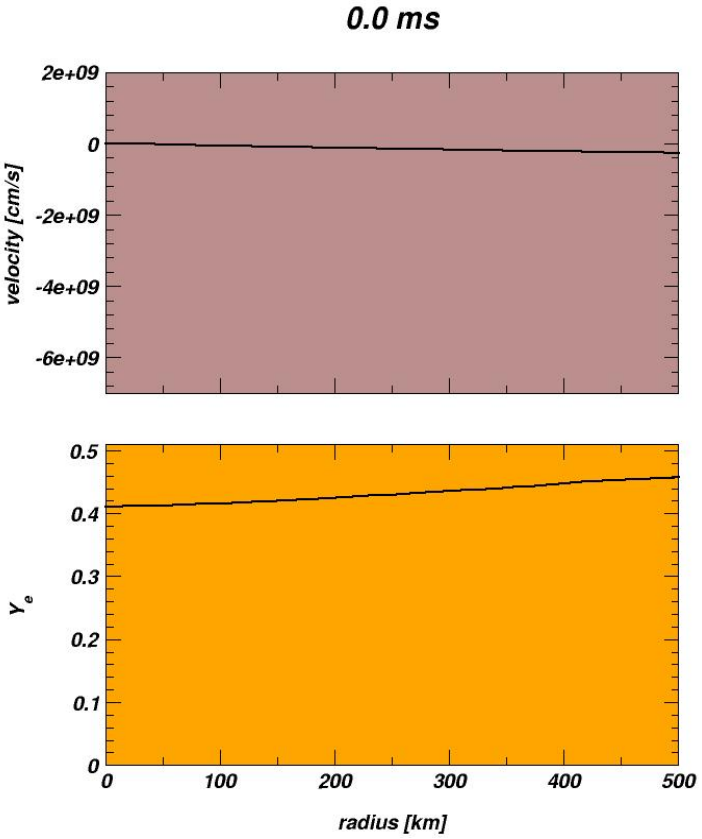

Figure 7.18: Animation depicting the velocity and Y_e profiles for the inner 500 km of the core (Quicktime format, Sorensen compression, 2.85 MB).

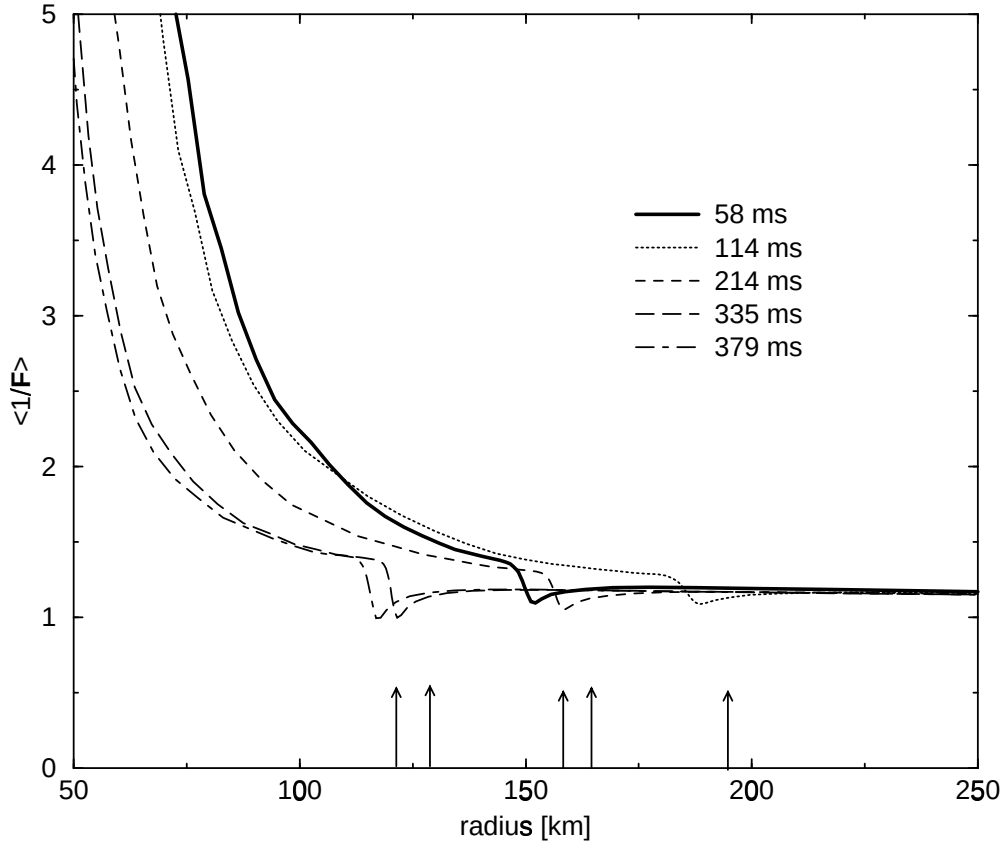

Figure 7.19: Inverse flux factors for electron neutrrinos at various post-bounce times for the Nomoto-Hashimoto $15M_{\odot}$ model

Angular aberration serves to decrease the neutrino isotropy for large local velocity fields. Note these features increase in size as the postshock velocities increase at late times. In Figure 7.20, where we plot the net neutrino heating rate from emission and absorption of electron type neutrinos and antineutrinos, we see that the decreased isotropy in the gain region is offset by the increasing RMS energies and neutrino luminosity, leading to increased neutrino heating as time progresses. The gain region is steadily compressed in radius, as implied by the compressed region of high entropy seen in Figures 7.13 through 7.17. Note the observer correction induced features near the shock in each heating curve. In this case, the frequency shift increases the neutrino RMS energies and luminosities, causing the local heating rate to increase just behind the shock. The maximum heating rate shown is at 214 ms, approximately 100 ms after the shock has started to recede. The heating rate has decreased markedly by 335 ms, but begins to grow again, even as the gain region becomes smaller and is translated inward. Nevertheless, this increased heating is not enough to reverse the inward motion of the shock. This failure is due to the increased cooling below the gain radius. This increased cooling reduces the pressure support beneath the shock, allowing it to recede further and preventing any prolonged period of heating of a given parcel of matter.

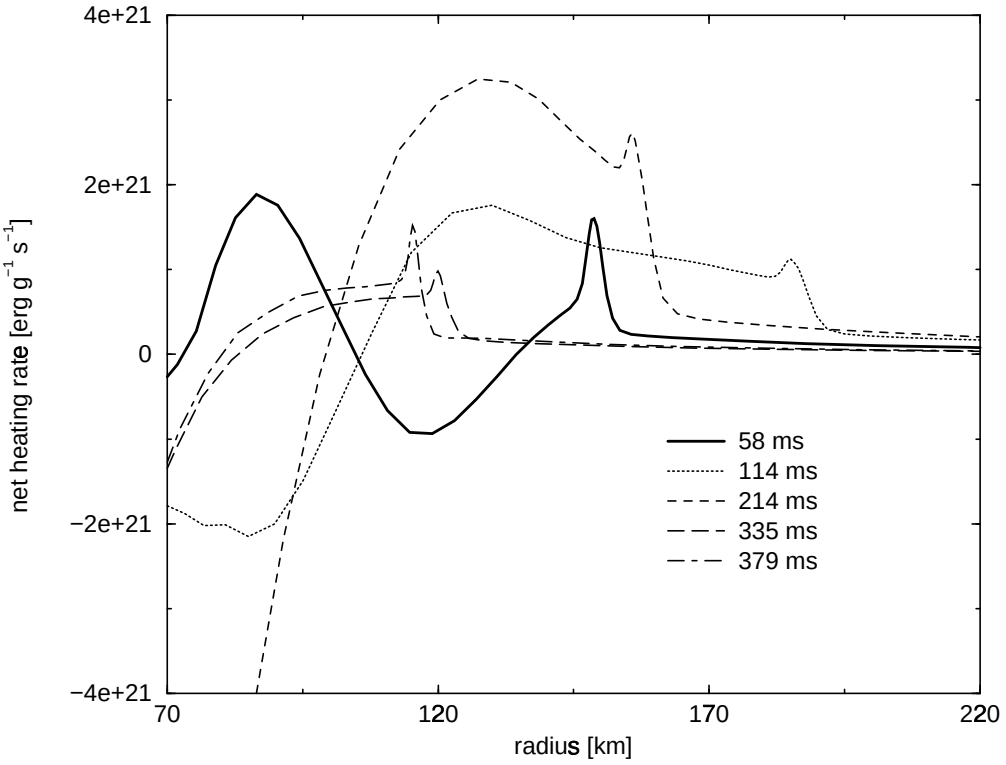

Figure 7.20: Net neutrino heating rates from emission and absorption of electron neutrinos and antineutrinos at various post-bounce times for the Nomoto-Hashimoto $15M_{\odot}$ model

Chapter 8

The Nomoto-Hashimoto 20 $M_\odot$ Simulation

This chapter describes the simulation of core collapse, bounce, shock propagation and stagnation of the core of a $20M_\odot$ progenitor star (Nomoto & Hashimoto 1988).

8.1 Introduction

We begin with the core of the 20 $M_\odot$ model of Nomoto & Hashimoto (1988) out to 1.647 $M_\odot$ and a radius of 2873 km. The core is divided into 103 radial adaptive zones. Once again, twelve geometrically spaced energy groups spanning the range from 5 to 330 MeV are used to resolve neutrino energies, and 6–point Gaussian quadrature is used to resolve the neutrino directions relative to the outgoing radial direction. The EOS and neutrino–matter couplings used are identical to the simulation in Chapter 7. The initial conditions are displayed in Figure 8.1. The spike at 1350 km in all the displayed quantities marks the edge of the iron core and the inner

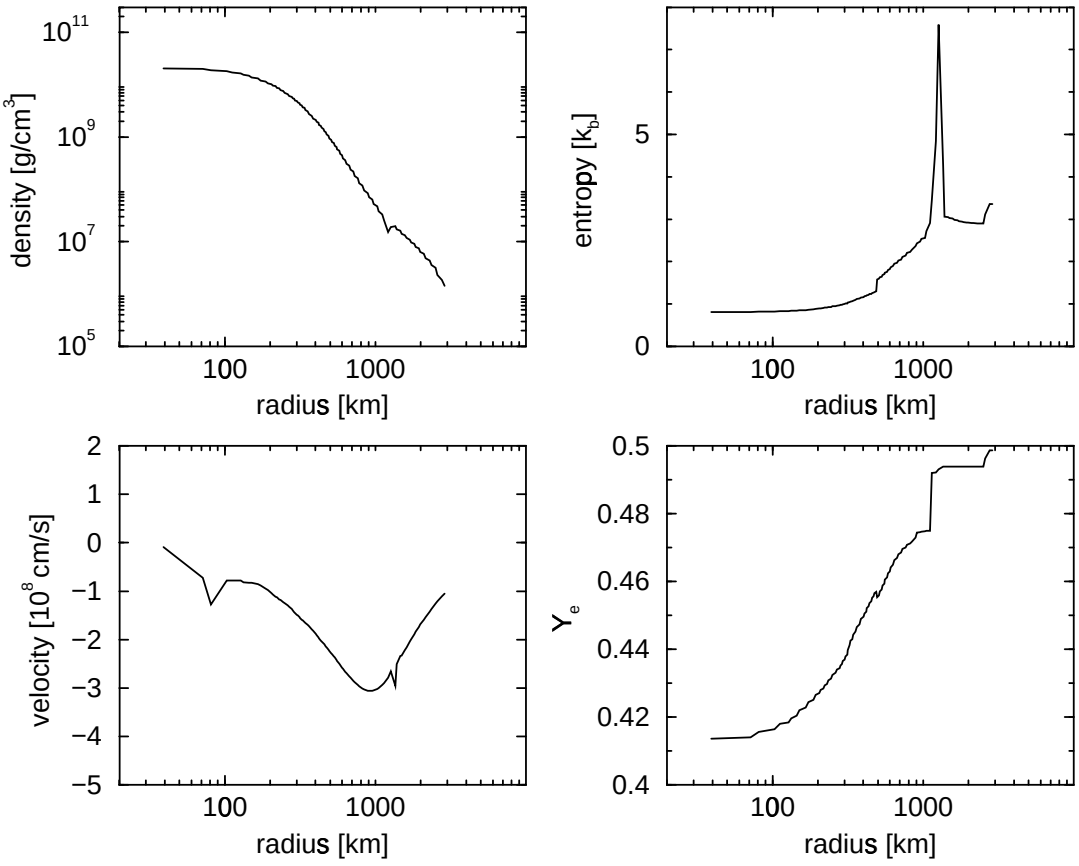

Figure 8.1: Initial conditions for the Nomoto-Hashimoto $20M_\odot$ model

edge of the silicon shell.

8.2 Results

Trajectories of equal mass shells are shown in Figure 8.2 for the duration of the run. The upper line across the plot marks the boundary between NSE and silicon throughout the simulation. The lower, heavy line marks the shock position. The shock is launched at 0.67 $M_{\odot}$ and $\approx$ 16 km and propagates out to a radius of 197 km. It subsequently recedes throughout the remainder of the simulation and sits at 100 km at the end of the run. The advection boundary condition has turned on at about 350 ms, as the outermost mass shell show on the plot has gone inside 2000 km. The simulation was stopped at 500 ms after the onset of collapse, before any of this artificially advected material has reached the shock. Looking at the upper trace on the plot, three discountinuous changes in the position of the NSE front are evident. These features, as in the $15M_{\odot}$ case, stem from our prescription for marking the position of the front; changing it's position one mass zone at a time when the critical flashing temperature is exceeded.

Figures 8.3 through 8.6 display the evolution of density, entropy, electron fraction, and velocity at various central densities during collapse. The edge of the iron shell is evident in Figure 8.4, marked by the sharp increase in entropy at about 1350 km. The core deleptonizes to a central Y_e of 0.275 at bounce. Core bounce occurs at 74.4 ms after the onset of collapse, at central density of $3.09 \times 10^{14} g/cm^3$. The location of shock formation is evident in the entropy, velocity, and electron fraction plots, where each of these quantities has a sharp discontinuity at 14 km. The initial shock position and central Y_e at bounce are strikingly similar to the $15M_{\odot}$ case.

The shock begins to propagate outward, encountering the electron antineutrino and mu/tau neutrinospheres $\approx$ 1 ms after bounce, and the electron neutrinosphere $\approx$ 2.5 ms after bounce. In

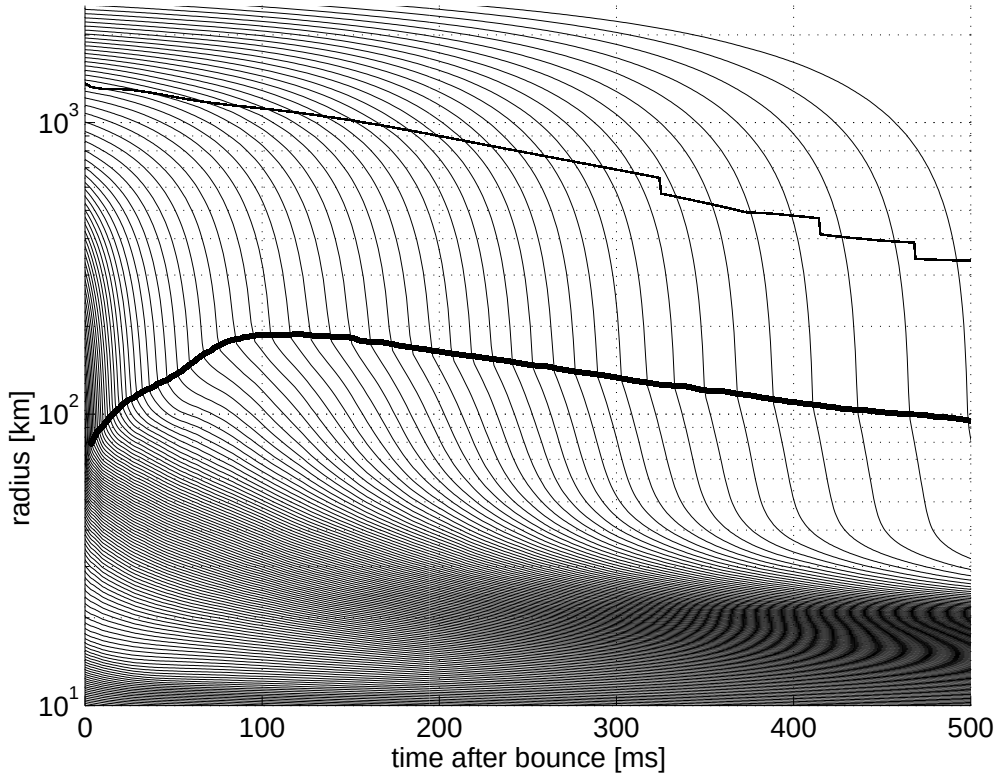

Figure 8.2: Radial trajectories of equal mass shells for the Nomoto-Hashimoto $20M_\odot$ model

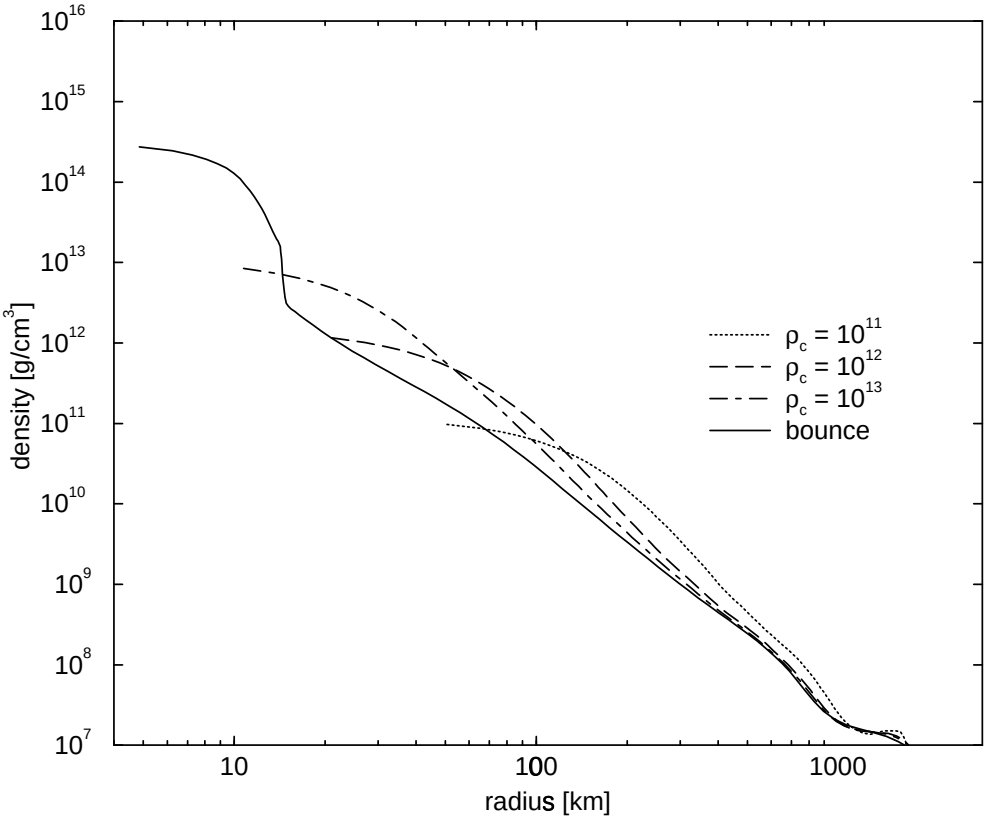

Figure 8.3: Density profiles at various central densities during collapse for the Nomoto-Hashimoto $20M_\odot$ model

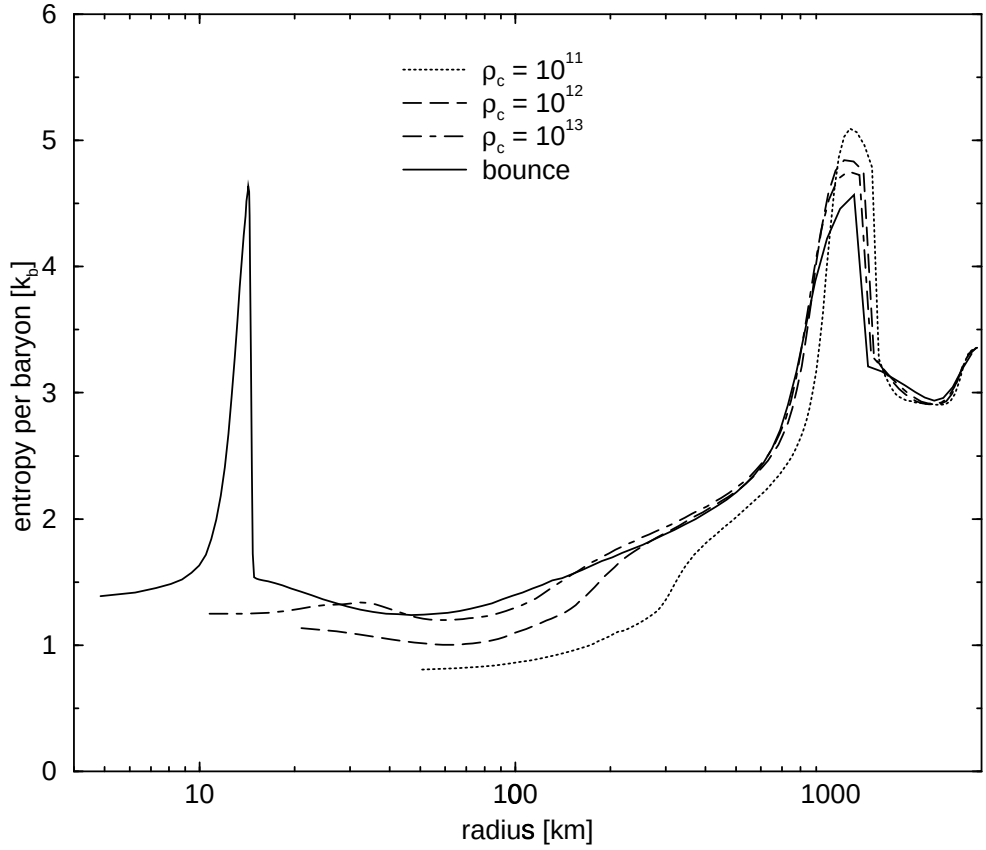

Figure 8.4: Entropy profiles at various central densities during collapse for the Nomoto-Hashimoto $20M_{\odot}$ model

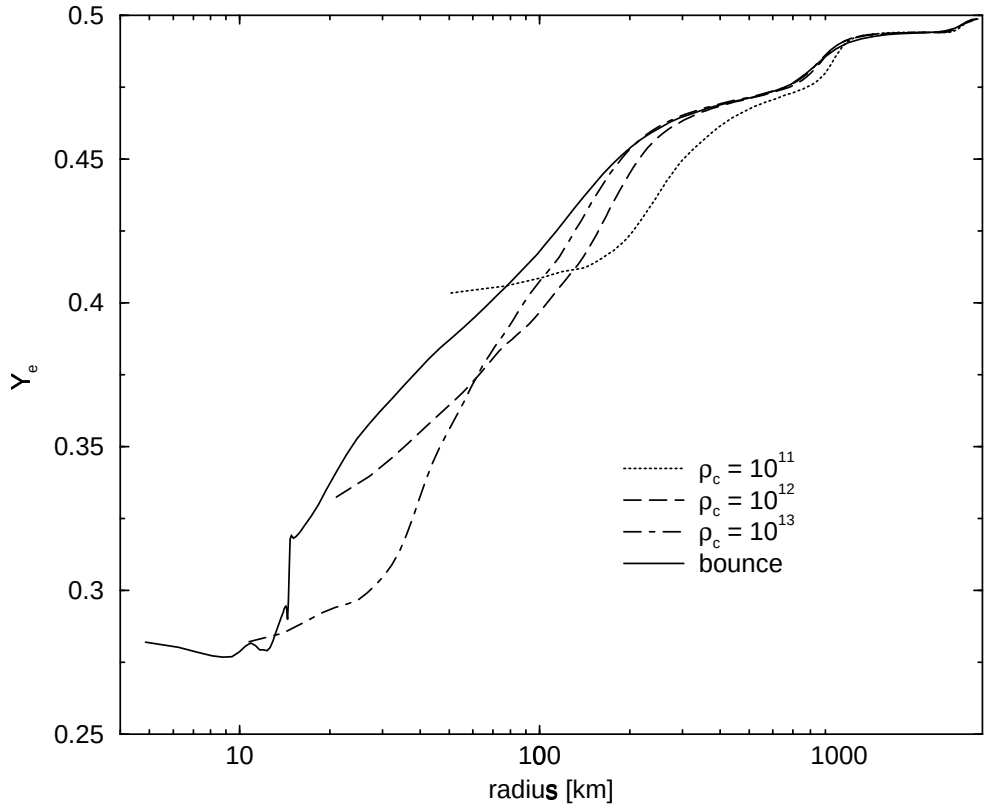

Figure 8.5: Y_e profiles at various central densities during collapse for the Nomoto-Hashimoto $20M_\odot$ model

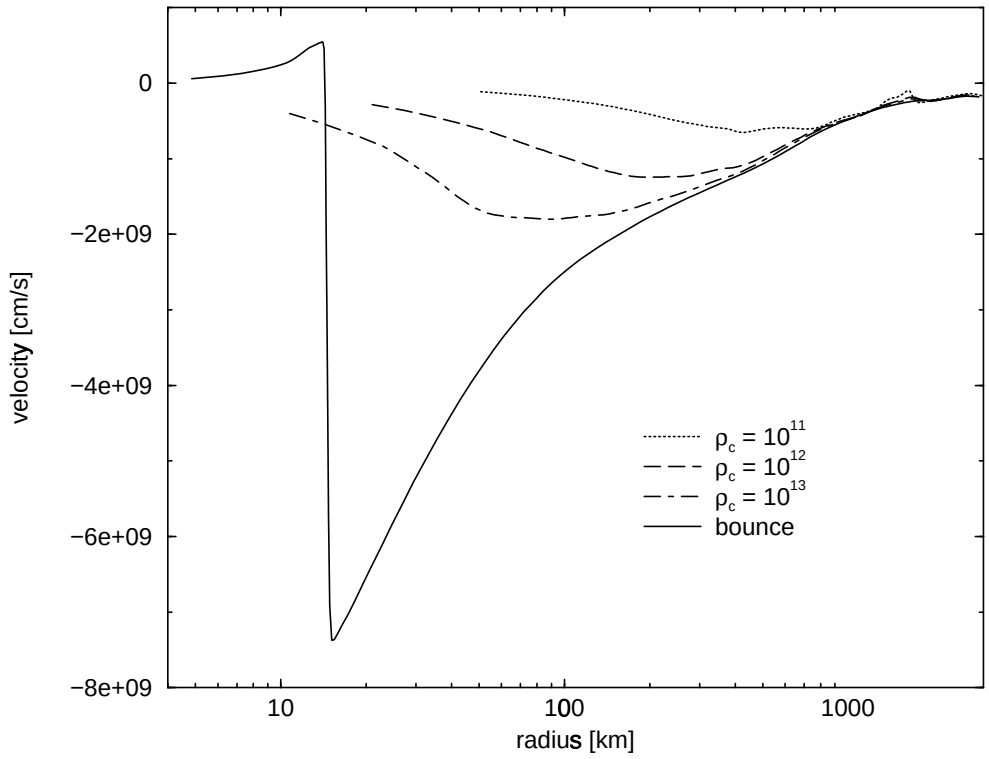

Figure 8.6: Velocity profiles at various central densities during collapse for the Nomoto-Hashimoto $20M_{\odot}$ model

Figure 8.7 the neutrino luminosities at 1000 km are plotted versus time. The luminosities for all flavors of neutrinos and antineutrinos are virtually indistinguishable from the $15M_{\odot}$ case until about 350 ms from the onset of collapse. As opposed to the $15M_{\odot}$ case, the neutrino luminosities begin to decline at this time in this model. The mass accretion rate has begun to decline by this time, and is not artificially enhanced by the constant density inflow boundary condition. The RMS energies of the neutrinos are plotted versus time in Figure 8.8. The RMS energies are also little different from the $15M_{\odot}$ simulation. They steadily increase as the neutrinospheres slip to smaller radii and higher temperatures.

Figures 8.9 through 8.18 display density, entropy, velocity, and electron fraction profiles for several postbounce times. Comparing 8.9 and 8.10, as for the $15M_{\odot}$ case, the enervating effect of shock breakout is clearly seen. The shock has become an accretion shock by 3.2 ms after bounce. The neutrino burst has formed a characteristic trough in Y_e directly behind the shock. This trough grows deeper as the simulation continues, reaching 0.064 by the last timeslice at 396 ms after bounce. Small oscillations are seen in Y_e for the earlier postbounce times, just as in the $15M_{\odot}$ case. These oscillations are again due to the coarseness of the energy grid used to resolve the degenerate neutrino distribution function. In Figure 8.13 the shock has reached its maximum radius of $\approx$ 194 km. The shock then begins to recede, as in the $15M_{\odot}$ model, and the postshock velocities steadily increase in absolute value. The same increase in postshock entropies for the $15M_{\odot}$ case is also seen here.

An animation containing velocity and Y_e profiles of the inner 500 km of the core is available in Figure 8.19. The time index at the top of the animation is measured from the onset of collapse.

Figure 8.20 is a plot of the inverse flux factor for electron neutrinos versus radius for the a variety of postbounce timeslices. The position of the shock at each time is indicated by

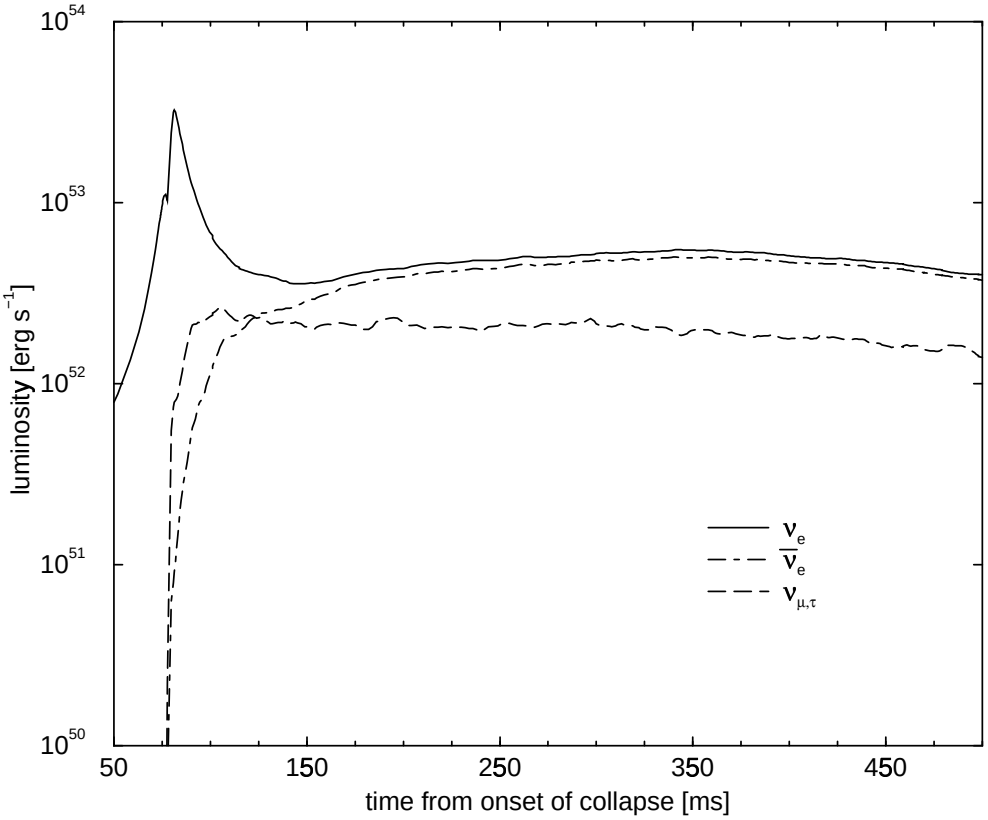

Figure 8.7: Neutrino luminosities as a function of time since the onset of collapse at 1000 km for the Nomoto-Hashimoto $20M_\odot$ model

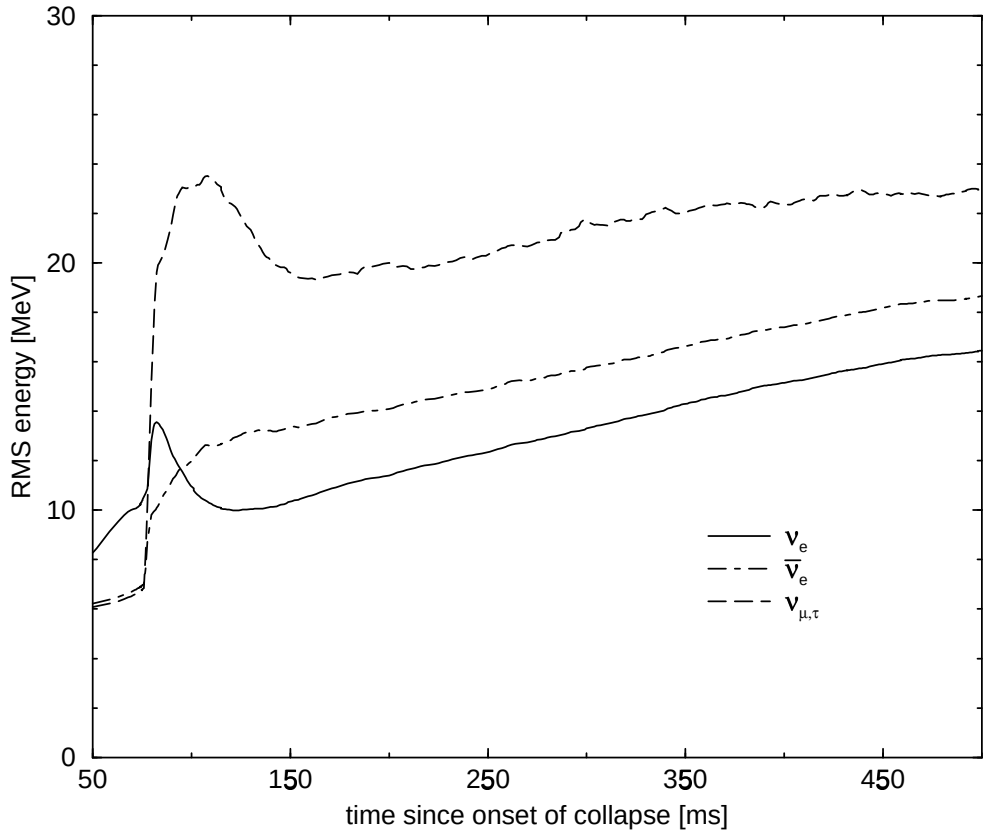

Figure 8.8: Neutrino RMS energies as a function of time since the onset of collapse at 1000 km for the Nomoto-Hashimoto $20M_\odot$ model

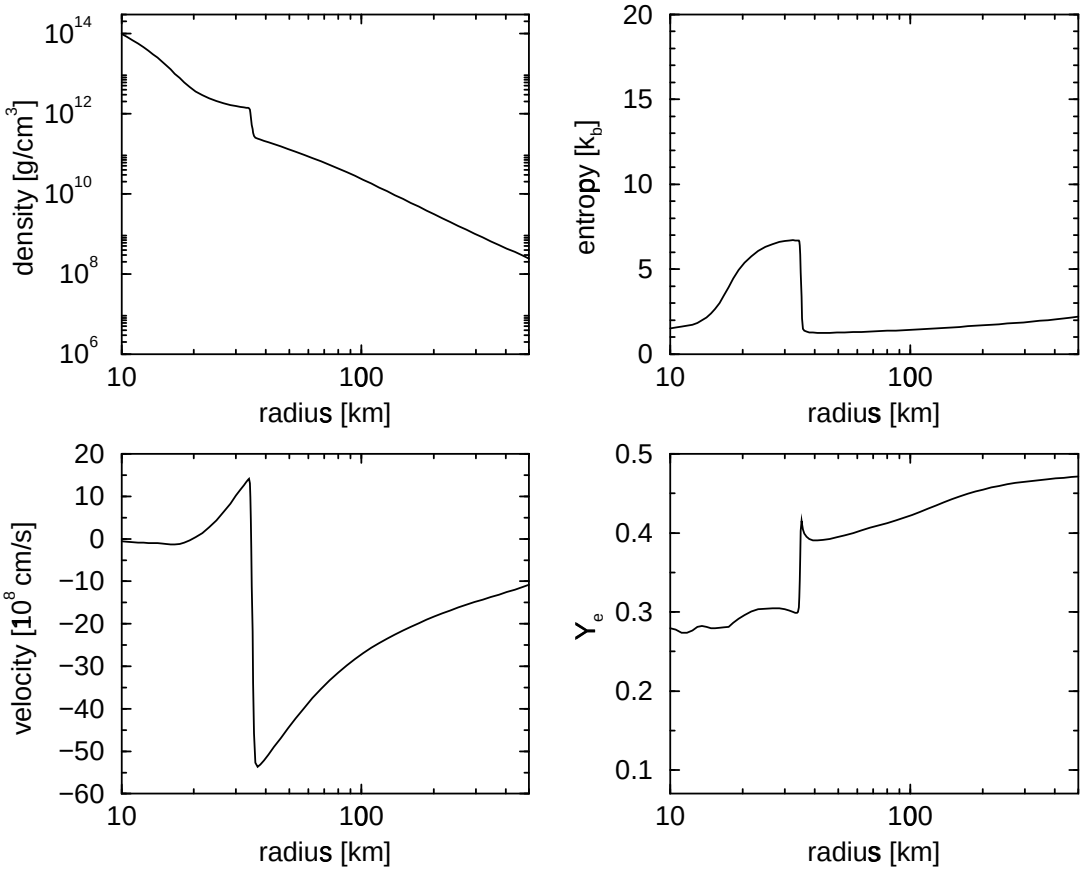

Figure 8.9: Core conditions at 0.5 ms after core bounce for the Nomoto-Hashimoto $20M_\odot$ model

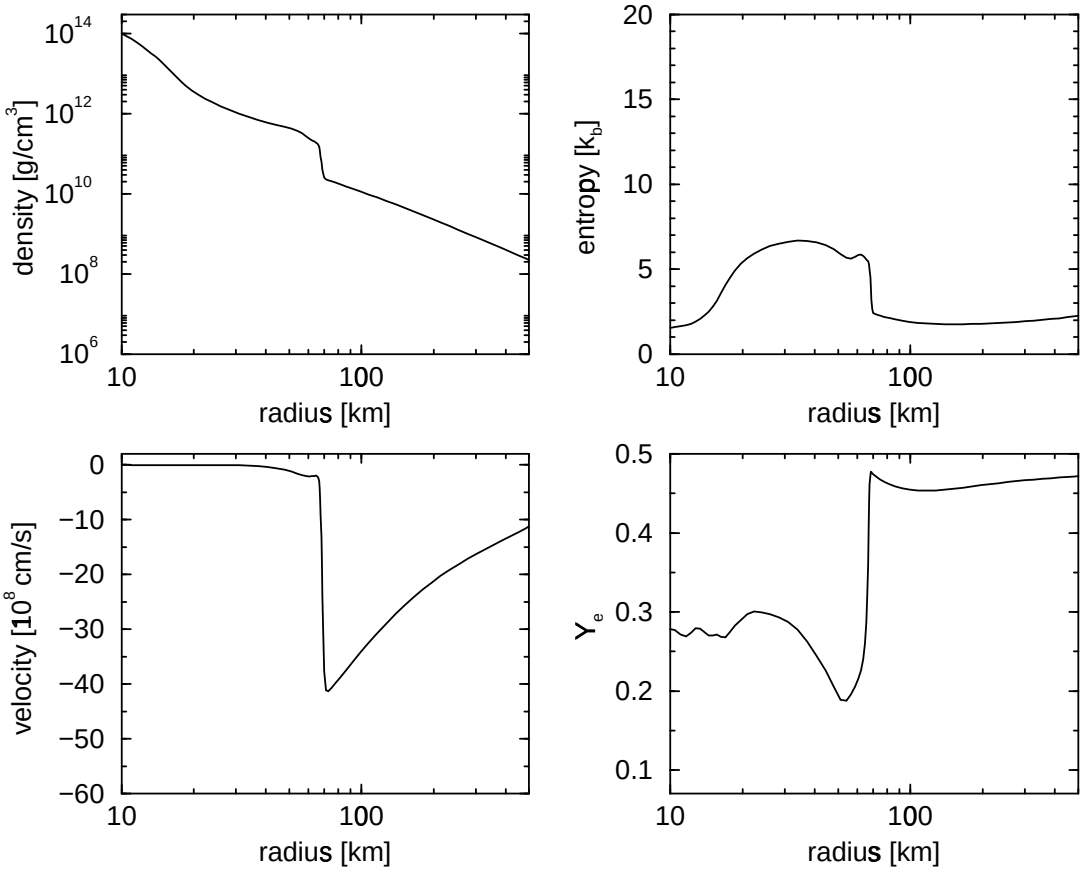

Figure 8.10: Core conditions at 3.2 ms after core bounce for the Nomoto-Hashimoto $20M_{\odot}$ model

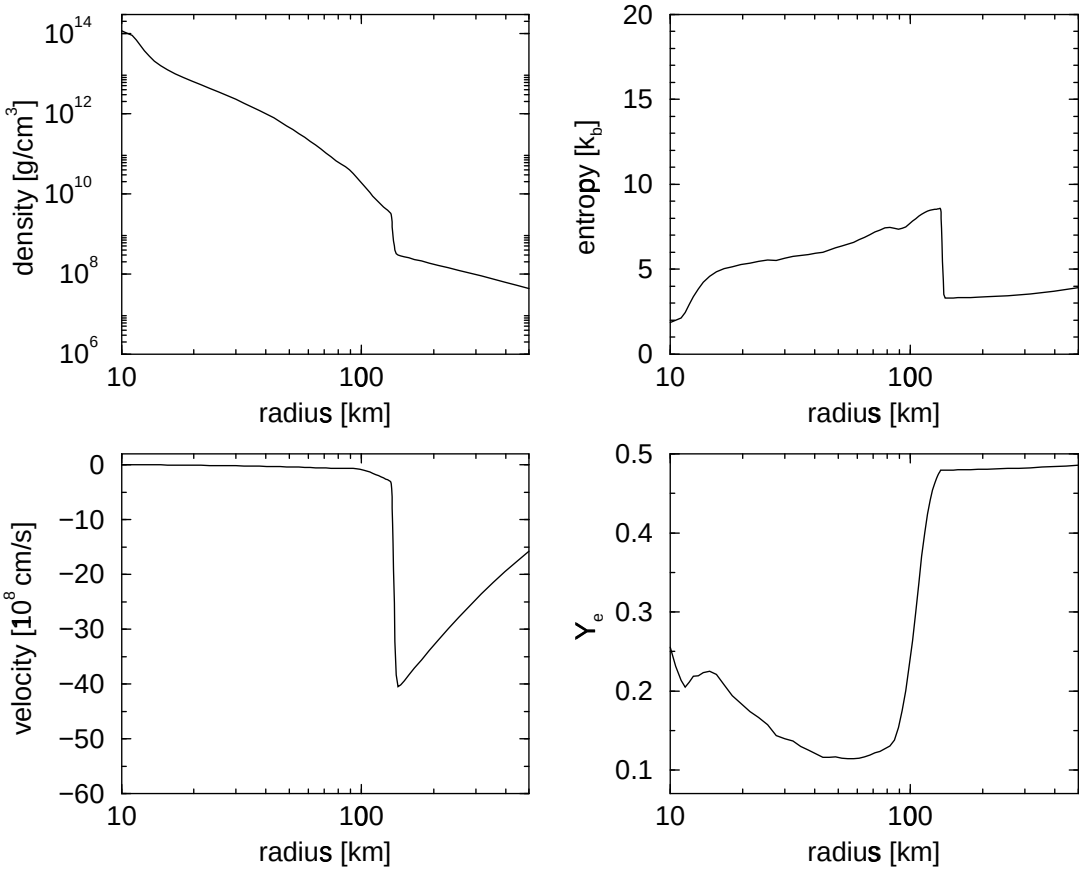

Figure 8.11: Core conditions at 57 ms after core bounce for the Nomoto-Hashimoto $20M_\odot$ model

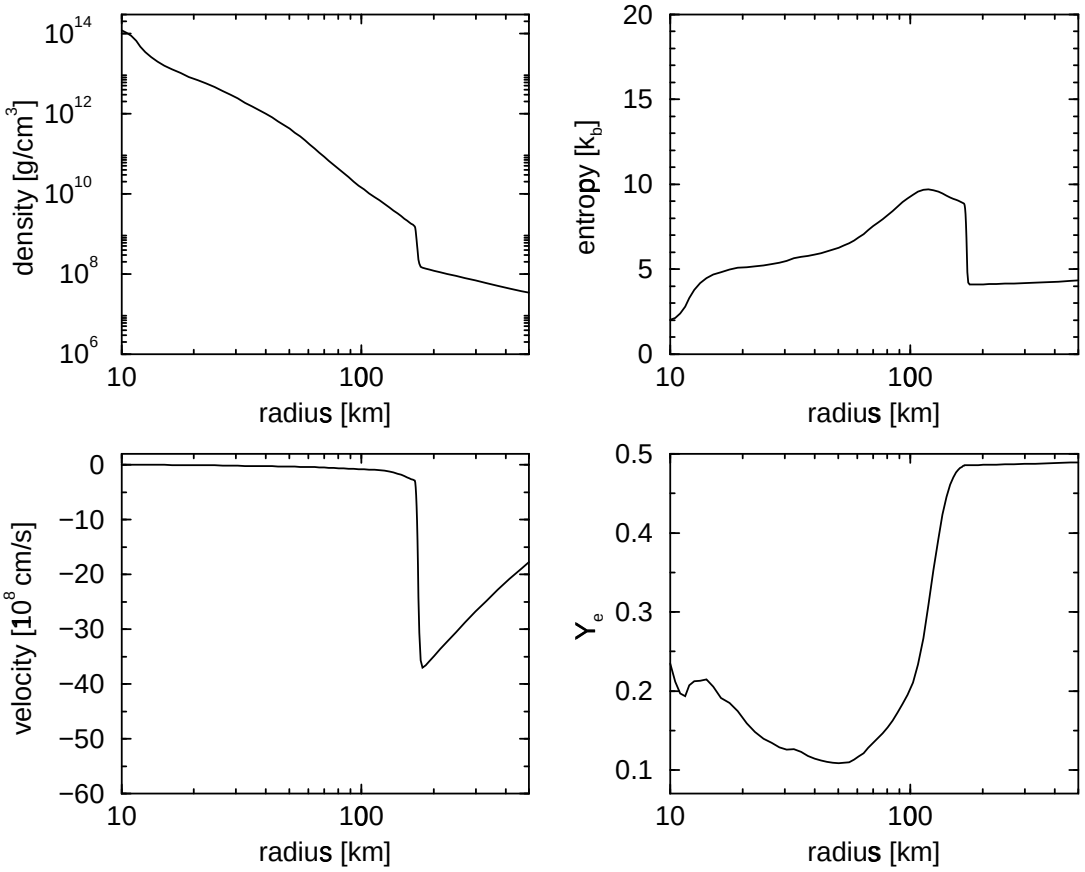

Figure 8.12: Core conditions at 81 ms after core bounce for the Nomoto-Hashimoto $20M_\odot$ model

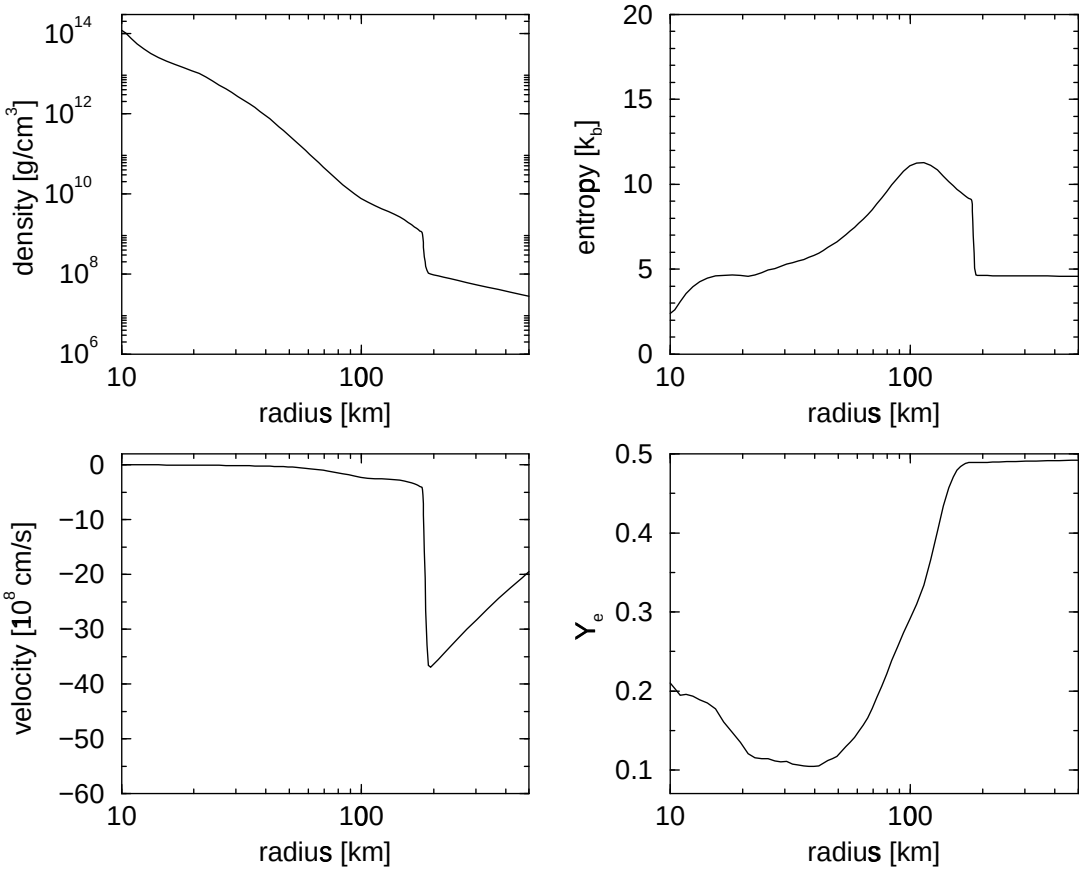

Figure 8.13: Core conditions at 146 ms after core bounce for the Nomoto-Hashimoto $20M_\odot$ model

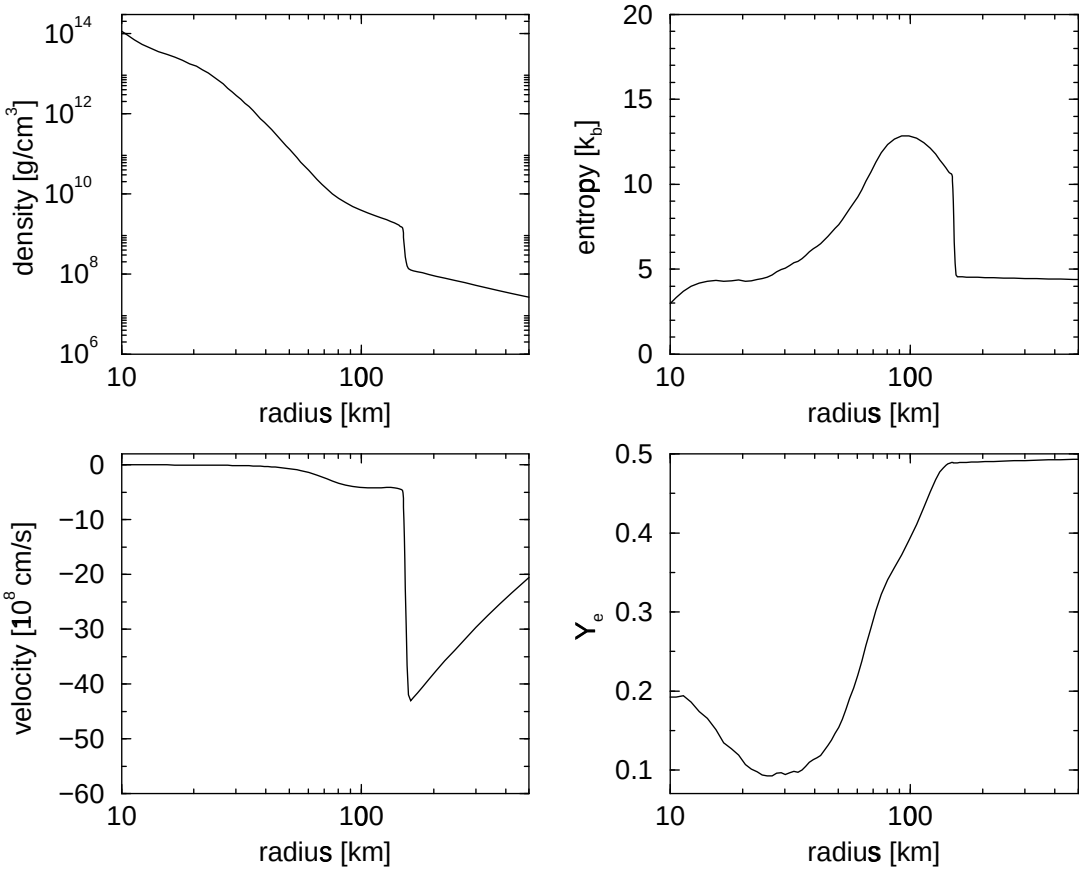

Figure 8.14: Core conditions at 239 ms after core bounce for the Nomoto-Hashimoto $20M_\odot$ model

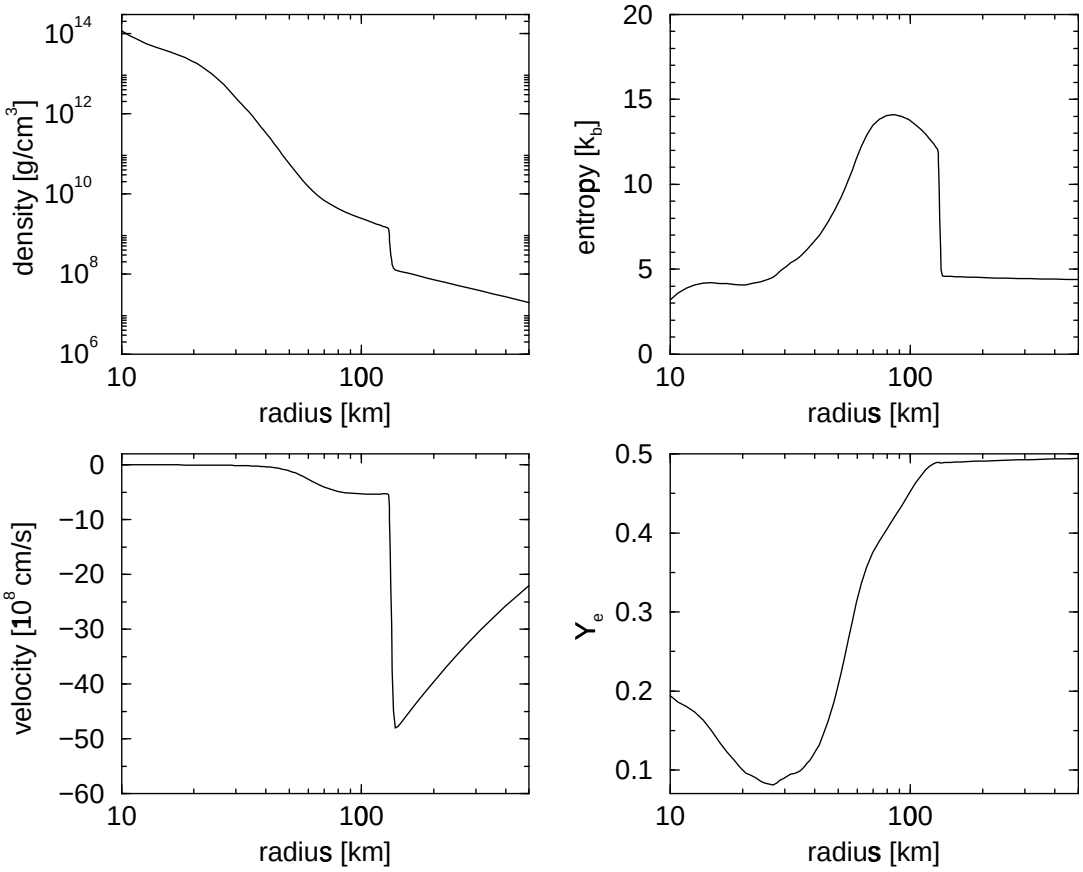

Figure 8.15: Core conditions at 307 ms after core bounce for the Nomoto-Hashimoto $20M_\odot$ model

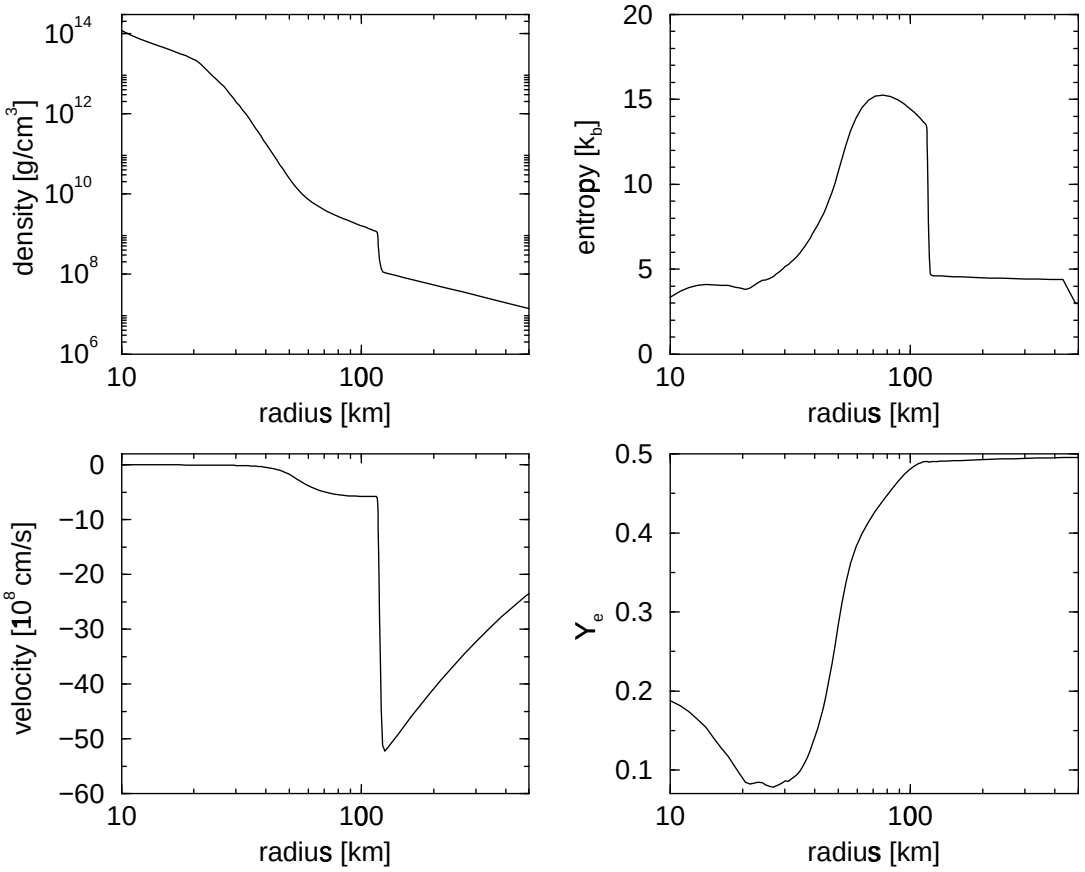

Figure 8.16: Core conditions at 359 ms after core bounce for the Nomoto-Hashimoto $20M_\odot$ model

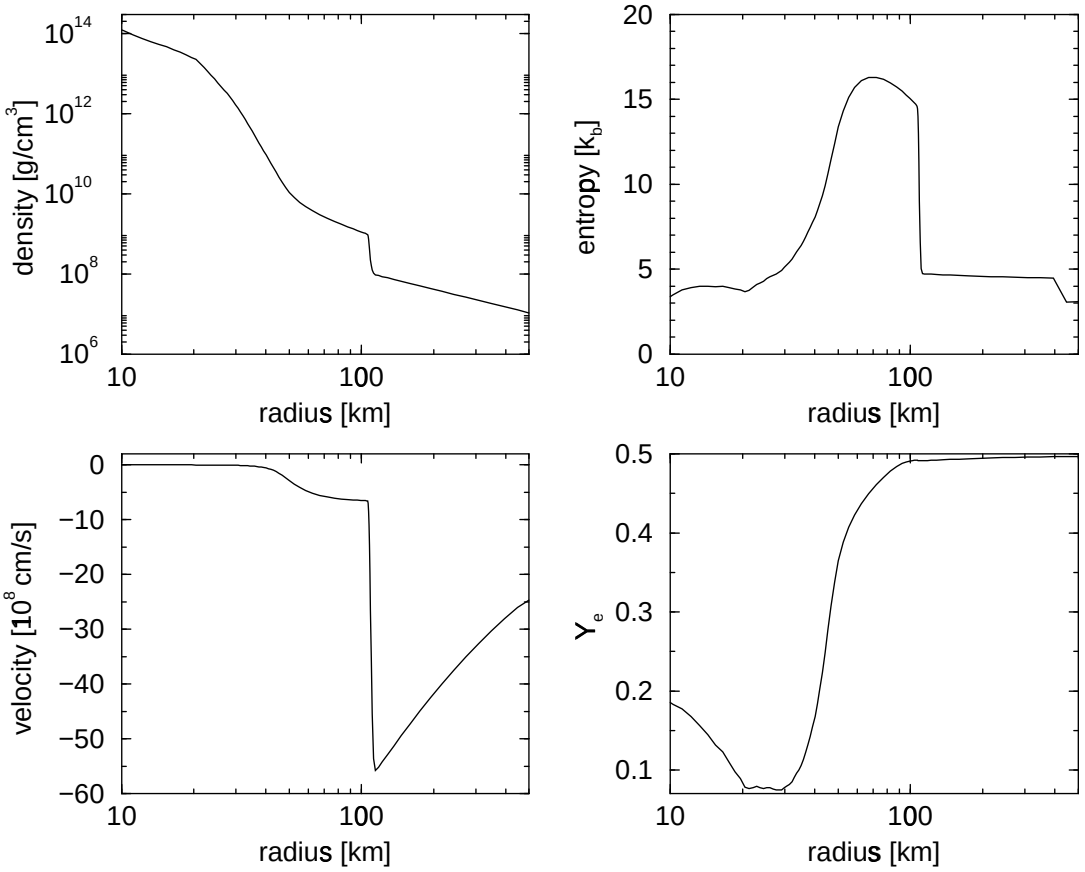

Figure 8.17: Core conditions at 396 ms after core bounce for the Nomoto-Hashimoto $20M_\odot$ model

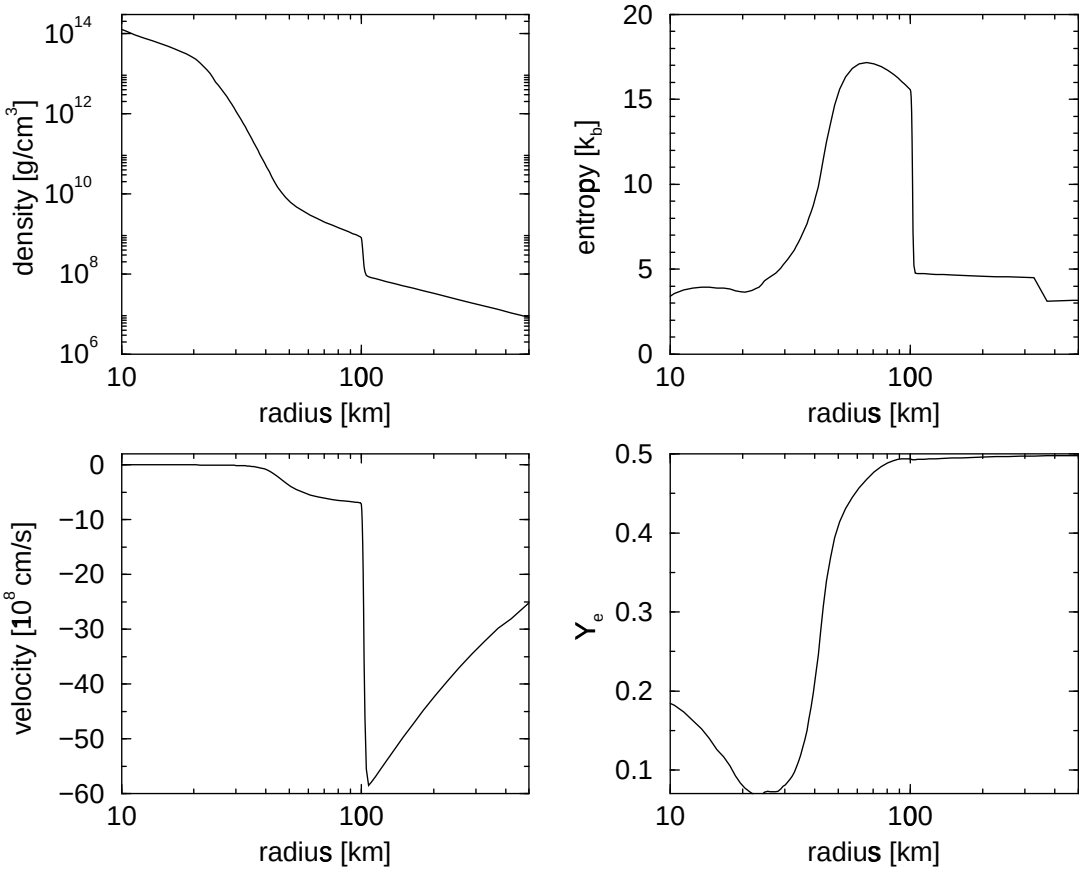

Figure 8.18: Core conditions at 448 ms after core bounce for the Nomoto-Hashimoto $20M_\odot$ model

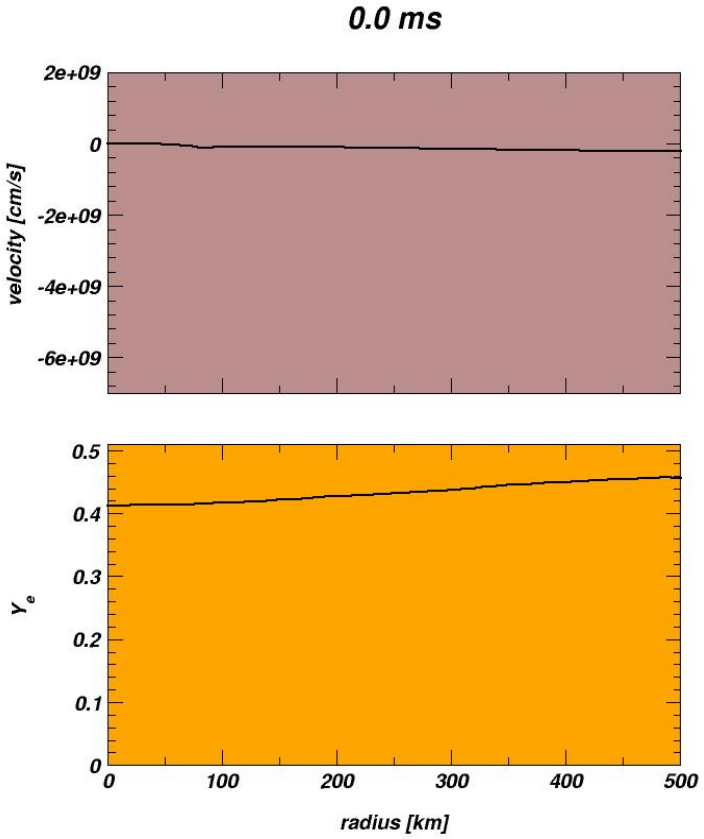

Figure 8.19: Animation depicting the velocity and Y_e profiles for the inner 500 km of the core (Quicktime format, Sorensen compression, 3.41 MB).

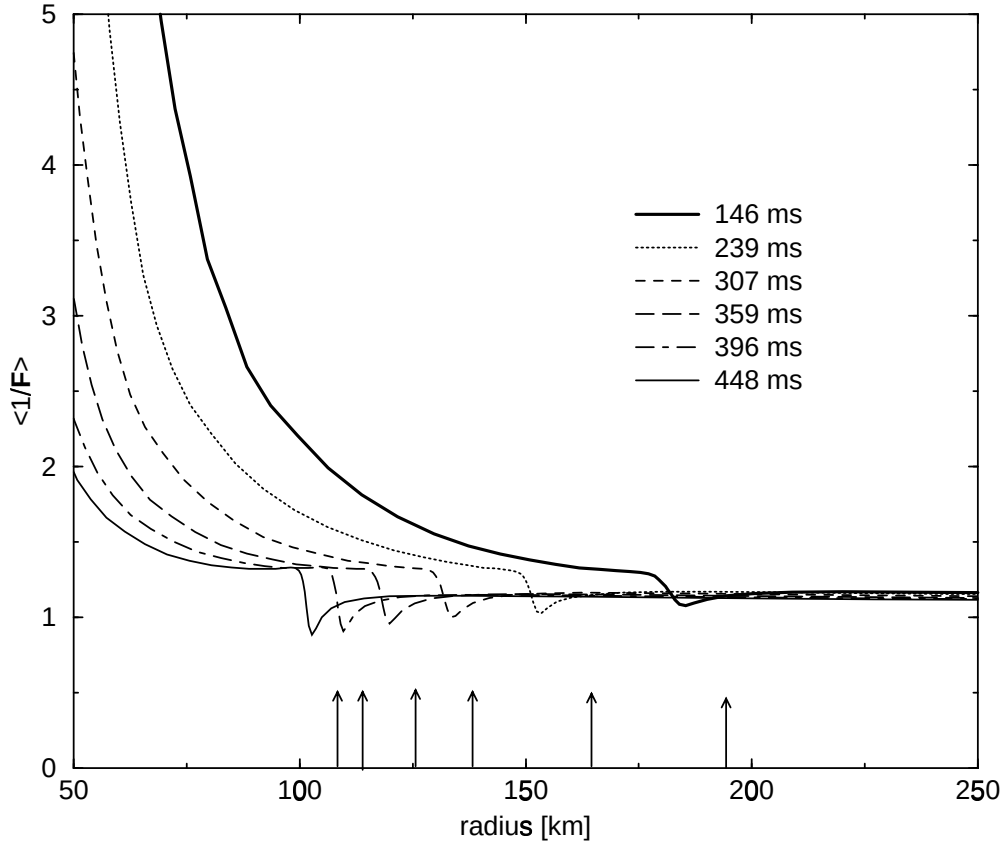

Figure 8.20: Inverse flux factors for electron neutrinos at various post-bounce times for the Nomoto-Hashimoto $20M_{\odot}$ model

an arrow. Again, as in the $15M_{\odot}$ simulation, the neutrino radiation field in the gain region becomes less isotropic with time. The small features just behind the shock for each timeslice are again caused by observer corrections in the large, local velocity gradient. In Figure 8.21, which contains net neutrino heating rates from emission and absorption of electron type neutrinos and antineutrinos for the same times shown in Figure 8.20, we see the same sort of behavior exhibited in the $15M_{\odot}$ case. After reaching a maximum at 146 ms after bounce, the net heating rate decreases. Thereafter, the gain region shrinks in extent, but the peak of net heating actually gets larger with time. Observer correction induced features are apparent in all the curves, just as in the $15M_{\odot}$ case. The frequency shift for comoving observers serves to boost the heating rate in a small region directly behind the shock, where the velocity gradient is greatest. Also note the marked increase in cooling below the gain radius with time. This increased cooling renders the increased heating above the gain region ineffective for shock revival. The fate of this model is determined, as it was for the $15M_{\odot}$ model, by the lack of pressure support beneath the shock. The gain region shrinks and moves inward with the shock. No parcel of matter is heated sufficiently, for sufficient time, to reenergize the shock.

Overall, the similarities to the $15M_{\odot}$ case are astonishing. The latetime neutrino luminosties decrease slightly more than in the $15M_{\odot}$ case, as they are not artificially mantained by the constant density inflow. However, the peak luminosities at breakout, and throughout much of the simulation, are very close to their counterparts for the $15M_{\odot}$ model. The RMS energies, aside from showing the same sort of slow decay at very late times, are even more akin to the $15M_{\odot}$ results. The plots are virtually indistinguishable for most of the simulation. All the matter profiles are alarmingly similar for each of the models. This convergence of results is due to the similarity of the initial progenitor models. The initial density, temperature, and Y_e profiles for both the $15M_{\odot}$ and the $20M_{\odot}$ simulations are all but identical. As was shown in

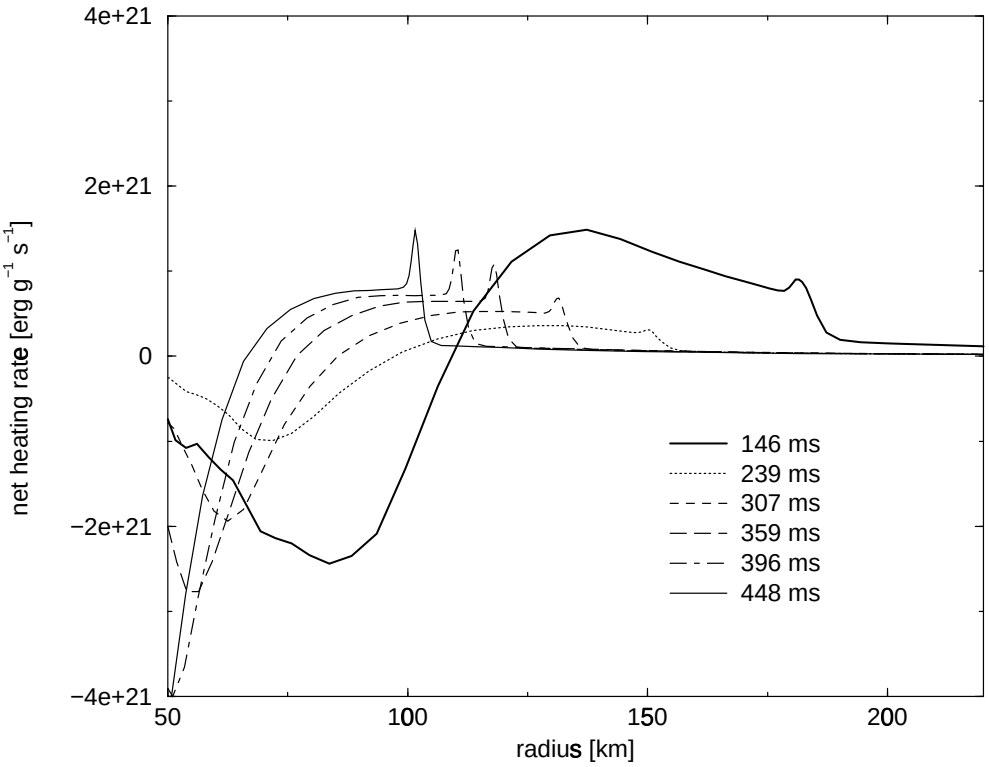

Figure 8.21: Net neutrino heating rates from emission and absorption of electron neutrinos and antineutrinos at various post-bounce times for the Nomoto-Hashimoto $20M_{\odot}$ model

Chapter 6, nearly identical initial conditions will result in identical collapse trajectories for each simulation. The similarity of these models, from the onset of collapse to almost 0.5 seconds after bounce, suggests a larger range of progenitor masses needs to be explored.

Chapter 9

Conclusions and Outlook

AGILE-BOLTZTRAN is a state-of-the-art radiation hydrodynamics code based on Boltzmann neutrino transport. We have provided a detailed description of the equations solved by the code and their numerical implementation. AGILE-BOLTZTRAN has been tested in several different ways, clearly delineating its strengths and weaknesses.

We have compared transport simulations in hydrostatic postbounce slices performed with AGILE-BOLTZTRAN to identical simulations performed with a sophisticated approximate scheme (MGFLD). Extensive differences in neutrino observables are seen, resulting in differences in neutrino net heating rates in postbounce environments as large as a factor of two.

The code has been used to investigate the impact of improved weak interaction physics in progenitor models on collapse evolution. A remarkable convergence of collapse dynamics is observed. Initial differences in electron fraction in progenitor models evolved using FFN versus shell model weak interaction rates are obliterated and lead to no discernable effect on shock formation position and postbounce evolution.

The collapse, rebound, and late-time evolution of two different progenitors has been sim-

ulated. Neither the $15M_{\odot}$ nor the $20M_{\odot}$ progenitor model of Nomoto & Hashimoto (1988) result in an explosion during the first ≈ 450 ms after core bounce. The dynamics and neutrino observables for both models show amazing similarities. The marked similarity of the two initial progenitor structures leads directly to this convergence of results. These results point to the need to explore fully the parameter space of progenitor models.

The development of AGILE-BOLTZTRAN is a necessary first step towards solving the supernova problem. Exact neutrino transport is a vital ingredient for any decisive supernova simulation. Spherically symmetric simulations with Boltzmann transport serve to isolate the effects of transport alone; without the complication of multidimensional effects. Multidimensional effects manifest themselves in the polarization of supernovae light (Wang et al. 1996), the formation of nickel bullets in SN1987A (Strom et al. 1995), and neutron star natal kicks (Harrison et al. 1993; Lyne & Lorimer 1994). But, the initiation of the explosion could be a spherically symmetric phenomenon. The observable effects of breaking spherical symmetry may be just that: only observable effects of setting off an explosion in an environment that is neither homogeneous nor completely isotropic. Also, although it is true supernovae are certainly not completely spherically symmetric, some supernovae might be close to spherically symmetric. Even if supernovae are multidimensional in character, one-dimensional simulations tell us whether it is possible to drive explosion with neutrino heating alone. The use of exact transport allows us to make, for the first time, unambiguous statements regarding the need for multidimensional effects. Exact transport in spherical symmetry is also the only means to effectively gauge transport approximations used in multidimensional simulations.

Our comparisons with MGFLD point out the necessity of Boltzmann transport. Macroscopic differences like the ones seen in Chapter 5 cannot be ignored. Although Boltzmann transport might be unable to turn a failed spherically symmetric supernova into an explosion, the dif-

ferences could have important effects on, for example, explosive nucleosynthesis and neutrino signatures, especially burst phenomena, in terrestrial detectors. Also, the increased heating seen using Boltzmann transport could lead to increased convection in multidimensional simulations.

Our studies of the core collapse of the two versions of the $15M_{\odot}$ progenitor of Woosley and Weaver highlight the need to improve the microphysics employed in AGILE-BOLTZTRAN. It is difficult to predict what effect inclusion of weak interaction physics like that in Heger et al. (2000) might have during core collapse. Weak interaction rates for nuclei have to be improved, along with the use of nuclear ensembles rather than our present use of a representative nucleus. Moreover, the inclusion of correlation effects and nucleon-nucleon bremsstrahlung in the PNS during the postbounce shock reheating phase are two immediate improvements to the microphysics that are currently being undertaken.

AGILE-BOLTZTRAN must become a parallel code. This transformation is the only reasonable path for performing simulations for a large range of progenitor masses, input physics, and resolutions. Building a library of simulations such as this is necessary to determine important parameters affecting supernova outcomes, as well as providing neutrino data for terrestrial detectors. AGILE-BOLTZTRAN is uniquely suited to provide neutrino signature predictions, and an extensive set of simulations is needed to make up a set of templates against which a future detection can be compared.

Three–dimensional radiation hydrodynamics simulations with Boltzmann transport are the only endpoint of investigation that will be truly satisfactory. Simulations will also have to be performed in full general relativity and incorporate stellar rotation and magnetic fields. This is a computational challenge on the terascale and beyond. Even optimistic extrapolations of computer technology fall short of the resources in computational speed and memory required for the immediate future. Nevertheless, the road to the Grail leads only across this frontier.

Bibliography

Bibliography

Arnett, W. D. 1966, Can. J. Phys., 44, 2553

—. 1967, Can. J. Phys., 45, 1621

—. 1977, Astrophys. J., 218, 815

Baade, W. & Zwicky, F. 1934, Proc. Natl. Acad. Sci. USA, 20, 259

Bahcall, J. 1989, Neutrino Astrophysics (New York: Cambridge University Press)

Baron, E., Cooperstein, J., & Kahana, S. 1985, Phys. Rev. Lett., 55, 126

Bethe, H. H., Brown, G., Applegate, J., & Lattimer, J. 1979, Nucl. Phys. A, 324, 487

Bethe, H. H. & Wilson, J. R. 1985, Astrophys. J., 295, 14

Bowers, R. L. & Wilson, J. R. 1982, Astrophys. J., Suppl. Ser., 50, 115

Bruenn, S. W. 1985, Astrophys. J., Suppl. Ser., 58, 771

Bruenn, S. W. 1993, in Nuclear Physics in the Universe, ed. M. W. Guidry & M. R. Strayer (Bristol: IOP Publishing), 31

Burbidge, E. M., Burbidge, G. R., Fowler, W. A., & Hoyle, F. 1957, Rev. Mod. Phys., 29, 547

Burrows, A. 1990, Annual Review of Nuclear and Particle Science, 40, 181

Burrows, A. 1998, in Proc. of the 18th Texas Symposium on Relativistic Astrophysics, ed. A. Olinto, J. Frieman, & D. Schramm (Singapore: World Scientific), 709

Burrows, A. & Goshy, J. 1993, Astrophys. J., Lett., 416, L75

Burrows, A., Hayes, J., & Fryxell, B. A. 1995, Astrophys. J., 450, 830

Burrows, A., Young, T., Pinto, P., Eastman, R., & Thompson, T. A. 2000, Astrophys. J., 539, 865

Castor, J. L. 1972, Astrophys. J., 178, 779

Colgate, S. A. & White, R. H. 1966, Astrophys. J., 143, 626

Cooperstein, J., van den Horn, L. J., & Baron, E. A. 1986, Astrophys. J., 309, 653

Duderstadt, J. & Martin, W. 1979, Transport Theory (New York: Wiley)

Fuller, G. M., Fowler, W. A., & Newman, M. J. 1980, Astrophys. J., Suppl. Ser., 42, 447

Gradshteyn, I. & Ryzhik, I. 1980, Table of Integrals, Series, and Products (Orlando: Academic)

Hansen, C. J. 1966, PhD thesis, Yale University

Harrison, P. A., Lyne, A. G., & Anderson, B. 1993, Mon. Not. R. Astron. Soc., 261, 113

Heger, A., Langanke, K., Martínez-Pinedo, G., & Woosley, S. E. 2000, submitted to Phys. Rev. Lett.; astro-ph/0007412

Herant, M., Benz, W., Hix, W. R., Fryer, C. L., & Colgate, S. A. 1994, Astrophys. J., 435, 339

Hillebrandt, W., Nomoto, K., & Wolff, R. G. 1984, Astron. Astrophys., 133, 175

Hix, W. R. & Thielemann, F.-K. 1999, Astrophysical Journal, 511, 862

Hoyle, F. & Fowler, W. A. 1960, Astrophys. J., 132, 565

Hummer, D. G. & Rybicki, G. B. 1971, Mon. Not. R. Astron. Soc., 152, 1

Janka, H.-T. & Müller, E. 1996a, Astrophys. J., Lett., 448, L109

—. 1996b, Astron. Astrophys., 306, 167

Kolbig, K., Mignaco, J., & Remiddi, E. 1970, Bol., Inst. Tonantzintta, 10, 38

Kosirev, N. A. 1934, Mon. Not. R. Astron. Soc., 94, 430

Landau, L. 1932, Phys. Z. Sowjetunion, 1, 285

Larsen, E. W., Morel, J. E., & Miller Jr, W. 1987, J. Comp. Phys., 69, 283

Lattimer, J. M. & Swesty, F. D. 1991, Nucl. Phys. A, 535, 331

Levermore, C. D. 1981, Astrophys. J., 248, 321

Lewis, E. E. & Miller, W. 1984, Computational Methods of Neutron Transport (New York: Wiley)

Liebendörfer, M. 2000, PhD thesis, University of Basel

Lund, C. M. 1985, in Numerical Astrophysics, ed. J. M. Centrella, J. M. LeBlanc, & R. L. Bowers (Boston: Jones and Bartlett), 498–533

Lyne, A. G. & Lorimer, D. R. 1994, Nature, 369, 127

Mazurek, T. J. 1973, PhD thesis, Yeshiva University

—. 1975, Astro. Space Sci., 35, 117

Messer, O. E. B., Mezzacappa, A., Bruenn, S. W., & Guidry, M. W. 1998, Astrophys. J., 507, 353

Mezzacappa, A. & Bruenn, S. W. 1993a, Astrophys. J., 405, 637

—. 1993b, Astrophys. J., 405, 669

—. 1993c, Astrophys. J., 410, 740

Mezzacappa, A., Calder, A. C., Bruenn, S. W., Blondin, J. M., Guidry, M. W., Strayer, M. R., & Umar, A. S. 1998a, Astrophys. J., 493, 848

—. 1998b, Astrophys. J., 495, 911

Mezzacappa, A. & Matzner, R. A. 1989, Astrophys. J., 343, 853

Mezzacappa, A. & Messer, O. E. B. 1998, Journal of Computational and Applied Mathematics, 109, 281

Mihalas, D. & Mihalas, B. W. 1984, Foundations of Radiation Hydrodynamics (New York: Oxford)

Milne, E. A. 1928, Mon. Not. R. Astron. Soc., 89, 3

Mitton, S. 1978, The Crab Nebula (New York: Charles Scribner's Sons)

Myra, E. & Burrows, A. 1990, Astrophys. J., 364, 222

Myra, E. S., Bludman, S. A., Hoffman, Y., Lichenstadt, I., Sack, N., & van Riper, K. A. 1987, Astrophys. J., 318, 744

Nomoto, K. & Hashimoto, M. 1988, Phys. Rep., 163, 13

Press, W. H., Teukolsky, S. A., Vetterling, W. T., & Flannery, B. P. 1996, Numerical Recipes in Fortran 77, Second Edition (New York: Cambridge)

Raffelt, G. 1996, Stars as Laboratories for Fundamental Physics: The Astrophysics of Neutrinos, Axions, and Other Weakly Interacting Particles (Chicago : University of Chicago Press)

Rampp, M. & Janka, H. . 2000, Astrophys. J., Lett., 539, L33

Roache, P. J. 1998, Computational Fluid Dynamics (Albuquerque: Hermosa)

Sato, K. 1975, Prog. Theor. Phys., 54, 1325

Schinder, P. J. 1990, Astrophys. J., Suppl. Ser., 74, 249

Schinder, P. J. & Bludman, S. A. 1989, Astrophys. J., 346, 350

Schinder, P. J. & Shapiro, S. L. 1982, Astrophys. J., Suppl. Ser., 50, 23

Strom, R., Johnston, H. M., Verbunt, F., & Aschenbach, B. 1995, Nature, 373, 590

Swesty, F. D. & Lattimer, J. 1994, Astrophys. J., 425, 195

Van Riper, K. A. & Lattimer, J. 1981, Astrophys. J., 249, 270

Wang, L., Wheeler, J. C., Li, Z. W., & Clocchiatti, A. 1996, Astrophys. J., 467, 435

Wilson, J. R. 1985, in Numerical Astrophysics, ed. J. M. Centrella, J. M. LeBlanc, & R. L. Bowers (Boston: Jones and Bartlett), 422–434

Wilson, J. R. & Mayle, R. W. 1988, Phys. Rep., 163, 63

—. 1993, Phys. Rep., 227, 97

Woosley, S. E. 1995, Private Communication

Woosley, S. E. & Weaver, T. A. 1995, Astrophys. J., Suppl. Ser., 101, 181

Yahil, A. 1983, Astrophys. J., 265, 1047

Yueh, W. & Buchler, J. 1977, Astrophys. J., 217, 565

Vita

Otis Earl Messer II (Bronson) was born in Bryson City, N.C. on July 10, 1970. He attended Swain County Public Schools until he matriculated into the University of Tennessee as an early-admission freshman in September, 1987. During his undergraduate career, he was a member of the University's ACF National Championship Collge Bowl team in 1991 and was inducted into the Sigma Pi Sigma physics honor society that same year. He earned a B. S. in Physics, with Honors, in May, 1991. He returned to the University in the fall of 1992, enrolling in the doctoral program in Physics. He was awarded the Paul H. Stelson Fellowship in Physics in April, 2000.